ABSTRACT

The proliferation of mobile communications technology increases the demands for faster and more robust services, in addition to the ever decreasing sizes of antennas. These demands can be satisfied using circularly polarized (CP) dielectric resonator antennas (DRAs) exhibiting wide operational bandwidth capability. By utilizing such antennas, the probability of linking the transmitted and received signals is higher, and the system is more reliable since the CP wave is transmitted in all planes and less susceptible to unwanted reflections and absorptions. As CP system is insensitive to the transmitter and receiver orientation, the time consuming practice of continuously aligning the antennas can be avoided. Furthermore, the antennas profile can be reduced simply by using dielectric material with higher permittivity.

The thesis focuses on the design and analysis of singly-fed regular-shaped DRAs with a wideband circular polarization. Two new single-point excitation schemes that can be easily used to excite an arbitrarily shaped DRA are introduced, where a square spiral and a rectangular open half-loop are used for DRA excitation. These proposed feeding methods are based on employing conformal conducting metal strips that are placed on the DRA surface. Additionally, two different approaches are employed onto the DRA design to enhance the CP bandwidth. The first approach is based on using a multilayer dielectric, and the second introduces a parasitic half-loop inside the feeding element. The generated broad CP bands have been achieved in conjunction with sufficient impedance matching bandwidths. The studied geometries have been modeled using a comprehensive self developed MoM code that employs the

volume surface integral equation (VSIE). The computed results have been validated against those obtained from measurements as well as CST microwave studio simulations. Theoretical and experimental results demonstrate a several folds enhancement in the CP bandwidths compared to those reported in the literature for identical DRA geometries.

ACKNOWLEDGEMENTS

PUBLICATIONS

- M.I. Sulaiman and S.K Khamas, "A Singly Fed Wideband Circularly Polarized Dielectric Resonator Antenna Using Concentric Open Half-Loops," *IEEE Antennas and Wireless Propagation Letters,* vol.10, pp.1305-1308, 2011

- M.I. Sulaiman and S.K Khamas, "A Singly Fed Rectangular Dielectric Resonator Antenna With a Wideband Circular Polarization," *IEEE Antennas and Wireless Propagation Letters,* vol.9, pp.615-618, 2010

- M.I. Sulaiman and S.K Khamas, "Correction to "A Singly Fed Rectangular Dielectric Resonator Antenna With a Wideband Circular Polarization" [2010 615-618]," *IEEE Antennas and Wireless Propagation Letters,* vol.9, pp.1286, 2010

- M.I. Sulaiman and S.K Khamas, "Singly-fed dielectric resonator antenna with a wideband circular polarization," *Antennas and Propagation (EUCAP), Proceedings of the 5th European Conference, 2011 Rome*, pp.1950-1952, 11-15 April 2011

- M.I. Sulaiman and S.K Khamas, "Frequency tuning of a singly-fed rectangular dielectric resonator antenna with a wideband circular polarization," *Antennas and Propagation Conference (LAPC), 2011 Loughborough* , pp.1-3, 14-15 Nov. 2011

TABLE OF CONTENTS

LIST OF FIGURES

LIST OF TABLES

LIST OF ACRONYMS

AMC	Artificial magnetic conducting
AR	Axial ratio
CEM	Computational electromagnetics
CP	Circularly polarized
DE	Differential equation
DRA	Dielectric resonator antenna
DWM	Dielectric waveguide model
E	Electric field
EFIE	Electric field integral equation
FD	Frequency-domain
FDDE	Frequency-domain differential equation
FDIE	Frequency-domain integral equation
FDTD	Finite-difference time-domain
FEM	Finite element method
FIT	Finite integration technique
H	Magnetic field
IE	Integral equation
LHCP	Left-hand circularly polarized
LP	Linearly polarized
MoM	Method of moments
NAG	Numerical Algorithms Group
PEC	Perfect electrically conducting
RHCP	Right-hand circularly polarized

RHS	Right hand side
RWG	Rao-Wilton-Glisson
SWG	Schaubert-Wilton-Glisson
TD	Time-domain
TDDE	Time-domain differential equation
TE	Transverse Electric
TLM	Transmission line method
TM	Transverse Magnetic
VSIE	Volume surface integral equation
VSWR	Voltage standing wave ratio

CHAPTER 1

INTRODUCTION

1.1   Background

Compact and highly efficient antennas exhibiting wide operational bandwidth capability are becoming increasingly popular for current research activity in the wireless communication technology. Dielectric resonator antenna (DRA) remains one of the most attractive candidates for such requirements. The size of the antenna can be minimized simply by increasing the dielectric constant, ε_r of the material [1] since the dimensions of the DRA are proportional to $\lambda_0 / \sqrt{\varepsilon_r}$, where λ_0 is the free-space wavelength. Additionally, very high radiation efficiency (>98%) can be achieved using DRA, even at millimetre-wave frequency operation, by selecting a low-loss dielectric material. This results from the absence of conductor losses and surface waves associated with the antenna [2]. Surface waves are EM waves that propagate along an interface between two different

media. Strong excitation of surface waves, such as in microstrip antenna design, is undesirable since power launched into the surface waves is power which will eventually be lost.

Furthermore, a DRA has a wider impedance bandwidth compared to other antenna types such as a microstrip antenna. This is mainly due to the fact that the waves radiate through the entire DRA surface, except for the ground, in contrast with the limited radiation of waves through two narrow edges of the patch in a microstrip antenna [3]. DRA also offers high design flexibility since its resonance frequency, excited modes and radiation characteristics are dependent on the antenna's aspect ratio, dielectric constant and coupling mechanism. Additionally, the required design specifications can be accomplished when a DRA is employed owing to the availability of dielectric materials offering a wide range of electrical permittivities, and the existence of several feeding mechanisms including slots, microstrip lines and probes.

The studies of dielectric resonator as antenna (instead of energy storage devices) began in early 1980s with investigations of the characteristics of basic DRA shapes such as hemispherical, cylindrical and rectangular geometries that have been conducted by Long, McAlister and Shen [4-6]. Since this breakthrough, researchers have investigated numerous DRA feeding mechanisms, and applied various analytical or numerical techniques to calculate the antenna's resonance frequency and operating bandwidth. Much of these works have been summarized in a review paper by Mongia and Bhartia [7]. Recently, the emphasis of researchers in this field has been on designing a CP DRA and enhancing its impedance matching bandwidth performance. This research adopts similar trend with additional aims and objectives outlined in the next section.

1.2 Aims and Objectives

The research is conducted with the aim of designing a wideband CP DRA using a single-point feeding system. Additionally, the antenna should offer a sufficient impedance matching bandwidth at the same frequency range of the achieved circular polarization. Several objectives must be satisfied in order to achieve these aims.

The first is to create a new single-point excitation schemes that can be easily applied to an arbitrarily shaped DRA. In this research, two variations of conformal conducting metal strips excitation are introduced, namely square spiral strip and rectangular open half-loop strip. The second objective is to develop a rigorous Computational Electromagnetics (CEM) model to simulate the electromagnetic fields interaction between the DRAs fed by the conformal conducting strip and its surrounding environment. For this purpose, the Method of Moments (MoM) has been chosen in conjunction with specialized basis functions as discussed in chapter 2.

The next objective is to build the prototypes of the singly-fed DRAs. Prior to production, near-field and far-field properties, such as S_{11} and axial ratio, should be optimized through simulation. Then, the performances of these DRAs are to be measured using a vector network analyzer.

Finally, the obtained experimental results are compared with the predicted results. In depth analysis and discussions of these results are presented in the thesis.

1.3   Circularly Polarized DRA

Initially, investigation of DRAs as wireless communication devices was mainly concentrated on those producing linearly polarized (LP) waves since they are easier to design than CP DRAs. However with the rapid advancement of satellite communications technology, more attention has been paid to the latter due to its known advantages.

The CP system is favoured over its LP counterpart owing to its insensitivity to the transmitter and receiver orientation. The probability of linking the transmitted CP wave is higher since it radiates in the horizontal, vertical as well as any plane in between. In contrast, LP wave is capable of radiating in one plane only, which is particularly problematic in space-borne applications. Based on Faraday's law, time varying magnetic flux induced electric field with rotation. Since ionosphere (85km to 600km altitude) consists of magnetized plasma with free electrons due to solar radiation, the polarization of EM waves passing through this layer will be rotated. To compensate for this effect, the receiver antenna should be aligned continuously which can be time consuming as this alignment must be precise.

 Additionally, a CP wave that is transmitting in all planes is less susceptible to unwanted reflection and absorption. This effectively eliminates multi-path problems which occur when an antenna receives the primary and reflected waves at approximately the same time, creating an out-of-phase problem which can cause dead-spots and reduce the system's overall performance.

In recent years, tremendous research efforts have been spent on designing CP DRAs of various shapes. Much of these works will be summarized and categorized in section 1.3.2.

1.3.1 Theory of Circular Polarization

It is crucial to understand the wave polarization theory when designing a CP antenna. Polarization is defined as the orientation of electric field vector, $\vec{E}$ during the wave propagation. $\vec{E}$ is perpendicular to both magnetic field vector, $\vec{H}$ and the direction of the travelling wave. To illustrate the polarization of an electromagnetic wave, consider a z-directed plane wave where the $\vec{E}$ field has components in both x and y direction. The time-harmonic $\vec{E}$ at $z = 0$ is represented by

$$\vec{E} = E_x \cos(\omega t + \phi_x)\hat{x} + E_y \cos(\omega t + \phi_y)\hat{y} \tag{1-1}$$

When the phase of these two $\vec{E}$ components are identical ($\phi_x = \phi_y = \phi_0$), its amplitude, $|\vec{E}|$, and angular orientation, Ψ, with regard to y-axis are given by

$$|\vec{E}| = \sqrt{(E_x^2 + E_y^2)}\cos(\omega t + \phi_0) \tag{1-2}$$

$$\Psi = \arctan\left(\frac{E_y}{E_x}\right) \tag{1-3}$$

In this case, the wave is said to be LP since Ψ has no time dependence and hence the field vector traces out as a straight line over time. On the other hand, when the magnitudes of the $\vec{E}$ components are equal ($E_x = E_y = E_0$) and there is a $\pi/2$ difference in the phase components, the $|\vec{E}|$ and Ψ are given by

$$|\vec{E}| = \sqrt{\left(\left(E_0 \cos\left(\omega t + \phi_y \pm \frac{\pi}{2}\right)\right)^2 + (E_0 \cos(\omega t + \phi_y))^2\right)} = E_0 \tag{1-4}$$

$$\Psi = \arctan\left(\frac{E_0 \cos\left(\omega t + \phi_y \pm \dfrac{\pi}{2}\right)}{E_x \cos(\omega t + \phi_y)}\right) = \arctan\left(\frac{\pm \sin(wt + \phi_y)}{\cos(\omega t + \phi_y)}\right) = \phi_y \pm \omega t \qquad (1\text{-}5)$$

This means the field vector is travelling with constant amplitude that rotates either in a clockwise, or an anticlockwise, direction. As a result, the vector traces out as a circle with time and thus the wave is said to be CP. Most of the time, the wave is elliptically polarized, for which the amplitude and orientation of $\vec{E}$ changes with time, tracing out an ellipse. In order to quantify the type of polarization, the axial ratio (AR) is used, which is defined as the ratio of the major to minor axes of this ellipse and usually expressed in decibels as

$$AR = 20\log\left(\frac{E_{max}}{E_{min}}\right) \qquad (1\text{-}6)$$

where E_{min} and E_{max} represent the magnitude of the minimum and maximum $\vec{E}$, respectively. The wave is said to be CP when AR is less or equal to 3dB.

Equations (1-4) and (1-5) show that circular polarization can be created using an antenna capable of producing two spatially orthogonal LP waves that have equal magnitudes and in phase quadrature, i.e. with a $\pi/2$ difference in the phase components. Therefore, CP DRA can be designed simply by applying two-point quadrature feeds on a DRA which is capable of supporting two orthogonal degenerate modes, i.e. modes that have the same resonance frequency. This dual-point feeding method typically yields a wide AR bandwidth that exceeds 10%. However, this approach has the disadvantages of increasing the complexity and size of the feed network considerably. Alternatively, CP DRA can be created using a single–point feeding system as described in section 1.3.2.2

1.3.2 Review of Circularly Polarized DRA

1.3.2.1 Dual-Point Feeding System

For the generation of two spatially orthogonal LP waves that are in phase quadrature and have equal amplitudes, the DRAs must have the capability of supporting two orthogonal degenerate modes. This requirement is satisfied by DRAs which exhibit symmetry along the x and y axes such as rectangular, ring, and cylindrical DRAs shown in Figure 1.1.
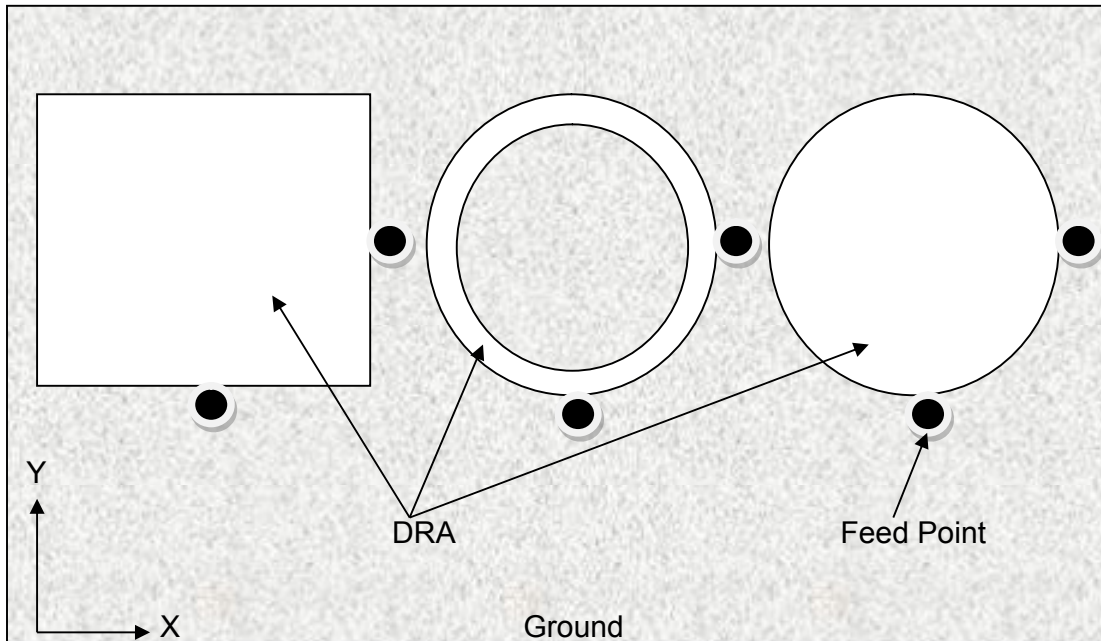
Figure 1.1: Top view of several DRAs which are capable of generating CP wave

These DRAs radiate CP waves when excited by two identical feeds placed on orthogonal DRA sides. The feeds must have signals of equal amplitudes and being in phase quadrature to each other. Typically, a power divider network such as a T-junction splitter and a hybrid coupler is used in order to obtain such feed excitation. The most popular shape used for dual-point feed CP DRA is cylindrical. Drossos et al [8] have reported a 20% 3dB AR bandwidth for a probe-fed DRA,

which has a relative permittivity of ε_r=37, using a microstrip quadrature hybrid feed network. A dual conformal strip-fed DRA, with ε_r=9.5, has been designed using a microstrip hybrid coupler network [9], achieving a 20% CP bandwidth. In [10], underlaid hybrid couplers were used to provide the required excitation for the two flat strips that are printed on the surface of an ε_r=9.5 cylindrical DRA, with a 3dB AR bandwidth of 25.9%. A simpler design using a T-junction splitter has been proposed for a strip-fed DRA with a narrower AR bandwidth of 3.5% [11]. For a cylindrical ring, a 2dB AR bandwidth of 11% was reported in [12] for a probe-fed DRA $\left(\varepsilon_r = 36.2 \right)$ using a quadrature coupler. Additionally, several examples of dual-point feed CP rectangular DRA have been published in literature. For example, a conformal strip-fed DRA $\left(\varepsilon_r = 12 \right)$ was designed in [13] using hybrid coupler network, achieving a 3dB AR bandwidth of 35%. When used in conjunction with underlaid hybrid couplers, 27.7% and 33.8% 3dB AR bandwidths have been reported for strip-fed and hollow rectangular DRAs $\left(\varepsilon_r = 10 \right)$, respectively [14] [15]. In all of the studies, the generated broad CP bands have been achieved in conjunction with sufficient impedance matching bandwidths.

Although wide AR bandwidths of >10% have been obtained in most cases, there are several major disadvantages of using the dual-point feeding system. For instance, incorporating an additional power divider network significantly increases the antenna's size. Furthermore, antenna designers should take into account the coupling effect between the two feeds. If the mutual coupling between the feeds is significant, the field components will be disturbed, and hence cause reduction in the resultant AR bandwidth. Therefore, it is important to establish a high isolation between the two feed ports in order to avoid degradation in the AR performance.

1.3.2.2 Single-Point Feeding System

A single-point feeding system is proven to be more attractive option for most researchers. Although the AR bandwidth of this system is usually less than that of a dual feed system, this method does not require complex feeding network and offers a smaller overall antenna profile. Additionally, it is easier to incorporate a single-point feeding system in an array environment. Several methods of generating CP waves from basic-shaped DRAs have been reported in literature.

A well-known procedure to design a singly-fed CP DRA is to introduce some modifications to the DRA geometry. The first reported singly-fed CP DRA is the chamfered DRA, which replicates a shape used in existing CP microstrip patch antenna technology. In such approach, two opposite corners of a square rectangular DRA have been truncated by cross-sectional areas of $g^2/2$ as illustrated in Figure 1.2. A probe-fed chamfered DRA$(\varepsilon_r = 38)$ has demonstrated a 3dB AR of 1.3% as reported in [16]. Another approach that has been borrowed from a concept used in the design of microstrip patches is the quasi square DRA [17-20], where a cross-sectional area of g × w is added on one side of a square DRA. The DRA can be fed either by an aperture placed near the centre or by a probe positioned along the diagonal surface as shown in Figure 1.3. An example of such a design for an aperture-fed DRA$(\varepsilon_r = 40)$ has reported a 2% 3dB AR bandwidth [17]. In both cases, the perturbation of one of the DRA's dimensions has caused the resonance of the two orthogonal modes to be separated such that their difference in phase response is $\pi/2$, hence making the DRA capable of generating the required CP wave. Additionally, analyses on a cross-shaped DRA have revealed its capability of producing two spatially orthogonal LP waves which

are necessary for a CP system. A 3dB AR bandwidth of approximately 4% was reported in [21] for an aperture-fed cross DRA$(\varepsilon_r = 10.8)$. Geometrical modification has also been applied to cylindrical DRA, as reported in [22] where a conformal strip-fed circular sector DRA$(\varepsilon_r = 12)$ has demonstrated a 3dB AR of 10%.
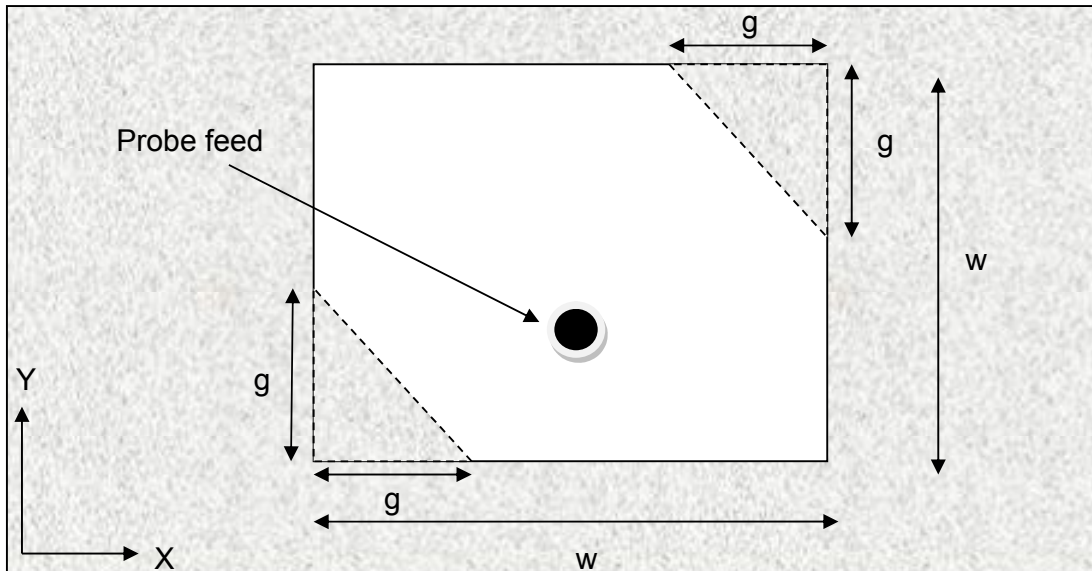
Figure 1.2: Top view of chamfered DRA
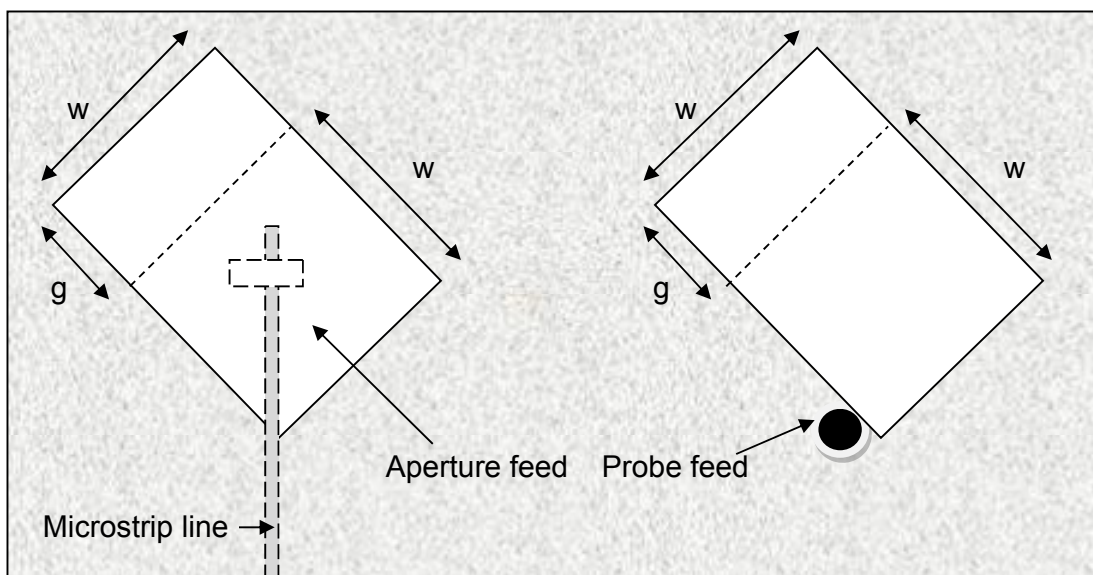
Figure 1.3: Top view of quasi square DRA fed by probe and aperture

Alternatively, modifications can to be done to the feed itself rather than the DRA's geometry. Huang et al [23] employed a cross-shaped slot fed with a microstrip line as shown in Figure 1.4 to generate CP waves from a cylindrical DRA. The desired $\pi/2$ phase difference between the degenerate modes has been achieved simply by manipulating the cross's arms lengths, l_u and l_v. A 3dB AR bandwidth of 3.91% was reported in [23] for a cylindrical DRA $(\varepsilon_r = 79)$ using this feeding configuration.
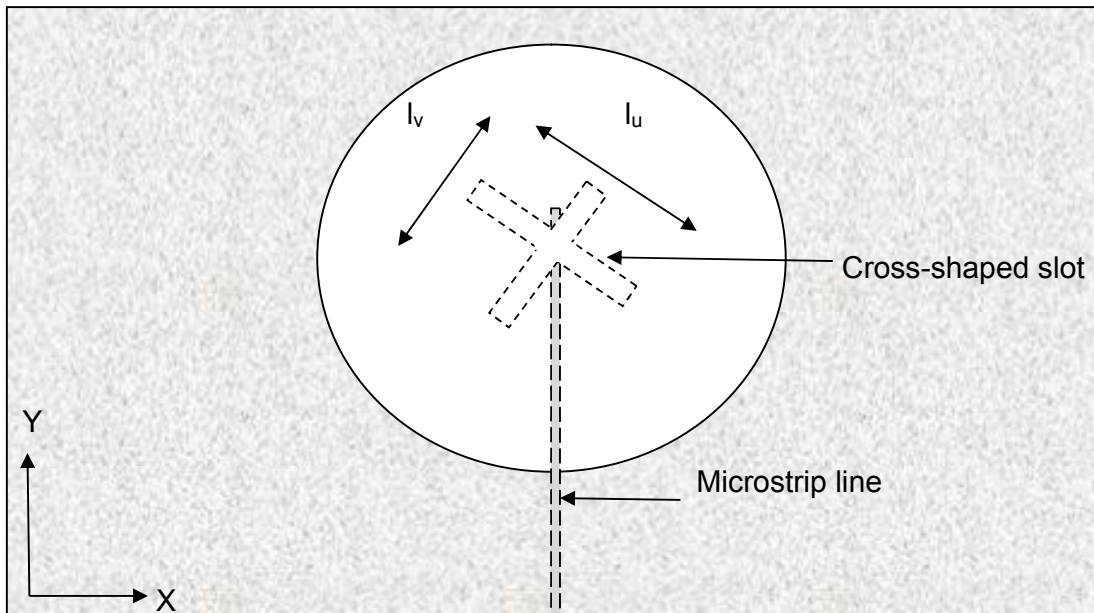
Figure 1.4: Top view of cylindrical DRA fed by cross-shaped slot

Furthermore, other special-shaped slots have been employed in the design of CP DRAs such as U-shaped slot for cylindrical DRA $(\varepsilon_r = 16)$ excitation [24], achieving a 2.4% 3dB AR bandwidth, and a tabbed annular slot used in [25] for a cylindrical DRA $(\varepsilon_r = 9.5)$ which produced a 3dB AR bandwidth of 3.4%. Although these slot excitations can be applied to various shapes DRA, it has the disadvantage of producing a high backlobe radiation which degrades the

antenna's performance. To suppress this unwanted radiation, a metallic cavity is used underneath the slot. Alternative feed modification methods have been reported in literature such as employing a U-shaped conformal strip [26] which reported a 3dB AR bandwidth of 2.3% for rectangular DRA $(\varepsilon_r = 30)$, and a conformal spiral wire used for a hemispherical DRA $(\varepsilon_r = 9.5)$ excitation which provided a 3.9% 3dB AR bandwidth [27].

An alternative way of generating a CP system is through the use of a parasitic element in the configuration. As a result, the tasks of generating circular polarization and impedance matching can be conveniently separated. Here, the parasitic element can be manipulated to obtain a wide AR bandwidth while the feed is independently adjusted to achieve an input match. As an example, two pairs of rectangular slots and a circular loop slot have been used as parasitic elements in [28] and [29], respectively, generating 3dB AR bandwidth of up to 2.7%. Alternative to parasitic slot, parasitic strips have been employed for a probe-fed DRA [30], a slot-fed DRA [31], a microstrip-fed DRA [32], and a conformal strip-fed DRA [33-35], where the reported 3dB AR bandwidths range between 1% and 3%. In those designs, the usage of a parasitic element has resulted in perturbation of one of the degenerate modes causing CP radiation.

In addition to the basic-shaped DRAs, some researchers have used complex-shaped DRAs to obtain an enhanced AR bandwidth for a single-point feed system. An aperture-fed stair-shaped DRA$(\varepsilon_r = 12)$ was designed in [36] as shown in Figure 1.5, achieving a CP bandwidth of10.6%. In a recent study, a trapezoidal DRA$(\varepsilon_r = 9.4)$ fed by a rectangular slot has been proposed as illustrated in Figure 1.6, which produced a 3dB AR bandwidth of 21.5% [37].
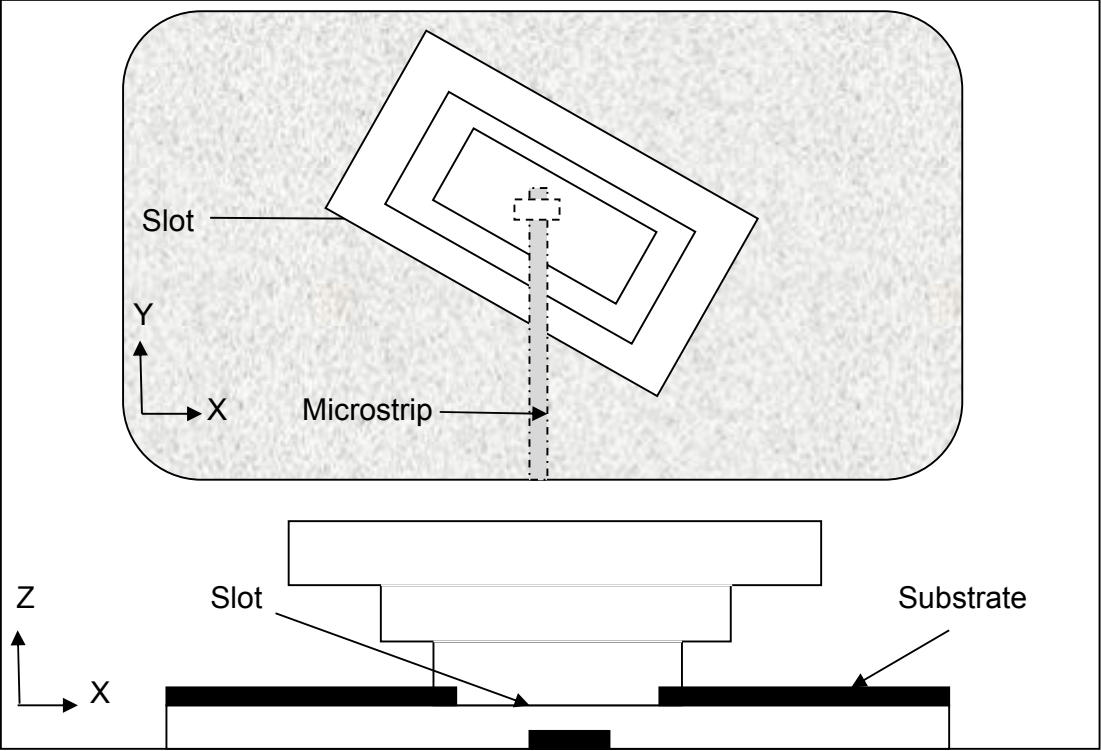
Figure 1.5: Top view and side view of aperture-fed stair-shaped DRA aperture
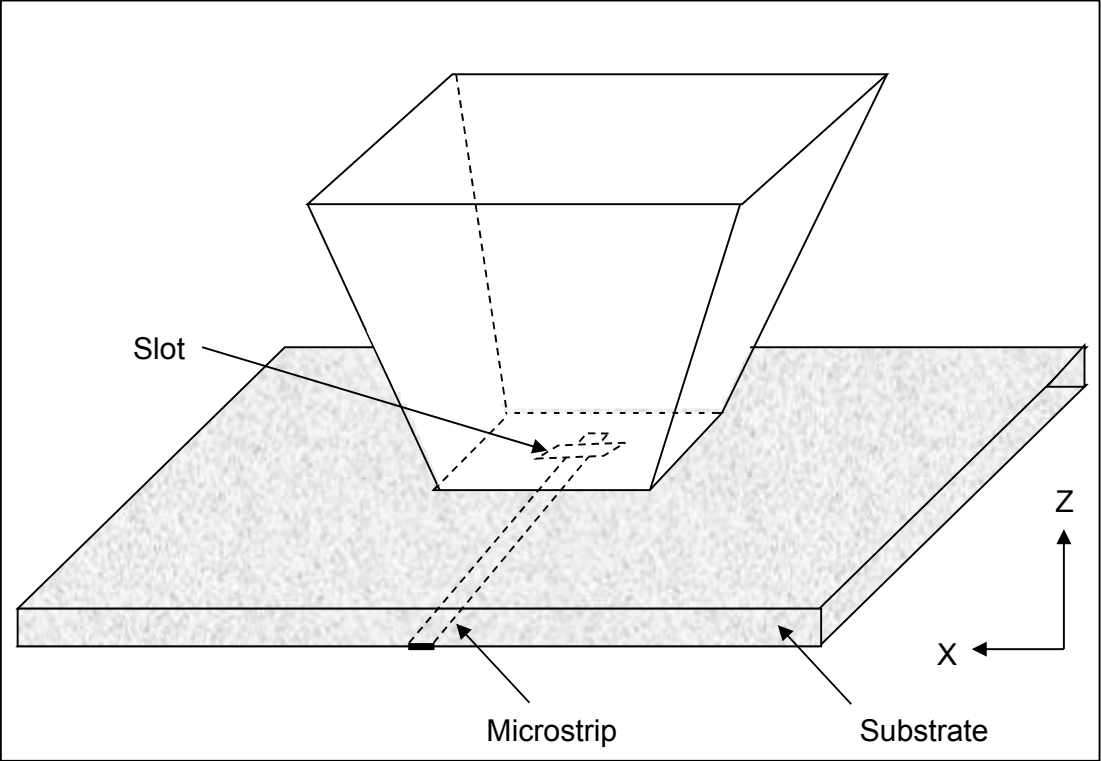
Figure 1.6: Aperture-fed trapezoidal DRA

Other irregular-shaped CP DRAs include a probe-fed elliptical DRA [38] which produced a 3.5% CP bandwidth. Unlike basic-shaped DRA, this DRA has the ability of generating several broadside radiating modes with close resonance frequencies, which results in a wider AR bandwidth. Although this is very desirable approach, a designer should take into account the high cost involved since these complex DRAs geometries are not readily available commercially. Also, the modelling of these complex geometries takes significantly longer computational time. Therefore, a flexible single-point feeding method that can be used to generate a wideband CP radiation from DRAs with regular geometries is needed. Such a feeding mechanism has not been reported in the published literature, and it represents the main aim of the work presented in this thesis.

1.4   Method of Analysis

The design and modelling of antenna plays a vital part in the wireless communication system. This important stage requires engineers and researchers to command a good understanding of electromagnetic field theory commonly referred to as EM. This theory is governed by Maxwell's equations, which contain a set of six fundamental partial differentiation equations that describes the interrelationship between electric and magnetic field, and relate them to their sources; current and charge density. EM modelling can be carried out either analytically or numerically. However, analytical solutions in closed form are known for limited number of cases only, involving simple structures which are hardly applicable in modern electromagnetic devices and systems. For complex

structures, the inability to derive closed form solutions of Maxwell's equations is solved by using computational numerical techniques.

The process of numerically modelling electromagnetic fields interactions with physical objects and the surrounding environment is called Computational electromagnetics (CEM). Typical modern computers have the capability of handling complex computation in relatively short time. This makes CEM stand out as an important tool in the design and modelling stages of antennas and other communication systems. Generally, in CEM, relevant Maxwell's equations are converted into chain or matrix equations which can be solved either by matrix inversion or by iteration.

It is highly beneficial for antenna designers using CEM to have a general understanding of the wide selection of methods available for the solution of electromagnetics problems, so that a well-informed choice can be made. With the correct application of the selected CEM method, the computation resources needed for designing an antenna can be optimized. As a result, the design and modelling stage is made faster and cheaper since the use of time consuming and costly antenna prototypes is minimized.

Modelling that yields accurate predictions requires full-wave analysis which considers all the relevant wave mechanism. To date, there are many full-wave EM methods that can be applied to model typical antenna structures. In general, these methods can be categorized into two types depending on their solution; either by differential equation (DE) or by integral equation (IE). During the pre-computer era, most research in CEM had taken place in the frequency-domain (FD) for which the time-harmonic behaviour is assumed despite the fact that the Maxwell equations are often first encountered in the time-domain (TD), where time is assumed to be

an independent variable. This is mainly because the FD approach was more tractable analytically, thus requiring less complex computation compared to a TD approach. Also, the FD approach is favoured because most antennas' measurement hardware at that time were largely confined to the FD system [39].

At the moment, the three major paradigms of CEM modelling are the Method of Moments (MOM), Finite-Difference Time-Domain (FDTD) and Finite Element Method (FEM). MOM is categorized as a Frequency-Domain Integral Equation (FDIE) model, where Maxwell's equations in integral form are discretized in order to determine the unknown field sources; induced current and charge density. Compared with other methods, MoM is very efficient for the treatment of highly conducting surfaces as the discretization involves the current density only and not the fields in the surrounding medium. Furthermore, solution process in MoM takes a relatively short time. However, since this method involves the solution of integral equation, the code implementation is harder compared to other modelling methods. MOM will be described further in Chapter 2. Examples of widely used MOM based software are FEKO [40], NEC [41] and WIPL-D Pro [42].

FDTD is classified as Time-Domain Differential Equation (TDDE) model. It involves the discretization of Maxwell's equations in a partial differential form using field components or potentials as unknowns on a uniform Cartesian grid of points. A major advantage of FDTD is the ability to obtain wideband data in one simulation only since the computation is not restricted to a single frequency as implemented in the FD approach. Generally, FDTD is efficient as it requires only few operations per grid point and can be easily adapted to solve variety of problems. However, FDTD is less efficient for the modelling of long, thin structures such as wire. This is because solution requires the entire computational domain to

be gridded, and since these grids must be small compared to the smallest wavelength, excessively large computational domain can be developed, which result in very long solution time. Examples of commercially available FDTD simulator are Apsim FDTD [43] and Remcom XFDTD [44].

As is the case with the MoM, FEM is mostly applied in frequency domain. In this case, FEM is classified as Frequency-Domain Differential Equation (FDDE). Using this approach, Maxwell's equations are solved numerically by dividing the region of interest into unstructured grids known as meshes. The complex boundaries approximation is much better than in FDTD model and hence provides more accurate results but the solution process require a larger memory size and relatively time consuming. Two of commercial software using FEM model are Ansoft HFSS [45] and Analyst STAAR [46].

Alternatively, other modelling methods such as Finite Integration Technique (FIT) and Transmission Line Method (TLM) can be employed for the solution of EM problems. In summary, these modelling methods have their own merits and drawbacks. Several researchers managed to achieve a better performance by combining this individual modelling method into a hybrid method. One such example is a MoM-FDTD hybrid modelling method formulated by R.A.Abd-Alhameed [47]. Additionally, a hybrid modelling method combining FDTD and FEM is developed by Rylander and Bondeson in [48]

In summary, each of the DE and IE solution method has its own strengths and weaknesses which are listed below [49, 50].

- DE method handles inhomogeneous, anisotropic or magneto-dielectric materials relatively easy, while IE method handling of such materials requires a high level of complexity.

- The implementation code required for DE method is simpler compared to IE method which requires solution of integral equation.

- In general, IE solutions are more accurate and efficient since the solution space is only confined to the object and radiation condition is automatically enforced by the Green's function where as the solution space in DE method take into account the object's surrounding environment where the radiation condition is not enforced which resulted in a certain anomalies. Additionally, spurious solution caused by numerical instability, which exists in DE method, is absent in the IE approach.

- With proper approximation, IE solution requires significantly shorter computation time, since much of the solution is pre-processed using fundamental electromagnetics theory and intensive mathematical modelling.

After evaluation of choices available, the modelling method selected for this research is MOM. Although this requires harder implementation code, the result obtained using MoM, which utilizes IE solution, is more accurate and efficient compared with other modelling methods such as FIT. This has been verified by comparing results from MoM and CST software with those obtained using measurements. Furthermore, the time required for the modelling of DRA configurations using MoM is shorter after appropriate approximation has been applied as discussed in Chapter 2.

1.5   Thesis Layout

Following this introduction, Chapter 2 provides details of the CEM modelling method used in this research. The steps involved in the adopted MoM computational method, in conjunction with specialized basis and testing functions are described comprehensively. In Chapter 3, the first single-point excitation scheme used in this research known as a square spiral strip is introduced. The results for spiral strip-fed wideband CP rectangular DRA are discussed and analyzed, together with its frequency tuning capability. In Chapter 4, the spiral strip-fed excitation is applied onto cylindrical DRA. The limitations of this feeding method are discussed in Chapter 5, which introduces an alternative simpler single-point excitation scheme used in this research, known as a rectangular open half-loop strip. This excitation is employed to basic-shaped DRAs, such as rectangular, cylindrical and hemispherical geometries. In Chapter 6, a further bandwidth enhancement method is proposed based on incorporating a parasitic half-loop in the regular shaped DRA structures. Finally, Chapter 7 presents concluding remarks, as well as recommendations for future work.

References

[1] J.L. Volakis, "Antenna Engineering Handbook," 4th ed., Chapter 17, pp.17-2, McGraw-Hill, 2007

[2] A. Petosa, "Dielectric Resonator Antenna Handbook," Chapter 1, pp.2, Artech House, 2007

[3] K.M. Luk and K.W. Leung, "Dielectric Resonator Antennas," Chapter 1, pp.2, Research Studies Press Ltd., 2002

[4] S.A. Long, M.W. McAllister and L.C. Shen, "The Resonant Cylindrical Dielectric Cavity Antenna," *IEEE Trans. Antennas Propag.*, vol.31, no.3, pp.406-412, Mar 1983

[5] M.W. McAllister and S.A. Long, "Rectangular Dielectric Resonator Antenna," *Electron. Lett.*, vol.19, pp.218-219, Mar 1983

[6] M.W. McAllister and S.A. Long, "Resonant Hemispherical Dielectric Resonator Antenna," *Electron. Lett.*, vol.20, pp.657-659, Aug1984

[7] R.K. Mongia and P. Bhartia, "Dielectric Resonator Antenna – A Review and General Design Relations for Resonant Frequency and Bandwidth," *International Journal of Microw. and Milimeter-Wave Computer Aided-Engineering*, vol.4, no.3, pp. 230-247,1994

[8] G. Drossos, Z. Wu and L.E. Davis, "Circular Polarised Cylindrical Dielectric Resonator Antenna," *Electron. Lett.*, vol.32, no. 4, pp.281-282, Feb 1996

[9] W.C. Wong, K.W. Leung, K.M. Luk and E.K.N. Yung, "Circular-Polarized Dielectric Resonator Antenna Excited by Dual Conformal Strips, "*Electron. Lett.*, vol.36, no.6, pp.484-486, Mar 2000

[10] K.W. Khoo, Y.X. Guo and L.C. Ong, "Wideband Circularly Polarized Dielectric Resonator Antenna," *IEEE Trans. Antennas Propag.*, vol. 55, no.7, pp.1929-1932, Jul 2007

[11] W.C. Wong and K.W. Leung, "Circularly Polarized Dielectric Resonator Antenna Excited by Dual Conformal Strips of Unequal Lengths, "*Microw. Opt. Tech. Lett.*, vol.29, no.5, pp.348-350, Jun 2001

[12] R.K. Mongia, A. Ittipiboon, M. Cuhaci and D. Roscoe, "Circularly Polarized Dielectric Resonator Antenna," *Electron. Lett.,* vol.30, no.17, pp.1361-1362, Aug 1994

[13] B. Li and X.Q. Sheng, "Quadrature-fed Wideband Circularly Polarized Dielectric Resonator Antenna," *Microw. Conference APMC 2008*, pp.1-4, Dec. 2008

[14] Y. Pan, K.W. Leung and E.H. Lim, "Compact Wideband Circularly Polarized Rectangular Dielectric Resonator Antenna with Underlaid Hybrid Coupler," *Microw. Opt. Tech. Lett.*, vol.52, no.12, pp.2789-2791, Jun 2010

[15] E. H. Lim, K. W. Leung, and X. S. Fang, "The Compact Circularly-Polarized Hollow Rectangular Dielectric Resonator Antenna With an Underlaid Quadrature Coupler," *IEEE Trans. Antennas Propag.*, vol.59, no.1, pp.288-293, Jan 2011

[16] S.A. Malekabedi and M.H. Neshati, "Circular Polarized Dielectric Resonator Antennas using a Single Probe Feed," *Progress in Electromagnetic Research C*, vol.3, pp.81-94, 2008

[17] M.B. Oliver,R.K. Mongia and Y.M.M. Antar, "A New Broadband Circularly Polarized Dielectric Resonator Antenna," *IEEE Antennas Propag. Symposium AP-S,* Newport Beach, CA, pp.738-741, 1995

[18] M.B.Oliver, Y.M.M. Antar, R.K. Mongia and A. Ittipiboon, "Circularly Polarised Rectangular Dielectric Resonator Antenna", *Electron. Lett.,* vol.35, no.6 pp.418-419, March 1995

[19] K.P.Esselle, "Circularly Polarised Higher-Order Rectangular Dielectric Resonator Antenna," *Electron. Lett.,,* vol.32, no.3 pp 150-151, 1996

[20] T.Inoue, N. Inagaki, N. Kikuma and K. Sakakibara, "Design of Circularly Polarized Dielectric Resonator Antenna Using Modal Polarization Current Model Method," *IEEE Antennas Propag. Symposium AP-S*, Columbus, OH, vol.3, pp.504-507, 2003

[21] A. Ittipiboon, "A Circularly Polarized Dielectric Guide Antenna with a Single Slot Feed," *Symposium on Antenna Tech. and Applied Electromagnetics ANTEM*, Ottawa Canada, pp.427-430, Aug 1994

[22] M.T.K. Tam and R.D. Murch, "Circularly polarized circular sector dielectric resonator antenna," *IEEE Trans. Antennas Propag.*, vol. 48, pp. 126–128, Jan 2000.

[23] Chih-Yu Huang, Jian-Yi Wu and Kin-Lu Wong, "Cross-Slot-Coupled Microstrip Antenna and Dielectric Resonator Antenna for Circular Polarization," *IEEE Trans. Antennas Propag.*, vol.47, no.4, pp.605-609, Apr 1999

[24] B. Li, K.K. So and K.W. Leung, "A Circularly Polarized Dielectric Resonator Antenna Excited by an Asymmetrical U-Slot with a Backing Cavity," *IEEE Antennas Wireless Propag. Lett.*, vol.2, pp.133-135, 2003

[25] K.W. Leung and S.K. Mok, "Circularly Polarised Dielectric Resonator Antenna Excited by Perturbed Annular Slot with Backing Cavity," *Electron. Lett.,,* vol.37, no.15, pp 934-936, 1996

[26] S. Jeon, H. Choi and H.Kim, "Circular Polarization Dielectric Resonator Antenna Excited by Single Loop Feed," ETRI Journal, vol.31, pp.74-76, Feb 2009

[27] S.K. Khamas, "Circular Polarized Dielectric Resonator Antenna Excited by a Conformal Wire," *IEEE Antennas Wireless Propag. Lett.*, vol.7, pp.240-242, 2008

[28] C.Y.Huang and C.W.Ling, "Frequency-Adjustable Circularly Polarized Dielectric Resonator Antenna with Slotted Ground Plane," *Electron. Lett.*, vol.39, no.14, pp.1030-1031, July 2003

[29] K.K. So, K.W. Leung and H.K. Ng, "Frequency Design of the Circularly Polarized Dielectric Resonator Antenna," *IEEE Antennas Propag.. Symposium Digest AP-S,* Monterrey, CA, vol.1, pp.1090-1093, 2004

[30] R.T. Long, R.J. Dorris, S.A. Long, M.A. Khayat and J.T. Williams, "Use of Parasitic Strip to Produce Circular Polarisation and Increased Bandwidth for Cylindrical Dielectric Resonator Antenna," *Electron. Lett.*, vol.37, no.7, pp.407-408, Mar 2001

[31] H.K.Ng abd K.W.Leung, "Excitation of CP Aperture-Coupled Dielectric Resonator Antenna with a Parasitic Patch," *IEEE Antennas and Propag. Symposium Digest AP-S,* San Antonio, TX, vol.4, pp.202-205, 2001

[32] M.T Lee, K.M. Luk, E.K.N. Yung and K.W. Leung, "Microstrip-Line Feed Circularly Polarized Cylindrical Dielectric Resonator Antenna," *Microw. Opt. Tech. Lett.*, vol.24, no.3, pp.206-207, Feb 2000

[33] B.Li and K.W.Leung, "Strip-Fed Rectangular Dielectric Resonator Antennas With/Without a Parasitic Patch," *IEEE Trans. Antennas Propag.*, vol.53, no.7, pp. 2200-2207, July 2005

[34] H.K. Ng and K.W. Leung, "Frequency Tuning of the Linearly and Circularly Polarized Dielectric Resonator Antennas Using Multiple Parasitic Strips," *IEEE Trans. Antennas Propag.*, vol.54, no.1, pp. 225-230, Jan 2006

[35] K.W. Leung and H.K. Ng, "Theory and Experiment of Circularly Polarized Dielectric Resonator Antenna with a Parasitic Patch," *IEEE Trans. Antennas Propag.*, vol.51, no.3, pp. 405-412, Mar 2003

[36] R. Chair, S.L.S. Yang, A.A. Kishk, K.F. Lee and K.M. Luk, "Aperture Fed Wideband Circularly Polarized Rectangular Stair Shaped Dielectric Resonator Antenna," *IEEE Trans. Antennas Propag.*, vol.54, no.4, pp. 1350-1352, Apr 2006

[37] Y. Pan and K.W. Leung, "Wideband Circularly Polarized Trapezoidal Dielectric Resonator Antenna," *IEEE Trans. Antennas Wireless Propag. Lett.*, vol.9, no.4, pp. 588-591, 2010

[38] A.A. Kishk, "An Elliptic Dielectric Resonator Antenna Designed for Circular Polarization with Single Feed," *Microw. Opt. Tech. Lett.*, vol.37, no.6, pp.454-456, Jun 2003

[39] S. M. Rao, "*Time Domain Electromagnetics"*, Academic Press, New York, June 1999.

[40] FEKO – Comprehensive Electromagnetic solutions. Internet: http://www.feko.info/, [Oct 24 2012]

[41] EZNEC - Antenna software by W7EL. Internet: http://www.eznec.com/, [Oct 24 2012]

[42] WIPL-D Pro – 3D EM solver. Internet: http://www.wipl-d.com/index.php [Oct 24 2012]

[43] Applied Simulation Technology – Advanced simulation for high speed design. Internet: http://www.apsimtech.com/ [Oct 24 2012]

[44]Remcom XFDTD – 3D EM simulation software. Internet: http://www.remcom.com/xf7 [Oct 24 2012]

[45] Ansys – Simulation driven product development. Internet: http://www.ansys.com/ [Oct 24 2012]

[46]Analyst STAAR– 3D FEM EM analysis Internet: http://www.awrcorp.com/products/analyst [Oct 24 2012]

[47] R.A. Abd-Alhameed, P.S. Excell, M.A Mangoud and J.A. Vaul, "Computation of radiated and scattered field using separate frequency domain moment-method regions and frequency domain MOM-FDTD hybrid methods," IEEE National Conference on Antennas and Propag.., pp.53-56, 1999

[48] T. Rylander and A. Bondeson, "Stability of Explicit-Implicit Hybrid Time-Stepping Schemes for Maxwell's Equation," Journal Comput. Phys., vol. 179, no.2, pp.426-438, Jul 2002,

[49] J.L. Volakis L.C. Kempel, "Electromagnetics: Computational Methods and Considerations*," IEEE Computational Science and Engineering*, vol.2, pp.42-57, 1995

[50] S.M.Rao and N.Balakrishnan, "Computational Electromagnetics – A Review*," Journal Current Science*, vol.77, no.10, 1999

CHAPTER 2

DEVELOPMENT OF THE METHOD

OF MOMENTS MODEL

2.1   Introduction

This chapter describes extensively the stages involved in the simulation of DRAs using MoM. Categorized as Frequency-Domain Integral Equation (FDIE) model, MoM has been one of the most widely used CEM model since the solution procedure was introduced by R.F. Harrington [1] in 1968.

Using this approach, an integral equation describing the unknown induced current and charge density is developed from the frequency-domain Maxwell's equations by applying the appropriate boundary conditions. To solve the Maxwell's equation, the integral equation is then sampled in space by applying suitable basis and testing functions. A set of simultaneous equations relating these unknown quantities, i.e. current and charge densities, with known quantities, such as

radiated or scattered field, is then introduced and transformed into a matrix equation. Solution of the matrix yields the current distribution, from which near-field and far-field parameters such as input impedance, return losses, radiation pattern, radar cross section, axial ratio, efficiency and gain can be calculated.

Mathematical representation of the MoM concept can be understood by considering the following linear equation

$$L(F) = Y \tag{2-1}$$

where L is the linear operator, Y is the excitation function and F is the unknown response function to be determined. By expanding F into a set of known expansion or basis functions $(f_1, f_2, f_3 ...)$ in the domain of L such that

$$F = \sum_{n=1}^{N} \alpha_n f_n \tag{2-2}$$

where α_i are the coefficients to be determined and using the linearity of L, equation (2-2) can be expressed as

$$\sum_{n=1}^{N} \alpha_n L(f_n) = Y \tag{2-3}$$

With the assumption that a suitable inner product $\langle F, Y \rangle$ has been determined by defining a set of weighting or testing functions $(w_1, w_2, w_3 ....)$ in the range of L and taking the inner product of equation (2-3) with each w_m, the previous equation can be expressed as

$$\sum_{n=1}^{N} \alpha_n \langle w_m, Lf_n \rangle = \langle w_m, Y \rangle \tag{2-4}$$

for *m*=1,2,3,…*N*.

This set of linear equations can then be presented in a matrix form as

$$[L_{mn}][\alpha_n] = [Y_m] \tag{2-5}$$

Finally, the α_n unknown coefficients are determined using a standard matrix solution procedure.

MoM is capable of producing very accurate result if a suitable set of basis and testing functions are chosen. In this research, the triangular-based Rao-Wilton-Glisson (RWG) basis functions [2], are used to model the two dimensional conducting surfaces, while the tetrahedral-based Schaubert-Wilton-Glisson (SWG) basis functions [3] are employed to model three dimensional dielectric structures. These basis functions are chosen because the triangular and tetrahedral patches are capable of accurately conforming to any arbitrarily shaped surfaces and volumes as noted in [4].

2.2   The RWG and SWG Basis Functions

A typical DRA structure consists of a metal surface and a dielectric volume. Using RWG basis function, the metal surface is discretized into small triangular patches defined in terms of appropriate faces, vertices, edges and boundary edges. Each basis function is associated with a pair of adjacent triangles linked by an interior edge and resembles a small spatial dipole with linear current distribution. One of the triangles in each basis function is associated with a positive charge, while the second triangle is associated with a negative charge. The geometrical parameters of an RWG basis function at a common edge n are shown in Figure 2.1 and as an example a spherical metal surface modelled by triangular patches is illustrated in the inset.
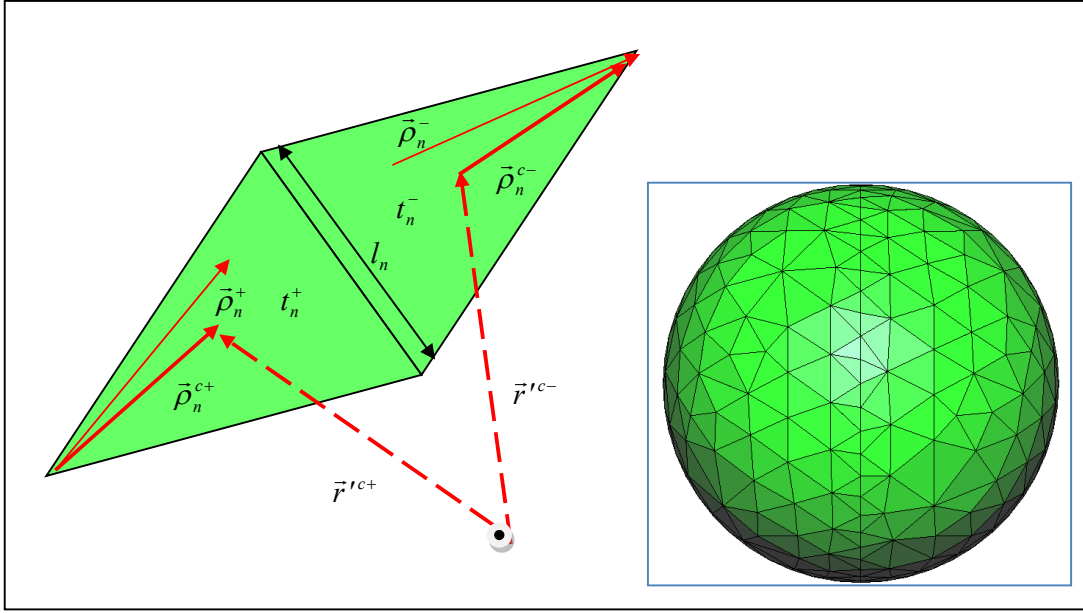
Figure 2.1: Geometrical parameters of an RWG basis function

The RWG basis function $\vec{f}_n^S$ consists of two adjacent triangles, t_n^+ and t_n^- having

areas of A_n^+ and A_n^- respectively, and sharing a common edge l_n defined as [2]

$$\vec{f}_n^s(\vec{r}') = \begin{cases} \dfrac{l_n}{2A_n^+}\vec{\rho}_n^+(\vec{r}') & ,\vec{r}' \in t_n^+ \\[4mm] \dfrac{l_n}{2A_n^-}\vec{\rho}_n^-(\vec{r}') & ,\vec{r}' \in t_n^- \end{cases} \tag{2-6}$$

and the surface divergence associated with each basis function is given by

$$\nabla_s \cdot \vec{f}_n^s(\vec{r}') = \begin{cases} \dfrac{l_n}{A_n^+} & ,\vec{r}' \in t_n^+ \\[4mm] -\dfrac{l_n}{A_n^-} & ,\vec{r}' \in t_n^- \end{cases} \tag{2-7}$$

where the position vector $\vec{\rho}_n^+(\vec{r}') = \vec{r}'_n - \vec{r}'^{+}_n$ signifies a vector drawn from the free

vertex of triangle t_n^+ to a source point $\vec{r}'$ on that triangle and $\vec{\rho}_n^-(\vec{r}') = \vec{r}'^{-}_n - \vec{r}'_n$ is a

vector drawn from a source point on triangle t_n^- towards the free vertex of the

same triangle. The RWG basis functions represent the surface current density, $\vec{J}_S$,

flowing on the metal. The component of current normal to the *n*th edge is constant and continuous since the normal component of $\vec{f}_n^S$ is equal to unity (i.e. $\hat{n} \cdot \vec{f}_n^S = 1$). At the boundary edges, there is no normal component of current and hence no line charges exist along this boundary.

The dielectric structure is modelled by subdividing the volume into small tetrahedrons on which the SWG basis functions are applied. Each basis function is associated with a pair of adjacent tetrahedrons, linked by a common face. The geometrical parameters of a basis function at the common edge *n* are shown in Figure 2.2, and as an example a rectangular volume modelled by tetrahedrons is illustrated in the inset.
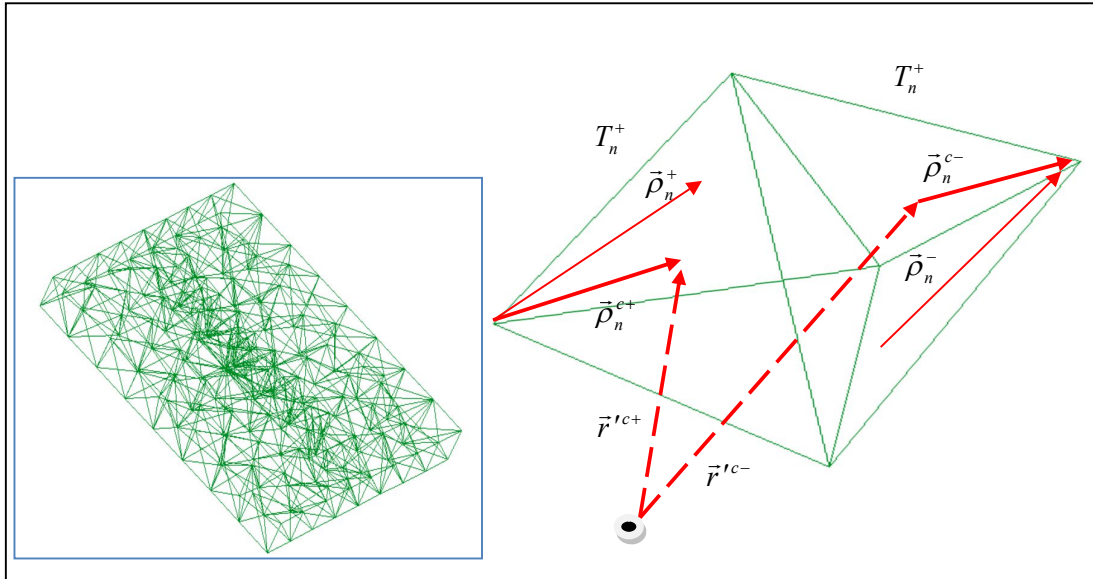
Figure 2.2: Geometrical parameters of SWG basis function

The SWG basis function $\vec{f}_n^V$ consists of two adjacent tetrahedrons, T_n^+ and T_n^-, having areas of V_n^+ and V_n^- respectively, and sharing a common face a_n that is defined as [3]

$$\vec{f}_n^V(\vec{r}') = \begin{cases} \dfrac{a_n}{3V_n^+}\,\vec{\rho}_n^+(\vec{r}') & ,\vec{r}' \in T_n^+ \\[3mm] \dfrac{a_n}{3V_n^-}\,\vec{\rho}_n^-(\vec{r}') & ,\vec{r}' \in T_n^- \end{cases} \tag{2-8}$$

and the divergence of each basis function is given by

$$\nabla \cdot \vec{f}_n^V(\vec{r}') = \begin{cases} \dfrac{a_n}{V_n^+} & ,\vec{r}' \in T_n^+ \\[3mm] -\dfrac{a_n}{V_n^-} & ,\vec{r}' \in T_n^- \end{cases} \tag{2-9}$$

where the position vector $\vec{\rho}_n^+(\vec{r}') = \vec{r}_n' - \vec{r}_n'^+$ signifies vector drawn from the free vertex of tetrahedron T_n^+ to a source point $\vec{r}'$ on the same tetrahedron, while $\vec{\rho}_n^-(\vec{r}') = \vec{r}_n'^- - \vec{r}_n'$ is the vector drawn from a source point on tetrahedron T_n^- towards the free vertex of that tetrahedron. The SWG basis functions represent the volume polarization current density, $\vec{J}_V$, or more precisely its intermediate quantity *D*, i.e. flux density, throughout the dielectric volume. The normal component of flux density to the *n*th face is constant and continuous. In the special case where the *n*th face is located at the boundary of the dielectric volume, then only one of the tetrahedrons, i.e. T_n^+ or T_n^-, is interior to the volume. Thus the corresponding basis function associated with *n*th face is only defined within T_n^+ or T_n^-

Through the application of RWG and SWG basis functions, the MoM integral equations are derived for pure metal, pure dielectric, and combined metal dielectric structures. Detailed derivatives of the required equations for each structure are presented in the next sections.

2.3 MoM Model for Metal Structures

For radiation problems, the "incident field", $\vec{E}^i(\vec{r})$ is defined as the applied electric field at the antenna's feed, while for scattering problem, it essentially means the incoming electric field from impressed source. The term "scattered field", $\vec{E}^s(\vec{r})$ refers to field radiated by the antenna in the case of radiation problem while for scattering problem, the interpretation is straightforward. The total electric field, $\vec{E}(\vec{r})$, is given by the combination of these field components as

$$\vec{E}(\vec{r}) = \vec{E}^i(\vec{r}) + \vec{E}^s(\vec{r}) \tag{2-10}$$

Enforcing the boundary condition $\hat{n} \times \left(\vec{E}^i(\vec{r}) + \vec{E}^s(\vec{r})\right) = 0$ on a perfectly conducting metal surface *S* results in $\vec{E}(\vec{r})_{\tan} = 0$ and hence the relationship between $\vec{E}^i(\vec{r})$ and $\vec{E}^s(\vec{r})$ reduces to

$$\vec{E}^i(\vec{r})_{\tan} = -\vec{E}^s(\vec{r})_{\tan} \tag{2-11}$$

Based on derivation of Maxwell's equations, using [5], $\vec{E}^s(\vec{r})$ can be expressed in terms of the surface current density, $\vec{J}_s(\vec{r}')$, and the free charges densities, $\rho(\vec{r}')$, on the metal surface, *S,* as

$$\vec{E}^s(\vec{r}) = -j\omega\vec{A}_S(\vec{r}) - \nabla\Phi_S(\vec{r}) \tag{2-12}$$

Substituting of equation (2-12) into (2-11) yields the following equation

$$\vec{E}^i(\vec{r}) = j\omega\vec{A}_s(\vec{r}) + \nabla\Phi_s(\vec{r}) \tag{2-13}$$

where the magnetic vector potential, $\vec{A}_S(\vec{r})$, describes the radiation due to $\vec{J}_s(\vec{r}')$ and expressed as

$$\vec{A}_S(\vec{r}) = \frac{\mu_0}{4\pi} \int_S \vec{J}_S(\vec{r}') G(\vec{r},\vec{r}') d\vec{r}' \qquad (2\text{-}14)$$

The electric scalar potential, $\Phi_S(\vec{r})$, refers to the radiation due to $\rho_s(\vec{r}')$ and

defined as

$$\Phi_S(\vec{r}) = \frac{1}{4\pi\varepsilon_0} \int_S \rho(\vec{r}') G(\vec{r},\vec{r}') d\vec{r}' \qquad (2\text{-}15)$$

In the above equations ε_0 and μ_0 represent the permittivity and permeability in

vacuum, respectively. The free space Green's function, $G(\vec{r},\vec{r}')$, is defined as

$$G(\vec{r},\vec{r}') = \frac{e^{-jk_0 R}}{R} \qquad (2\text{-}16)$$

The time dependency $\exp(j\omega t)$ has been assumed and the propagation constant

is $k_0 = \omega\sqrt{\mu_0\varepsilon_0} = 2\pi/\lambda_0$, where λ_0 is the free space wavelength. In the expression

of Green's function, $R = |\vec{r} - \vec{r}'|$, is the separation distance between the test, or

observation, point $\vec{r}$ and the source point $\vec{r}'$.

2.3.1 Application of the Testing Functions

Equation (2-13) can be sampled in space into triangular elements. Multiplication

by a testing function $\vec{f}_m^S(\vec{r})$ that covers the entire region of *S*, and integration over

S yields

$$\int_{S_m} \vec{E}^i(\vec{r}) \cdot \vec{f}_m^S(\vec{r}) dr = j\omega \int_{S_m} \vec{A}_S(\vec{r}) \cdot \vec{f}_m^S(\vec{r}) d\vec{r} + \int_{S_m} (\nabla\Phi_S(\vec{r})) \cdot \vec{f}_m^S(\vec{r}) d\vec{r} \qquad (2\text{-}17)$$

According to Divergence theorem, the last term of equation (2-17) is given by

$$\int_{S_m} \nabla\Phi_S(\vec{r}) \cdot \vec{f}_m^S(\vec{r}) d\vec{r} = \int_{l_m} \Phi_S(\vec{r}) \left(\hat{n} \cdot \vec{f}_m^S(\vec{r})\right) d\vec{l} - \int_{s_m} \Phi_S(\vec{r}) \left(\nabla \cdot \vec{f}_m^S(\vec{r})\right) d\vec{r} \qquad (2\text{-}18)$$

where $\hat{n}$ is the unit normal vector.

From the properties of RWG basis functions described in section 2.2, all edges in t_m^+ and t_m^- are free of line charges, hence the first term on the right hand side (RHS) of equation (2-18) will vanish, which simplifies equation (2-17) to

$$\int_{S_m} \vec{E}^i(\vec{r}) \cdot \vec{f}_m^S(\vec{r}) d\vec{r} = j\omega \int_{S_m} \vec{A}_S(\vec{r}) \cdot \vec{f}_m^S(\vec{r}) d\vec{r} - \int_{S_m} \Phi_S(\vec{r}) \left(\nabla \cdot \vec{f}_m^S(\vec{r}) \right) d\vec{r} \qquad (2\text{-}19)$$

Substituting $\vec{f}_m^S(\vec{r})$ with equation (2-6), the first term on the RHS of equation (2-19) becomes

$$\int_{S_m} \vec{A}_S(\vec{r}) \cdot \vec{f}_m^S(\vec{r}) d\vec{r} = \frac{l_m}{2} \left[\frac{1}{A_m^+} \int_{t_n^+} \vec{A}_S(\vec{r}) \cdot \vec{\rho}_m^+(\vec{r}) d\vec{r} + \frac{1}{A_m^-} \int_{t_n^-} \vec{A}_S(\vec{r}) \cdot \vec{\rho}_m^-(\vec{r}) d\vec{r} \right] \qquad (2\text{-}20)$$

An approximation to equations (2-19) and (2-20) is needed in order to reduce the computational time. Such an approximation can be obtained using the assumption that the average value of $\vec{A}_s(\vec{r})$ over each triangle is given by the value of $\vec{A}_s(\vec{r})$ at the triangle centroid. As a result, the surface integrals in equation (2-20) can be eliminated and the equation is then simplified to

$$\int_{S_m} \vec{A}_S(\vec{r}) \cdot \vec{f}_m^S(\vec{r}) dr = \frac{l_m}{2} \left[\vec{A}_S\left(\vec{r}_m^{c+}\right) \cdot \vec{\rho}_m^{c+} + \vec{A}_S\left(\vec{r}_m^{c-}\right) \cdot \vec{\rho}_m^{c-} \right] \qquad (2\text{-}21)$$

Applying similar approximation to the last term in equation (2-19) yields

$$-\int_{S_m} \Phi(\vec{r}) \left(\nabla \cdot \vec{f}_m^S(\vec{r}) \right) d\vec{r} = -l_m \left[\frac{1}{A_m^+} \int_{t_n^+} \Phi(\vec{r}) d\vec{r} - \frac{1}{A_m^-} \int_{t_m^-} \Phi(\vec{r}) d\vec{r} \right] \qquad (2\text{-}22)$$

$$= l_m \left[\Phi\left(\vec{r}_m^{c-}\right) - \Phi\left(\vec{r}_m^{c+}\right) \right]$$

The approximations in equations (2-20) and (2-21), which eliminate surface integrals for the potentials quantities, are justified since the potentials are locally smooth within each subdomain [6].

2.3.2 Application of the Expansion Functions

The surface current density, $\vec{J}_s(\vec{r}')$ can be expanded into a set of simultaneous equations that employ the RWG basis functions in the form of

$$\vec{J}_S(\vec{r}') = \sum_{n=1}^{N_M} I_{sn} \vec{f}_n^S(\vec{r}') \tag{2-23}$$

where N_M is the total number of edges inside *S*. Application of the continuity equation, $\nabla \cdot \vec{J}_S(\vec{r}') = -j\omega\rho(\vec{r}')$, yields

$$\rho(\vec{r}') = -\frac{1}{j\omega} \sum_{n=1}^{N_M} I_{sn}\left(\nabla \cdot \vec{f}_n^S(\vec{r}')\right) \tag{2-24}$$

Substitution of equation (2-23) into (2-14) and equation (2-24) into (2-15) gives a set of equation for the potentials given by

$$\vec{A}_S(\vec{r}) = \frac{\mu_0}{4\pi} \sum_{n=1}^{N_M} \left\{ \int_{Sn} \vec{f}_n^S(\vec{r}')G(\vec{r},\vec{r}')d\vec{r}' \right\} I_{sn} \tag{2-25}$$

$$\Phi_S(\vec{r}) = -\frac{1}{4\pi\varepsilon_0} \sum_{n=1}^{N_M} \left\{ \int_{S_n} \nabla \cdot \vec{f}_n^S(\vec{r}')G(\vec{r},\vec{r}')d\vec{r}' \right\} I_{sn} \tag{2-26}$$

The moment method matrix equation is then derived by substituting equations (2-25) and (2-26) into (2-19)

$$\int_{S_m} \vec{E}^i(\vec{r}) \cdot \vec{f}_m^S(\vec{r})dr = \left\{ \begin{array}{l} \dfrac{j\omega\mu_0}{4\pi} \displaystyle\int_{S_m}\int_{S_n} \vec{f}_m^S(\vec{r}) \cdot \vec{f}_n^S(\vec{r}')G(\vec{r},\vec{r}')d\vec{r}'d\vec{r} \\[2mm] + \dfrac{1}{4\pi j\omega\varepsilon_0} \displaystyle\int_{S_m}\int_{S_n}\left(\nabla \cdot \vec{f}_m^S(\vec{r})\right)\left(\nabla \cdot \vec{f}_n^S(\vec{r}')\right)G(\vec{r},\vec{r}')d\vec{r}'d\vec{r} \end{array} \right\} \{I_{Sn}\} \tag{2-27}$$

The above equation is usually represented in terms of its symbolic notation of

$$V_m^M = \sum_{n=1}^{N_m} Z_{mn}^{MM} I_{sn} \tag{2-28}$$

where the voltage excitation V_m^M is given by

$$V_m^M = \int_{S_m} \vec{E}^i(\vec{r}) \cdot \vec{f}_m^S(\vec{r}) dr \tag{2-29}$$

and the impedance matrix elements Z_{mn}^{MM} are given by

$$Z_{mn}^{MM} = \frac{j\omega\mu_0}{4\pi} \int_{S_m}\int_{S_n} \vec{f}_m^S(\vec{r}) \cdot \vec{f}_n^S(\vec{r}') G(\vec{r},\vec{r}') d\vec{r}' d\vec{r}$$

$$+ \frac{1}{4\pi j\omega\varepsilon_0} \int_{S_m}\int_{S_n} \left(\nabla \cdot \vec{f}_m^S(\vec{r})\right)\left(\nabla \cdot \vec{f}_n^S(\vec{r}')\right) G(\vec{r},\vec{r}') d\vec{r}' d\vec{r} \tag{2-30}$$

in which the superscripts *M* refer to a metallic structure. The solution of this equation is obtained by expanding the RWG basis functions given by equation (2-6). Applying the approximations in equations (2-20) to (2-22), the integral expressions of equation (2-30) can be simplified to

$$\int_{S_m}\int_{S_n} \vec{f}_m^S(\vec{r}) \cdot \vec{f}_n^S(\vec{r}') G(\vec{r},\vec{r}') d\vec{r}' d\vec{r}$$

$$= \frac{l_m}{2}\left(\frac{l_n}{2A_n^+}\int_{t_n^+}\vec{\rho}_n^+(\vec{r}')G(\vec{r}_m^{c+},\vec{r}')d\vec{r}'\right)\cdot\vec{\rho}_m^{c+} + \frac{l_m}{2}\left(\frac{l_n}{2A_n^-}\int_{t_n^-}\vec{\rho}_n^-(\vec{r}')G(\vec{r}_m^{c+},\vec{r}')d\vec{r}'\right)\cdot\vec{\rho}_m^{c+} \tag{2-31}$$

$$+ \frac{l_m}{2}\left(\frac{l_n}{2A_n^+}\int_{t_n^+}\vec{\rho}_n^+(\vec{r}')G(\vec{r}_m^{c-},\vec{r}')d\vec{r}'\right)\cdot\vec{\rho}_m^{c-} + \frac{l_m}{2}\left(\frac{l_n}{2A_n^-}\int_{t_n^-}\vec{\rho}_n^-(\vec{r}')G(\vec{r}_m^{c-},\vec{r}')d\vec{r}'\right)\cdot\vec{\rho}_m^{c-}$$

and $\int_{S_m}\int_{S_n} \left(\nabla \cdot \vec{f}_m^S(\vec{r})\right)\left(\nabla \cdot \vec{f}_n^S(\vec{r}')\right) G(\vec{r},\vec{r}') d\vec{r}' d\vec{r}$

$$= l_m\left(\frac{l_n}{A_n^+}\int_{t_n^+}G(\vec{r}_m^{c+},\vec{r}')d\vec{r}'\right) - l_m\left(\frac{l_n}{A_n^-}\int_{t_n^-}G(\vec{r}_m^{c+},\vec{r}')d\vec{r}'\right)$$

$$-l_m\left(\frac{l_n}{A_n^+}\int_{t_n^+}G(\vec{r}_m^{c-},\vec{r}')d\vec{r}'\right) + l_m\left(\frac{l_n}{A_n^-}\int_{t_n^-}G(\vec{r}_m^{c-},\vec{r}')d\vec{r}'\right) \tag{2-32}$$

Calculation of Z_{mn}^{MM} can be made by naively computing the elements directly for each index combination of edge *m* and edge *n,* i.e. edge-pair calculation. However, this is extremely inefficient since the integral required for a combination of *m* and *n* is also required for other combinations as well. To overcome this problem, the integrals should be computed using face-pair calculation. Consider a surface *S* that is discretized into *N* triangular patches i.e. $t = 1,2,3,....N$. Figure 2.3 illustrates the combination of source triangle, t^q and observation triangle, t^p ($p,q = 1,2,3,....N$) together with the geometrical parameters after local indexing scheme has been employed.
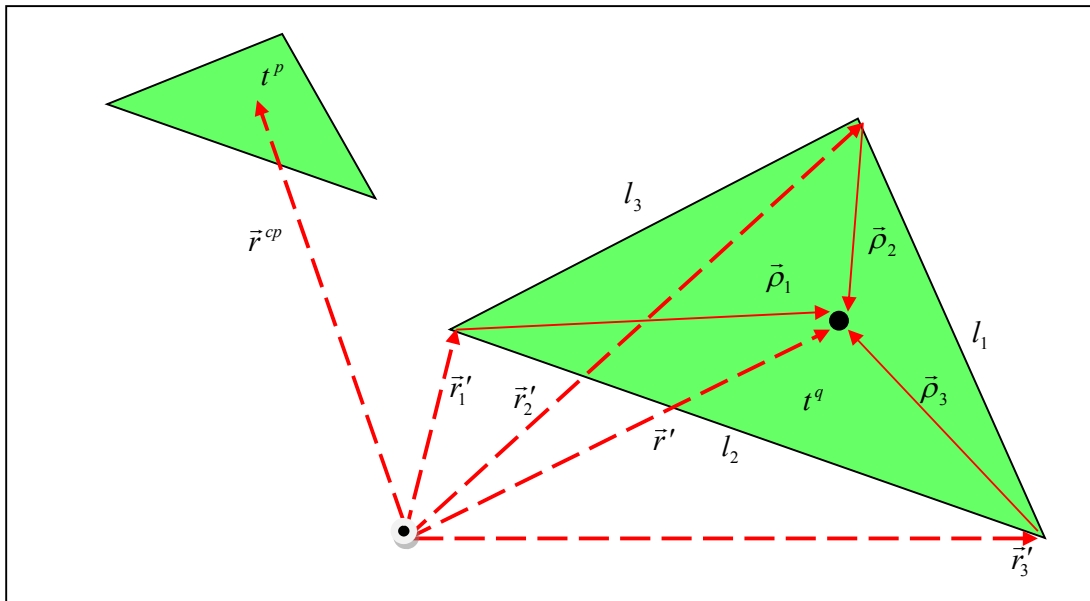
Figure 2.3: Local coordinates for t^q with observation point at t^p

A point inside a source triangle, $\vec{r}'$ with vertices $\vec{r}_1', \vec{r}_2'$ and $\vec{r}_3'$ can be described by the normalized area coordinates [7] of $\varsigma = \dfrac{A_1}{A^q}, \eta = \dfrac{A_2}{A^q}, \xi = \dfrac{A_3}{A^q}$ where $\varsigma + \eta + \xi = 1$.

Applying this, any point inside the source triangle can be described as

$$\vec{r}' = \vec{r}_1'\zeta + \vec{r}_2'\eta + \vec{r}_3'\xi \tag{2-33}$$

The position vector $\vec{\rho}_i$ used to define the basis function, $\vec{f}_i(\vec{r}') = \dfrac{l_i}{2A^q}\vec{\rho}_i(\vec{r}')$ inside

t_q is given by

$$\vec{\rho}_i = \pm(r' - r_i') \qquad , \ i = 1,2,3 \tag{2-34}$$

where r_i is the vertex opposite local edge i in t_q. These definitions in terms of the

fixed vertices and area coordinates allow integrals over the source triangles to be

expressed using scalar integrals, in which a typical term for potentials due to

$\vec{f}_i(\vec{r}')$ in t_q has the form of

$$\vec{A}_i^{pq} = \frac{\mu_0}{4\pi}\left[\frac{l_i}{2A^q}\left(2A^q\iint \pm(\vec{r}' - \vec{r}_i')\frac{e^{-jkR^p}}{R^p}\,d\zeta d\eta\right)\right]$$

$$= \pm\frac{\mu_0 l_i}{4\pi}\int_0^1\int_0^{1-\eta}\left((\vec{r}_1' - \vec{r}_3')\zeta + (\vec{r}_2' - \vec{r}_3')\eta + (\vec{r}_3' - \vec{r}_i')\right)G(\vec{r}', r^{cp})\,d\zeta d\eta \tag{2-35}$$

$$= \pm\frac{\mu_0 l_i}{4\pi}\left[(\vec{r}_1' - \vec{r}_3')I_\zeta^{pq} + (\vec{r}_2' - \vec{r}_3')I_\eta^{pq} + (\vec{r}_3' - \vec{r}_i')I^{pq}\right]$$

$$\Phi_i^{pq} = \mp\frac{2l_i}{4\pi j\omega\varepsilon_0}I^{pq} \tag{2-36}$$

where the scalar integrals are given by

$$I^{pq} = \int_0^1\int_0^{1-\eta}G(\vec{r}', \vec{r}^{cp})\,d\zeta d\eta \ , \ I_\zeta^{pq} = \int_0^1\int_0^{1-\eta}\zeta G(\vec{r}', \vec{r}^{cp})\,d\zeta d\eta \ , \ I_\eta^{pq} = \int_0^1\int_0^{1-\eta}\eta G(\vec{r}', \vec{r}^{cp})\,d\zeta d\eta \tag{2-37}$$

Finally it should be noted that for radiation problems, the calculation of V_m^M is

straightforward and can be implemented using a delta gap model. However, for

scattering problems, the voltage excitation is due to a plane wave incidence.

Therefore the incident field is given by

$$\vec{E}^i(\vec{r}) = (\vec{E}_\theta\hat{\theta}_0 + \vec{E}_\phi\hat{\phi}_0)\cdot e^{-j\vec{k}\cdot\vec{r}} \tag{2-38}$$

where the propagation vector, $\vec{k}$ is equal to

$$\vec{k} = k\left(\sin\theta_0 \cos\phi_0 \hat{x} + \sin\theta_0 \sin\phi_0 \hat{y} + \cos\theta_0 \hat{z}\right) \tag{2-39}$$

and $\left(\hat{\theta}_0, \hat{\phi}_0\right)$ denotes the angle of arrival of the plane wave in terms of spherical coordinate system.

2.4 MoM Model for Dielectric Structures

For a configuration that entirely consists of dielectric components, the EFIE can be used in conjunction with the SWG basis functions to develop a moment method matrix for the dielectric volume. For a purely dielectric object, only scattering problem is considered. Unlike metal structure, the required derivations are implemented in terms of an intermediate quantity called electric flux density, $D(\vec{r})$, since the boundary condition of a homogeneous dielectric structure is given by

$$\hat{n} \cdot \left(\vec{D}_1(\vec{r}) - \vec{D}_2(\vec{r})\right) = \rho_S \tag{2-40}$$

where $\vec{D}_1(\vec{r})$ corresponds to flux density inside the structure, $\vec{D}_2(\vec{r})$ is the flux density outside the structure, and ρ_S refers to free charges on the surface of dielectric volume. As $\vec{E}(\vec{r})$ is given by $\vec{E}(\vec{r}) = \vec{D}(\vec{r}) / \hat{\varepsilon}(\vec{r})$, equation (2-10) becomes

$$\frac{\vec{D}(\vec{r})}{\hat{\varepsilon}(\vec{r})} = \vec{E}^i(\vec{r}) + \vec{E}^s(\vec{r}) \tag{2-41}$$

Substituting $\vec{E}^S(\vec{r})$ from equation (2.12) yields

$$\vec{E}^i(\vec{r}) = \frac{\vec{D}(\vec{r})}{\hat{\varepsilon}(\vec{r})} + j\omega\vec{A}_V(\vec{r}) + \nabla\Phi_v(\vec{r}) \tag{2-42}$$

where the volume vector potential, $\vec{A}_v(\vec{r})$, describes the radiation due to $\vec{J}_V(\vec{r}')$,

and it is expressed as

$$\vec{A}_V(\vec{r}) = \frac{\mu_0}{4\pi} \int_V \vec{J}_V(\vec{r}') G(\vec{r},\vec{r}') d\vec{r}' \qquad (2\text{-}43)$$

On the other hand, the volume scalar potential, $\Phi_S(\vec{r})$, describes the radiation due

to the volume bound and surface charges, $\rho(\vec{r}')$, and it is given by

$$\Phi_V(\vec{r}) = \frac{1}{4\pi\varepsilon_0} \int_V \rho(\vec{r}') G(\vec{r},\vec{r}') d\vec{r}' \qquad (2\text{-}44)$$

The symbols in equation (2-43) and (2-44) carries the same meaning as described

previously in section 2.3.

2.4.1 Application of the Testing Functions

 The required model is developed by using a testing function $\vec{f}_m^V(\vec{r})$ that covers the

entire dielectric region *V*. Then the multiplication of equation (2-42) by $\vec{f}_m^V(\vec{r})$ in

conjunction with an integration over *V* yields

$$\int_{V_m} \vec{E}^i(\vec{r}) \cdot \vec{f}_m^V(\vec{r}) dr = \int_{V_m} \frac{\vec{D}(\vec{r})}{\hat{\varepsilon}(\vec{r})} \cdot \vec{f}_m^V(\vec{r}) dr + j\omega \int_{V_m} \vec{A}_V(\vec{r}) \cdot \vec{f}_m^V(\vec{r}) d\vec{r} + \int_{v_m} (\nabla\Phi_v(\vec{r})) \cdot \vec{f}_m^V dr \qquad (2\text{-}45)$$

According to Divergence theorem, the last term of equation (2-45) is given by

$$\int_{V_m} \nabla\Phi_V(\vec{r}) \cdot \vec{f}_m^V(\vec{r}) d\vec{r} = \int_{A_m} \Phi_V(\vec{r})\left(\hat{n} \cdot \vec{f}_m^V(\vec{r})\right) dr - \int_{V_m} \Phi_V(\vec{r})\left(\nabla \cdot \vec{f}_m^V(\vec{r})\right) d\vec{r} \qquad (2\text{-}46)$$

where A refers to the surface encircling the dielectric volume. Thus, equation

(2-45) becomes

$$\int_{V_m} \vec{E}^i(\vec{r}) \cdot \vec{f}_m^V(\vec{r}) dr = \int_{V_m} \frac{\vec{D}(\vec{r})}{\hat{\varepsilon}(\vec{r})} \cdot \vec{f}_m^V(\vec{r}) d\vec{r} + j\omega \int_{V_m} \vec{A}_V(\vec{r}) \cdot \vec{f}_m^V(\vec{r}) d\vec{r}$$

$$(2\text{-}47)$$

$$-\int_{v_m}\Phi_V(\vec{r})\left(\nabla\cdot\vec{f}_m^V(\vec{r})\right)d\vec{r}+\int_{A_M}\Phi_V(\vec{r})\left(\hat{n}\cdot\vec{f}_m^V(\vec{r})\right)d\vec{r}$$

Substituting $\vec{f}_m^V(\vec{r})$ with equation (2-8), the second term on the RHS of equation (2-47) may be written as

$$\int_{V_m}\vec{A}_V(\vec{r})\cdot\vec{f}_m^V(\vec{r})d\vec{r}=\frac{a_m}{3}\left[\frac{1}{V_m^+}\int_{T_n^+}\vec{A}_V(\vec{r})\cdot\vec{\rho}_m^+(\vec{r})d\vec{r}+\frac{1}{V_m^-}\int_{T_n^t}\vec{A}_V(\vec{r})\cdot\vec{\rho}_m^-(\vec{r})d\vec{r}\right]\qquad(2\text{-}48)$$

Once more, the numerical integration can be avoided by assuming the average value of $\vec{A}_V(\vec{r})$ over each tetrahedron is given by the value of $\vec{A}_V(\vec{r})$ at the tetrahedron centroid. Therefore, equation (2-48) can be reduced to

$$\int_{V_m}\vec{A}_V(\vec{r})\cdot\vec{f}_m^V(\vec{r})dr=\frac{a_m}{3}\left[\vec{A}_V\left(\vec{r}_m^{c+}\right)\cdot\vec{\rho}_m^{c+}+\vec{A}_V\left(\vec{r}_m^{c-}\right)\cdot\vec{\rho}_m^{c-}\right]\qquad(2\text{-}49)$$

Applying a similar approximation to the third term in equation (2-47) yields

$$-\int_{V_m}\Phi_V(\vec{r})\left(\nabla\cdot\vec{f}_m^V(\vec{r})\right)d\vec{r}=-a_m\left[\frac{1}{V_m^+}\int_{T_n^+}\Phi_V(\vec{r})d\vec{r}-\frac{1}{V_m^-}\int_{T_m^-}\Phi_V(\vec{r})d\vec{r}\right]$$
$$=a_m\left[\Phi_V\left(\vec{r}_m^{c-}\right)-\Phi_V\left(\vec{r}_m^{c+}\right)\right]\qquad\text{for }T_n^+\text{ and }T_n^+\in V\qquad(2\text{-}50)$$

It should be noted that if the common face m is located on A, where $\vec{f}_m^V(\vec{r})$ is defined only within T_n^+, the average value of $\Phi_v(\vec{r})$ over the exterior tetrahedron is assumed to be the value of $\Phi_v(\vec{r})$ at the centroid of the m-th face

$$-\int_{V_m}\Phi_V(\vec{r})\left(\nabla\cdot\vec{f}_m^V(\vec{r})\right)d\vec{r}=a_m\left[\Phi\left(\vec{r}_m^{c+}\pm\frac{1}{3}\vec{\rho}_m^{c+}\right)-\Phi\left(\vec{r}_m^{c+}\right)\right]\qquad(2\text{-}51)$$

2.4.2 Application of the Expansion Functions

The volume polarization current density is given by [3]

$$\vec{J}_V(\vec{r}')=j\omega\left(\hat{\varepsilon}(\vec{r}')-\varepsilon_0\right)\vec{E}(\vec{r}')\qquad(2\text{-}52)$$

Substitution of $\vec{E}(\vec{r}') = \vec{D}(\vec{r}')/\hat{\varepsilon}(\vec{r}')$ into this equation yields

$$\vec{J}_V(\vec{r}') = j\omega \underbrace{\left(\frac{\hat{\varepsilon}(\vec{r}') - \varepsilon_0}{\hat{\varepsilon}(\vec{r}')} \right)}_{\kappa(\vec{r}')} \vec{D}(\vec{r}')$$

$$= j\omega\kappa(\vec{r}')\vec{D}(\vec{r}')$$

(2-53)

where the contrast ratio, $\kappa(\vec{r}')$, takes into account all discontinuities in the normal component of $\vec{J}_V(\vec{r}')$ at the media interfaces. Furthermore, $\vec{D}(\vec{r}')$, can be expanded into a set of simultaneous equations that consist of the SWG basis function in the form of

$$\vec{D}(\vec{r}') = \sum_{n=1}^{N_D} D_n \vec{f}_n^V(\vec{r}')$$

(2-54)

where N_D is the total number of faces throughout the dielectric structure. By substituting equation (2-54) into (2-53), $\vec{J}_V(\vec{r}')$ can be represented in the form of

$$\vec{J}_V(\vec{r}') = j\omega \sum_{n=1}^{N_D} \kappa_n D_n \vec{f}_n^V(\vec{r}')$$

(2-55)

Applying the equation of continuity to equation (2-55) and making use of the divergence theorem, the charge density can be expressed as

$$\rho(\vec{r}') = -\sum_{n=1}^{N_D} D_n \kappa(\vec{r}') \left(\nabla \cdot \vec{f}_n^V(\vec{r}') \right) - \sum_{n=1}^{N_D} D_n \left(\nabla \kappa(\vec{r}') \right) \vec{f}_n^V(\vec{r}')$$

(2-56)

The first term on the RHS of equation (2-56) corresponds to the volume charge density ρ_V, and the second term refers to surface charge density ρ_S. It should be noted that ρ_V exists in each tetrahedron in which the medium parameters are different from those of free space, while ρ_S exists only on faces that separate different media for which $\kappa(\vec{r}')$ is discontinuous, that is, $\kappa_n^- - \kappa_n^+ \neq 0$. Substitution of

equations (2-55) and (2-56) into the potentials equations in (2-43) and (2-44) yields

$$\vec{A}_V(\vec{r}) = j\omega \left[\frac{\mu_0}{4\pi} \sum_{n=1}^{N_M} \left\{ \int \kappa(\vec{r}')\vec{f}_n^V(\vec{r}')G(\vec{r},\vec{r}')d\vec{r}' \right\} Dn \right] \tag{2-57}$$

$$\Phi_V(\vec{r}) = j\omega \left[-\frac{1}{4\pi j\omega\varepsilon_0} \sum_{n=1}^{N_D} \left\{ \int_{V_n} \kappa(\vec{r}')\left(\nabla \cdot \vec{f}_n^V(\vec{r}')\right)G(\vec{r},\vec{r}')d\vec{r}' + \int_{V_n} \vec{f}_n^V(\vec{r}') \cdot (\nabla\kappa(\vec{r}'))G(\vec{r},\vec{r}')d\vec{r}' \right\} D_n \right] \tag{2-58}$$

Applying Gauss's Law into the last term in equation (2-58), $\Phi_V(\vec{r})$ becomes

$$\Phi_V(\vec{r}) = j\omega \left[-\frac{1}{4\pi j\omega\varepsilon_0} \sum_{n=1}^{N_D} \left\{ \int_{V_n} \kappa(\vec{r}')\left(\nabla \cdot \vec{f}_n^V(\vec{r}')\right)G(\vec{r},\vec{r}')d\vec{r}' + \int_{A_n} \hat{n} \cdot \vec{f}_n^V(\vec{r}')(\nabla\kappa(\vec{r}'))G(\vec{r},\vec{r}')d\vec{r}' \right\} D_n \right] \tag{2-59}$$

Finally the MoM matrix equation can be derived by substituting equation (2-54), (2-57) and (2-59) into (2-47). In terms of symbolic notation,

$$V_m^D = \sum_{n=1}^{N_D} Z_{mn}^{DD} I_{vn} \qquad m = 1,2,....,N_D \tag{2-60}$$

where the voltage excitation V_m^D is equal to

$$V_m^D = \int_{V_M} \vec{E}^i(\vec{r}) \cdot \vec{f}_m^V(\vec{r})d\vec{r} \tag{2-61}$$

and the superscript *D* refers to a dielectric structure. For a scattering problem, in which the voltage excitation is due to a plane wave incidence, the incident field is given by equation (2-38) and (2-39). It should be noted that the $j\omega$ term had been intentionally brought out from terms in equation (2-57) and (2-59) so that the volume current coefficient, I_{V_n}, can be equated to

$$I_{V_n} = j\omega D_n \tag{2-62}$$

Hence, the MoM impedance matrix elements are given by

$$Z_{mn}^{DD} = \frac{1}{j\omega}\int_{V_m}\frac{\vec{f}_m^V(\vec{r})\cdot\vec{f}_n^V(\vec{r}')}{\hat{\varepsilon}(\vec{r}')} + j\omega\left[\frac{\mu_0}{4\pi}\int_{V_m}\int_{V_n}\kappa_n(\vec{r}')\vec{f}_m^V(\vec{r})\cdot\vec{f}_n^V(\vec{r}')G(\vec{r},\vec{r}')d\vec{r}'d\vec{r}\right] \quad (2\text{-}63)$$

$$= +\left[\frac{1}{4\pi j\omega\varepsilon_0}\left(\int_{V_m}\int_{V_n}\kappa_n(\vec{r}')(\nabla\cdot\vec{f}_m^V(\vec{r}))(\nabla\cdot\vec{f}_n^V(\vec{r}'))G(\vec{r},\vec{r}')d\vec{r}'d\vec{r}\right)+\left(\int_{V_m}\int_{A_n}(\nabla\kappa(\vec{r}'))(\nabla\cdot\vec{f}_m^V(\vec{r}))(\hat{n}\cdot\vec{f}_n^V(\vec{r}'))G(\vec{r},\vec{r}')d\vec{r}'d\vec{r}\right)\right]$$

$$-\left[\frac{1}{4\pi j\omega\varepsilon_0}\left(\int_{A_m}\int_{V_n}\kappa_n(\vec{r}')(\hat{n}\cdot\vec{f}_m^V(\vec{r}))(\nabla\cdot\vec{f}_n^V(\vec{r}'))G(\vec{r},\vec{r}')d\vec{r}'d\vec{r}\right)+\left(\int_{A_m}\int_{A_n}(\nabla\kappa(\vec{r}'))(\hat{n}\cdot\vec{f}_m^V(\vec{r}))(\hat{n}\cdot\vec{f}_n^V(\vec{r}'))G(\vec{r},\vec{r}')d\vec{r}'d\vec{r}\right)\right]$$

The first term on the RHS of equation (2-63) exists only when face *m* coincides with face *n*. The solution of this MoM equation is obtained by recalling the properties of SWG basis function described in section 2.2. Applying the approximations in equation (2-49)-(2-51), the integration part of equation (2-63) becomes

$$\int_{V_m}\int_{V_n}\kappa_n(\vec{r}')\vec{f}_m^V(\vec{r})\cdot\vec{f}_n^V(\vec{r}')G(\vec{r},\vec{r}')d\vec{r}'d\vec{r}$$

$$=\frac{a_m}{3}\left[\frac{a_n\kappa_n^+}{3V_n^+}\int_{T_n^+}\vec{\rho}^+(\vec{r}')G(\vec{r}_m^{c+},\vec{r}')d\vec{r}'\right]\cdot\vec{\rho}_m^{c+}+\frac{a_m}{3}\left[\frac{a_n\kappa_n^-}{3V_n^-}\int_{T_n^-}\rho^-(\vec{r}')G(\vec{r}_m^{c+},\vec{r}')d\vec{r}'\right]\cdot\rho_m^{c+}$$

$$+\frac{a_m}{3}\left[\frac{a_n\kappa_n^+}{3V_n^+}\int_{T_n^+}\vec{\rho}^+(\vec{r}')G(\vec{r}_m^{c-},\vec{r}')d\vec{r}'\right]\cdot\vec{\rho}_m^{c-}+\frac{a_m}{3}\left[\frac{a_n\kappa_n^-}{3V_n^-}\int_{T_n^-}\rho^-(\vec{r}')G(\vec{r}_m^{c-},\vec{r}')d\vec{r}'\right]\cdot\rho_m^{c-}$$
$$(2\text{-}64)$$

$$\int_{V_m}\int_{V_n}\kappa(\vec{r}')(\nabla\cdot\vec{f}_m^V(\vec{r}))(\nabla\cdot\vec{f}_n^V(\vec{r}'))G(\vec{r},\vec{r}')d\vec{r}'d\vec{r}$$

$$= a_m\left[\frac{a_n\kappa_n^+}{V_n^+}\int_{T_n^+}G(\vec{r}_m^{c+},\vec{r}')d\vec{r}'\right]-a_m\left[\frac{a_n\kappa_n^-}{V_n^-}\int_{T_n^-}G(\vec{r}_m^{c+},\vec{r}')d\vec{r}'\right]$$

$$-a_m\left[\frac{a_n\kappa_n^+}{V_n^+}\int_{T_n^+}G(\vec{r}_m^{c-},\vec{r}')d\vec{r}'\right]+a_m\left[\frac{a_n\kappa_n^-}{V_n^-}\int_{T_n^-}G(\vec{r}_m^{c-},\vec{r}')d\vec{r}'\right]$$
$$(2\text{-}65)$$

$$\int\limits_{V_m}\int\limits_{A_n}\left(\nabla\kappa(\vec{r}')\right)\left(\nabla\cdot\vec{f}_m^V(\vec{r})\right)\left(\hat{n}\cdot\vec{f}_n^V(\vec{r}')\right)G(\vec{r},\vec{r}')d\vec{r}'d\vec{r}$$

$$= a_m\left[\left(\kappa_n^- - \kappa_n^+\right)\int\limits_{t_n} G\left(\vec{r}_m^{c+},\vec{r}'\right)d\vec{r}'\right] - a_m\left[\left(\kappa_n^- - \kappa_n^+\right)\int\limits_{t_n} G\left(\vec{r}_m^{c-},\vec{r}'\right)d\vec{r}'\right]$$

(2-66)

$$\int\limits_{A_m}\int\limits_{V_n}\kappa_n(\vec{r}')\left(\hat{n}\cdot\vec{f}_m^V(\vec{r})\right)\left(\nabla\cdot\vec{f}_n^V(\vec{r}')\right)G(\vec{r},\vec{r}')d\vec{r}d\vec{r}'$$

$$= a_m\left[\frac{a_n\kappa_n^+}{V_n^+}\int\limits_{T_n^+} G\left(\vec{r}_m^{c+} + \frac{1}{3}\vec{\rho}_m^{c+},\vec{r}'\right)d\vec{r}'\right] - a_m\left[\frac{a_n\kappa_n^-}{V_n^-}\int\limits_{T_n^-} G\left(\vec{r}_m^{c+} + \frac{1}{3}\vec{\rho}_m^{c+},\vec{r}'\right)d\vec{r}'\right]$$

(2-67)

$$\int\limits_{A_m}\int\limits_{A_n}\kappa_n(\vec{r}')\left(\hat{n}\cdot\vec{f}_m^V(\vec{r})\right)\left(\nabla\cdot\vec{f}_n^V(\vec{r}')\right)G(\vec{r},\vec{r}')d\vec{r}'d\vec{r}$$

$$= a_m\left[\left(\kappa_n^- - \kappa_n^+\right)\int\limits_{t_n} G\left(\vec{r}_m^{c+} + \frac{1}{3}\vec{\rho}_m^{c+},\vec{r}'\right)d\vec{r}'\right]$$

(2-68)

$$\int\limits_{V_m}\frac{\vec{f}_m^V(\vec{r})\cdot\vec{f}_n^V(\vec{r}')}{\hat{\varepsilon}(\vec{r}')}d\vec{r}'$$

$$= \frac{a_m a_n}{9V_m^+V_m^+}\int\limits_{T_m^+}\vec{\rho}_m^+(\vec{r})\cdot\vec{\rho}_m^+(\vec{r})dr + \frac{a_m a_n}{9V_m^-V_m^-}\int\limits_{T_m^-}\vec{\rho}_m^-(\vec{r})\cdot\vec{\rho}_m^-(\vec{r})dr$$

(2-69)

Calculation of integral in equation (2-69) can be made faster using analytical formula given in [8]

$$\int\limits_{T^p}\vec{f}_i(\vec{r})\cdot\vec{f}_j(\vec{r})dr = \frac{a_i a_j}{9V^p}\left[\begin{array}{l}\frac{8}{5}\left|\vec{r}^{cp}\right|^2 - \left(\vec{r}_i + \vec{r}_j\right)\cdot\vec{r}^{cp} + \left(\vec{r}_i\cdot\vec{r}_j\right) \\ -\frac{1}{10}\left(\vec{r}_1\cdot\vec{r}_r + \vec{r}_1\cdot\vec{r}_3 + \vec{r}_1\cdot\vec{r}_4 + \vec{r}_2\cdot\vec{r}_3 + \vec{r}_2\cdot\vec{r}_4 + \vec{r}_3\cdot\vec{r}_4\right)\end{array}\right]$$

(2-70)

As with the integrals calculation in the case of metal structures, the tetrahedrons-pair calculations should be applied instead of face-pair combinations to reduce the computational time. Assuming *V* is subdivided into *N* tetrahedron elements i.e. $T = 1,2,3,....N$, Figure 2.4 shows the combination of source tetrahedron, T^q, and observation tetrahedron, T^p, ($p,q = 1,2,3,....N$) together with the geometrical parameters after a local indexing scheme has been employed.
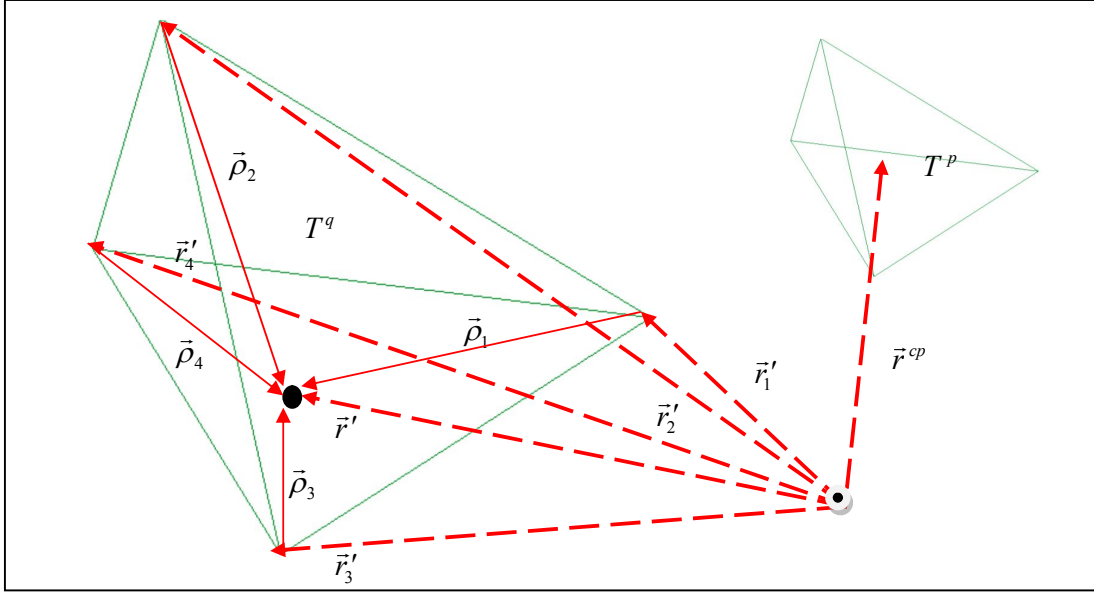
Figure 2.4: Local coordinates for T^q with observation point at T^p

A point inside a source tetrahedron, $\vec{r}'$,with vertices $\vec{r}_1', \vec{r}_2', \vec{r}_3'$ and $\vec{r}_4'$ can be expressed in terms of the normalized volume coordinates [7] of $\varsigma = \dfrac{V_1}{V^q}, \eta = \dfrac{V_2}{V^q}$,

$\xi = \dfrac{V_3}{V^q}$ and $\alpha = \dfrac{V_4}{V^q}$, where $\varsigma + \eta + \xi + \alpha = 1$

Applying this, any point inside the source tetrahedron can be described as

$$\vec{r}' = \vec{r}_1'\varsigma + \vec{r}_2'\eta + \vec{r}_3'\xi + \vec{r}_4'\alpha \tag{2-71}$$

The position vector $\vec{\rho}_i$ that is used to define the basis function, $\vec{f}_i(\vec{r}') = \dfrac{a_i}{3V^q}\vec{\rho}_i(\vec{r}')$,

inside T^q is given by

$$\vec{\rho}_i = \pm(r' - r_i') \qquad , i = 1, 2, 3, 4 \tag{2-72}$$

where r_i is the vertex opposite local face i in T^q. These definitions in terms of

fixed vertices and volume coordinates allow integrals over the source tetrahedron

to be written in terms of scalar integrals, where a typical term for potentials due to

$\vec{f}_i(\vec{r}')$ in T^q is given as

$$\vec{A}_i^{pq} = \frac{\mu_0}{4\pi}\left[\frac{a_i}{3V^q}\left(6V^q\int_0^1\int_0^{1-\eta}\int_0^{1-\eta-\xi}\pm(\vec{r}'-\vec{r}_i')\frac{e^{-jkR^p}}{R^p}d\zeta d\eta d\xi\right)\right]$$

$$= \pm\frac{\mu_0 a_i}{2\pi}\int_0^1\int_0^{1-\eta}\int_0^{1-\eta-\xi}((\vec{r}_1'-\vec{r}_4')\zeta+(\vec{r}_2'-\vec{r}_4')\eta+(\vec{r}_3'-\vec{r}_4')\xi+(\vec{r}_4'-\vec{r}_i'))G(\vec{r},\vec{r}')d\zeta d\eta d\xi$$

$$= \pm\frac{\mu_0 a_i}{2\pi}\left[(\vec{r}_1'-\vec{r}_4')I_\zeta^{pq}+(\vec{r}_2'-\vec{r}_4')I_\eta^{pq}+(\vec{r}_3'-\vec{r}_4')I_\xi^{pq}+(\vec{r}_4'-\vec{r}_i')I^{pq}\right] \qquad (2\text{-}73)$$

$$\Phi_i^{pq} = \mp\frac{3a_i}{2\pi j\omega\varepsilon_0}I^{pq} \qquad (2\text{-}74)$$

where the scalar integrals are given by

$$I^{pq} = \int_0^1\int_0^{1-\eta}\int_0^{1-\eta-\zeta}G(\vec{r},\vec{r}')d\zeta d\eta d\xi, \quad I_\zeta^{pq} = \int_0^1\int_0^{1-\eta}\int_0^{1-\eta-\zeta}\zeta G(\vec{r},\vec{r}')d\zeta d\eta d\xi$$

$$I_\eta^{pq} = \int_0^1\int_0^{1-\eta}\int_0^{1-\eta-\zeta}\eta G(\vec{r},\vec{r}')d\zeta d\eta d\xi, \quad I_\xi^{pq} = \int_0^1\int_0^{1-\eta}\int_0^{1-\eta-\zeta}\xi G(\vec{r},\vec{r}')d\zeta d\eta d\xi \qquad (2\text{-}75)$$

2.5   MoM Model for Combined Metal-Dielectric Structures

For metal-dielectric interface, the EFIE is used in conjunction with RWG and SWG basis functions to model the structure. Consider a metal surface *S* that is attached to a dielectric volume *V*. In this case, the $\vec{E}^s(\vec{r})$ component has two contributions; the first is due to the volume polarization current, $\vec{J}_V(\vec{r}')$, and its associated bound charges, $\rho_V(\vec{r}')$ and $\rho_S(\vec{r}')$, and the second is due to surface current, $\vec{J}_S(\vec{r}')$, and free charge density on the metal surface, $\rho_S(\vec{r}')$, as shown in the equations listed below

$$\vec{E}^S(\vec{r}) = -j\omega\vec{A}_V(\vec{r}) - \nabla\Phi_v(\vec{r}) - j\omega\vec{A}_S(\vec{r}) - \nabla\Phi_S(\vec{r}) \ , \quad \text{for } \vec{r} \text{ throughout } V \qquad (2\text{-}76)$$

$$\vec{E}^S(\vec{r}) = -j\omega\vec{A}_S(\vec{r}) - \nabla\Phi_S(\vec{r}) - j\omega\vec{A}_V(\vec{r}) - \nabla\Phi_V(\vec{r}) \ , \quad \text{for } \vec{r} \text{ on } S \qquad (2\text{-}77)$$

where the potential terms in eq. (2-76) and (2-77) carries the same meaning as discussed previously. By enforcing the boundary conditions of

$$\vec{E}(\vec{r}) = \frac{\vec{D}(\vec{r})}{\hat{\varepsilon}(\vec{r})} \qquad , \text{ for } \vec{r} \in V \qquad (2\text{-}78)$$

$$\vec{E}(\vec{r})_{\tan} = 0 \qquad , \text{ for } \vec{r} \in S \qquad (2\text{-}79)$$

a complete EFIE can be derived for the whole structure

$$\vec{E}^i(\vec{r}) = \frac{\vec{D}(\vec{r})}{\hat{\varepsilon}(\vec{r})} + j\omega\vec{A}_V(\vec{r}) + \nabla\Phi_v(\vec{r}) + j\omega\vec{A}_S(\vec{r}) + \nabla\Phi_S(\vec{r}) \qquad , \text{ for } \vec{r} \in V \qquad (2\text{-}80)$$

$$\vec{E}^i(\vec{r})_{\tan} = \left[j\omega\vec{A}_S(\vec{r}) + \nabla\Phi_S(\vec{r}) + j\omega\vec{A}_V(\vec{r}) + \nabla\Phi_V(\vec{r})\right]_{\tan} \qquad , \text{ for } \vec{r} \in S \qquad (2\text{-}81)$$

2.5.1 Application of the Testing Functions

Once more, the EFIE is sampled in space using the testing functions $\vec{f}_m^V(\vec{r})$ or $\vec{f}_m^S(\vec{r})$. Most of the works described here have been discussed previously in section 2.3 and 2.4. To avoid confusion, the section, is divided into two subsections; one describing electrical parameters inside *V,* and the other describing electrical parameters on *S*.

2.5.1.1 Observation point located throughout *V*

For calculations involving a dielectric volume, assuming $\vec{f}_m^V(\vec{r})$ covers the entire dielectric region *V*, then multiplication of eq. (2-80) by $\vec{f}_m^V(\vec{r})$ and integrating over *V* yields

$$\int_{V_m}\bar{E}^i(\bar{r})\cdot\vec{f}_m^V(\bar{r})dr=\int_{V_m}\frac{\bar{D}(\bar{r})}{\hat{\varepsilon}(\bar{r})}\cdot\vec{f}_m^V(r)dr+j\omega\int_{V_m}\vec{A}_V(\bar{r})\cdot\vec{f}_m^V(\bar{r})d\bar{r}-\int_{v_m}\Phi_V(\bar{r})\Big(\nabla\cdot\vec{f}_m^V(\bar{r})\Big)d\bar{r}+\int_{A_M}\Phi_V(\bar{r})\Big(n\cdot\vec{f}_m^V(\bar{r})\Big)dr$$

$$+j\omega\int_{V_m}\vec{A}_S(\bar{r})\cdot\vec{f}_m^V(\bar{r})dr-\int_{V_m}\Phi_S(\bar{r})\Big(\nabla\cdot\vec{f}_m^V(r)\Big)d\bar{r}+\int_{A_m}\Phi_S(\bar{r})\Big(\hat{n}\cdot\vec{f}_m^V(\bar{r})\Big)d\bar{r} \tag{2-82}$$

Note that the first four terms on the RHS of equation (2-81) are essentially the terms required for the calculation of Z_{mn}^{DD} as demonstrated in equation (2-63). On the other hand, the last three terms in this equation are used to calculate Z_{mn}^{DM} which accounts for the radiation from a source point on the metal structure *M* that is tested on an observation point inside dielectric structure *D*.

2.5.1.2 Observation point located on *S*

Assuming that $\vec{f}_m^S(\bar{r})$ covers a metal surface *S*, then the multiplication of equation (2-81) by $\vec{f}_m^S(\bar{r})$ in conjunction with integration over *S* yields

$$\int_{S_m}\bar{E}^i(\bar{r})\cdot\vec{f}_m^S(\bar{r})dr=j\omega\int_{S_m}\vec{A}_S(\bar{r})\cdot\vec{f}_m^S(\bar{r})d\bar{r}-\int_{S_m}\Phi_S(\bar{r})\Big(\nabla\cdot\vec{f}_m^S(\bar{r})\Big)d\bar{r}$$

$$+j\omega\int_{S_m}\vec{A}_V(\bar{r})\cdot\vec{f}_m^S(\bar{r})d\bar{r}-\int_{S_m}\Phi_V(\bar{r})\Big(\nabla\cdot\vec{f}_m^S(\bar{r})\Big)d\bar{r} \tag{2-83}$$

Once more, the first two terms on the RHS of eq. (2-83) are essentially the terms required for the calculation of Z_{mn}^{MM} as demonstrated in equation (2-30), while the last two terms are required for the calculation of Z_{mn}^{MD} which describes the contribution of radiation from a source point inside *D* tested at an observation point on *M*.

2.5.2 Application of the Expansion Functions

The expansion of volume current, charge and flux density has been explained in section 2.4, whilst the expansion of surface current and charge density has been described in section 2.3. The complete moment method matrix equation can be obtained by appropriately substituting the expansions into equations (2-82) and (2-83). In terms of symbolic notation,

$$V_m^D = \sum_{n=1}^{N_D} Z_{mn}^{DD} I_{vn} + \sum_{n=1}^{N_M} Z_{mn}^{DM} I_{sn} \tag{2-84}$$

$$V_m^M = \sum_{n=1}^{N_M} Z_{mn}^{MM} I_{vsn} + \sum_{n=1}^{N_M} Z_{mn}^{MD} I_{vn} \tag{2-85}$$

where the voltage excitation is given by

$$V_m^D = \int_{V_M} \vec{E}^i(\vec{r}) \cdot \vec{f}_m^V(\vec{r}) d\vec{r} \tag{2-86}$$

$$V_m^M = \int_{S_m} \vec{E}^i(\vec{r}) \cdot \vec{f}_m^S(\vec{r}) dr \tag{2-87}$$

Since terms required for calculation of Z_{mn}^{DD} and Z_{mn}^{MM} have been outlined in equations (2-63) and (2-30) respectively, only the derivations of Z_{mn}^{MD} and Z_{mn}^{DM} are described here. The impedance matrix elements of Z_{mn}^{DM} can be obtained by the substitutions of equations (2-25) and (2-26) to the last three terms of equations (2-82), which gives

$$Z_{mn}^{DM} = \frac{j\omega\mu_0}{4\pi} \int_{V_m} \int_{S_n} \vec{f}_m^V(\vec{r}) \cdot \vec{f}_n^S(\vec{r}') G(\vec{r},\vec{r}') d\vec{r}' d\vec{r}$$

$$= +\frac{1}{4\pi j\omega\varepsilon_0} \left[\begin{array}{l} \int_{V_m} \int_{S_n} \left(\nabla \cdot \vec{f}_m^V(\vec{r})\right)\left(\nabla \cdot \vec{f}_n^S(\vec{r}')\right) G(\vec{r},\vec{r}') d\vec{r}' d\vec{r} \\ -\int_{A_m} \int_{S_n} \hat{n} \cdot \vec{f}_m^V(\vec{r})\left(\nabla \cdot \vec{f}_n^S(\vec{r}')\right) G(\vec{r},\vec{r}') d\vec{r}' d\vec{r} \end{array} \right] \qquad (2\text{-}88)$$

Similarly, expressions for the impedance matrix elements of Z_{mn}^{MD} can be derived through the substitutions of equations (2-57) and (2-59) to the last two terms of equations (2-83), which provides

$$Z_{mn}^{MD} = \frac{j\omega\mu_0}{4\pi} \int_{S_m} \int_{V_n} \vec{f}_m^S(\vec{r}) \cdot \vec{f}_n^V(\vec{r}') \kappa(\vec{r}') G(\vec{r},\vec{r}') d\vec{r}' d\vec{r}$$

$$= \frac{1}{4\pi j\omega\varepsilon_0} \left[\begin{array}{l} \int_{S_m} \int_{V_n} \left(\nabla \cdot \vec{f}_m^S(\vec{r})\right)\left(\nabla \cdot \vec{f}_n^V(\vec{r}')\right) \kappa(\vec{r}') G(\vec{r},\vec{r}') d\vec{r}' d\vec{r} \\ +\int_{S_n} \int_{A_n} \left(\nabla \cdot \vec{f}_m^S(\vec{r})\right)\hat{n} \cdot \vec{f}_n^v(\vec{r}')\left(\nabla\kappa(\vec{r}')\right) G(\vec{r},\vec{r}') d\vec{r}' d\vec{r} \end{array} \right] \qquad (2\text{-}89)$$

Since the gradient of dielectric contrast is given by $\nabla\kappa(r') = \kappa_n^- - \kappa_n^+$, a relation between Z_{mn}^{MD} and Z_{mn}^{DM} can be derived.

$$Z_{mn}^{MD} = \hat{\kappa} \cdot Z_{mn}^{DM^T} \qquad (2\text{-}90)$$

where $\hat{\kappa}$ refers to the contrast ratio coefficient, and $Z_{mn}^{DM^T}$ corresponds to the transpose of Z_{mn}^{MD} matrix, i.e. the inner and outer integrals interchanged.

Using this relationship, calculations of Z_{mn}^{MD} and Z_{mn}^{DM} can be performed by computing integrals contained in either one of them. It is preferable to compute integrals in Z_{mn}^{DM} using equation (2-88) rather than in Z_{mn}^{MD} via equation (2-89) since the computational time for surface integrals at the source elements is less than those for volume integrals. The integration terms of equation (2-88) are listed below after taking into account the approximation used in equations (2-49)-(2-51)

$$\int_{V_m} \int_{S_n} \vec{f}_m^V(\vec{r}) \cdot \vec{f}_n^S(\vec{r}') G(\vec{r},\vec{r}') d\vec{r}' d\vec{r}$$

$$
= \frac{a_m}{3} \left[\frac{l_n}{2A_n^+} \int_{t_n^+} \vec{\rho}_n^+(\vec{r}') G(\vec{r}_m^{c+}, \vec{r}') d\vec{r}' \right] \cdot \vec{\rho}_m^{c+} + \frac{a_m}{3} \left[\frac{l_n}{2A_n^-} \int_{t_n^-} \vec{\rho}_n^-(\vec{r}') G(\vec{r}_m^{c+}, \vec{r}') d\vec{r}' \right] \cdot \vec{\rho}_m^{c+}
$$

$$
+ \frac{a_m}{3} \left[\frac{l_n}{2A_n^+} \int_{t_n^+} \vec{\rho}_n^+(\vec{r}') G(\vec{r}_m^{c-}, \vec{r}') d\vec{r}' \right] \cdot \vec{\rho}_m^{c-} + \frac{a_m}{3} \left[\frac{l_n}{2A_n^-} \int_{t_n^-} \vec{\rho}_n^-(\vec{r}') G(\vec{r}_m^{c-}, \vec{r}') d\vec{r}' \right] \cdot \vec{\rho}_m^{c-}
$$

(2-91)

$$
\int_{V_m} \int_{S_n} \left(\nabla \cdot \vec{f}_m^V(\vec{r}) \right) \left(\nabla \cdot \vec{f}_n^S(\vec{r}') \right) G(\vec{r}, \vec{r}') d\vec{r}' d\vec{r}
$$

$$
= a_m \left[\frac{l_n}{A_n^+} \int_{t_n^+} G(\vec{r}_m^{c+}, \vec{r}') d\vec{r}' \right] - a_m \left[\frac{l_n}{A_n^-} \int_{t_n^-} G(\vec{r}_m^{c+}, \vec{r}') d\vec{r}' \right]
$$

(2-92)

$$
- a_m \left[\frac{l_n}{A_n^+} \int_{t_n^+} G(\vec{r}_m^{c-}, \vec{r}') d\vec{r}' \right] + a_m \left[\frac{l_n}{A_n^-} \int_{t_n^-} G(\vec{r}_m^{c-}, \vec{r}') d\vec{r}' \right]
$$

$$
\int_{A_m} \int_{S_n} \hat{n} \cdot \vec{f}_m^V(\vec{r}) \left(\nabla \cdot \vec{f}_n^S(\vec{r}') \right) G(\vec{r}, \vec{r}') d\vec{r}' d\vec{r}
$$

$$
= a_m \left[\frac{l_n}{A_n^+} \int_{t_n^+} G\left(\vec{r}_m^{c+} + \frac{1}{3} \vec{\rho}_m^{c+}, \vec{r}' \right) d\vec{r}' \right] - a_m \left[\frac{l_n}{A_n^-} \int_{t_n^-} G\left(\vec{r}_m^{c+} + \frac{1}{3} \vec{\rho}_m^{c+}, \vec{r}' \right) d\vec{r}' \right]
$$

(2-93)

As in the calculation of the integrals in Z_{mn}^{MM}, the equations above are calculated using a face-pair combination rather than an edge-pair combination, which significantly enhances the computation efficiency.

2.6   Efficient Calculations of the Integrals

It is well known that the numerical computations of MoM integrals accounts for most of the total computational time. Therefore, the task of minimizing the integrals calculation time is essential in order to reduce the overall computational time. An effective way to perform this is by employing the Gaussian quadrature formula [7] onto the integrals in equation (2-37) and equation (2-75). The formulas

used for integrals calculation involving a source triangle and a source tetrahedron are listed in Tables 2.1 and 2.2, respectively. In order to ensure efficient calculation of the integrals, the formula is applied based on the separation distance between the source point, $\vec{r}'$, and the observation point, $\vec{r}$, i.e. $R = |\vec{r} - \vec{r}'|$. In order to maintain the required accuracy, more number of points, n_p, is needed for smaller R. However, for the integrals calculation involving points separated by larger R, it is more efficient to use a smaller n_p since the solution yields results just as accurate as that obtained using a higher n_p.

Expansion from equation (2-37): $\int_0^1 \int_0^{1-\eta} f(\zeta,\eta)d\zeta d\eta = \sum_{i=1}^{n_p} f(\zeta_i,\eta_i)W_i$				
No of points	Iteration	Unit Coordinates		Weights
n_p	i	η_i	ζ_i	W_i
1	1	1/3	1/3	1/2
3	1	1/6	1/6	1/6
	2	2/3	1/6	1/6
	3	1/6	2/3	1/6
4	1	1/3	1/3	- 9/32
	2	3/5	1/5	25/96
	3	1/5	3/5	25/96
	4	1/5	1/5	25/96
7	1	0	0	1/40
	2	1/2	0	1/15
	3	1	0	1/40
	4	1/2	1/2	1/15
	5	0	1	1/40
	6	0	1/2	1/15
	7	1/3	1/3	9/40

Table 2.1: Symmetric quadrature for unit triangle (taken from [7], pp. 197)

Expansion from equation (2-75): $\int_0^1 \int_0^{1-\eta} \int_0^{1-\eta-\xi} (f(\zeta,\eta,\xi))d\zeta d\eta d\xi = \sum_{i=1}^{n_p} f(\zeta_i,\eta_i,\xi_i)W_i$				
No of points	Iteration	Unit Coordinates		Weights
n_p	i	η_i	ζ_i	ζ_i	W_i
1	1	1/4	1/4	1/4	1/6
4	1	a	b	b	1/24
	2	b	a	b	1/24
	3	b	b	a	1/24
	4	b	b	a	1/24
5	1	1/4	1/4	1/4	- 2/15
	2	1/2	1/6	1/6	3/40
	3	1/6	1/2	1/6	3/40
	4	1/6	1/6	1/2	3/40
	5	1/6	1/6	1/6	3/40
11	1	1/4	1/4	1/4	-4/5625
	2	11/14	1/14	1/14	343/45000
	3	1/14	11/14	1/14	343/45000
	4	1/14	1/14	11/14	343/45000
	5	1/14	1/14	1/14	343/45000
	6	c	c	d	56/2250
	7	c	d	c	56/2250
	8	c	d	d	56/2250
	9	d	c	c	56/2250
	10	d	c	d	56/2250
	11	d	d	c	56/2250
where $a = (5+3\sqrt{5})/20$, $b = (5-3\sqrt{5})/20$, $c = (1+\sqrt{(5/14)})/4$, $d = (1-\sqrt{(5/14)})/4$					

Table 2.2: Symmetric quadrature for unit tetrahedral (taken from [7], pp. 198)

Although applying the Gaussian quadrature formula has significantly reduced the computational time, this technique is not suitable for the treatment of self integrals. When the source and observation points coincides with one another

(*m=n*), a singularity problem exists since the separation distance, $R = |\vec{r} - \vec{r}'|$ becomes zero. Thus, the solution of these integrals using the quadrature formula yields unstable results.

For the treatment of self integrals, a singularity extraction technique proposed by D.R. Wilton et. al in [9] can be employed. For a pure metal structures, the equations describing the vector and scalar potentials in (2-35) and (2-36) can be simplified into

$$\vec{A}_i^{pq} \propto \int_{t^q} (\vec{r}' - \vec{r}_i) \frac{e^{-jk_0 R}}{R} d\vec{r}' \qquad (2\text{-}94)$$

$$\Phi_i^{pq} \propto \int_{t^q} \frac{e^{-jk_0 R}}{R} d\vec{r}' \qquad (2\text{-}95)$$

Applying vector projection, the vector potential in (2-94) is proportional to the vector $\vec{\rho}' - \vec{\rho}_i'$, where $\vec{\rho}'$ and $\vec{\rho}_i'$ are the projection of $\vec{r}'$ and $\vec{r}_i'$, respectively, onto the plane of triangle t^q,

$$\vec{A}_i^{pq} \propto \int_{t^q} (\vec{\rho}' - \vec{\rho}_i') \frac{e^{-jk_0 R}}{R} d\vec{r}' \qquad (2\text{-}96)$$

which can be expanded into

$$\vec{A}_i^{pq} \propto \int_{t^q} (\vec{\rho}' - \vec{\rho}) \frac{e^{-jk_0 R}}{R} d\vec{r}' + \int_{t^q} (\vec{\rho} - \vec{\rho}_i') \frac{e^{-jk_0 R}}{R} d\vec{r}' \qquad (2\text{-}97)$$

where $\vec{\rho}$ is the vector projection of $\vec{r}$ onto the plane of t^q. Thus, applying singularity extraction technique, this vector potential is then proportional to

$$= \int_{t^q} (\vec{\rho}' - \vec{\rho}) \frac{e^{-jk_0 R} - 1}{R} d\vec{r}' + \int_{t^q} (\vec{\rho} - \vec{\rho}_i') \frac{e^{-jk_0 R} - 1}{R} d\vec{r}' + \int_{t^q} \frac{\vec{\rho}' - \vec{\rho}}{R} d\vec{r}' + + (\vec{\rho} - \vec{\rho}_i') \int_{t^q} \frac{d\vec{r}'}{R} \qquad (2\text{-}98)$$

Similarly, applying singularity extraction technique to the scalar potential in (2-95) yields

$$\Phi_i{}^{pq} \propto \int\limits_{t^q} \frac{e^{-jk_0R}-1}{R}d\vec{r}' + \int\limits_{t^q} \frac{d\vec{r}'}{R} \qquad (2\text{-}99)$$

The last two terms in equation (2-98) and the last term in equation (2-99) are calculated using analytical formulas derived in [9] while the preceding terms can be efficiently calculated using Gaussian quadrature formula. This singularity extraction technique can also be applied for pure dielectric structure.

The analytical formulas given in [9] are discussed briefly. These formulas provide an accurate and faster solution to the singularity problem in both surface and volume integrations. Figure 2.5, which illustrates a source point within a plane of triangle *t*, is useful in visualizing many variables needed for the computation of these self- integrals.
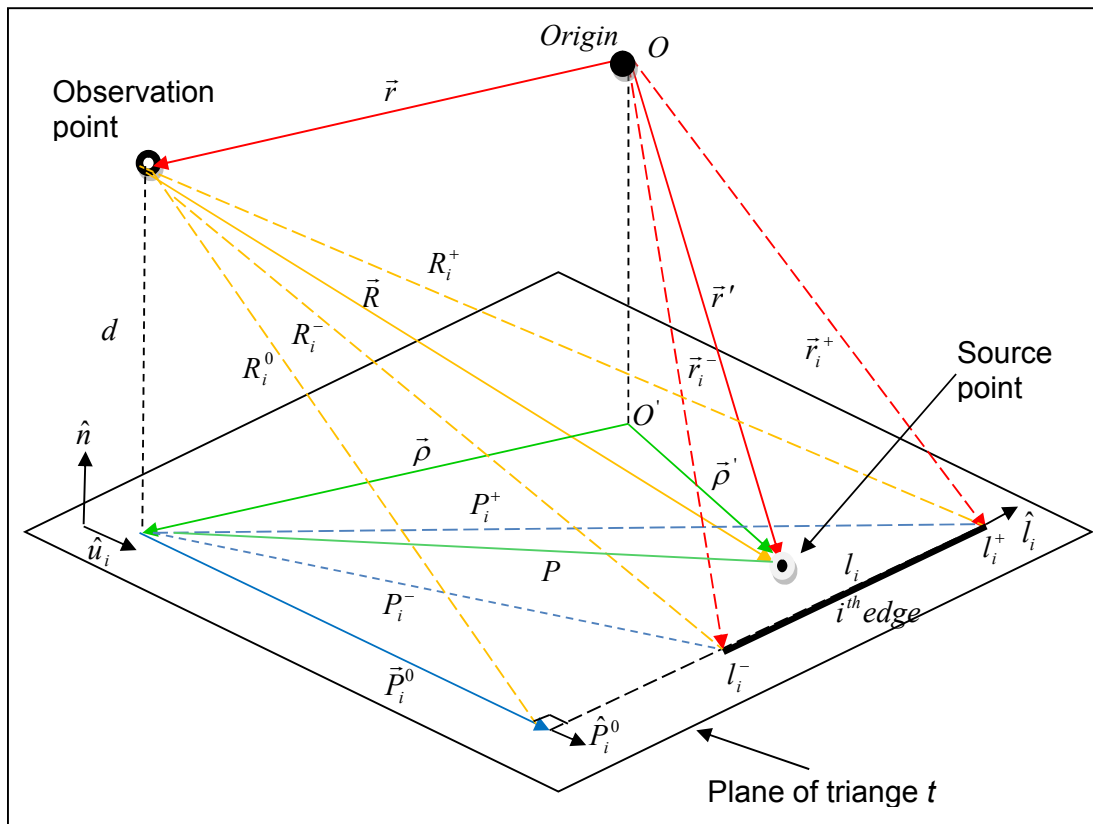
Figure 2.5: Geometrical quantities associated with a source point within a plane of

triangle *t*

Here, $\vec{\rho}\,'$ is the vector projection of $\vec{r}\,'$ onto the plane of triangle *t* and $\vec{\rho}$ is

the similar projection of $\vec{r}$. The distance between these vectors is given by

$P = \left|\vec{\rho} - \vec{\rho}\,'\right|$. Additionally, the perpendicular distance from a point located by $\vec{\rho}$ to

the ith edge is given by P_i^0, where i^{th} edge is parameterized by the length

variable l_i. The endpoints of the edge are located at l_i^+ and l_i^-. The distance

(measured in P) from $\vec{\rho}$ to the given endpoints $\vec{\rho}_i^+$ and $\vec{\rho}_i^-$ are denoted P_i^+ and

P_i^-, respectively. Using these definitions, the quantities of $\hat{l}_i$, $l_i^{\pm}$, P_i^0, $P_i^{\pm}$ and

$\hat{P}_i^0$ can be calculated in terms of $\vec{\rho}_i^+$, $\vec{\rho}_i^-$ and $\vec{\rho}$ by the following equations.

$$\hat{l}_i = \frac{\vec{\rho}_i^+ - \vec{\rho}_i^-}{\left|\vec{\rho}_i^+ - \vec{\rho}_i^-\right|} \tag{2-100}$$

$$l_i^{\pm} = \left(\vec{\rho}_i^{\pm} - \vec{\rho}\right)\bullet\hat{l} \tag{2-101}$$

$$P_i^0 = \left|\left(\vec{\rho}_i^{\pm} - \vec{\rho}\right)\bullet\hat{u}_i\right| \qquad \text{where } \hat{u}_i = \hat{l}_i \times \hat{n}_i \tag{2-102}$$

$$P_i^{\pm} = \left|\vec{\rho}_i^{\pm} - \vec{\rho}\right| = \sqrt{\left(P_i^0\right)^2 + \left(l_i^{\pm}\right)^2} \tag{2-103}$$

$$\hat{P}_i^0 = \frac{\left(\vec{\rho}_i^{\pm} - \vec{\rho}\right) - l_i^{\pm}\hat{l}}{P_i^0} \tag{2-104}$$

For surface sources distributed on a planar polygon *S*, the potential observed at $\vec{r}$

due to an elemental source on *S* at $\vec{r}\,'$ is proportional to $\dfrac{1}{R}$. In this case, the

distance R is denoted in terms of R_i^0 and $R_i^{\pm}$ which are given by

$$R_i^0 = \sqrt{\left(P_i^0\right)^2 + d^2}$$ (2-105)

$$R_i^\pm = \sqrt{\left(P_i^\pm\right)^2 + d^2}$$ (2-106)

where d is the height of the observation point above the plane of S, measured in the direction of $\hat{n}_i$ as

$$d = \hat{n}_i \bullet \left(\vec{r} - \vec{r}_i^\pm\right)$$ (2-107)

The vectors $\hat{l}_i$ and $\vec{\rho}_i^\pm$ can now be defined in terms of $\vec{r}_i^\pm$. These are given by

$$\hat{l}_i = \frac{\vec{r}_i^+ - \vec{r}_i^-}{\left|\vec{r}_i^+ - \vec{r}_i^-\right|}$$ (2-108)

$$\vec{\rho}_i^\pm = r_i^\pm - \hat{n}_i\left(\hat{n}_i \bullet r_i^\pm\right)$$ (2-109)

Based on these definitions, analytical formulas to solve the singularity problem in surface and integration can be formulated. The derivation of these formulas has been discussed in detail in [9]. The analytical formulas for surface integrals are expressed in the form of

$$\int_S \frac{dS'}{R} = \sum_i \hat{P}_i^0 \bullet \hat{u}_i \left[P_i^0 \ln\frac{R_i^+ + l_i^+}{R_i^- - l_i^-} - |d| \left(\tan^{-1}\frac{P_i^0 l_i^+}{\left(R_i^0\right)^2 + |d|R_i^+} - \tan^{-1}\frac{P_i^0 l_i^-}{\left(R_i^0\right)^2 + |d|R_i^-} \right) \right]$$ (2-110)

$$\int_S \frac{\vec{\rho}' - \vec{\rho}}{R} dS' = \frac{1}{2}\sum_i \hat{u}_i \left[\left(R_i^0\right)^2 \ln\frac{R_i^+ + l_i^+}{R_i^- + l_i^-} + l_i^+ R_i^+ - l_i^- R_i^- \right]$$ (2-111)

Additionally, the analytical formulas for volume integrals are given by

$$\int_V \frac{dV'}{R} = \sum_j d_j \sum_i \hat{P}_i^0 \bullet \hat{u}_i$$

$$\times \left[|d_j| \left(\tan^{-1}\frac{P_{ij}^0 l_{ij}^+}{\left(R_{ij}^0\right)^2 + |d_j|R_{ij}^+} - \tan^{-1}\frac{P_{ij}^0 l_{ij}^-}{\left(R_{ij}^0\right)^2 + |d_j|R_{ij}^-} \right) - P_{ij}^0 \ln\frac{R_{ij}^+ + l_{ij}^+}{R_{ij}^- + l_{ij}^-} \right]$$ (2-112)

$$\int_S \frac{\vec{r}' - \vec{r}}{R} dV' = \frac{1}{3} \sum_j \hat{n}_j \left\{ \sum_i \hat{P}_{ij}^0 \bullet \hat{u}_{ij} \left[\frac{P_{ij}^0 \left[(R_{ij}^0)^2 + 2d_j^2 \right]}{2} \right] \ln \frac{R_{ij}^+ + l_{ij}^+}{R_{ij}^- + l_{ij}^-} \right.$$

(2-113)

$$\left. + \frac{P_{ij}^0}{2} \left(l_{ij}^+ R_{ij}^+ - l_{ij}^- R_{ij}^- \right) - \left| d_j \right|^3 \left(\tan^{-1} \frac{P_{ij}^0 l_{ij}^+}{(R_{ij}^0)^2 + \left| d_J \right| R_{ij}^+} - \tan^{-1} \frac{P_{ij}^0 l_{ij}^-}{(R_{ij}^0)^2 + \left| d_J \right| R_{ij}^-} \right) \right\}$$

where the double subscript *ij* signifies a quantity associated with the ith edge of the
jth face, while the single subscript *j* denotes a quantity associated with the *j*th face
only. Equations (2-110) to (2-113) are used once the singularity extraction
technique has been applied to both potential integrals as shown in equations (2-
98) and (2-99).

2.7 Solution of the MoM Block Matrix

Once the impedance matrices for the structure are obtained, the total block
impedance matrix *Z* can be calculated by combining the metal's impedance matrix
Z_{mn}^{MM} with the dielectric's impedance matrix Z_{mn}^{DD} as well as the mutual impedance
matrices Z_{mn}^{DM} and Z_{mn}^{MD} in the form of

$$Z = \begin{bmatrix} Z_{mn}^{MM} & Z_{mn}^{MD} \\ Z_{mn}^{DM} & Z_{mn}^{DD} \end{bmatrix}$$

(2-114)

Consequently, the resultant system of linear equations

$$\vec{V} = Z\vec{I}$$

(2-115)

is solved using Gaussian elimination [10]. For this purposes, subroutines F07ARF and F07ASF from Numerical Algorithms Group (NAG) FORTRAN library are used, which allows for a faster computation time. In summary, these subroutines compute the solution to a complex system of linear algebraic equation

$$\hat{A}\vec{X} = \vec{B}$$ (2-116)

where $\vec{X}$ and $\vec{B}$ corresponds to column vectors of length *n* and $\hat{A}$ refers to an *n×n* symmetric complex matrix. Subroutine F07ARF factorizes $\hat{A}$ as a product of lower triangular matrix and upper triangular matrix, in a process called LU factorization. This factored form of $\hat{A}$ is then used as an input by the second subroutine, which uses Gaussian elimination with backward and forward substitution, depending on the form of $\hat{A}$, to solve the system of linear equations.

References

[1] R.F.Harrington, "Field Computation by Moment Methods," pp 5-9, Macmillan, New York, 1993

[2] S.M.Rao, D.R.Wilton and A.W.Glisson, "Electromagnetic Scattering by Surfaces of Arbitrary Shape," *IEEE Trans. Antennas Propag.*, vol.30, No.3, pp.409-418, May 1982

[3] D.H.Schaubert,D.R.Wilton,A.W.Glisson, "A Tetrahedral Modelling Method for Electromagnetic Scattering by Arbitrarily Shaped Inhomogeneous Dielectric Bodies," *IEEE Trans. Antennas Propag.*, vol.32, No.1, pp. 77-85, Jan 1984

[4] A. Sankar and T.C. Tong, "Current computation on complex structures by finite element method*," Electron. Lett.*, vol.19, pp.218-219, Mar 1983

[5] C.A. Balanis, "Antenna Theory: Analysis and Design", 2nd edition, Chapter 3, pp. 117-118, John Wiley and Sons Inc., 1997

[6] A.W. Glisson and D.R.Wilton, "Simple and efficient numerical methods for problems of electromagnetic radiation and scattering from surfaces," *IEEE Trans. Antennas Propag.*, vol.AP-28, No.5, pp. 593-603, Sept 1980

[7] J.E.Akin, "Finite Elements for Analysis and Design," pp.197-200, Academic Press Inc., San Diego, 1995

[8] O.C.Zienkiewicz, "The Finite Element Method in Engineering Science", McGraw-Hill, New York,1971

[9] D.R.Wilton, S.M.Rao, D.H.Schaubert, O.M.Al-Bundak and C.M.Butlers, "Potential Integrals for Uniform and Linear Source Distributions on Polygonal and Polyhedral Domains*", IEEE Trans. Antennas Propag.*, vol.32, No.3, pp. 276-282, Mar 1984

[10] H.P.William and A.T.Saul, "Numerical Recipes: the Art of Science Computing*",* pp.46, Cambridge University Press, Cambridge, 2007

CHAPTER 3

WIDEBAND CIRCULARLY

POLARIZED RECTANGULAR DRA

USING a SPIRAL EXCITATION

3.1   Introduction

Throughout this research, regular-shaped DRAs are used due to their ease of production, low cost, and modelling simplicity. These include rectangular, cylindrical, and hemispherical DRAs. Out of the three regular geometries, rectangular-shaped DRA offers the greatest flexibility in choosing the design parameters. In this chapter, a rectangular DRA that is characterized by a height a, a width b, a depth c, and a dielectric constant ε_r, has been excited using a square spiral metal strip to generate a wideband circular polarization. Additionally, the frequency tuning ability of this rectangular DRA has been demonstrated.

3.1.1 Degree of Freedom

The rectangular shape offers two degrees of freedom, where the aspect ratio of height to width ($\frac{a}{b}$) and depth to width ($\frac{c}{b}$) directly influence the resonance frequency and the radiation Q-factor. This gives the designer a greater control over the antenna profile and its impedance bandwidth in tailoring the DRA to suit particular applications. For example, since these ratios can be chosen independently, the designer can choose either to use a thin and wide or a tall and a slender antenna to achieve the required resonance frequency and Q-factor for a given dielectric constant.

3.1.2 Resonance Modes

The EM fields inside a rectangular DRA mounted on a perfect electrically conducting (PEC) ground plane, as shown in Figure 3.1, are assumed to be equivalent to those of an isolated rectangular dielectric waveguide [1, 2] having similar dimensions of b, c, ε_r and a height of 2a. Here, the tangential components of the EM fields are assumed to be continuous across the two surfaces of the DRA that are perpendicular to the direction of propagation in the dielectric guide, whilst perfect magnetic walls are assumed along the other four surfaces that are parallel to the direction of propagation.   According to Okaya and Barash [3], the modes of an isolated dielectric waveguide can be divided into two families: Transverse Magnetic (TM) and Transverse Electric (TE). The TM modes are characterized by having a zero value for the radial component of the magnetic field (H_r=0), while the TE modes have a zero radial component of the electric field (E_r=0). However, for any DRA mounted on the ground plane, it is the TE modes

that are usually excited since the presence of lower-order TM modes cannot be confirmed experimentally [4], due to the lack of coupling between the inside and outside resonator fields . For such rectangular DRAs, TE^x, TE^y and TE^z modes are possible, in which the radiation would be similar to those of a short magnetic dipole located at the centre of the DRA and oriented along x, y and z directions, respectively. The resonance frequency of each of these modes depends on the DRA's dimensions and permittivity. The lowest order TE mode, i.e. TE mode with the lowest resonance frequency, corresponds to the direction in which the smallest dimension of the DRA is located. For example, if the DRA's dimensions are such that c > b > a, then the TE modes in terms of increasing resonance frequencies are $TE^z_{11\delta}$ < $TE^y_{1\delta1}$ < $TE^x_{\delta11}$, where the mode indices denote variation of EM fields along the x, y and z directions inside the resonator and the value of δ ranges between $0 \leq \delta \leq 1$, which approaches 1 for high values of dielectric permittivity [5].
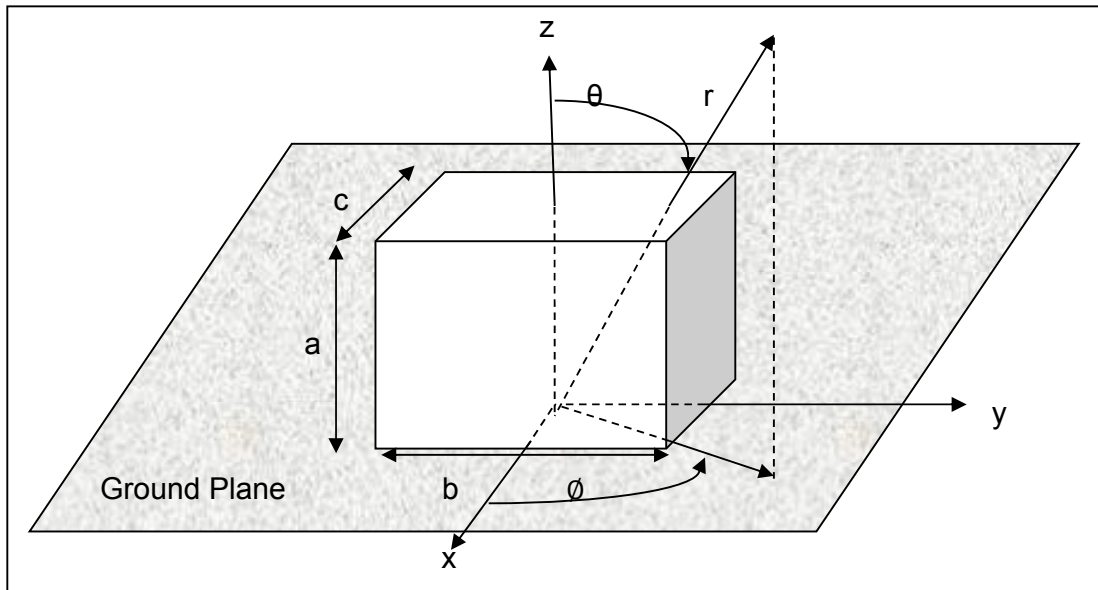
Figure 3.1: Geometry of a rectangular DRA mounted on ground plane

The resonance frequencies of the TE modes can be approximately predicted using the dielectric waveguide model (DWM) method [4]. Since the

analysis of all the modes is similar, it is adequate to describe the analysis of one of these modes only. For the TE$^z_{mn\delta}$ mode, where *m* and *n* are integers, the *z*-directed fields inside the resonator can be expressed in the following form [2]:

$$H_z = A\cos(k_x x)\cos(k_y y)\cos(k_z z)$$
(3-1)

$$E_z = 0$$
(3-2)

in which *A* is an arbitrary constant. k_x, k_y and k_z respectively denote the wavenumbers in the *x*, *y* and *z* directions inside the DRA. By enforcing the magnetic wall boundary condition $\vec{E} \bullet \vec{n} = 0$ at the surfaces of the resonator, the following equations are obtained for the wavenumbers

$$k_x = \frac{m\pi}{c}, \ k_y = \frac{n\pi}{b}$$
(3-3)

$$k_z \tan(k_z a) = \sqrt{(\varepsilon_r - 1)k_0^2 - k_z^2}$$

where k_0 represents the free-space wavenumber. Additionally, the wavenumbers must satisfy the following equation.

$$k_x^2 + k_y^2 + k_z^2 = \varepsilon_r k_0^2$$
(3-4)

in which k_0 corresponds to the resonance frequency, i.e.

$$k_0 = \frac{2\pi}{\lambda_0} = \frac{2\pi f_0}{c}$$
(3-5)

where λ_0 is the free-space wavelength, and *c* is the speed of light in vacuum. Substitution of equation (3-5) in equation (3-4) yields the resonance frequency as

$$f_0 = \frac{c}{2\pi\varepsilon_r}\sqrt{k_x^2 + k_y^2 + k_z^2}$$
(3-6)

3.1.3 Axial Ratio and Gain Measurements Procedures

The measurement of the antenna's far-field parameters such as axial ratio (AR) and gain is not as straightforward as measuring the S_{11} or far-field pattern. For the calculation of the AR, the following expression can be used [6]

$$AR = \frac{|E_R| + |E_L|}{|E_R| - |E_L|}$$ (3-7)

in which the right-hand CP electric field component, E_R, and the left-hand CP electric field component, E_L, can be derived using the following equations [7]

$$E_R = \frac{1}{\sqrt{2}}\left(E_\phi + jE_\theta\right)$$ (3-8)

$$E_L = \frac{1}{\sqrt{2}}\left(E_\phi - jE_\theta\right)$$ (3-9)

where E_ϕ represents the electric field component in the ϕ-direction and E_θ denotes the electric field component in the θ-direction. In order to determine E_ϕ and E_θ experimentally, the DRA has been placed in the receiving terminal inside an anechoic chamber as shown in Figure 3.2, where it can be observed that a standard horn has been used as a transmitting antenna. The component E_φ has been obtained by measuring the received signal at each elevation angle θ (θ = 1º, 2º, 3º ….360º) while the transmitting antenna has been fixed at azimuthal angle of ϕ = 0º. The same procedure has been repeated for the measurement of E_θ with the horn antenna rotated at ϕ= 90º.

The previous method of measuring AR is preferred compared to an alternative method presented in [8] that use multiple magnitude components of E_ϕ and E_θ without the need of measuring their phases. The magnitude of the electric field components are taken at four planes in the azimuthal direction (ϕ = 45º, 90º,

135º and 180º). This method has not been considered because it is more susceptible to experimental errors since the horn antenna need to be rotated twice as much as the previous method. Furthermore, the calculations of E_R and E_L components are not possible without the phase information.
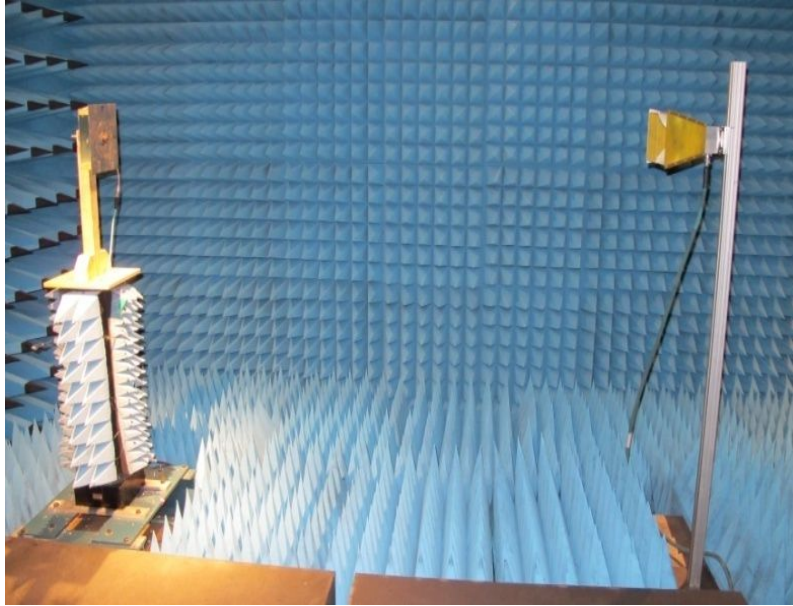
Figure 3.2: Measurement setup for the DRA's far-field parameters

For the gain measurements, a comparison method has been applied in which another horn antenna has been used at the receiving end. The gain of the rectangular DRA, G_{DRA} can be calculated from the known gain of the reference horn, G_{Horn} using the following expression [9],

$$G_{DRA \, in \, dB} = G_{Horn \, in \, dB} + 10 \log_{10}\left(\frac{P_{DRA}}{P_{Horn}}\right) - 20 \log_{10}\left(\frac{1 - |\Gamma_{DRA}|}{1 + |\Gamma_{Horn}|}\right) \tag{3-10}$$

where P and Γ represent the received power and reflection coefficient, respectively.

3.2   Circularly Polarized Rectangular DRA

It is well known that a spiral antenna can radiate CP waves if a travelling-wave current distribution is established along its length [10]. That is because this type of current distribution is capable of radiating two far-field components which are equal in amplitude and in phase quadrature that are needed to generate the circular polarization. In this research, a conformal square spiral strip has been employed to regular-shaped DRAs, producing wideband axial ratio.

3.2.1 Antenna Configuration

Figure 3.3 presents the geometry of a rectangular DRA that is excited using a spiral strip. The DRA has the dimensions of *a*, *b*, *c* and a dielectric constant of ε_r, whereas the feeding strips have the same width, *w,* and lengths of l_1, l_2, l_3, l_4 and l_5. The feed point is located at a distance of *d* from the nearest side wall.
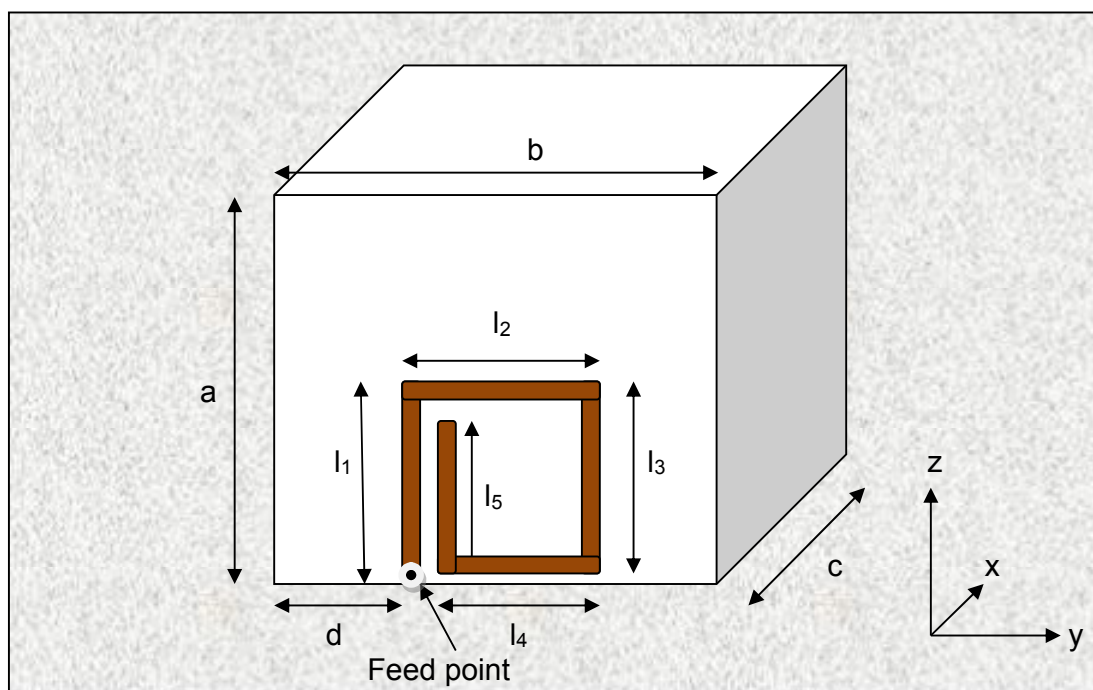
Figure 3.3: A rectangular DRA excited by a square spiral metal strips

The configuration has been simulated using the MoM in conjunction with the combined RWG and SWG basis functions described in Chapter 2. Meshing has been achieved using the Cimne-GiD [11] commercial software, where the rectangular dielectric has been meshed to 2546 tetrahedrons and the metallic strips to 86 triangular patches, giving a total of 5530 unknowns. Image theory has been applied in order to take into account the effects of the PEC ground plane. The memory size requirement for the solution of EM modeling has been reduced with the application of image theory, as the need to physically model the ground plane has been eliminated. The source feed has been simulated using a delta-gap voltage generator model. The computation time is approximately 55 seconds per frequency point, which is significantly faster than the simulation time of 1200 seconds using CST Microwave studio for the same antenna configuration.

An iterative design procedure has been followed to determine the optimum dimensions of the feeding metallic strips that are needed to establish a travelling-wave current distribution along the spiral-shaped monopole as well as exciting a DRA mode within the same frequency range. The existence of this travelling-wave current on the DRA surface generates a circularly polarized wave with two orthogonal field components that have the same amplitudes and a phase difference of 90° which can be attributed to the fact that the spiral antenna and its image have currents of equal magnitude but of opposite phase [10]. Since the travelling-wave current distribution changes slowly with frequency, a wider CP bandwidth is expected.

The DRA parameters are similar to those used in [12], that is, a = 26.1 mm, b = 25.4 mm, c = 14.3 mm and ε_r = 9.3. The results of the design procedure are summarized in Table 3.1, which shows several selected dimensions of l_1, l_2, l_3, l_4

and l_5 that are capable of generating circular polarization in conjunction with sufficient impedance matching bandwidth. The formula used to calculate the percentage of overlapping AR and S11 bandwidth is given by

$$\text{Overlapping Bandwidth}\,(\%) = \frac{\text{AR bandwidth with sufficient S11 bandwidth}}{\text{AR bandwidth}} \times 100 \quad (3\text{-}11)$$

As can be seen from the table, the achieved AR bandwidth is rather sensitive to the strips lengths, as changing the latter may generate a standing wave current distribution, which deteriorates the circular polarization.

L_1 (mm)	L_2 (mm)	L_3 (mm)	L_4 (mm)	L_5 (mm)	3db AR Bandwidth (%)	10dB S11 Bandwidth (%)	Overlapping AR & S11 Bandwidth (%)
8.25	10	6	8	6	3.24	9.43	100
		7	8	6	2.65	9.18	100
	12	6	10	4	3.23	8.92	100
				5	3.64	7.65	100
				6	4.87	7.40	100
		7	10	4	3.17	7.14	93.1
				5	4.08	8.67	76.2
				6	6.07	8.42	66.2
		8	10	4	2.64	8.16	90.5
				5	3.28	5.63	86.3
				6	4.25	5.38	100
10.25	**10**	8	8	6	1.17	6.89	100
				7	2.32	6.63	100
				8	4.59	6.38	100
		9	8	8	4.43	6.13	100
		10	**8**	**8**	**6.60**	**8.50**	**100**
	12	10	10	7	2.07	4.90	48.3
12.25	8	10	6	10	3.15	4.42	77.5
		11	6	9	1.71	4.20	100
				10	4.08	3.97	43.4
		12	6	9	3.15	3.75	100
				10	3.10	3.54	100
	10	12	8	9	2.30	3.34	100
				10	7.47	7.91	60.3
	12	11	10	9	1.05	4.66	100

Table 3.1: AR and S_{11} bandwidths for different spiral dimensions

3.2.2 Results and Discussions

A rectangular DRA prototype has been built using Alumina (Al_2O_3) ceramic material, which has a relative permittivity of ε_r = 9.3. The square spiral has been constructed using five individually cut strips of an adhesive-backed copper tape that can be stuck easily on the surface of the DRA. The strips have been electrically connected to each other using a conductive silver paint. The dimensions of the strips have been optimized based on the aforementioned iterative design procedure. With reference to Table 3.1, the optimized lengths of the individual strips are found to be l_1 = 10.25 mm, l_2 = 10 mm, l_3 = 10 mm, l_4 = 8 mm and l_5 = 8 mm. The DRA has been mounted on a square aluminum ground plane with a side length of 400 mm. An HP8720D vector network analyzer has been used in the measurements. Feeding has been implemented by soldering the one end of the spiral strip to an SMA connector that is connected to the network analyzer using a 50 Ω coaxial cable. It should be noted that the feed point is located at a distance of d=7.7 mm from the DRA edge as illustrated in Figure 3.2. Any possible air gaps between the DRA and the ground plane have been eliminated by employing a procedure described in [13], in which the DRA has been attached to a double sided adhesive conducting tape that is placed above the ground-plane. The existence of such air gaps causes measurements errors, since the air gaps (ε_r = 1) reduces the ε_r for the whole antenna structure, which subsequently increases the resonance frequency and bandwidth of the resonance.

A travelling-wave current distribution has been attained along the spiral metal strip at the frequency band of operation as illustrated in Figure 3.4. The current distribution consists of outbound and reflected travelling waves along the spiral arm, decaying as they radiate. Close to the feed point, the wave outbound

from the feed has not yet decayed much, while that reflected from the end of the arm has decayed twice, radiating significantly in both directions, thus causing least interference. Therefore, the net result is close to a decaying travelling wave, as can be observed in the relatively linear phase progression and smoother amplitude decay. It is the predominant travelling wave close to the feed that is responsible for the good axial ratio [11].
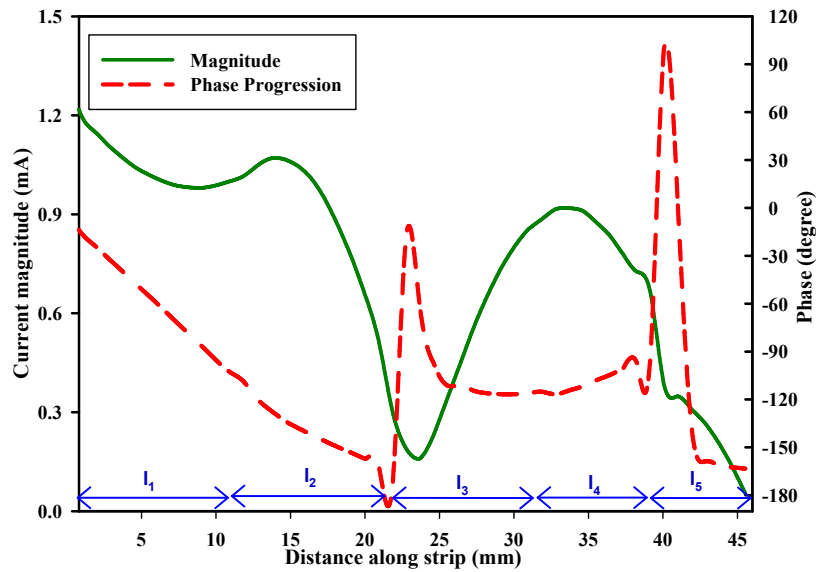
Figure 3.4: Current distribution along the spiral strip at 4.1 GHz

The spiral strip has a perimeter of 1.39*λg*, where *λg* is the guided wavelengths at 4.1 GHz that has been calculated as [14],

$$\lambda_g = \frac{\lambda_0}{\sqrt{(\varepsilon_r + 1)/2}} \tag{3-12}$$

It should be noted that this spiral perimeter is comparable to that of 1.25*λg* obtained for a CP spiral antenna design reported in [15]. This circumference supports the first-mode of radiation, for which the conditions are ideal for CP wave radiation. It has been noted in [16] that currents existing beyond the one-

wavelength circumference continue experiencing change of phase as they progress outward. For a large spiral structure, these currents will be out-of-phase at the second-wavelength circumference and in-phase at the radius where the circumference is three wavelengths. No radiation occurs from the two-wavelength circumference because the currents on adjacent spiral arms are anti-phase in contrast to strong radiation from the three-wavelength circumference.

The computed and the measured return losses are shown in Figure 3.5, where it can be noticed that there is a good agreement between simulation and measurements. From these results, it can be seen that an $|S_{11}| \leq -10\,\text{dB}$, that is, a voltage standing wave ratio (VSWR) of ≤ 2, has been achieved over a bandwidth of 8.5 % in both cases. The minimum S_{11} has been measured at 4.10 GHz compared to 4.14 GHz in the computations, which constitute a marginal difference of 0.97 % between the two sets of results.
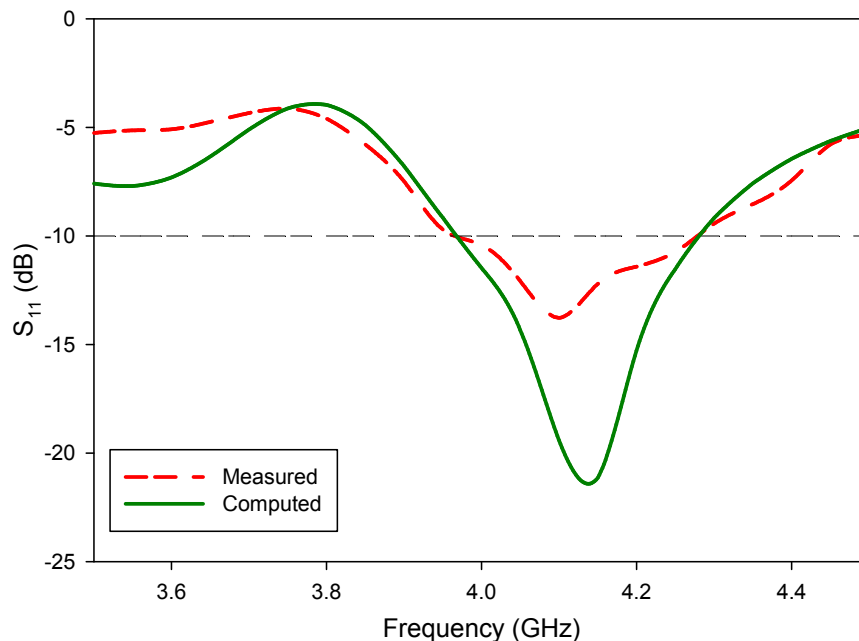
Figure 3.5: Return losses of a rectangular DRA fed by square spiral strip.

Apart from the computed and measured results, the resonance frequency has also been studied using DWM model as described in section 3.1.2. Using this simple and approximate technique, the resonance frequency has been predicted as 3.82 GHz for the $TE^{y}_{1\delta1}$ mode in which the DRA has been excited. The electric field distribution across an isolated rectangular DRA with similar dimensions of *b*, *c*, ε_r and height of 2*a,* due to the ground plane removal, operating in this mode is presented in Figure 3.6 (a). As can be seen from Figure 3.6 (b), the DRA has a strong magnetic field near the ground plane along both side walls parallel to the y-axis; hence it can be excited by the spiral strips that have a maximum current magnitude at the feed point close to the ground plane.
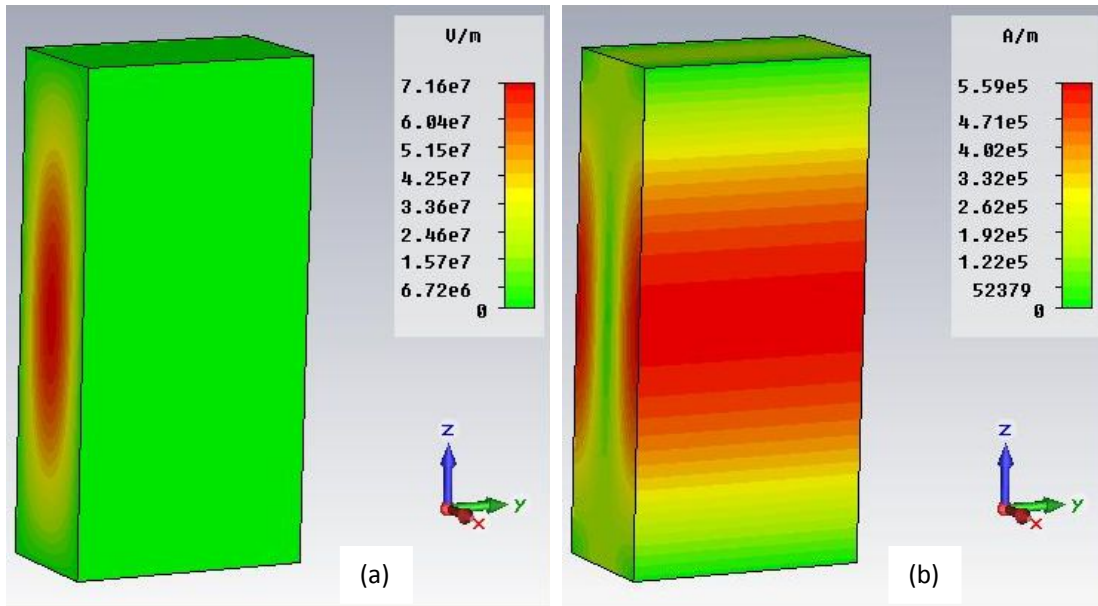
Figure 3.6: Fields distribution for TE^{y}_{111} mode; (a) E-field and (b) H-field

By applying equation (3-7), the AR of the rectangular DRA has been computed and measured at the bore-sight direction, *θ*=0. The variation of AR as a function of frequency is shown in Figure 3.7, where it can be seen that the minimum computed value is 1.23 dB at 4.1 GHz, which is close to the

corresponding measured value of 1.39 dB at the same frequency. From these results it can be observed that the theoretical 3 dB AR bandwidth extends from 4.01-4.27 GHz compared to 4.00-4.28 GHz in the measurements. These figures show that a circular polarization has been achieved over bandwidths of 6.60 % and 7.07 % in the analysis and the measurements, respectively. These are significantly higher than the typical bandwidths of less than 3% for singly-fed rectangular DRAs as described in section 1.3.2.2. Employing a finite ground plane and experimental tolerances have produced a slight discrepancy between the predicted and the measured bandwidths. Furthermore, with reference to Figure 3.8 which illustrates the region of overlapping AR and S11 bandwidths for the rectangular DRA design, it can be observed that a sufficient impedance matching bandwidth has been obtained throughout the achieved circular polarization bandwidth.
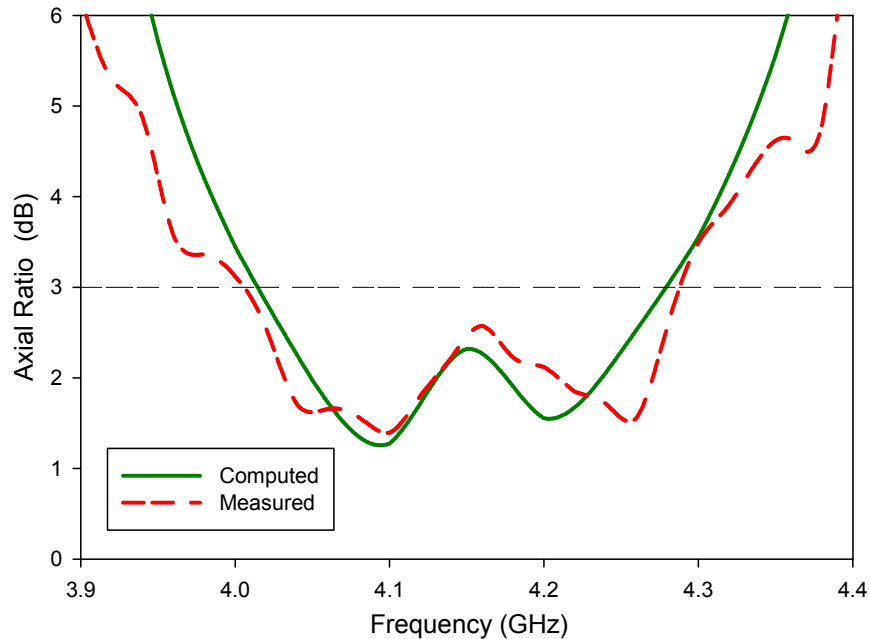
Figure 3.7: Axial ratio of a rectangular DRA fed by square spiral strip
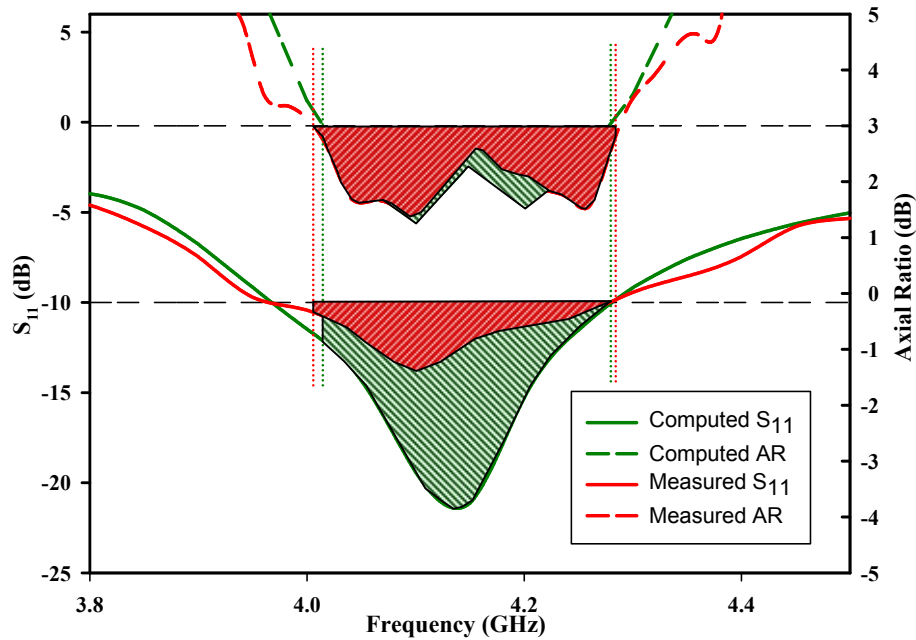
Figure 3.8: Region of overlapping bandwidths for S_{11} and AR

Additionally, the theoretical and experimental variations of the axial ratio, as functions of the elevation angle, are illustrated in Figures 3.9 and 3.10, where it is evident that the DRA produces a CP radiation over beam-width of $25°$ in both $\phi = 0°$ and $\phi = 90°$ principle planes, respectively, at the minimum AR frequency of 4.1 GHz. These relatively narrow beam-widths can be attributed to the fact that the main beam throughout the circular polarization bandwidth is slightly shifted to ~$10°$ from the bore-sight direction due to the position of the feed point.
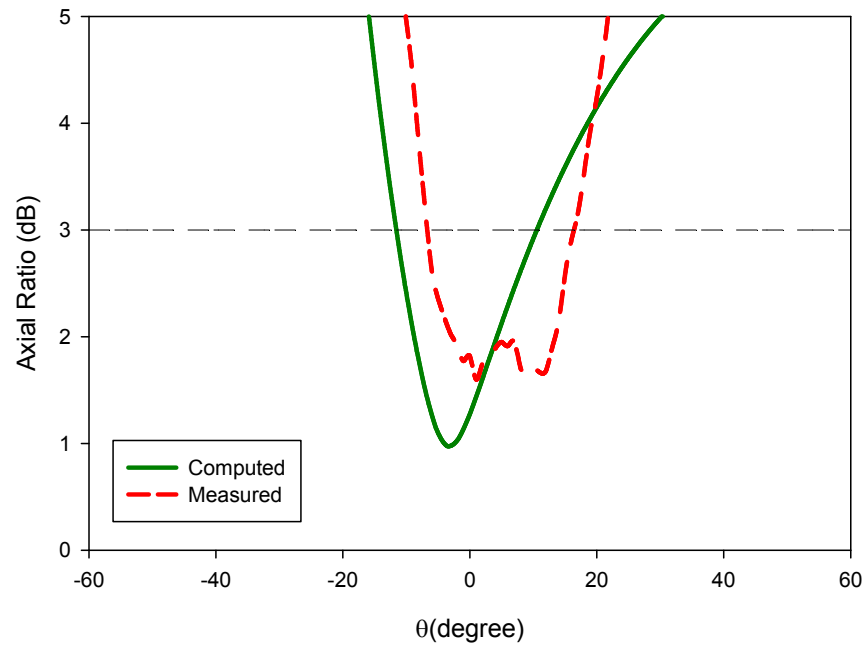
Figure 3.9: Axial ratio beam-width of the rectangular DRA at $\phi = 0°$
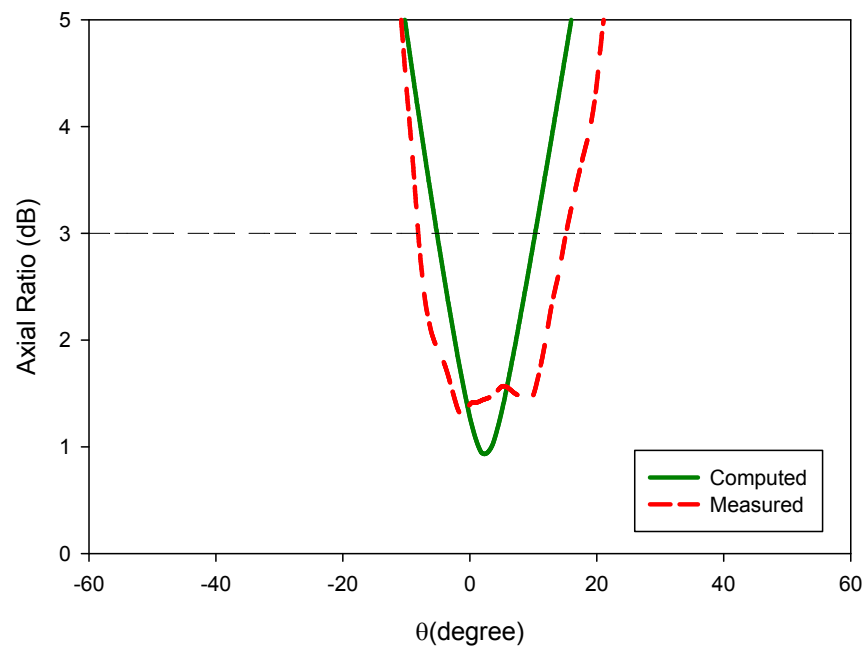
Figure 3.10: Axial ratio beam-width of the rectangular DRA at $\phi = 90°$

A comparison between the calculated and the measured radiation patterns is shown in Figure 3.11 with reasonable agreement and stability across the circular polarization bandwidth. It is evident from these results that this is a right-hand CP DRA, and the right-hand, RHCP, field component is stronger than the left-hand counterpart, LHCP, by more than 20 dB in the bore-sight direction at 4.1 GHz. Furthermore, a left-hand CP DRA can be attained by changing the square spiral arm winding from a clockwise to a counter-clockwise direction.
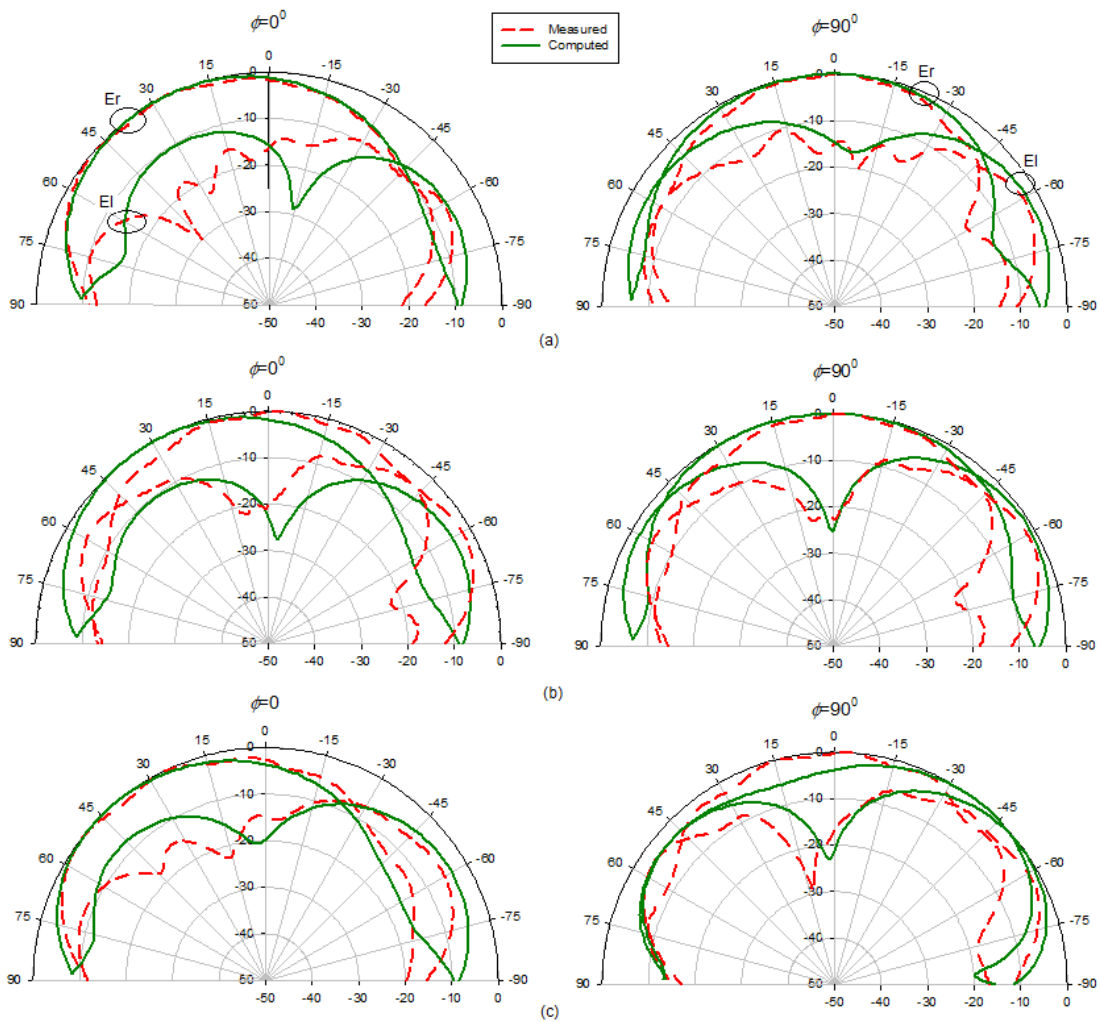
Figure 3.11: Radiation pattern of the rectangular DRA at

(a) 4.01, (b) 4.10, and (c) 4.27 GHz

With the aid of equation (3-10), the antenna bore-sight gain has been measured and the results are illustrated in Figure 3.12, where it can be observed that a satisfactory gain of 2.9 dBi has been achieved at the optimum AR frequency of 4.1 GHz. However, the gain decreases rapidly to approximately 0 dBi at the upper end of the CP bandwidth, which is due to the shift in the main beam at that frequency.
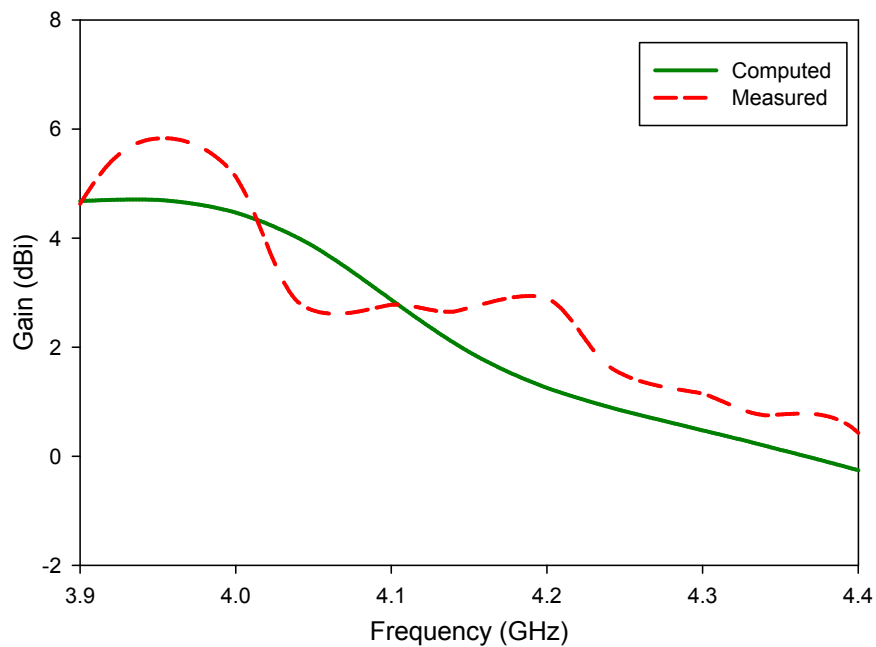
Figure 3.12: Gain of a rectangular DRA fed by square spiral strip

3.3   Frequency Tuning of the Circularly Polarized Rectangular DRA

3.3.1 Antenna's Configuration

The possibility of achieving a wideband CP radiation at a different resonance mode is investigated next, where the spiral position has been shifted from the centre of the DRA surface as illustrated in Figure 3.13. This is important as it demonstrates the possibility of tuning the operation frequency if needed. The DRA parameters are similar to those used in section 3.2, except the distance d, which has been changed to 15.4mm. This distance has been chosen so as to excite the TE^x_{111} mode that has a strong magnetic field at that position as shown in Figure 3.14 (b), which maps the magnetic field distribution across an isolated rectangular DRA with similar dimensions of b, c, ε_r and height of $2a$ due to the ground plane removal.
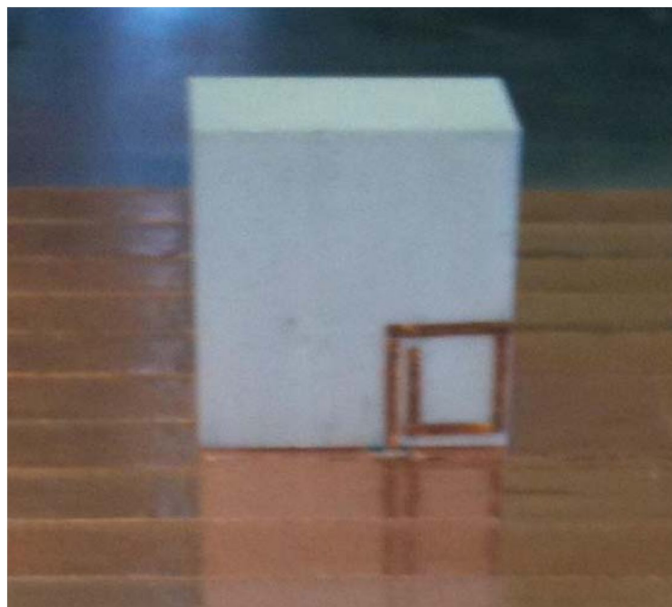
Figure 3.13: Rectangular DRA excited by a shifted square spiral strip metal
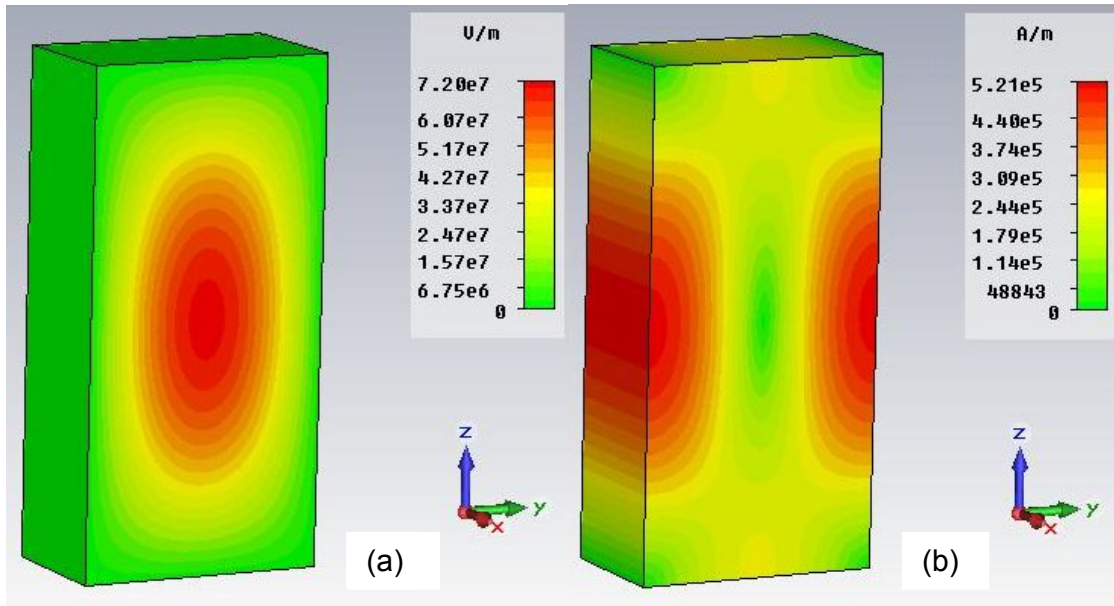
Figure 3.14: Fields distribution for TE^x_{111} mode; (a) E-field and (b) H-field

3.3.2 Results and Discussions

The current distribution along the spiral arm is illustrated in Figure 3.15, where, again, a travelling-wave current distribution has been attained, which is needed to produce the CP wave. The spiral strip has a perimeter of $1.07\lambda g$ at 3.1 GHz, which is ideal for CP radiation. Good agreement has been obtained between the computed and measured return losses as illustrated in Figure 3.16, where it can be seen that an $S_{11} \leq$ -10 dB has been achieved over a bandwidth of 33% and 30% in computations and measurements, respectively. The S_{11} bandwidth is much wider than those achieved previously due to the merging of the two minimum S11 points caused by the excitation of $TE^x_{\delta 11}$ and $TE^y_{\delta 11}$ modes. It should be noted that the possibility of exciting the $TE^y_{\delta 11}$ mode using the new position of feed point is still high, since the magnetic field inside the DRA operating in this mode is very strong along the side wall parallel to the y-axis and around the ground plane as can be seen in Figure 3.6 (b). The first minimum S_{11} point has

been measured at 2.95 GHz compared to a computed value of 2.93 GHz, that is, a marginal difference of 1% has been achieved between the two sets of results. Furthermore, the resonant frequency has also been calculated using the DWM approximation technique as 2.83 GHz for the $TE^x_{\delta 11}$ in which the DRA is excited.
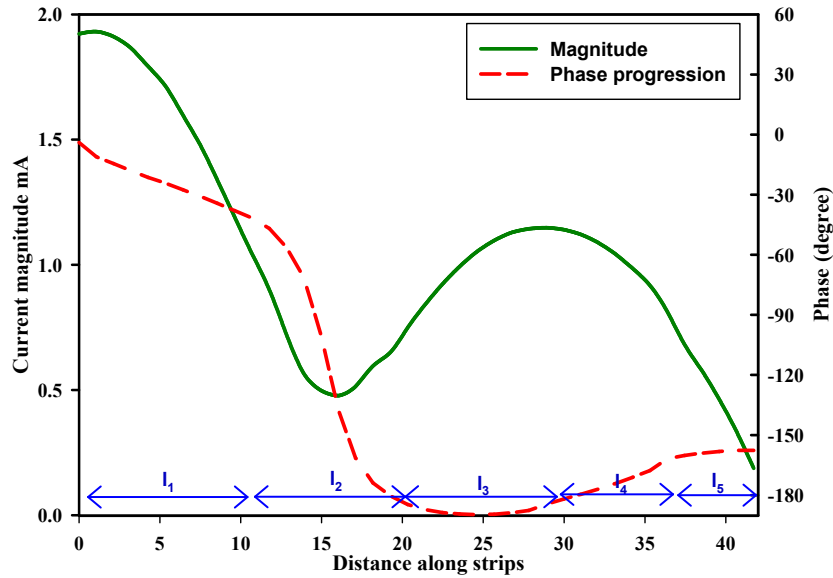
Figure 3.15: Current distribution along the shifted spiral at 3.10 GHz
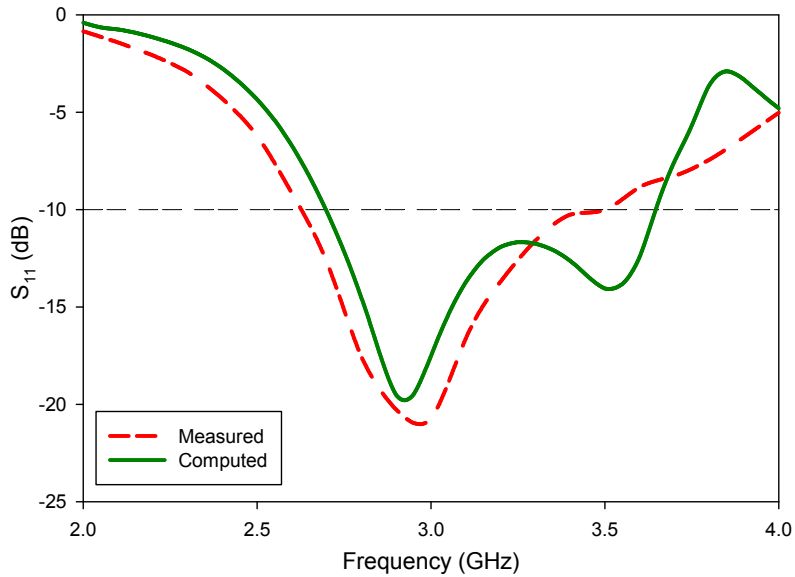
Figure 3.16: Return losses of the rectangular DRA fed by a shifted spiral.

The axial ratio has been computed and measured at the bore-sight direction as shown in Figure 3.17, where it can be seen that a minimum value of 1.5 dB has been attained at 3.10 GHz in both simulations and measurements. From these results it can be observed that the achieved 3 dB AR bandwidths are 6.4% and 6.7% in the analysis and measurements, respectively. This is similar to the achieved bandwidth for a DRA supporting the TE^y_{111} mode at 4.10 GHz as described in section 3.2. These results confirm the robustness of the presented feed mechanism as the CP operating frequency and the resonance mode have been varied easily by shifting the spiral from the centre of the DRA surface. The slight discrepancy between the predicted and measured results can be attributed to experimental tolerance and the finite ground plane used. Additionally, the circular polarization bandwidth has been achieved in conjunction with sufficient impedance matching bandwidth as illustrated in Figure 3.18.
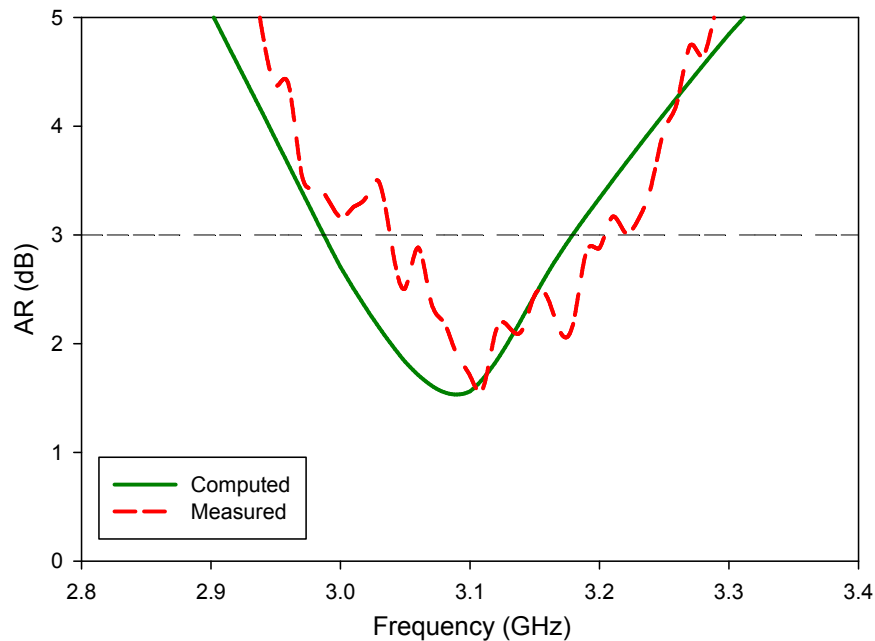
Figure 3.17: Axial ratio of the rectangular DRA fed by a shifted spiral.
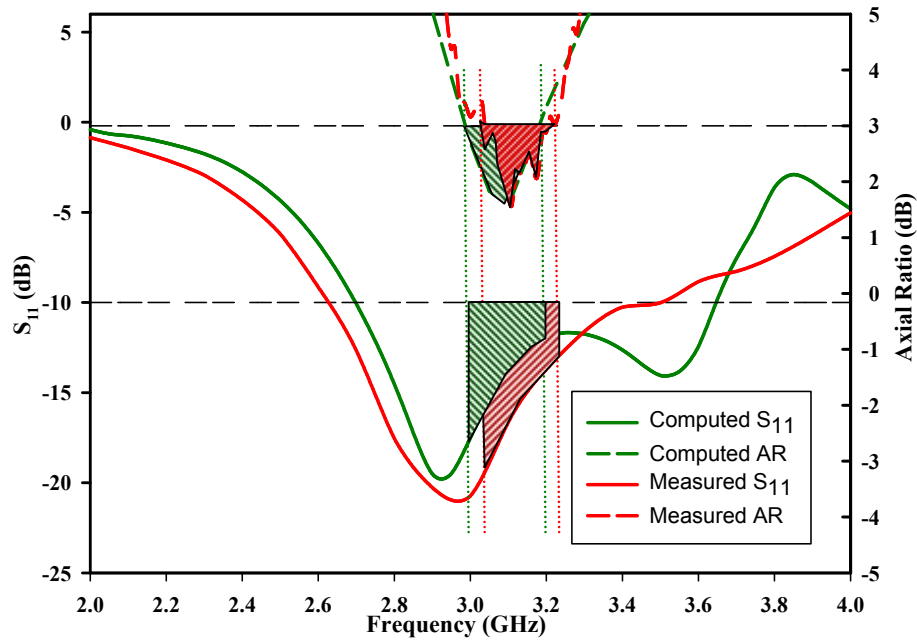
Figure 3.18: Region of overlapping bandwidths for S_{11} and AR

The variation of the axial ratio with the elevation angle is demonstrated in Figures 3.19 and 3.20, where it can be seen that the DRA offers circular polarization over useful computed beam-widths of $93°$ and $72°$ in the $\phi = 0°$ and $\phi = 90°$ planes, respectively. These beam-widths are significantly wider than those achieved in the previous design because the main beam position is at the bore-sight direction.
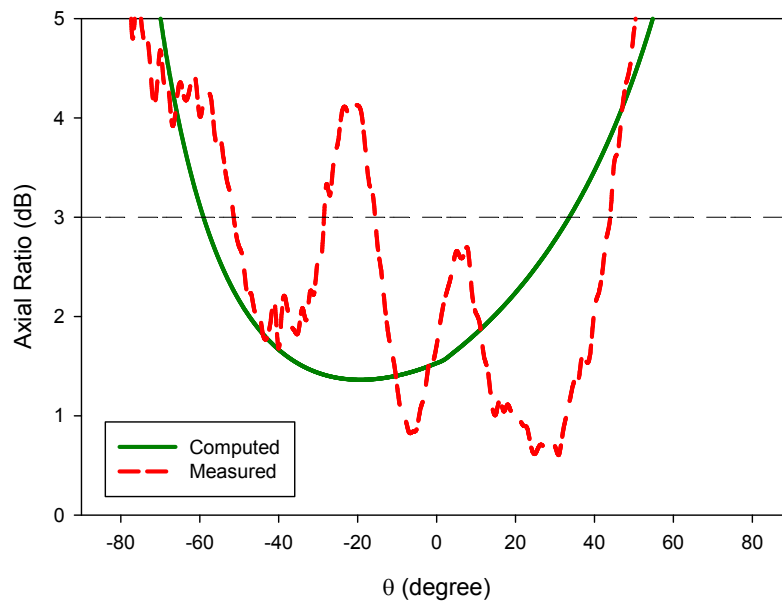
Figure 3.19: Axial ratio beam-width of the rectangular DRA at $\phi = 0^\circ$
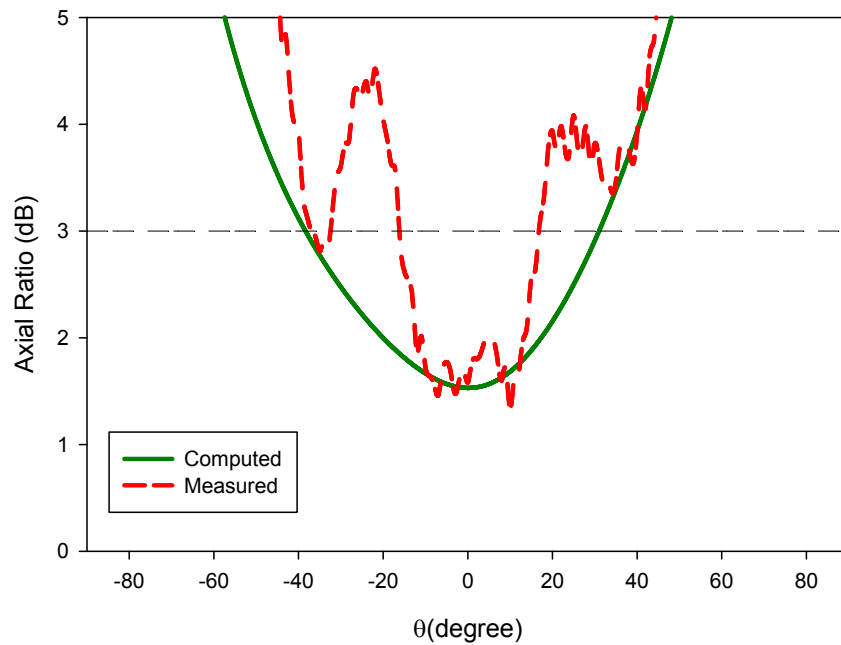
Figure 3.20: Axial ratio beam-width of the rectangular DRA at $\phi = 90^\circ$

A comparison between the calculated and measured radiation patterns is shown in Figure 3.21 with reasonable agreement. It is evident from Figure 3.21 (b) that this is a right-hand CP DRA, in which the RHCP field is stronger than the LHCP field by more than 20 dB in the bore-sight direction at 3.10 GHz. Again, as in the case with the previous design, a left-hand CP DRA can be attained by changing the square spiral arm winding from clockwise to counter clockwise direction.
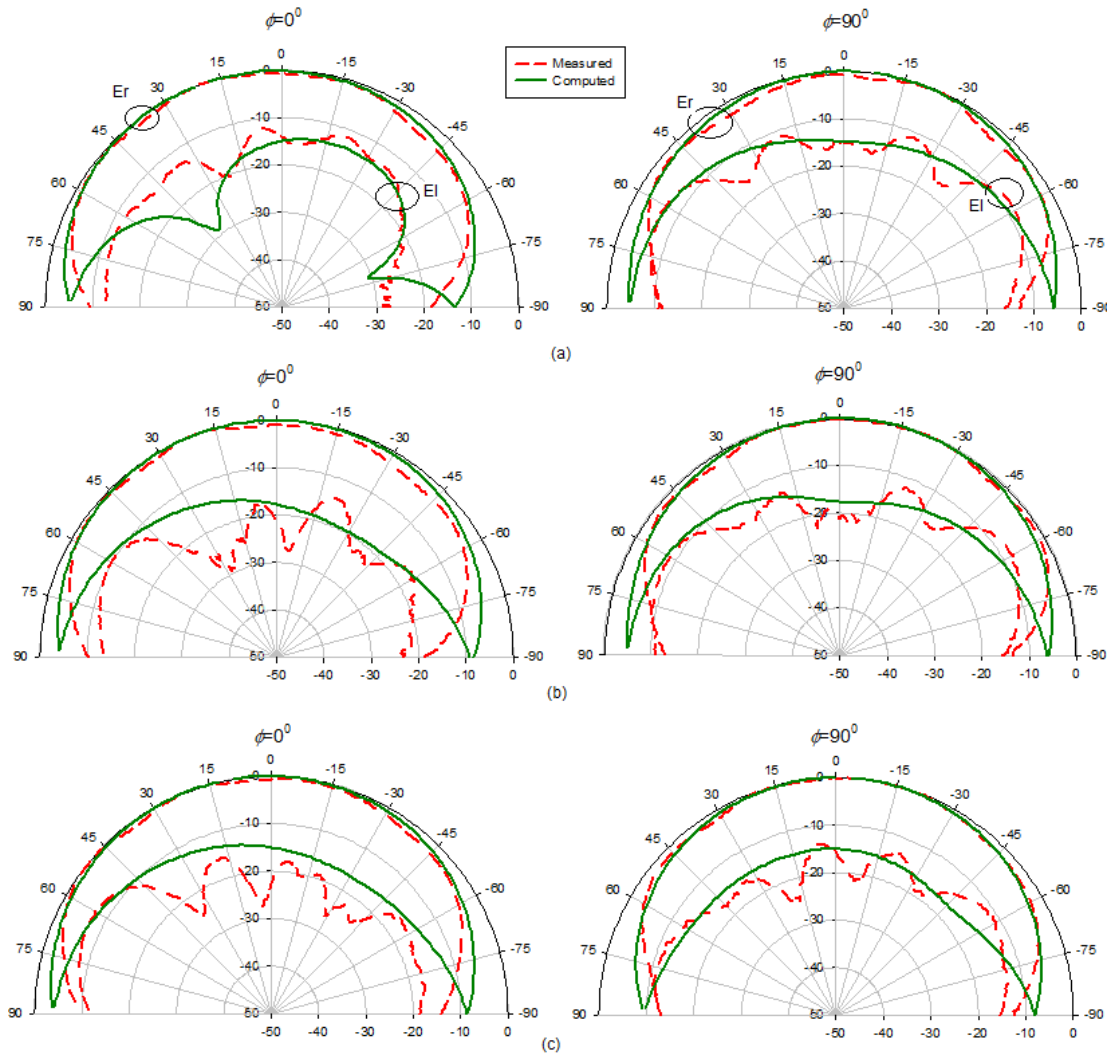
Figure 3.21: Radiation pattern of the rectangular DRA at

(a) starting, (b) minimum, and (c) ending of AR frequencies

Finally, the antenna gain of the rectangular DRA, with the shifted spiral feed, has been measured at bore-sight. The results are illustrated in Figure 3.22, where it can be seen that the antenna offers a good gain of approximately 5dBi across the whole frequency range of the achieved circular polarization. The achieved gain is stronger than those achieved by previous DRA configuration because the main beam is located near to $\theta=0^0$ throughout the achieved CP frequency band.
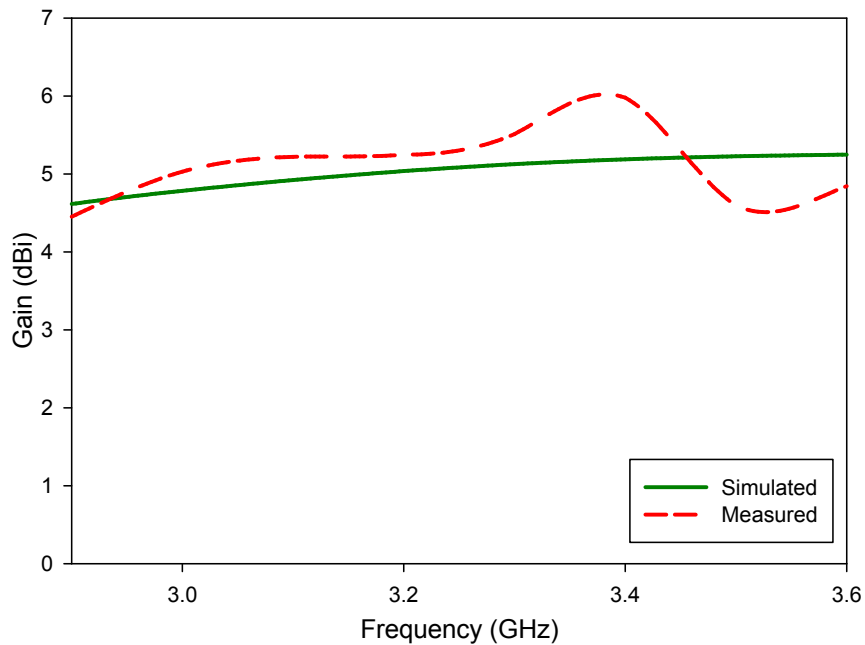
Figure 3.22: Antenna gain of a rectangular DRA fed by a shifted spiral.

3.4   Conclusions

A wideband CP rectangular DRA has been designed using a square spiral strip for excitation. The antenna provides a 3 dB AR bandwidth of approximately 7%, which is considerably greater than what has been reported in earlier studies for a

singly-fed CP DRA. This has been achieved in conjunction with a sufficient impedance-matching bandwidth across the same frequency range. The frequency tuning of the wide band circularly polarized DRA antenna has been demonstrated, where shifting the spiral position from the centre to the right of the DRA surface has shifted the operating frequency from 4.10 GHz to 3.10 GHz. This corresponds to a change in the supported modes from TE^{y}_{111} to TE^{x}_{111}. In both modes a wide CP bandwidth has been achieved. Furthermore, the spiral feed can be constructed using adhesive conducting strips. A good agreement has been obtained between experimental and theoretical results.

References

[1] J.C. Sethares and J. Naumann, "Design of Microwave Dielectric Resonators," *IEEE Trans. On Microwave Theory and Technique,* vol.14, no.1, pp.2-7, Jan 1966

[2] R.K. Mongia and O. Bhartia, "Dielectric Resonator Antennas – A Review and General Design Relations for Resonant Frequency and Bandwidth," *International Journal of Microwave Milimeter-Wave Computer-Aided Engineering.*, vol.4, no.3, pp.230-247, 1994

[3] A.K. Okaya and L.F. Barash, "The Dielectric Microwave Resonator," *IEEE Proc. IRE*, vol.50, pp.2081-2092, Oct 1962

[4] R.K. Mongia, "Theoretical and Experimental Investigations on Rectangular Dielectric Resonators," *IEEE Proc.H*, vol.139, pp.98-104, Feb 1992

[5] A. Petosa, "*Dielectric Resonator Antenna Handbook*," Chapter 1, pp.18, Artech House, 2007

[6] C.A. Balanis, "Modern Antenna Handbook," 3rd ed., Chapter 6, pp.276, Wiley & Sons Inc., 2008

[7] B.Y. Toh, "Understanding and Measuring Circular Polarization", *IEEE Trans. Antennas Propagat.,* vol. 46, No. 3, pp. 313-318, Aug 2003.

[8] W.L.Stutzman, *Polarization in electromagnetics systems*. Boston: Artech House, Inc., 1993.

[9] S. Gregson, J. McCormick and C. Parini, "Principles of planar near-field antenna measurements." pp. 182-183, MPG Books Ltd, 2007

[10] H. Nakano, K. Nogami, S. Arai, H. Mimak, and J. Yamauchi, "A spiral antenna backed by a conducting plane reflector", *IEEE Trans. Antennas Propag.*, vol. 34, pp. 791-796, June 1986.

[11] International Center for Numerical Methods in Engineering, "GiD – The Personal Pre and Post Processor. Internet: http://www.gidhome.com/home, [Feb 13 2012]

[12] B. Li, and K.W. Leung, "Strip-fed rectangular dielectric resonator antenna with/without a parasitic patch", *IEEE Trans. Antennas Propag.,* vol. 53, pp. 2200-2207, July 2005.

[13] K.W. Leung, "Conformal strip excitation of dielectric resonator antenna", *IEEE Trans. Antennas Propagat.,* vol. 48, pp. 961-967, Jul. 2000.

[14] C. A. Balanis, "*Antenna Theory Analysis and Design*", New York, Wiley 1995.

[15] H. Nakano, M. Ikeda, K. Hitosugi and J. Yamauchi, "A Spiral Antenna Sandwiched by Dielectric Layers", *IEEE Trans. Antennas Propag.,* vol. 52, no. 6, pp.1417-1423, June 2004.

[16] J. A. Kaiser, "The Archimedean two-wire spiral antenna", *IEEE Trans. Antennas Propag.,* vol. AP-8, pp. 312-323, May 1960.

CHAPTER 4

A WIDEBAND CIRCULARLY

POLARIZED CYLINDRICAL DRA

4.1   Introduction

Out of the three regular geometries used throughout this project, cylindrical DRA offers the second greatest design flexibility. Additionally, the fabrication of a cylindrical structure is simpler than that of a hemispherical DRA. In this chapter, the versatility of the excitation method introduced previously is assessed by employing the spiral feed to a cylindrical DRA to generate a wide circular polarization bandwidth. Furthermore, a multilayer DRA configuration is proposed for further enhancement of the CP bandwidth. The cylindrical shape offers one degree of freedom, where both the resonance frequency and the radiation Q-factor are exclusively dependent on the radius to height aspect ratio, i.e. $(\frac{a}{h})$.

Therefore, for a given dielectric constant, a wide and thin DRA can be made to resonate at the same frequency as a tall and slender DRA. As a result, antenna designers have the choice of using different antenna profiles to achieve the desired resonance frequency.

4.1.1 Resonance Modes
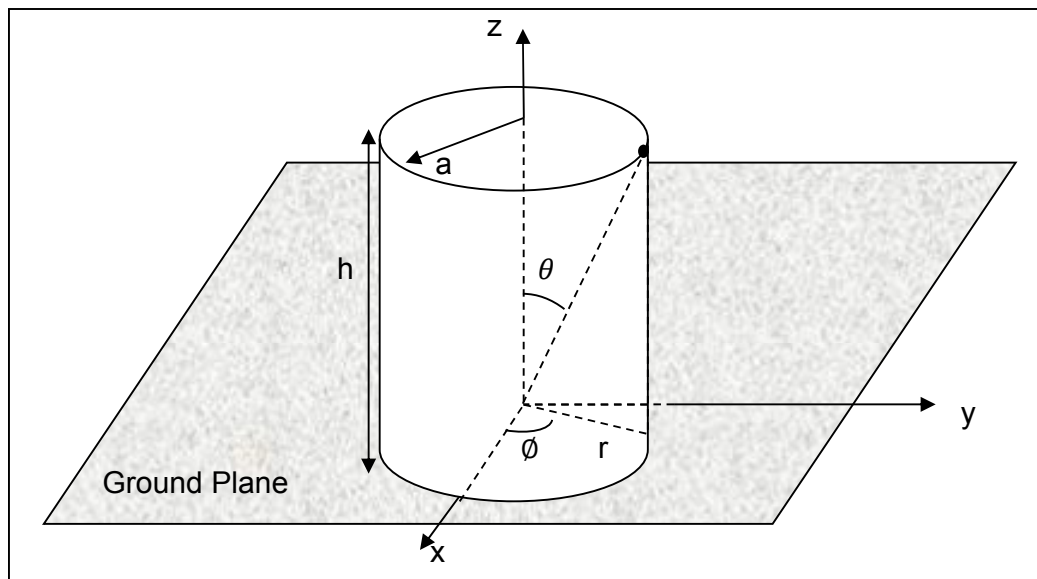
Figure 4.1: Geometry of a cylindrical DRA mounted on ground plane

Figure 4.1 illustrates a cylindrical DRA that is mounted on a PEC ground plane. The EM fields inside this antenna can be assumed to be equivalent to those of an isolated cylindrical dielectric waveguide [1] having the same parameters of a, ε_r and a height of $2h$. As in the rectangular DRA model, the H_z component is assumed to be zero at all surfaces parallel to the z-axis, i.e. a perfect magnetic walls condition, whilst the tangential EM fields are continuous across surfaces perpendicular to the z-axis. These EM fields are assumed to decay exponentially outside the DRA from their values at the boundary to zero at an infinite distance away from the DRA [2].

According to Kobayashi [3], the modes of an isolated cylindrical dielectric waveguide can be categorized into three distinct types: TM, TE, and hybrid modes. The fields of TM and TE modes are axially symmetric and the fields of the hybrid modes are azimuthally dependent. The hybrid modes can be further categorized into EH and HE types [4], depending on the relative strength between the electric (E) and magnetic (H) field components. In the case of EH modes, the H_z component is significantly stronger than the E_z component. Hence, from the knowledge of the H_z component only, other field components can be obtained. The reverse is true for the HE modes.

The modes in each category are classified as $TM_{0mp+\delta}$, $TE_{0mp+\delta}$, $EH_{nmp+\delta}$ and $HE_{nmp+\delta}$. The mode subscripts denote the order of variations of fields in azimuthal ($\emptyset$), radial (r) and axial (z) directions, respectively. The first index (n = 0, 1, 2…) indicates the variation of fields in the azimuth direction, while the second index (m = 1, 2...) denotes the radial variation of field. Similarly, the index p+δ (p=0, 1, 2…) indicates the variation of field in axial direction, where the value of δ ranges between $0 \leq \delta \leq 1$ depending on the DRA's permittivity. It should be noted that the most commonly used modes are $TM_{01\delta}$, $TE_{01\delta}$ and $HE_{11\delta}$ [5]. The far-field radiation of $TM_{01\delta}$ mode is similar to that of a small vertical electric monopole, while the $TE_{01\delta}$ mode radiates like a small vertical magnetic monopole. Additionally, the far-field radiation of $HE_{11\delta}$ mode is similar to those radiated from a small horizontal magnetic monopole.

The resonance frequencies of these commonly used modes can be approximately predicted using equations that are based on extensive numerical calculations and curve fittings [1]. Results obtained from these equations typically lie within 10% of those calculated rigorously using numerical methods. For given

values of $\dfrac{a}{h}$ and ε_r, the parameter of interest is the normalized wavenumber, k_0a.

When ε_r is very high ($\varepsilon_r \geq 100$), the normalized wavenumber is solely dependent

on ε_r [6], i.e.

$$k_0a \propto \frac{1}{\sqrt{\varepsilon_r}} \qquad (4\text{-}1)$$

However, when $\varepsilon_r \leq 100$, the following equation can be used as a good

approximation

$$k_0a \propto \frac{1}{\sqrt{\varepsilon_r + X}} \qquad (4\text{-}2)$$

where the value of X (X=1, 2…) is obtained empirically by comparing the results

from numerical methods available in literature. For a DRA with a lower value of ε_r,

the value of X for the TM$_{01\delta}$ mode was found to be equal to 2 after comparison

with the results from numerical method available in [7] that led to the following

expression

$$k_0a = \frac{2\pi f_0 a}{c} = \frac{\sqrt{3.83^2 + \left(\dfrac{\pi a}{2h}\right)^2}}{\sqrt{\varepsilon_r + 2}} \qquad (4\text{-}3)$$

which is valid when the aspect ratio is in the range of $0.33 \leq \dfrac{a}{h} \leq 5$

For the $TE_{01\delta}$, the resonant frequency can be calculated using the equation proposed by DeSmedt [8], which is valid for any value of ε_r and an aspect ratio in the range of $0.33 \le \dfrac{a}{h} \le 5$

$$k_0 a = \frac{2.327}{\sqrt{\varepsilon_r + 1}}\left[1.0 + 0.2123\left(\frac{a}{h}\right) - 0.00898\left(\frac{a}{h}\right)^2\right]$$ (4-4)

Finally, the expression for the normalized wave number for the $HE_{11\delta}$ mode is given by

$$k_0 a = \frac{6.324}{\sqrt{\varepsilon_r + 2}}\left[0.27 + 0.36\left(\frac{a}{2h}\right) - 0.02\left(\frac{a}{2h}\right)^2\right]$$ (4-5)

which can be used for any value of ε_r and an aspect ratio in the range of

$0.4 \le \dfrac{a}{h} \le 6$

4.2   Circularly Polarized Cylindrical DRA

4.2.1 Antenna Configuration

A cylindrical DRA that is excited using a conformal square spiral metal strip is illustrated in Figure 4.2. The DRA has a radius of *a*, a height of *h* and a dielectric constant of ε_r, whereas the feeding strips have lengths of l_1, l_2, l_3, l_4 and l_5 as well as a width of *w = 1 mm*. In order to assess the performance of the cylindrical DRA, the dimensions have been chosen to be as the same as those reported in [9]. Therefore, the relative permittivity, radius, and height have been chosen as 9.2, 7.01 mm, and 10.54 mm, respectively.
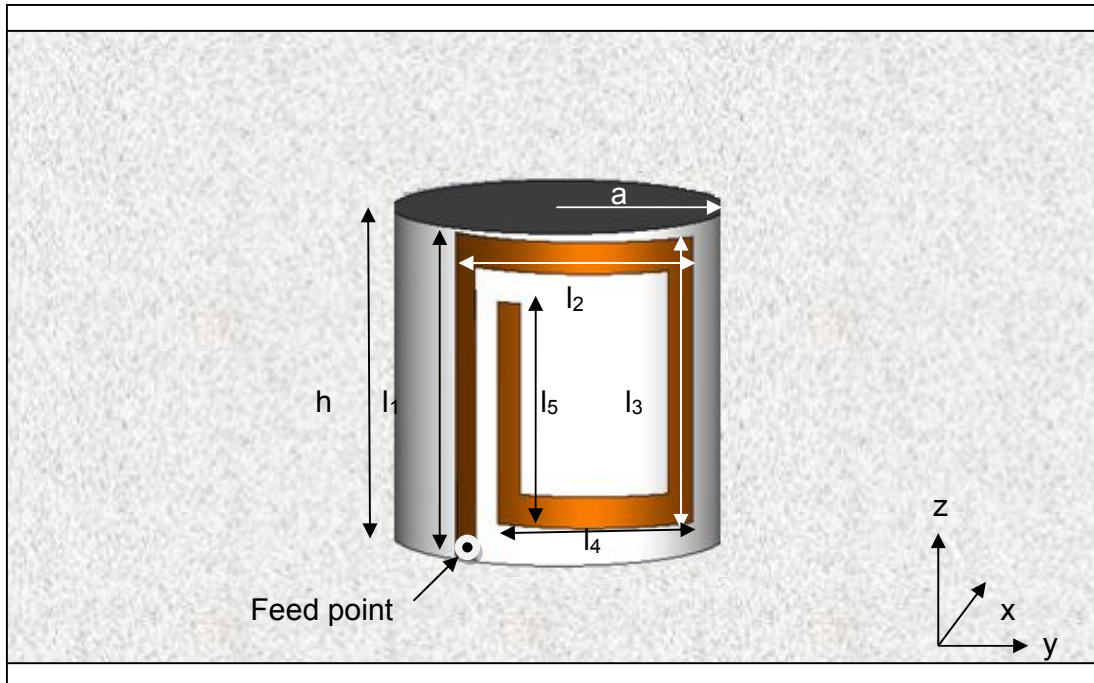
Figure 4.2: Configuration of a cylindrical DRA excited

using a conformal square spiral

The structure has been modeled using the method of moments together with the combined RWG and SWG basis and test functions described in chapter 2. The dielectric cylinder has been meshed to 2260 tetrahedrons, and the metallic strips to 86 triangular patches, giving a total of 5060 unknowns. Once more, the PEC ground plane has been considered using the image theory, and the feed has been simulated using a delta-gap voltage source model. The computation time has been reduced by employing analytical equations for singularity extraction, and Gaussian quadrature formula in conjunction with the approximate Galerkin MoM as described in section 2.6. The computation time is approximately fifty seconds per frequency point, which is significantly faster than the simulation time using CST Microwave studio for the same structure.

The optimum dimensions of the feeding metallic strips that are required to establish a travelling-wave current distribution along the conformal spiral-shaped monopole, as well as exciting a DRA mode within the same frequency range, have been determined through an iterative design procedure. The existence of this travelling-wave current produces a circularly polarized wave which radiates from the DRA surfaces. As mentioned earlier, the travelling-wave current distribution changes slowly with frequency, hence a wider CP bandwidth is expected.

Table 4.1 presents the AR bandwidth, impedance matching bandwidth, and the bandwidths overlapping percentage for several strips dimensions. From the table, the achieved AR bandwidth is rather sensitive to the strips lengths, as changing the latter may generate a standing wave current distribution, which deteriorates the circular polarization. The optimized dimensions of the individual strips have been found to be l_1 = 10.54 mm, l_2 = 10 mm, l_3 = 9 mm, l_4 = 8 mm, and l_5 = 5 mm, which give an AR and S_{11} bandwidths of 3.48% and 15.65%, respectively. Furthermore, it can be clearly seen that in some cases, the circular polarization radiation has been achieved without sufficient impedance matching bandwidth, thus making the antenna design inefficient when used in CP communication system. In these cases, no mode has been excited at the CP frequency band. As explained earlier, the CP wave is radiated by the DRA due to the existence of travelling-wave current distribution along the spiral feed whereas the antenna's resonance frequency and S_{11} bandwidth are mainly dependent on the aspect ratios and permittivity of the DRA. Additionally, the resonance frequency can be affected by various factors such as efficiency of fields coupling between feed and DRA, load of, and location of feed.

l_1 (mm)	l_2 (mm)	l_3 (mm)	l_4 (mm)	l_5 (mm)	3 dB AR Bandwidth (%)	-10 dB S11 Bandwidth (%)	Overlapping AR & S11 Bandwidth (%)
8	10	6.5	8	4.5	0	0	0
8.5		7		5	0	0	0
9		7.5		5.5	1.07	11.45	100
9.5		8		6	2.83	12.31	64
10		8.5		6.5	3.21	12.95	73
10.25		8.75		6.75	3.25	13.21	79
10.54		*9*		*7*	*3.1*	*13.02*	*94*
10.54	8	9	6	7	0	0	0
	9		7		2.64	8.98	2
	10		*8*		*3.1*	*13.02*	*94*
	11		9		1.58	4.28	0
	12		10		0	0	0
10.54	10	10	8	7	0	0	0
		9.5			0	0	0
		9			*3.1*	*13.02*	*94*
		8.5			2.11	13.93	100
10.54	**10**	**9**	**8**	7	3.10	13.02	94
				6.5	3.29	14.10	96
				6	2.87	14.73	100
				5.5	3.39	15.05	100
				5	**3.48**	**15.65**	**100**
				4.5	2.98	16.98	100
				4	1.94	23.24	100
				3.5	0	0	0

Table 4.1: Optimization of the feeding strips dimensions.

4.2.2 Results and Discussions

A prototype of cylindrical DRA has been built using Alumina ceramic material. The conformal square spiral has been constructed using five individually cut strips of an adhesive-backed copper tape which have been electrically connected to each other using a conductive silver paint. As mentioned in the

previous chapter, possible air gaps between the DRA and the ground plane have been eliminated by employing the procedure described in [10].

Comparison between the calculated and measured input impedances is illustrated in Figure 4.3, which illustrates a close agreement between the results. Figure 4.4 shows the return losses, where it can be observed that an $S_{11} \le -10$ dB has been achieved over bandwidths of 15.65% and 14.3% in the simulation and measurements, respectively. The minimum S_{11} has been computed at 5.89 GHz compared to 5.96 GHz in the measurements, which constitutes a marginal difference of 1.18% between the two sets of results.
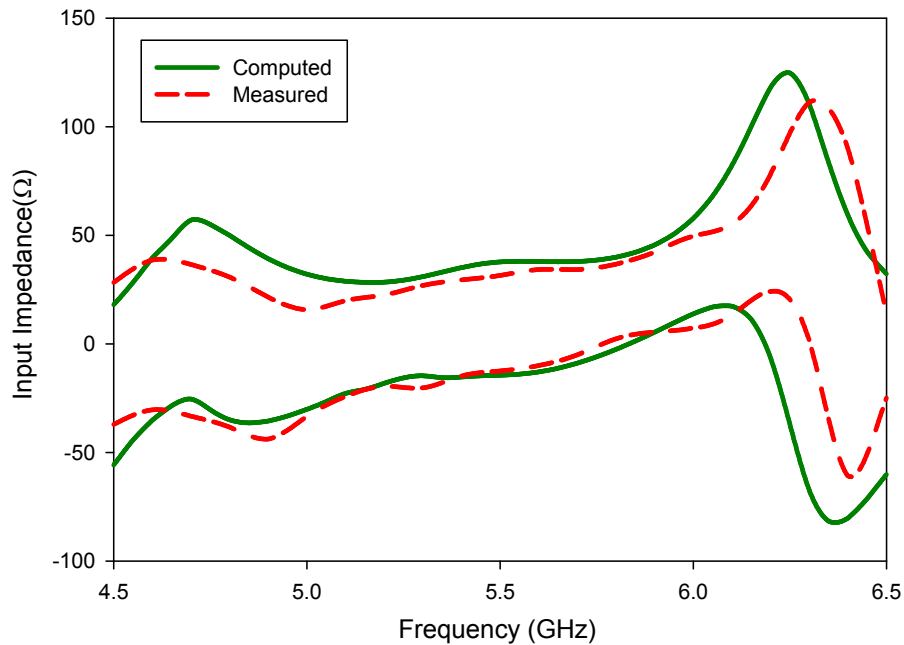
Figure 4.3: Input impedance of the cylindrical DRA
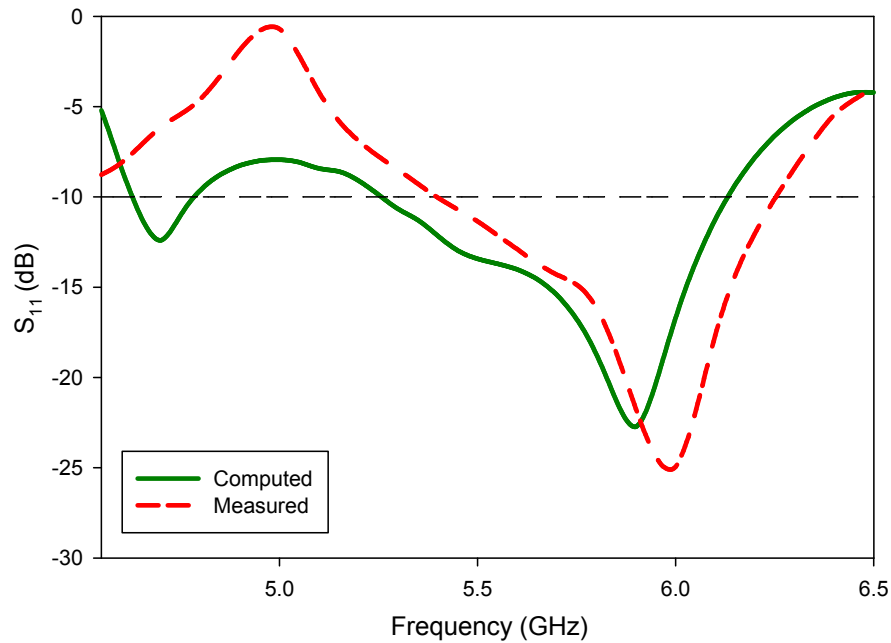
Figure 4.4: Return losses of the cylindrical DRA

The resonant frequency obtained from theoretical and measurement results agree well with the predicted resonance frequency of 5.61 GHz for the $TE_{01\delta}$ mode calculated using equation (4-4), in which the DRA is excited. The EM fields distribution across an isolated cylindrical DRA with similar parameters of a, ε_r and height of $2h$ operating in this mode are shown in Figure 4.5. It is evident from Figure 4.5 (b) that the DRA exhibits strong magnetic field along the curved surface, thus it can be excited by the spiral strips attached on that curved surface, which have a maximum current magnitude at the feed point.
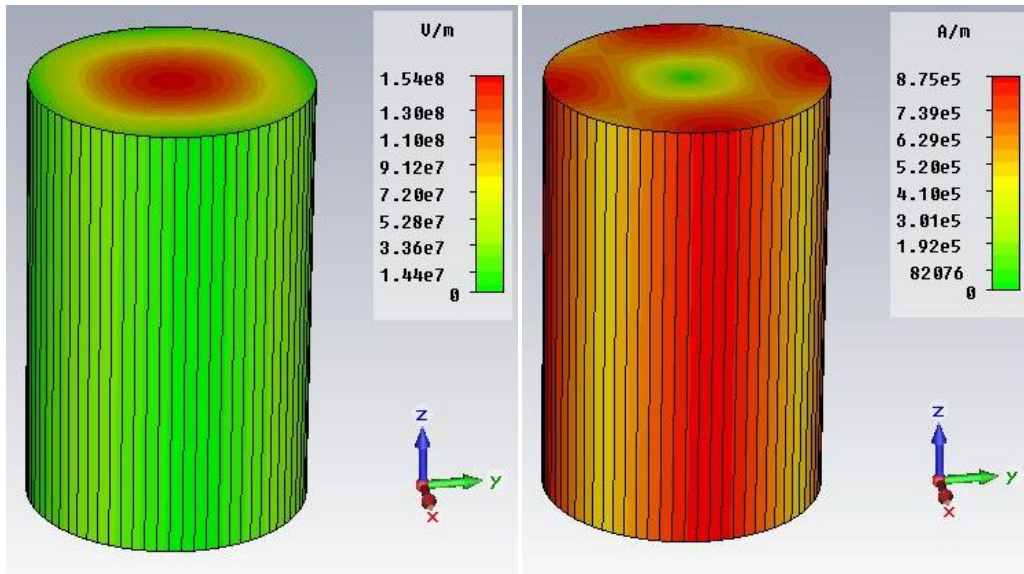
Figure 4.5: EM Fields distribution for $TE_{01\delta}$ mode; (a) E-field and (b) H-field

Furthermore, a travelling-wave current distribution achieved along the spiral at the frequency band of operation is shown in Figure 4.6. The spiral strip has a perimeter of $1.7\lambda_g$ at 5.38 GHz. This circumference supports the first-mode of radiation, for which the conditions are ideal for CP wave radiation.
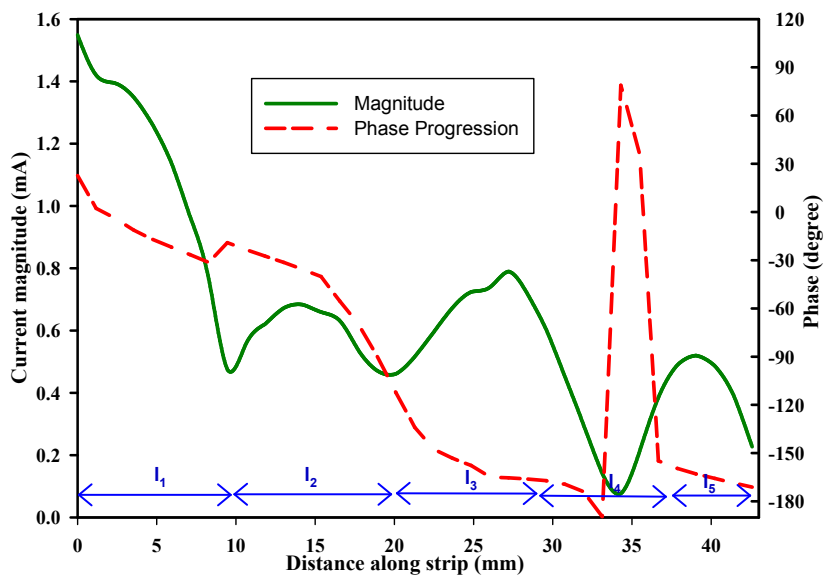
Figure 4.6: Current distribution along the spiral strip at 5.38 GHz

The bore-sight axial ratio has been computed and measured as demonstrated in Figure 4.7, where it can be seen that the minimum computed AR value is 1.3 dB at 5.38 GHz, which is close to the corresponding measured value of 1.6 dB at 5.55 GHz. From these results it can be noticed that the theoretical 3 dB AR bandwidth extends from 5.28-5.48 GHz compared to 5.44-5.66 GHz in the measurements. Therefore, circularly polarized radiation has been achieved over bandwidths of 3.48% and 4.20% in the analysis and the measurements, respectively, which is higher than a bandwidth of ~2% that has been achieved earlier for a singly-fed CP cylindrical DRA with similar dimensions [9]. It should be noted that this frequency band for CP radiation is achieved at lower frequency than those achieved in [9]. The slight discrepancy between the computed and measured results can be attributed to experimental tolerance and the use of finite ground plane. Additionally, compared to the rectangular counterpart, the cylindrical DRA has a much lighter weight which has caused some difficultly in positioning it firmly on the PEC ground plane, hence the air gaps couldn't be eliminated totally and this may have contributed to the discrepancy between theory and experiment. Furthermore, based on graphs in Figure 4.7, it can be observed that a sufficient impedance matching bandwidth has been obtained throughout the frequency band of the achieved circular polarization.
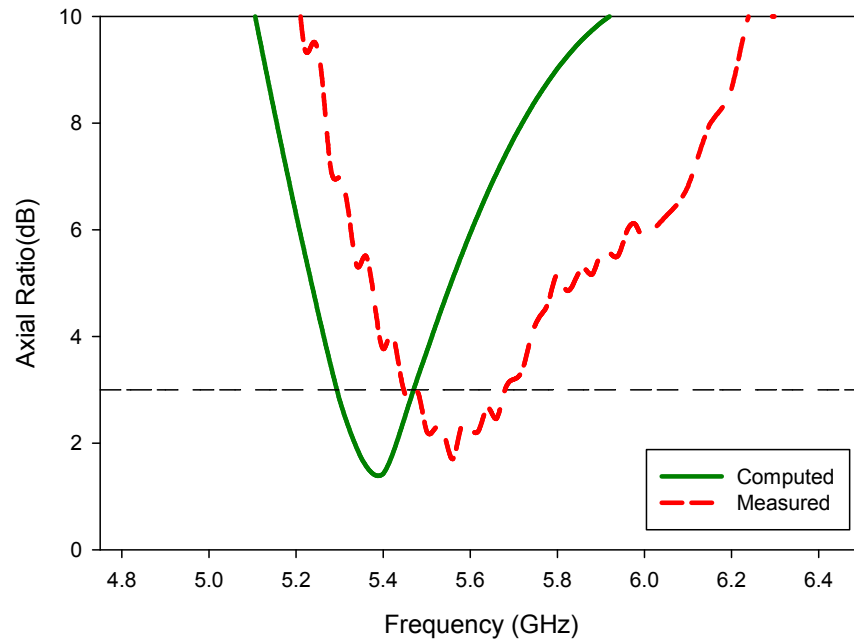
Figure 4.7: Axial ratio of a cylindrical DRA fed by square spiral strip
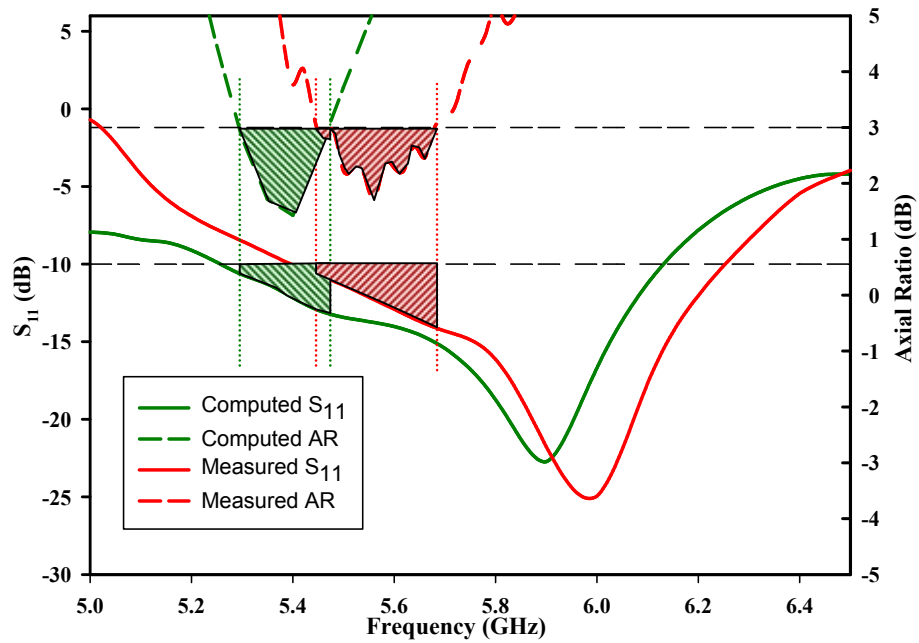
Figure 4.8: Region of overlapping bandwidths for S_{11} and AR

The variation of the axial ratio with the elevation angle is demonstrated in Figures 4.9 and 4.10, where it can be noticed that the DRA offers circular polarization over a useful computed beam-widths of over $65°$ and $90°$ in the $\phi = 0°$ and $\phi = 90°$ planes, respectively. In terms of measurements, the beam-widths have been achieved over $61°$ in the $\phi = 0°$ plane and $82°$ in the $\phi = 90°$ planes.
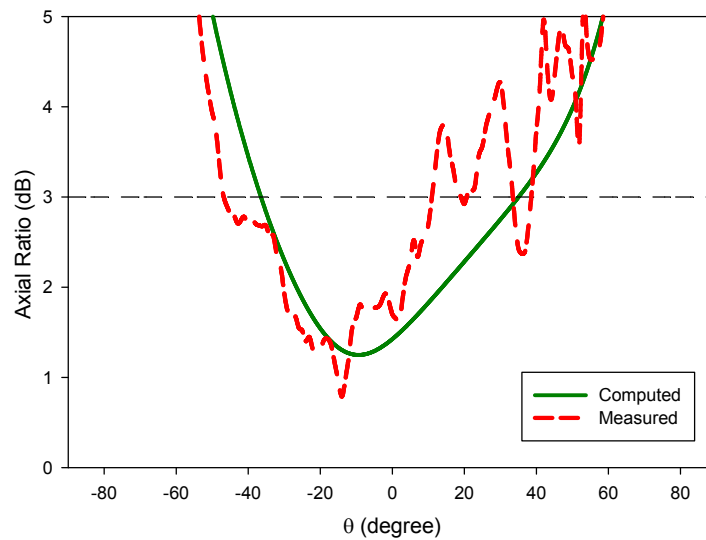
Figure 4.9: Axial ratio beam-width of the cylindrical DRA at $\phi = 0°$
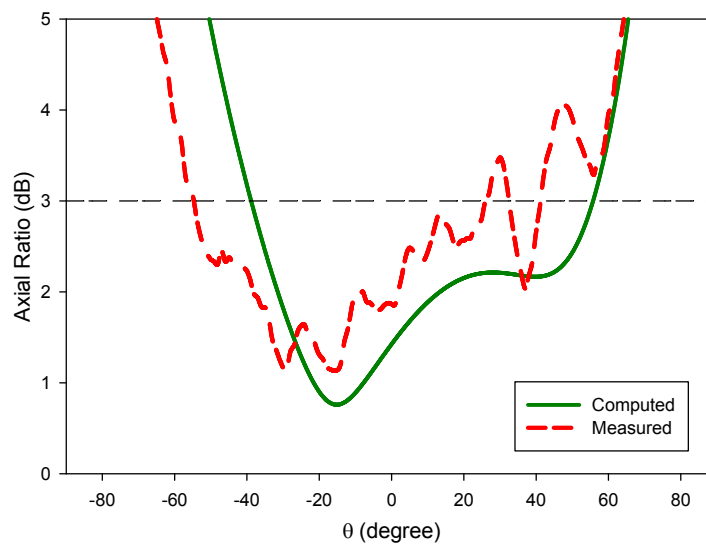
Figure 4.10: Axial ratio beam-width of the cylindrical DRA at $\phi = 90°$

The stability of radiation pattern has been studied as illustrated in Figure 4.11, where it is evident that the patterns are stable across the whole CP bandwidth, and an isolation of more than 18 dB has been achieved between the co-, and cross-, polarization components at the minimum AR frequency point. The discrepancy in the pattern of LHCP at $\phi = 90°$ in Figure 4.11 (a) and (b) can be attributed to the discretization error. This problem can be solved by taking more measurement points, such as every $\theta = 0.1°$ step instead of $\theta = 1°$.
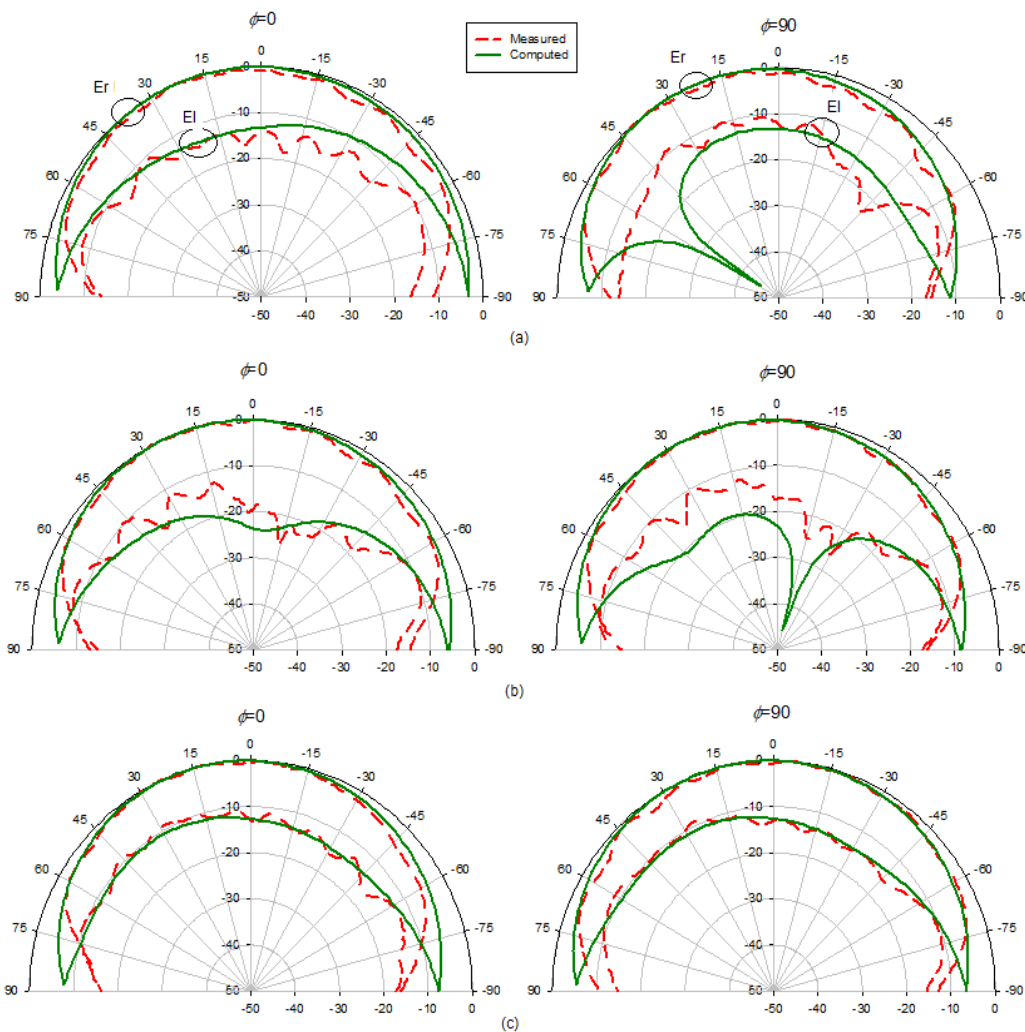
Figure 4.11: Radiation patterns of the cylindrical DRA at the (a) beginning, (b) centre, and (c) end of the CP bandwidth.

Figure 4.12 presents the calculated and measured bore-sight gain of the cylindrical DRA, where it can be observed that a useful gain of more than 4 dBi has been achieved throughout the CP bandwidth in the theoretical and experimental results.
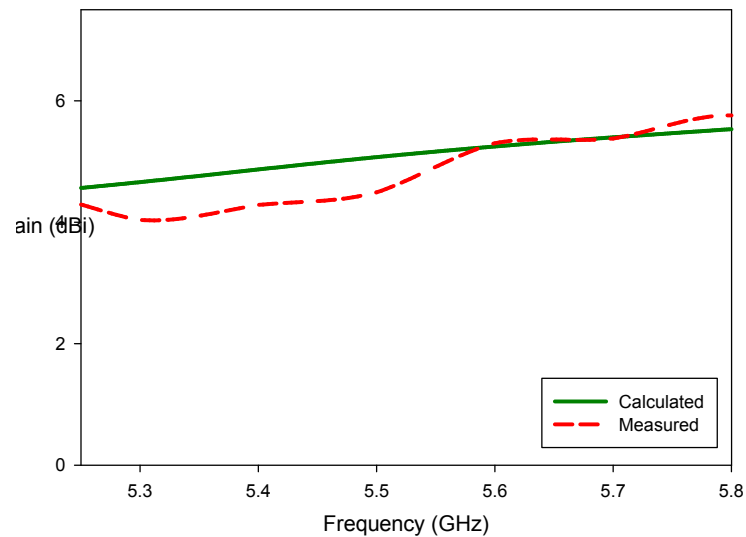
Figure 4.12: Gain of a cylindrical DRA fed by a square spiral strip

4.3   Bandwidth Enhancement of the Circularly Polarized Cylindrical DRA using Multi Dielectric Layers

4.3.1 Antenna's Configuration

The possibility of enhancing the AR bandwidth by employing multi dielectric layers is investigated next. It should be noted that shortly after the measurements of this approach, few studies have been published on the same idea of enhancing the CP bandwidth using a layered DRA configuration [11-13]. For instance, an increase of 100% in the 3dB AR bandwidth has been reported in [11] when a

multilayer rectangular DRA fed by cross slot is used instead of single layer structure. Additionally, investigations done in [12-13] demonstrate that the AR bandwidth of the multilayer structure is approximately three times that of a single layer DRA. In these cases, removing the central portion of the single layer DRA and filling the gap with material of lower permittivity decreases the effective dielectric constant of the overall structure, which caused a reduction the radiation Q factor of the DRA and thus increases the S_{11} and AR bandwidths.

In this research, a smaller dielectric cylinder of different permittivity has been embedded within the cylindrical DRA. Figure 4.13 shows the configuration of the two layer DRA, where a machinable-glass ceramic known as Macor with a relative permittivity of 5.67 has been chosen as the inner layer owing to lower cost and excellent insulation properties, as well as ease of fabrication since it is machinable to any desired shape with standard metalworking tools.
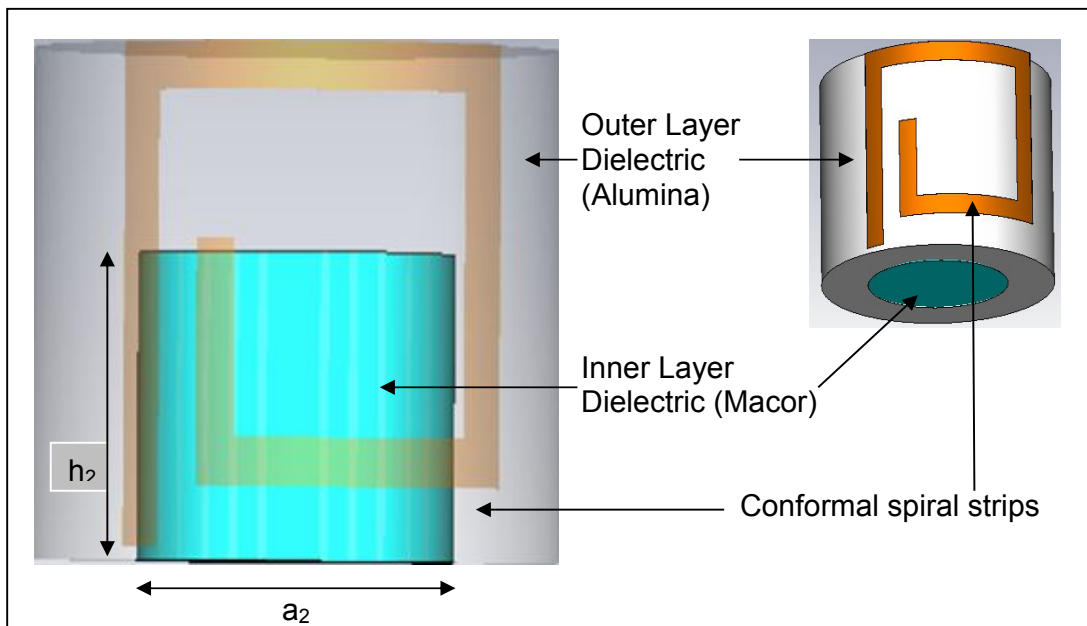
Figure 4.13: Configuration of a multilayer cylindrical DRA

(**Inset**: side-bottom view of the DRA)

The parameters of the outer layer and conformal spiral are similar to those used in section 4.3. The height, h_2, and radius, a_2, of this inner layer have been varied in proportion to the dimensions of the outer layer. This parameter, P has been used to speed up the optimization process. The AR bandwidth and the corresponding minimum AR frequency point are shown in Figure 4.14 as functions of the inner layer aspect ratio. From these results, it can be noticed that as P increases, the resonance frequency for the $TE_{01\delta}$ mode also increases. This can be attributed to the decrease in the effective permittivity of the DRA. Consequently, this leads to an AR bandwidth increment when the dimensions of inner layer increases up to $P=0.9$. It should be noted that when $P=1$, a single dielectric is achieved with a permittivity of 5.67, which changes the electrical dimensions of the spiral and produces a narrower AR bandwidth. Therefore, the optimum dimensions of the inner dielectric layer have been determined as $h_2=$ 9.49 mm and $a_2=$ 6.31 mm.
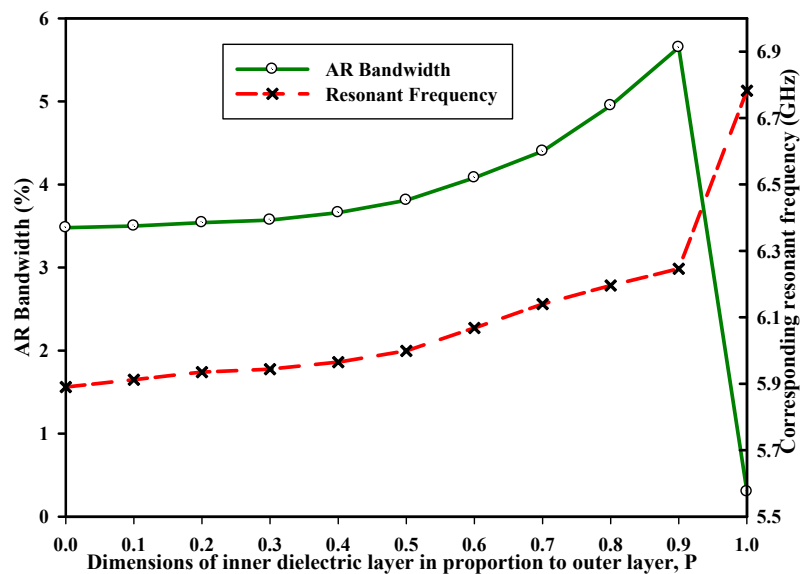
Figure 4.14: Axial ratio bandwidth and corresponding resonance frequency as a function of the size of inner layer.

4.3.2 Results and Discussions

A prototype of the multilayer cylindrical DRA is illustrated in Figure 4.15. The parameters of the outer layer dielectric and conformal spiral are similar to those used in section 4.3 and the inner layer has a parameter of *P*=0.9.

Figure 4.15: A multilayer cylindrical DRA excited by a conformal spiral strip

The input impedance has been measured and compared to the MoM computation with close agreement as illustrated in Figure 4.16. Additionally, the simulated and measured return losses agree well with each other as shown in Figure 4.17, in which it is evident that $S_{11} \leq$ -10 dB bandwidths of 15.2% and 14.4% have been achieved in computations and measurements, respectively. The minimum S_{11} has been computed at 6.25 GHz compared to 6.33 GHz in the measurements, that is, a marginal difference of 1.41% between the MoM model and the experiment. In order to compare the resonance frequency obtained by these results with those predicted by equation (4-4), extra calculation needs to be implemented by taking into account the presence of inner dielectric layer. From

[14], when another dielectric layer of parameters ε_{r2}, a_2 and h_2 is added, the effective permittivity of the overall DRA structure becomes

$$\varepsilon_{eff} = (m)\varepsilon_{r2} + (1-m)\varepsilon_r \qquad (4\text{-}6)$$

where *m* is the volume fraction of the inner layer dielectric which is given by

$$m = V_2 / V_{overall} \qquad (4\text{-}7)$$

Since the cylindrical volume is computed using

$$V = \pi a^2 h \qquad (4\text{-}8)$$

therefore the effective permittivity of the overall DRA structure can be determined as ε_{eff}=6.62. Using this value, the predicted resonance frequency for the broadside TE$_{01\delta}$ mode has been calculated using equation (4-4) as 6.55 GHz, which is reasonably close to those obtained by the theory and experiment
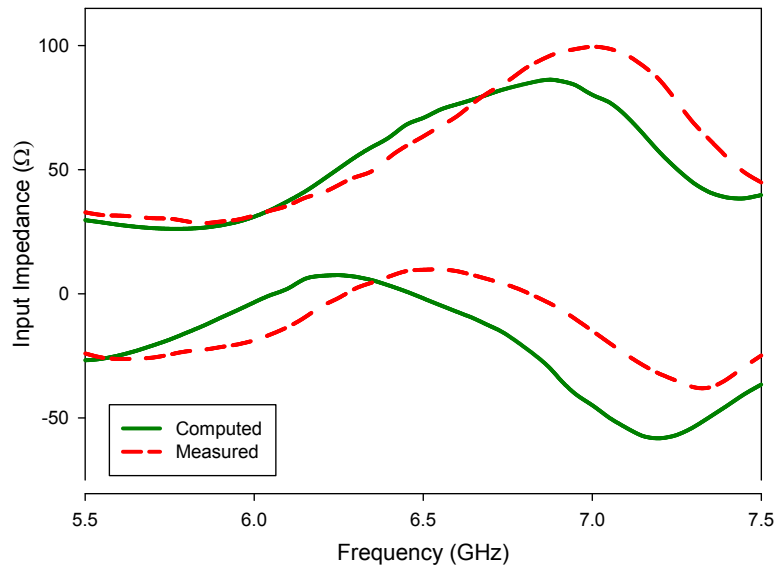
Figure 4.16: Input impedance of the multilayer cylindrical DRA
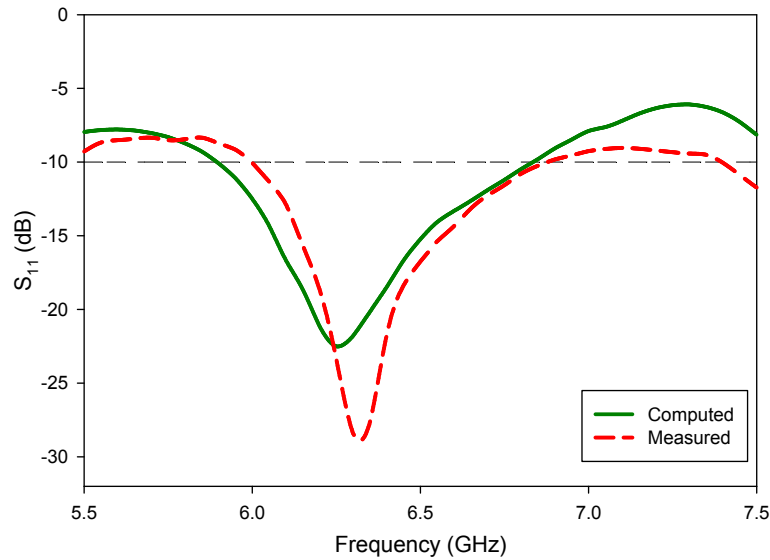
Figure 4.17: Return losses of the multilayer cylindrical DRA

A travelling-wave current distribution has been obtained along the feeding spiral as illustrated in Figure 4.18, where it can be observed that smoothly decaying current amplitude has been achieved in conjunction with an approximately linear phase progression. The spiral strip has a perimeter of $1.72\lambda_g$ at 6.25 GHz, which supports the first-mode of radiation.
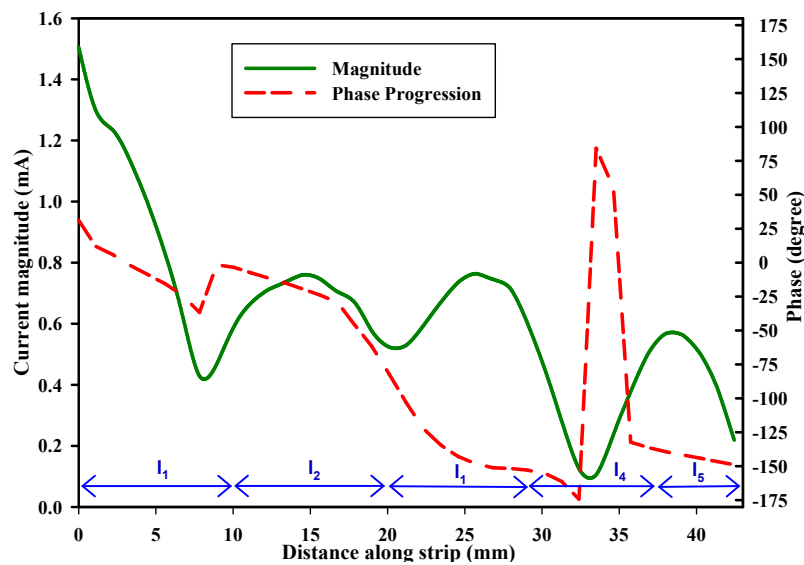
Figure 4.18: Current distribution along the spiral strip at 6.25 GHz

The axial ratio has been computed and measured at the bore-sight direction as shown in Figure 4.19, where it can be seen that the minimum computed AR is 0.67 dB at 6.25 GHz, compared to the corresponding measured value of 1.71 dB at 6.36 GHz. The measured and computed minimum AR frequency points are close to each other with a slight difference of 1.5%. From these results it can be observed that the achieved 3 dB AR bandwidths are 5.63% and 5.9% in the analysis and measurements, respectively. This represents an increase of over 66% in both computations and measurements for the AR bandwidth compared with those achieved using a single layer cylindrical DRA as discussed in section 4.2. It should also be noted that this AR bandwidth is substantially wider than what has been reported in the literature for cylindrical DRAs. Furthermore, with reference to Figure 4.20, it can be seen that a sufficient impedance matching bandwidth has been obtained throughout the achieved circular polarization bandwidth.
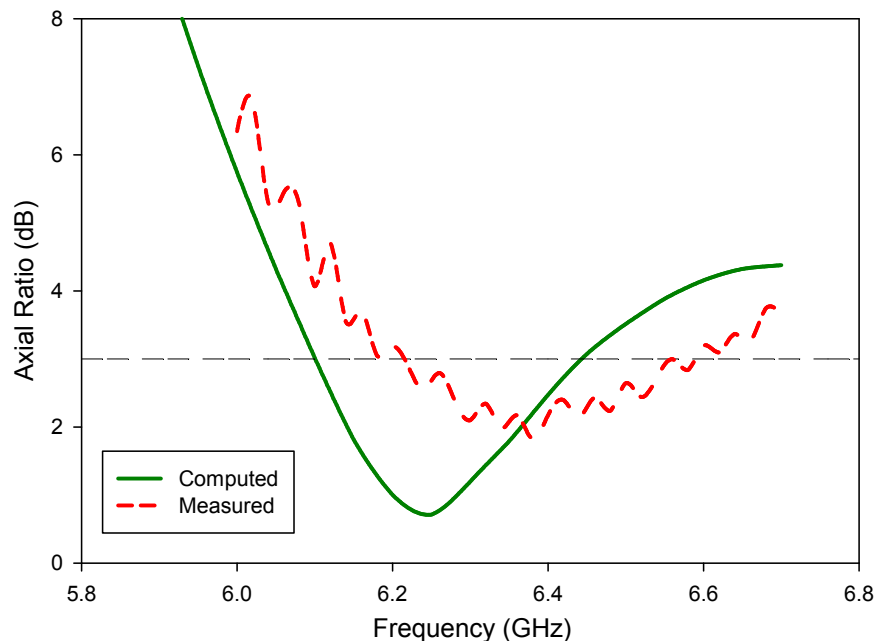
Figure 4.19: Axial ratio of the multilayer cylindrical DRA fed by a spiral metal.
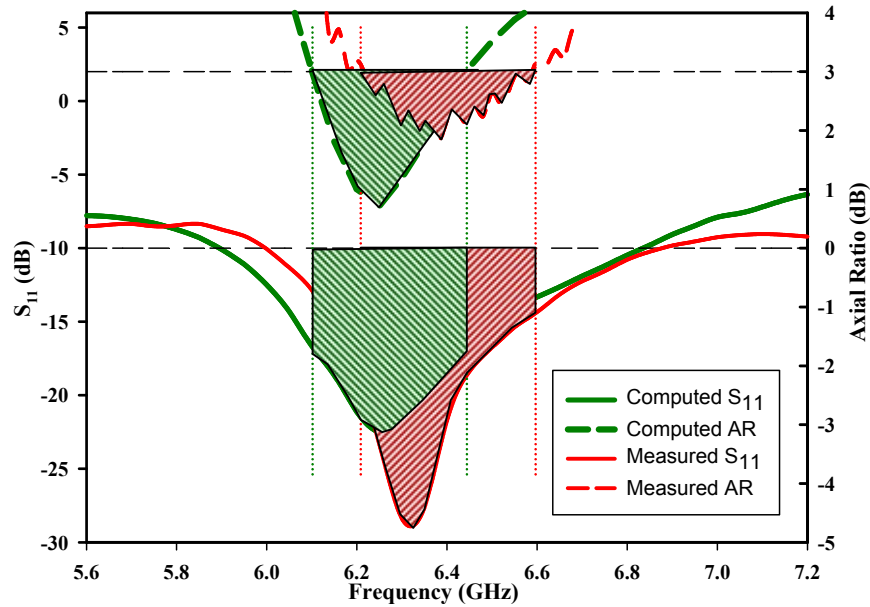
Figure 4.20: Region of overlapping bandwidths for S_{11} and AR

Figures 4.21 and 4.22 present the axial ratio beam-width. With reference to the computational result, the DRA offers circular polarization over useful computed beam-widths of $58°$ and $78°$ in the $\phi = 0°$ and $\phi = 90°$ planes, respectively.
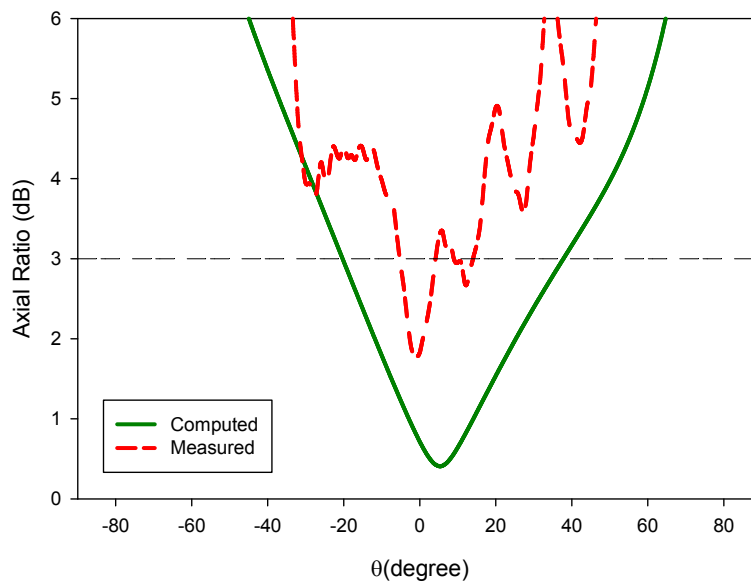
Figure 4.21: Axial ratio beam-width of the multilayer cylindrical DRA at $\phi = 0°$
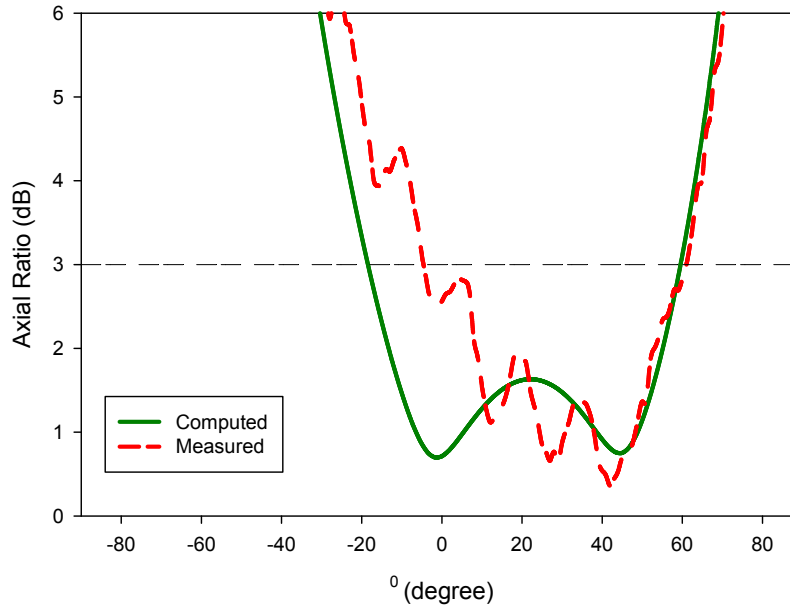
Figure 4.22: Axial ratio beam-width of the multilayer cylindrical DRA at $\phi = 90°$

A comparison between the calculated and measured radiation patterns at the optimum AR frequency is shown in Figure 4.23 with reasonable agreement. It is evident from these results that this is a right-hand CP DRA, in which the RHCP field is stronger than the LHCP field by more than 18 dB in the bore-sight direction. Again, as in the case with the previous design, a left-hand CP DRA can be attained by changing the square spiral arm winding from clockwise to counter clockwise direction. Finally, the antenna gain of the multilayer cylindrical DRA has been measured at bore-sight. The results are shown in Figure 4.24, where it can be seen that the antenna offers a satisfactory gain of over 3 dBi across the whole frequency range of the achieved circular polarization. The gain is lower than that achieved by the single layer design due to the slight shift of approximately 5° in the main beam from the bore-sight direction at the CP frequency band as can be seen in Figure 4.23.
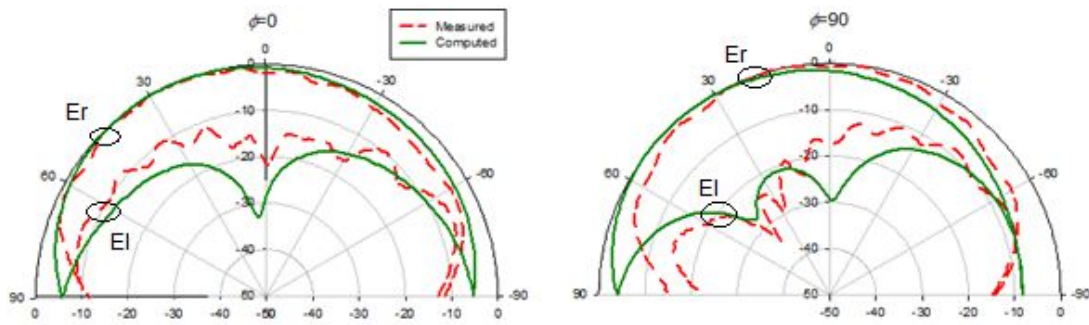
Figure 4.23: Radiation patterns of the multilayer cylindrical DRA

at the optimum AR frequency point.
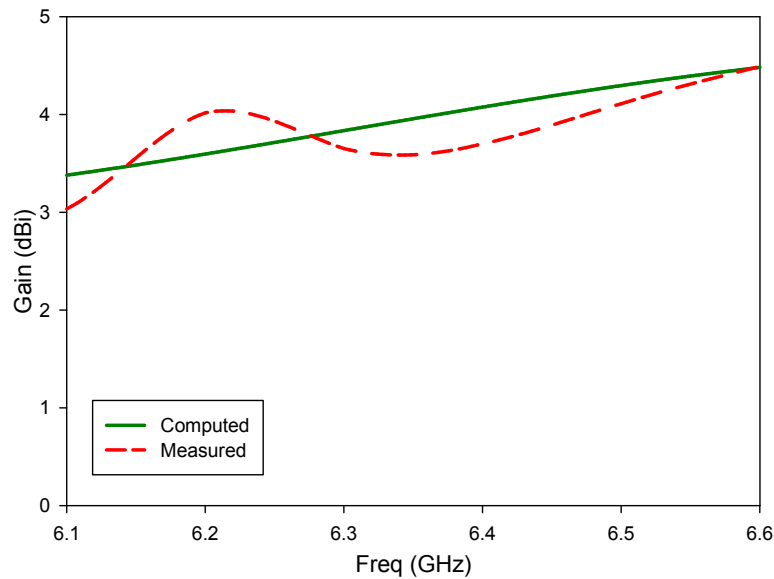
Figure 4.24: Gain of the multilayer cylindrical DRA fed by conformal spiral strips

4.4   Conclusions

In order to prove the versatility of a square spiral metal strip excitation introduced

in previous chapter, the excitation method has been applied to a cylindrical DRA.

This antenna configuration has achieved a 3 dB AR bandwidth of more than 3.4%,

which is higher than what has been reported in the literature for a singly-fed

cylindrical DRA. The CP bandwidth is associated with a satisfactory gain of over 4 dB as well as an impedance matching bandwidth of approximately 14.3%. Additionally, a novel approach has been introduced for further CP bandwidth enhancement, which is based on employing a multilayer DRA. The results represent an additional AR bandwidth increment of ~66% on top of the enhancement achieved using the spiral excitation. Therefore, respective CP and S_{11} bandwidths of ~5.6%, and 15% have been achieved by using the multilayer cylindrical DRA. Throughout the research, a good agreement has been obtained between experimental and theoretical results.

References

[1] R.K. Mongia and O. Bhartia, "Dielectric Resonator Antennas – A Review and General Design Relations for Resonant Frequency and Bandwidth*," International Journal of Microwave Milimeter-Wave Computer-Aided Engineering.*, vol.4, no.3, pp.230-247, 1994

[2] J.C. Sethares and J. Naumann, "Design of Microwave Dielectric Resonator*," IEEE Transc. On Microwave Theory and Techniques*, vol.14, no.1, pp.1023-1029, Jan 1966

[3] Y. Kobayashi and M. Miura, "Optimum Design of Shielded Dielectric Rod and Ring Resonators for obtaining the Best Mode Seperation*," IEEE International Microwave Symp. Dig.*, pp.184-186, 1984

[4] Y. Kobayashi and S. Tanaka, "Resonant Modes of a Dielectric Rod Resonator Short Circuited at Both Ends by Parallel Conducting Plates*," IEEE Transc. Microwave Theory and Techniques*, vol.28, pp.1077-1085, Oct 1980

[5] A. Petosa, "Dielectric Resonator Antenna Handbook," Chapter 2, pp.18, Artech House, 2007

[6] J. Van Bledel, "On the Resonances of a Dielectric Resonator of Very High Permittivity*," IEEE Transc. Microwave Theory and Techniques*, vol.23, pp.199-208, Feb 1975

[7] M. Tsuji, h. Shigesawa and K. Takiyama, "Analytical and Experrimental Investigations on Several Resonant Modes in Open Dielectric Resonators*," IEEE Transc. Microwave Theory and Techniques*, vol.32, pp.628-633, June 1984

[8] R. DeSmedt, "Correction due to a Finite Permittivity for a Ring Resonator in Free Space*," IEEE Transc. Microwave Theory and Techniques*, vol.32, pp.1288-1293, Oct 1984

[9] M.T. Lee, K.M. Luk, E.K.N. Yung, and K.W. Leung, "Microstrip line fed circularly polarized cylindrical dielectric resonator antenna", *Microwave and Optic. Tech. Lett.* , Vol. 24, pp. 206-207, Feb 2000

[10] K.W. Leung, "Conformal strip excitation of dielectric resonator antenna", *IEEE Trans. Antennas Propagat.,* vol. 48, pp. 961-967, Jul. 2000.

[11] H. S. Lee and M. S. Lee, "A study on the enhancement of gain and axial ratio bandwidth of the multilayer CP-DRA," *5th European Conference on Circuits and Systems for Communications (ECCSC), 2010*, vol., no., pp.248-252, 23-25 Nov. 2010

[12] K. Lu, K. W. Leung and Y. M. Pan;, "Theory and Experiment of the Hollow Rectangular Dielectric Resonator Antenna," *IEEE Antennas and Wireless Propagation Letters,* vol.10, pp.631-634, 2011

[13] K. Lu and K. W. Leung, "Wideband circularly polarized hollow dielectric resonator antenna with a parasitic strip," *Cross Strait Quad-Regional Radio Science and Wireless Technology Conference (CSQRWC)*, vol.1, no., pp.514-515, 26-30 July 2011

[14] D.S. Killips, L. Kempel, D. Nyquist and E. Rothwell , "Analysis of layering dielectrics on effective permittivity using wave matrices"*, IEEE Antennas and Propag. Soc. International Symposium,* vol. 3A, pp. 216-, 2005.

CHAPTER 5

WIDEBAND CP DRAs USING

CONFORMAL RECTANGULAR

HALF-LOOP EXCITATION

5.1   Introduction

In this chapter, another variation of the conformal strip excitation scheme developed in this research is introduced. Instead of employing spiral metal strips, a simpler feeding method is proposed using a rectangular open half-loop antenna to generate a wide CP bandwidth. Utilizing such an excitation scheme onto the rectangular DRA designed in section 3 has provided results comparable to those obtained using the spiral excitation. Additionally, the flexibility of this feeding method has been demonstrated by employing the half-loop feed onto other regular shaped DRAs such as cylindrical and hemispherical geometries.

5.1.1 Problem Formulation

Although the square spiral feed can be used to achieve a wide CP radiation from an arbitrarily shaped DRA, it has been noticed that the AR bandwidth is very sensitive to the spiral dimensions. For example, a deviation of less than 1 mm in the spiral dimension can significantly diminishes the DRA capability of radiating CP wave. Therefore, the requirement to maintain a precisely small separation distance between the spiral arms makes this approach difficult and time consuming to follow especially in normal laboratory environment. This limitation is particularly noticeable with curved DRA surfaces, where conformal strips with precise dimension and spacing are needed.

As a result, a simpler feeding method capable of generating a broadband CP radiation from regular, as well as irregular, shaped DRAs is needed. Such a feeding mechanism is introduced, where a rectangular open half-loop antenna that consists of three metallic strips has been employed for DRA excitation. In addition to its simplicity, the proposed feed facilitates the incorporation of a concentric parasitic half-loop that can be used to enhance the CP bandwidth further as demonstrated in the next chapter.

It is well-known that a closed-loop antenna serves as a standing wave resonant antenna and thus is commonly used in LP communication systems [1]. However, it has been proven theoretically in [2] that introducing a gap of appropriate dimensions and placement within the closed-loop can induce a travelling-wave current distribution along the loop. As a result, an open-loop antenna can be used to generate CP radiation as reported in [3-5].

5.2   Circularly Polarized Rectangular DRA

5.2.1 Antenna Configuration

Figure 5.1 presents the geometry of a rectangular DRA that has been excited using a rectangular open half-loop antenna. The DRA has the dimensions of *a*, *b*, *c* and a dielectric permittivity of ε_r, whereas the feeding structure has a width of w_d, a height of h_d and a gap size of g_d located at a gap position of $\vec{g}_p$ within the metallic strips. The feed point is placed at a distance of *d* from the nearest side wall.
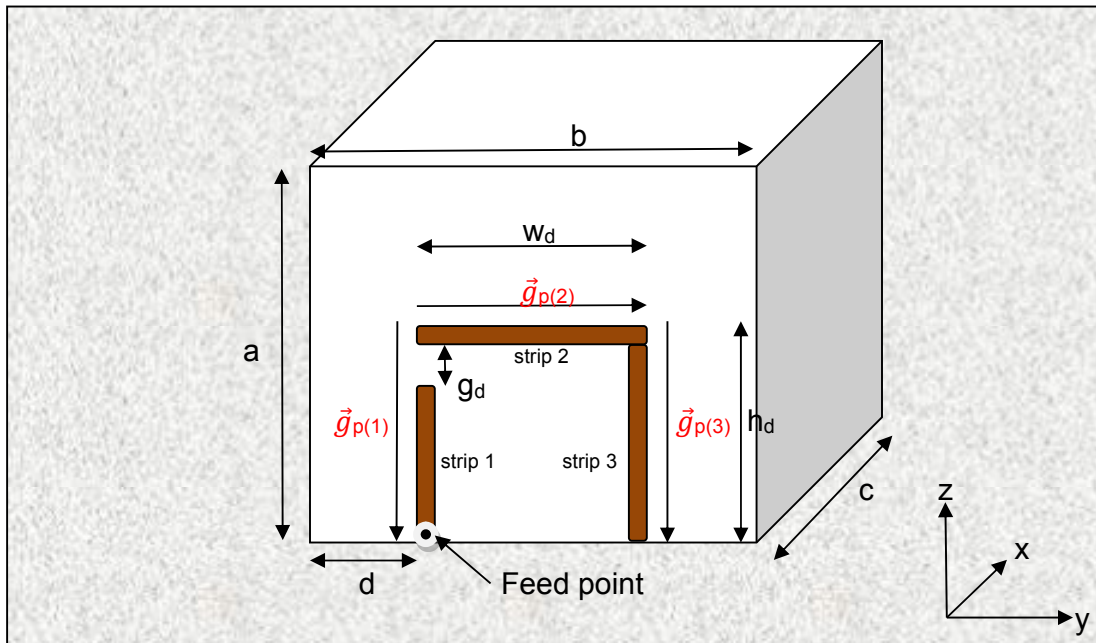
Figure 5.1: Configuration of a rectangular DRA fed by a rectangular open half loop

The antenna configuration has been modeled using the method of moments in conjunction with the combined RWG and SWG basis functions described in Chapter 2, where the rectangular dielectric has been meshed to 2463

tetrahedrons and the metallic strips to 59 triangular patches, giving a total of 5305 unknowns. Once more, an iterative design procedure has been employed to determine the optimum dimensions of the feeding metallic strips that are needed to establish a travelling-wave current distribution along the rectangular open half-loop antenna as well as exciting a DRA mode within the same frequency range. This travelling-wave current provides a circular polarization radiation and excites a DRA mode within the CP frequency band. Since the travelling-wave current distribution changes slowly with frequency, a broadband CP radiation is obtained.

In order to assess the performance of the open half-loop design, the rectangular dielectric has the same parameters as those used in Chapter 3 with a relative permittivity of ε_r = 9.2, and dimensions of *a* = 26.1 mm, *b* = 25.4 mm and *c* = 14.3 mm [6]. The gap position, $\vec{g}_p$, has been optimized initially when the half-loop dimensions are fixed as h_d = w_d = 10 mm, g_d = 1 mm and *d* = 7.7 mm. Figure 5.2 shows the actual AR bandwidth and effective AR bandwidth, i.e. AR bandwidth obtained in conjunction with impedance matching bandwidth, as functions of $\vec{g}_p$ when the gap was placed within strip 1, strip 2 and strip 3, respectively (labelled as $\vec{g}_{p(1)}$, $\vec{g}_{p(2)}$ and $\vec{g}_{p(3)}$ in Figure 5.1). It should be noted that due to the convention used for the gap position, $\vec{g}_{p(1)}$ = 0 mm is essentially the same as $\vec{g}_{p(2)}$ = 0 mm. This also applies to $\vec{g}_{p(2)}$ = 9 mm and $\vec{g}_{p(3)}$ = 0 mm. With reference to Figure 5.2, the highest AR bandwidth of 4.06% has been obtained when $\vec{g}_{p(1)}$ = 1 mm. The minimum S_{11} obtained using this feeding structure configuration has been computed at a frequency of 3.71 GHz, with an AR that covers this frequency.
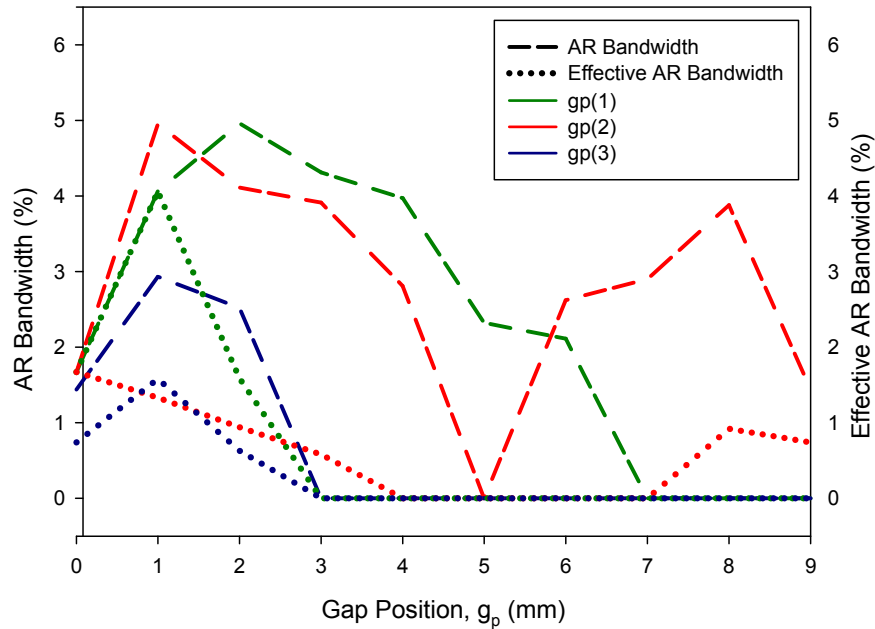
Figure 5.2: AR bandwidth and Effective AR bandwidth as a function of gap

position, for gap placed within strip 1, strip 2 and strip 3

Table 5.1 presents the AR, impedance matching and the percentage overlapping bandwidths for various half-loop dimensions, h_d, and w_d, when the optimized $\vec{g}_p$ is used and g_d is fixed to 1 mm. The results illustrate that the CP radiation can be attained easily using strips' dimensions range of 9 to 13 mm, which is a desired feature in the DRA design. On the contrary, there is a significant change in the S_{11} bandwidth for different strip's dimensions. Based on these results, the optimized dimensions for the half-loop are $h_d = w_d = 13$ mm. The reason for such an open loop configuration producing a good AR and S_{11} bandwidths is due to the presence of travelling-wave current distribution along the metal strip, as discussed in the next section. Using the optimized dimensions, the computed minimum S_{11} has been determined at a frequency of 3.50 GHz.

Height, h_d (mm)	Width, w_d (mm)	3db AR Bandwidth (%)	-10dB S11 Bandwidth (%)	Overlapping AR & S11 Bandwidth (%)
9	9	3.39	7.86	53
	10	3.69	8.17	42
	11	4.01	4.98	11
	12	4.63	1.32	0
	13	4.94	4.24	0
10	9	3.69	10.32	88
	10	4.06	13.6	100
	11	4.65	15.05	100
	12	4.91	3.05	58
	13	5.19	3.05	58
11	9	3.95	13.42	94
	10	4.32	15.63	100
	11	4.63	17.07	100
	12	4.9	5.66	97
	13	5.27	5.40	88
12	9	4.07	10.14	79
	10	4.65	13.33	100
	11	4.27	17.66	100
	12	4.85	23.46	100
	13	5.42	4.86	76
13	9	4.59	2.45	5
	10	4.96	4.27	100
	11	5.04	5.75	100
	12	5.44	22.15	100
	13	**6.50**	**18.74**	**100**

Table 5.1: AR and S_{11} bandwidths for different dimensions of the half-loop feed

By employing the aforementioned optimized dimensions together with g_d = 1 mm, the position of the gap has been optimised once more, where it has been noticed that the optimum overlapping bandwidth can be achieved when the gap is located at a distance of 10-14 mm from the feed point as shown in Table 5.2. Furthermore, when the optimized h_d, w_d, and $\vec{g}_p$ are used, varying g_d has little effect on the AR bandwidth compared to that on the S11 bandwidth as demonstrated in Table 5.3.

Distance of gap from feed point (mm)	3db AR Bandwidth (%)	-10dB S11 Bandwidth (%)	Overlapping AR & S11 Bandwidth (%)
9	0	15.95	0
10	5.52	15.43	100
11	**6.50**	**18.74**	**100**
12	5.91	19.02	91
13	5.56	19.52	69
14	4.91	10.34	41
15	1.43	5.59	16

Table 5.2: AR and S11 bandwidths for different position of gap

Gap size, g_d (mm)	3db AR Bandwidth (%)	-10dB S11 Bandwidth (%)	Overlapping AR & S11 Bandwidth (%)
0.25	6.26	21.02	100
0.5	6.35	19.95	100
0.75	6.43	19.42	100
1	**6.50**	**18.74**	**100**
1.25	6.56	15.32	96
1.5	6.64	12.46	93
1.75	6.69	7.89	85
2	6.71	4.35	64

Table 5.3: AR and S11 bandwidths for different g_d

5.2.2 Results and Discussions

A prototype of a rectangular DRA that is excited using open half-loop antenna is illustrated in Figure 5.3. From the results obtained using the iterative design procedure, the used optimized dimensions of the feeding loop are h_d = w_d = 13 mm, g_d = 1 mm, d = 6.5 mm and the gap is located at a distance of 11 mm from the feed point. The half-loop, has been connected to the ground plane at two ends using a conductive silver paint. The measurements have been conducted using the same set-up described in Chapter 3.
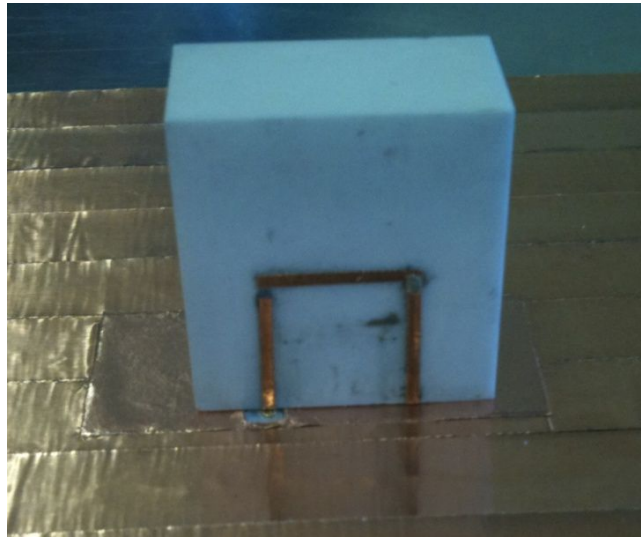
Figure 5.3: A rectangular DRA excited using open half-loop antenna

The computed and measured input impedance and return losses are shown in Figures 5.4 and 5.5, respectively, where it can be observed that good agreement has been achieved between the two sets of results. The impedance matching has been attained over bandwidths of 18.74% and 21.8% in the theoretical and experimental results, respectively. The minimum S_{11} has been computed at a frequency of 3.50 GHz compared to 3.59 GHz in the measurements, which constitute a marginal difference of 2.5%. These results agree reasonably well with a predicted resonance frequency of 3.8 GHz for the TE^{y}_{111} mode in which the DRA is excited, as calculated using DWM method proposed in [7]. As reported in [6], the broadside TE^{y}_{111} mode of this DRA has a strong magnetic field near the ground plane; hence it can be excited by a half-loop antenna that has a maximum current magnitude at that point to generate CP radiation within this mode. The EM fields distribution across the rectangular DRA operating in this mode has been shown in Figure 3.6.
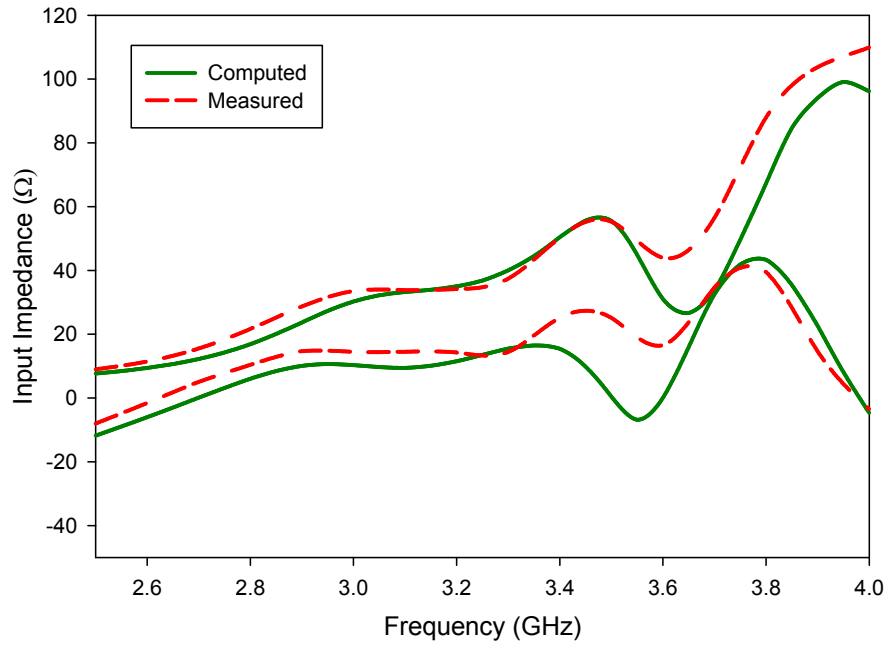
Figure 5.4: Input impedance of a rectangular DRA fed using a half-loop
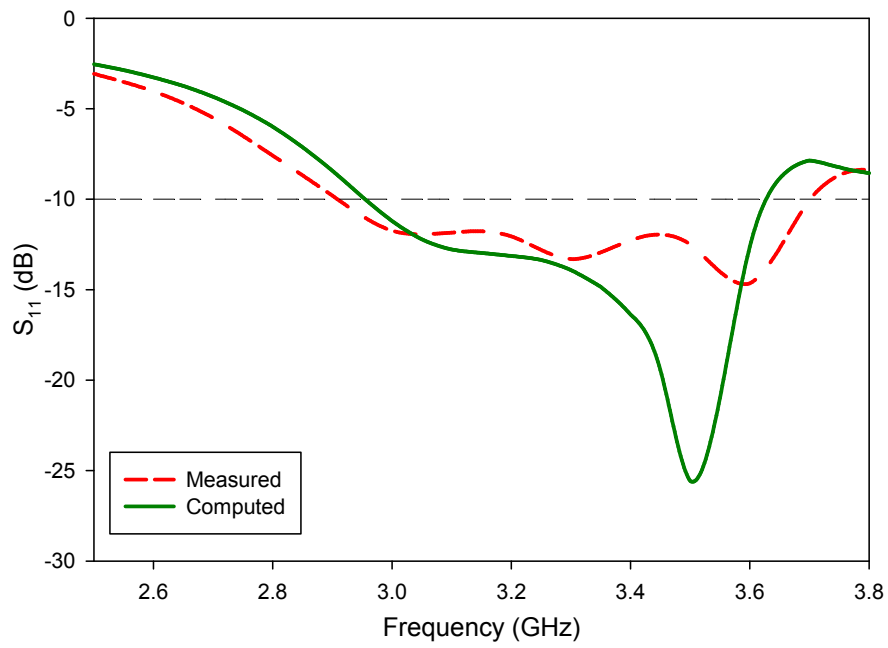
Figure 5.5: Return losses of the rectangular DRA

Furthermore, the current distribution has been studied where it has been observed from Figure 5.6 that a travelling-wave current distribution has been attained along the feeding strips with a smoothly decaying magnitude and approximately linear phase progression. Along the first metallic strip, the magnitude of current decreases to zero rapidly, owing to the limited distance between the feed point and gap. The rectangular half-loop has a perimeter of ~$1\lambda_g$ at 3.24 GHz that represents the first-mode of radiation band, for which the conditions are ideal for CP wave radiation [8, 9]. Changing the aspect ratio of the one wavelength perimeter maintains the travelling wave nature of the current as long as $9 \leq w_d \leq 15$ mm, otherwise a folded-dipole is formed on the DRA surface that only supports standing wave current, hence making the rectangular DRA radiates LP wave only. This may also results in a noticeable shift of the feed point position which effects the excited resonance mode and hence the S_{11} bandwidth.
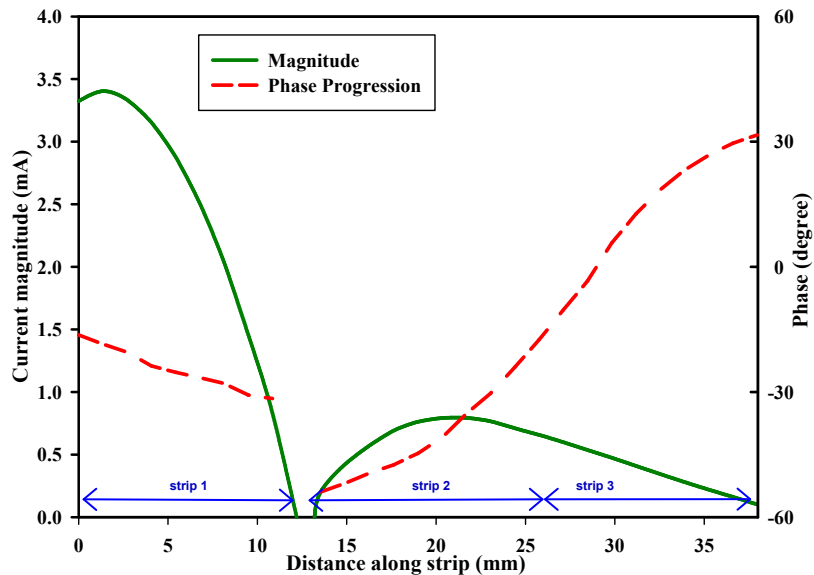
Figure 5.6: Current distribution along the feeding strips at 3.24 GHz

The variation of the bore-sight axial ratio as a function of frequency has been computed and measured as shown in Figure 5.7, where it can be noticed that the minimum computed AR value is 1.6 dB at 3.24 GHz, which is close to the corresponding measured value of 1.3 dB at 3.26 GHz. From these results it can be seen that the theoretical 3dB AR bandwidth extends from 3.14-3.35 GHz compared to 3.14-3.39 GHz in the measurements. As a result, a CP radiation has been achieved over bandwidths of 6.50% and 7.75% in the analysis and measurements, respectively, which is comparable to that obtained using the spiral excitation as discussed in section 3.2.2. Furthermore, with reference to Figure 5.8, it can be observed that a sufficient impedance matching bandwidth has been obtained throughout the whole frequency band of the achieved circular polarization.
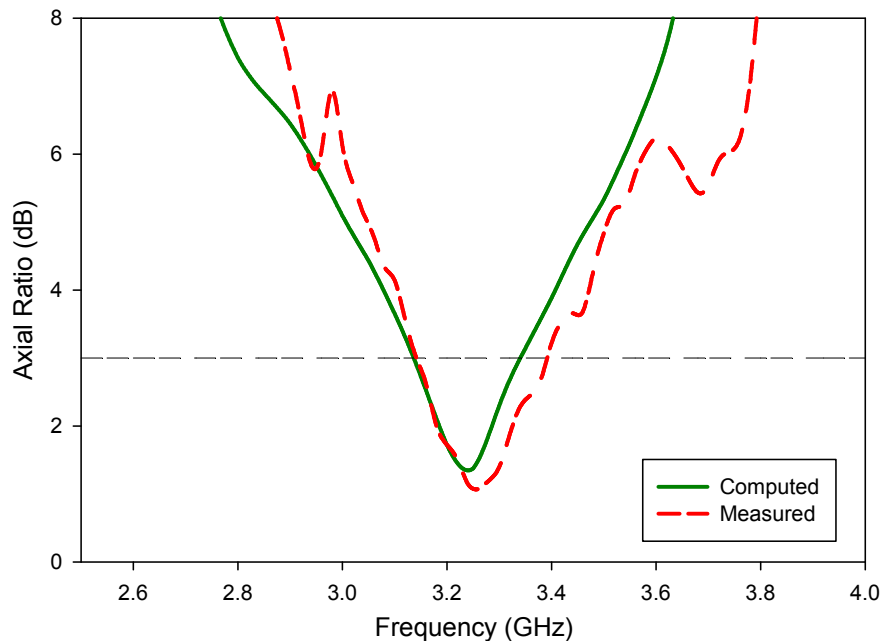
Figure 5.7: Axial ratio of a rectangular DRA fed by half-loop strip
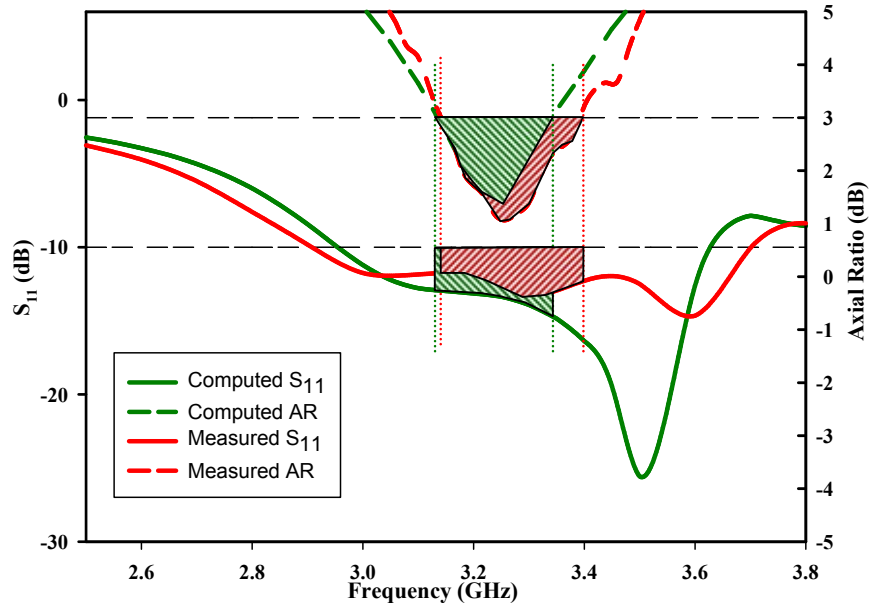
Figure 5.8: Region of overlapping bandwidths for S_{11} and AR

The theoretical and experimental variations of the axial ratio with the elevation angle are demonstrated in Figures 5.9 and 5.10, which show that the rectangular DRA offers CP radiation over a useful beam-widths of over $98°$ in both $\phi = 0°$ and $\phi = 90°$ planes at the minimum AR frequency.
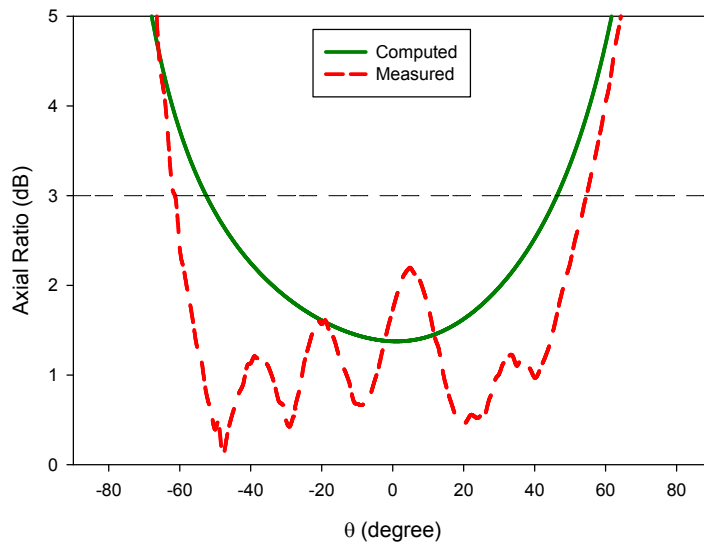
Figure 5.9: Axial ratio beam-width of the rectangular DRA at $\phi = 0°$
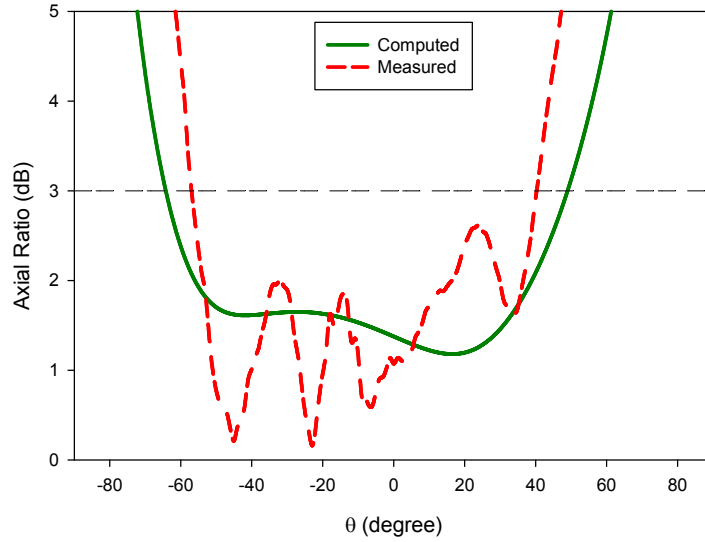
Figure 5.10: Axial ratio beam-width of the rectangular DRA at $\phi = 90°$

Figure 5.11 presents the calculated and measured bore-sight gain of the rectangular DRA fed by an open half-loop antenna, where it can be noticed that a useful gain of over 4dBi has been achieved throughout the obtained circular polarization bandwidth.
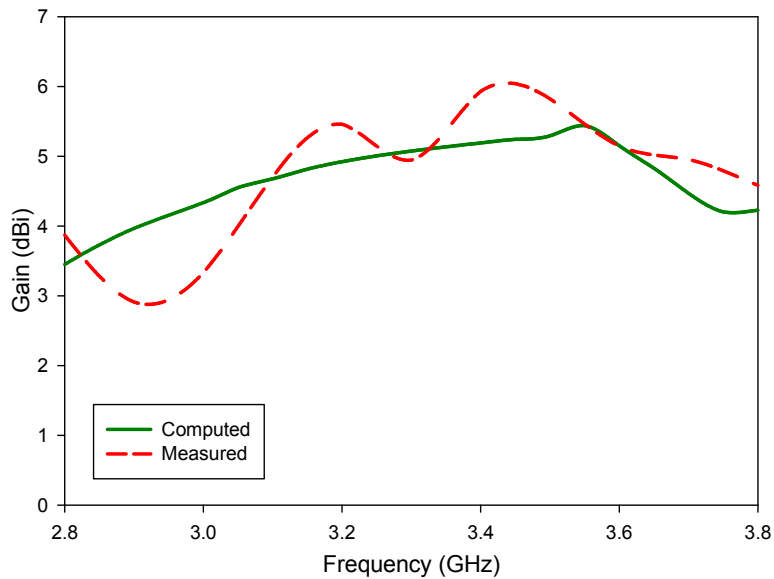
Figure 5.11: Gain of the rectangular DRA

Additionally, the computed and measured radiation patterns are presented in Figure 5.12, where it can be seen that good agreement has been achieved between the two sets of results. The radiation patterns are stable throughout the CP frequency band. With reference to Figure 5.12(b), which shows the radiation pattern taken at minimum AR frequency, an isolation of more than 20 dB has been achieved between the co-, and cross-, polarization components. It is evident from these results that this is a right-hand CP DRA, as RHCP is the stronger field.
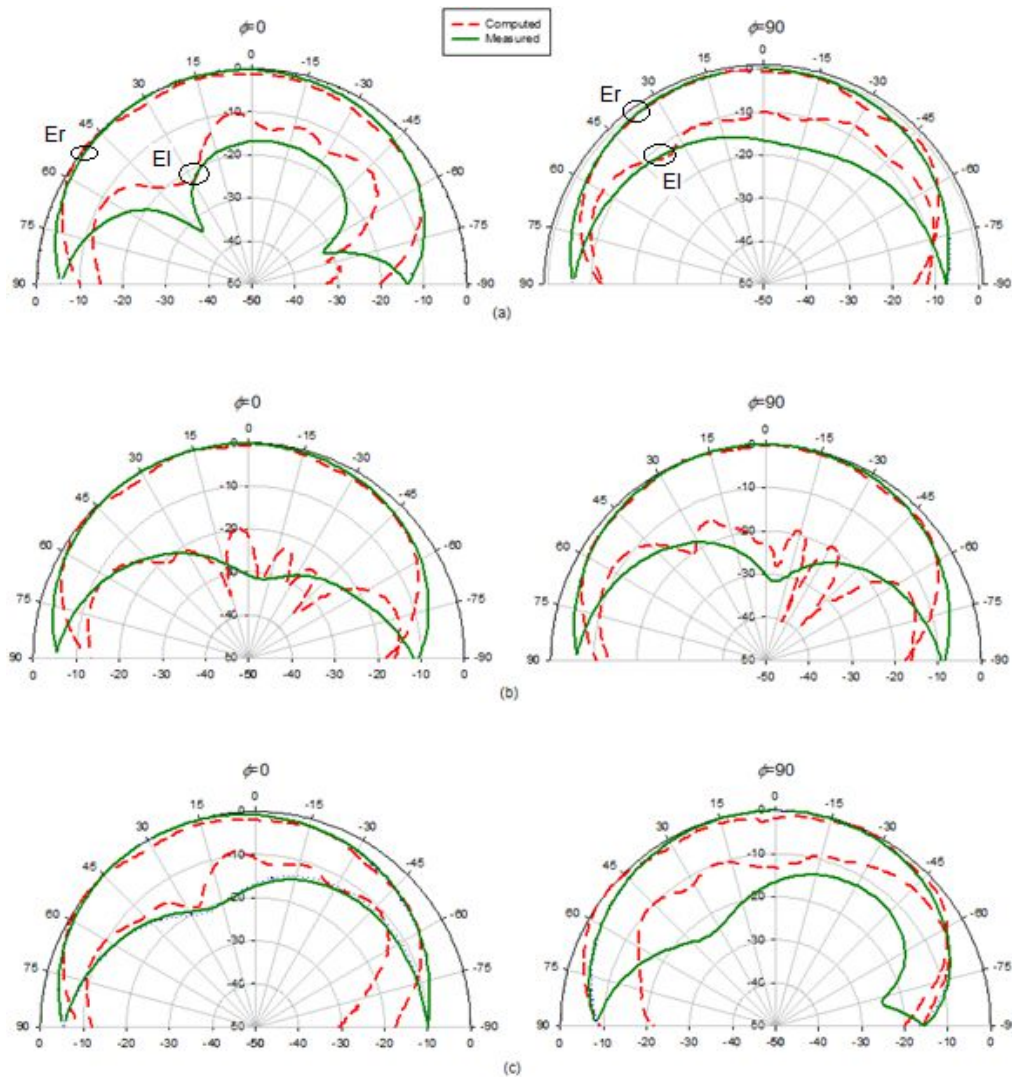
Figure 5.12: Radiation pattern of the rectangular DRA at (a) starting, (b) minimum, and (c) ending of AR frequencies

5.3   Circularly Polarized Cylindrical DRA

5.3.1   Antenna's Configuration

The versatility of the rectangular half-loop feeding method is demonstrated next, by employing such an excitation scheme onto the single layer cylindrical DRA used previously in section 4.2, as illustrated in Figure 5.13. The DRA has a radius of a, a height of h and a dielectric constant of ε_r, whilst the feeding structure has a width of w_d, a height of h_d, and a gap size of g_d located at a gap position of $\vec{g}_p$ within the metallic strips.
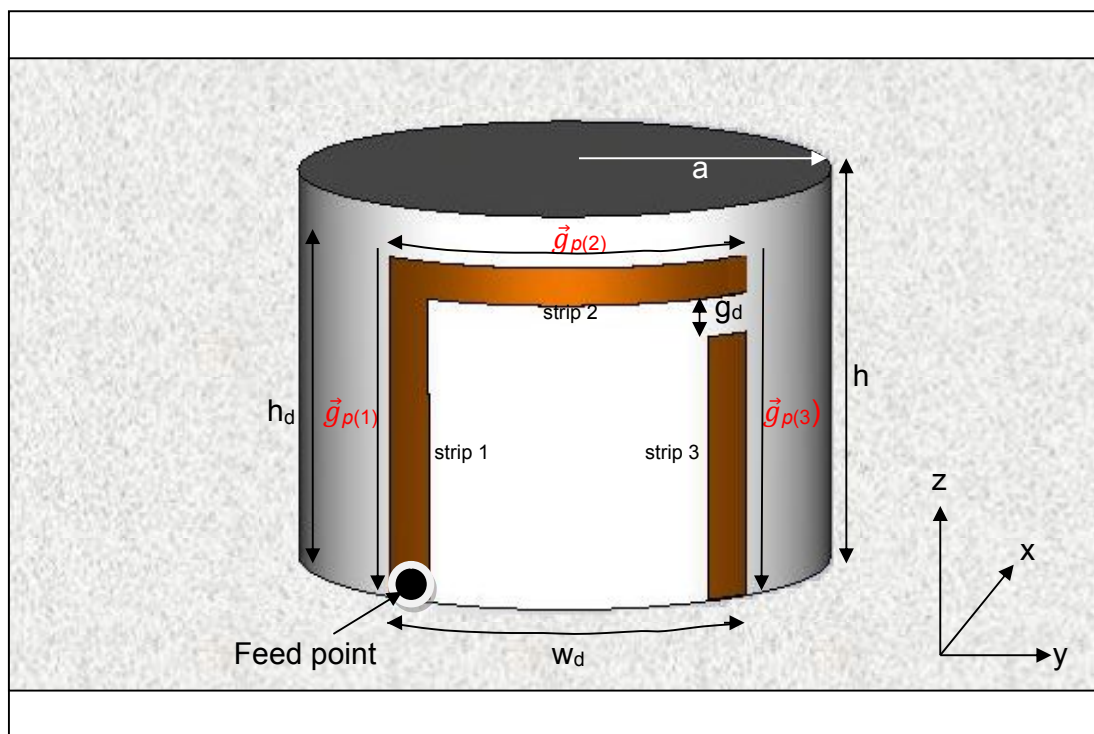
Figure 5.13: Configuration of a cylindrical DRA

excited by an open half-loop antenna

The antenna configuration has been simulated using the method of moments, where the cylindrical dielectric has been meshed to 2470 tetrahedrons and the metallic strips to 59 triangular patches, giving a total of 5323 unknowns. The optimum dimensions of the feeding metallic strips that are required to establish a travelling-wave current distribution along the half-loop, as well as exciting a DRA mode within the same frequency range, have been determined after employing an iterative design procedure.

In order to assess the performance of the cylindrical DRA fed by an open half-loop design, the parameters of the cylindrical dielectric have been chosen similar to those used in Chapter 4, that is h = 10.54 mm, a = 7.01 mm and ε_r = 9.2 [10]. Initially, in order to obtain the optimized gap position, $\vec{g}_p$, the half-loop dimensions were fixed to h_d = 10.54, w_d = 10 mm and g_d = 1 mm. The simulation results of the actual and effective AR bandwidths are shown in Figure 5.14 when the gap is placed at any of the three copper strips. Again, due to the convention used for the gap position, $\vec{g}_{p(1)}$ = 0 mm is essentially the same as $\vec{g}_{p(2)}$ = 0 mm. This also applies to $\vec{g}_{p(2)}$ = 9 mm and $\vec{g}_{p(3)}$ = 0 mm. Based on the results from Figure 5.14, it can be observed that the highest effective AR bandwidth of 3.01% was obtained when the gap is located within strip 3 at $\vec{g}_{p(3)}$ = 1 mm. This effectively means the optimum $\vec{g}_p$ is located between the last two metallic strips as shown in Figure 5.13. The minimum S_{11} obtained using this feeding structure configuration has been computed at a frequency of 5.8 GHz.
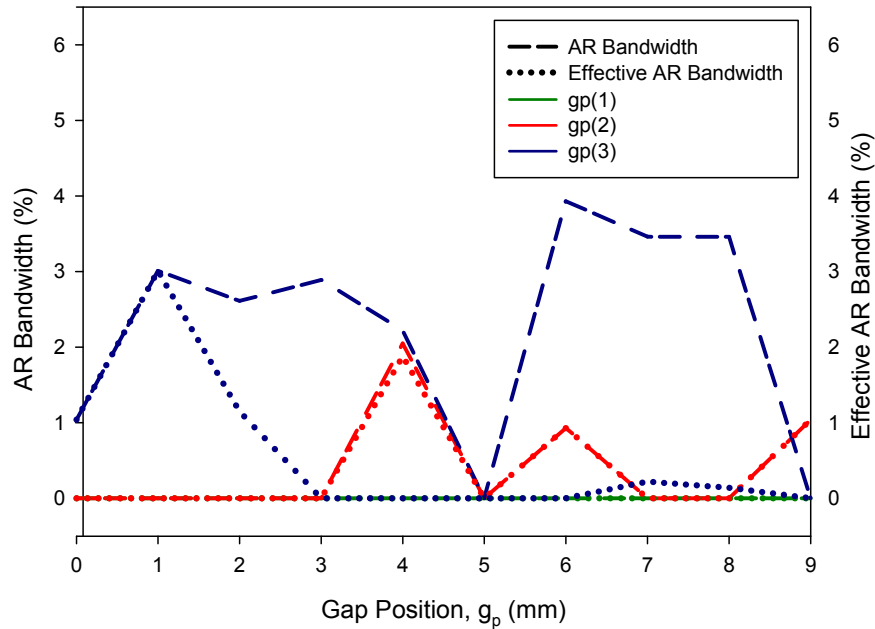
Figure 5.14: Actual and Effective AR bandwidths as functions of the gap position

The results obtained from the optimization process for parameters h_d and w_d, using optimized $\vec{g}_p$ and g_d = 1 mm, are shown in Table 5.4, where the change in the AR bandwidth remains relatively stable in contrast to the fluctuation in the S_{11} bandwidth when the half-loop width is varied within a range of $8 \leq w_d \leq 10$ mm for a given height value in the range of $7.54 \leq h_d \leq 10.54$ mm. Based on these results, h_d and w_d have been adjusted to attain optimum respective values of 10.54 mm, and 10 mm that provide maximum AR and impedance matching bandwidths. Consequently, the results for different value of g_d are shown in Table 5.5, when the optimized parameters of h_d, w_d and $\vec{g}_p$ are employed. With reference to the table, an optimum value of g_d is 2 mm has been chosen as it proved an AR bandwidth of 3.63%. The minimum S_{11} obtained using this feeding structure configuration has been computed at a frequency of 3.77 GHz.

Height, h_d (mm)	Width, w_d (mm)	3db AR Bandwidth (%)	-10dB S11 Bandwidth (%)	Overlapping AR & S11 Bandwidth (%)
7.54	7	0	7.71	0
	8	1.29	11.81	71
	9	1.46	7.71	100
	10	1.96	12.6	100
8.54	7	0	8.96	0
	8	1.81	14.27	87
	9	2.11	17.62	100
	10	2.47	21.98	100
9.54	7	0	12.04	0
	8	2.77	16.13	100
	9	3.05	21.21	100
	10	2.87	20.63	100
10.54	7	0	14.32	0
	8	2.36	21.18	100
	9	**3.15**	**22.71**	**100**
	10	3.01	20.41	100

Table 5.4: AR and S11 bandwidths for different dimensions of the half-loop feed

Gap size, g_d (mm)	3db AR Bandwidth (%)	-10dB S11 Bandwidth (%)	Overlapping AR & S11 Bandwidth (%)
0.25	2.53	21.61	100
0.50	2.79	21.99	100
0.75	2.97	22.18	100
1.00	3.15	22.71	100
1.25	3.32	22.97	100
1.50	3.44	23.20	100
1.75	3.61	23.40	100
2.00	**3.63**	**22.23**	**100**
2.25	3.63	23.81	100
2.50	3.43	23.91	100
2.75	3.08	23.84	100
3.00	2.29	23.98	100

Table 5.5: AR and S11 bandwidths for different gap sizes

5.3.2   Results and Discussions

Figure 5.15 presents the prototype of a cylindrical DRA that is excited using open half-loop. Based on Table 5.4 and Table 5.5, the optimized dimensions of open half-loop metal strips are found to be h_d = 10.54 mm, w_d = 9 mm and $g_{d =}$ 2 mm.
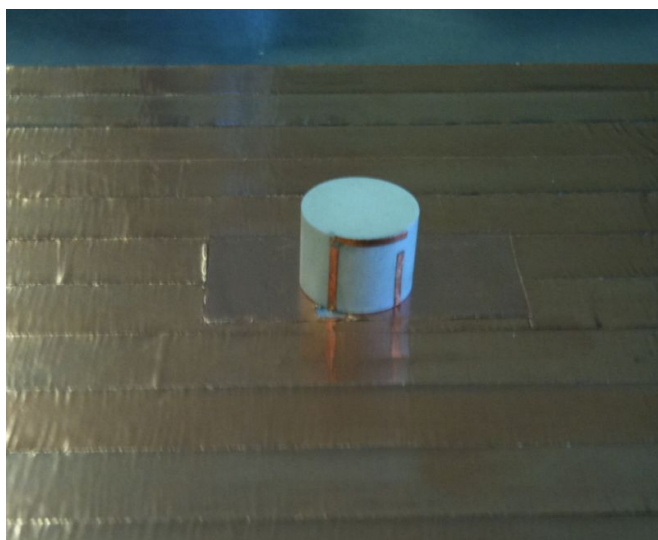
Figure 5.15: A cylindrical DRA excited by an open half-loop antenna

Good agreement has been obtained between the computed and measured input impedance and return losses as shown in Figures 5.16 and 5.17, respectively, with slight discrepancy owing to employing a finite ground plane and experimental tolerance. Additionally, the light weight of this DRA made it difficult to totally eliminate the potential air gaps. From Figure 5.17, the return losses bandwidth has been computed to be 22.2%, which is slightly higher than 20.55% in the measurements. There is a marginal difference of 1.55% between the two sets of results as the minimum S_{11} has been computed 5.76 GHz compared to 5.85 GHz in the measurements. Consequently, the results agree well with the predicted resonance frequency of 5.61 GHz for the $TE_{01\delta}$ mode calculated using

DWM method, in which the DRA is excited. The distribution of fields across the

cylindrical DRA operating in this mode has been presented in Figure 4.5.
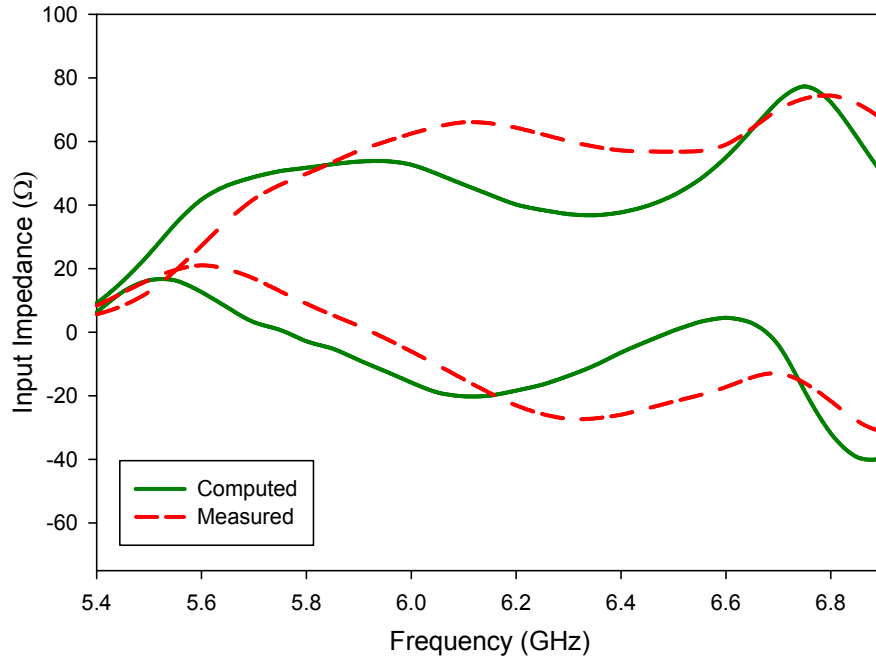
Figure 5.16: Input impedance of the cylindrical DRA
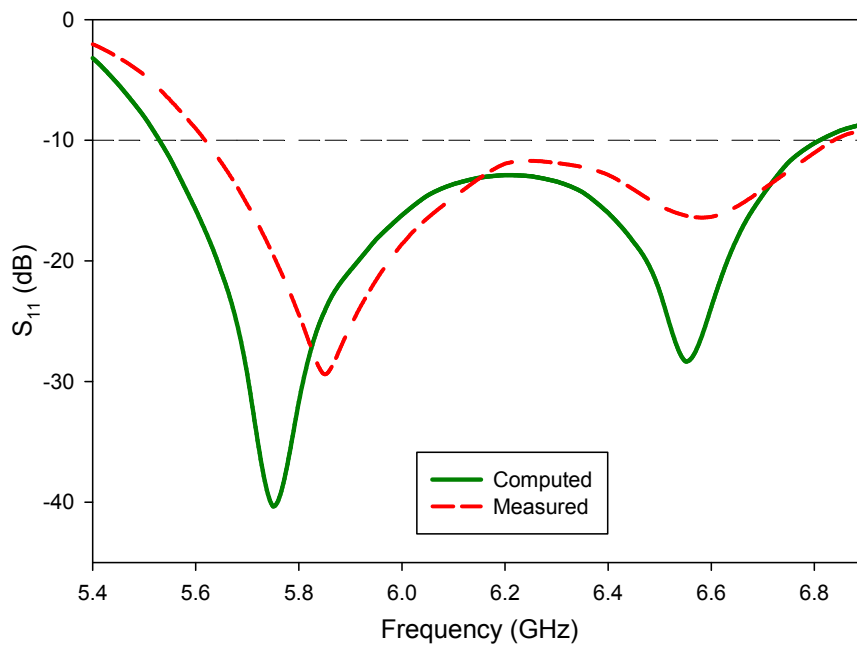
Figure 5.17: Return losses of the cylindrical DRA
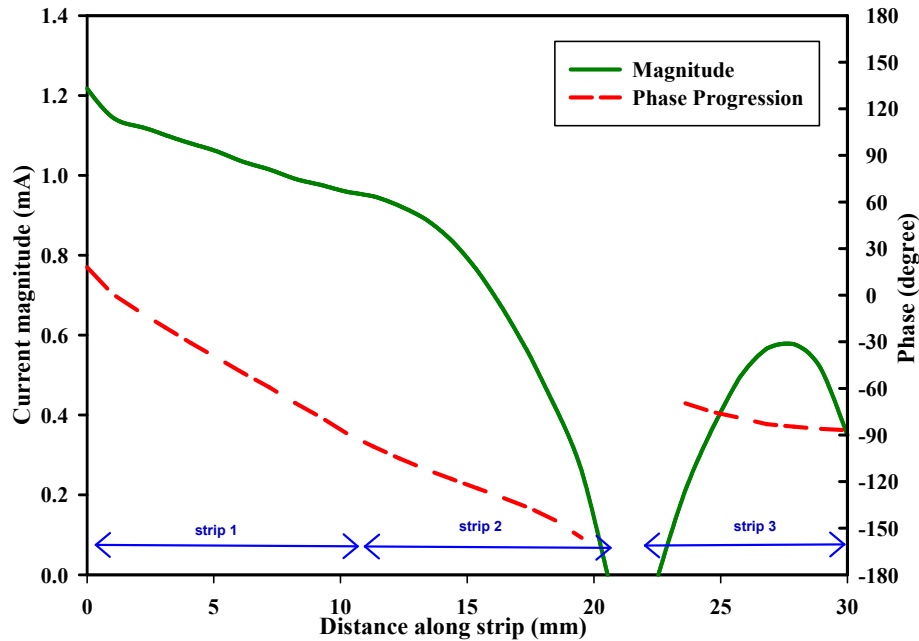
Figure 5.18: Current distribution along the half-loop strip at 5.85 GHz.

Additionally, a travelling-wave current distribution has been obtained along the half-loop at the frequency band of operation as shown in Figure 5.18. The half-loop has perimeter of ~1.19λ_g at 5.85 GHz. The antenna exhibits strong CP radiation as the loop's one-wavelength circumference supports the first-mode of radiation. Figure 5.19 shows the computed and measured axial at the bore-sight direction, where it can be seen that the minimum computed AR value is 1.23 dB at 5.85 GHz, compared to the corresponding measured value of 1.25 dB at 5.94 GHz. From these results it can be observed that the achieved 3 dB AR bandwidths are 3.63% and 4.14% in the analysis and measurements, respectively, which is comparable to the results obtained by the cylindrical DRA of similar dimensions using the spiral excitation albeit with a simpler feeding method. Furthermore, based on Figure 5.20, it can be seen that a sufficient impedance matching

bandwidth has been attained throughout the achieved circular polarization bandwidth.
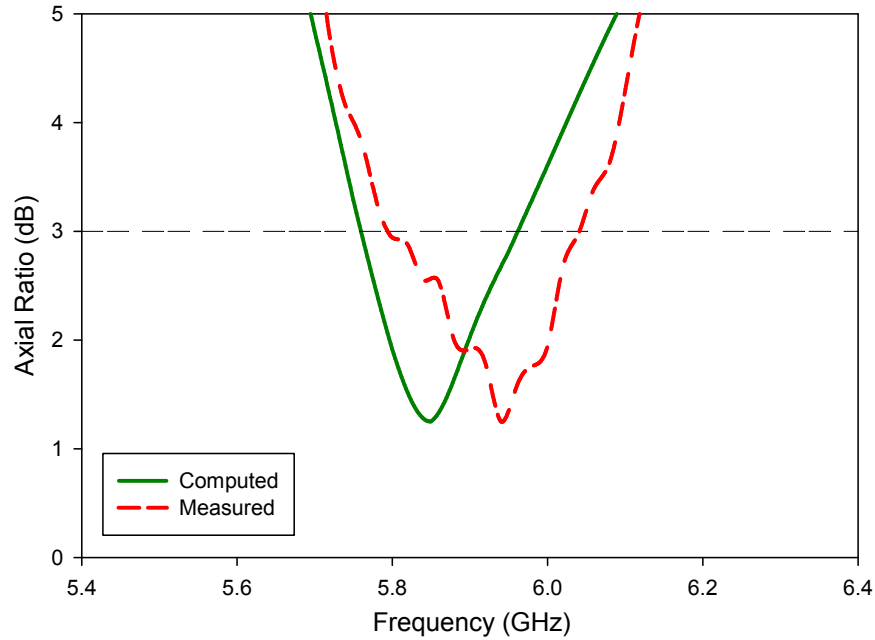
Figure 5.19: Axial ratio of the cylindrical DRA fed by a open half-loop strips.
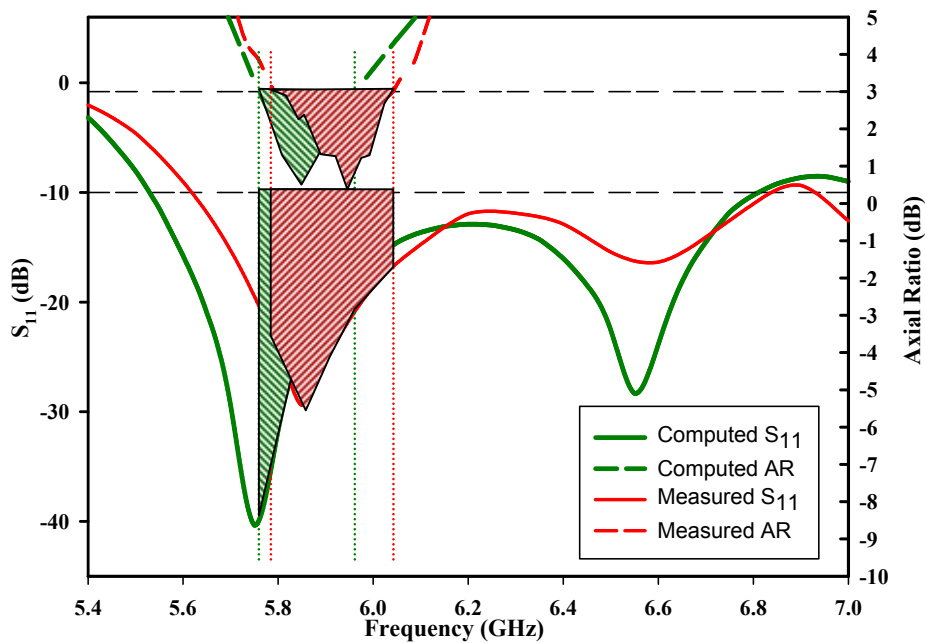
Figure 5.20: Region of overlapping bandwidths for S_{11} and AR

The axial ratio beam-width is shown in Figures 5.21 and 5.22. With reference to the computational result, the DRA offers circular polarization over a measured beam-widths of $63°$ and $40°$ in the $\phi = 0°$ and $\phi = 90°$ plane, respectively. As expected, the beam-width in the 0º plane is wider than that in the 90º plane because the height of the rectangular loop is longer than its width [11].
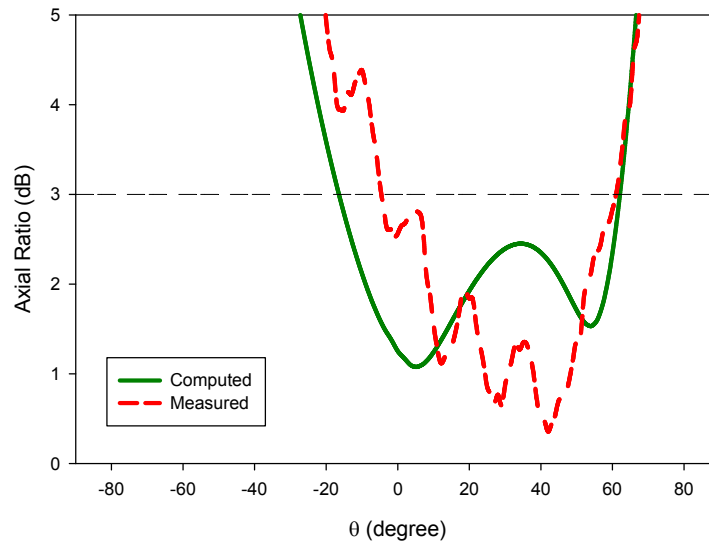
Figure 5.21: Axial ratio beam-width of the cylindrical DRA at $\phi = 0°$
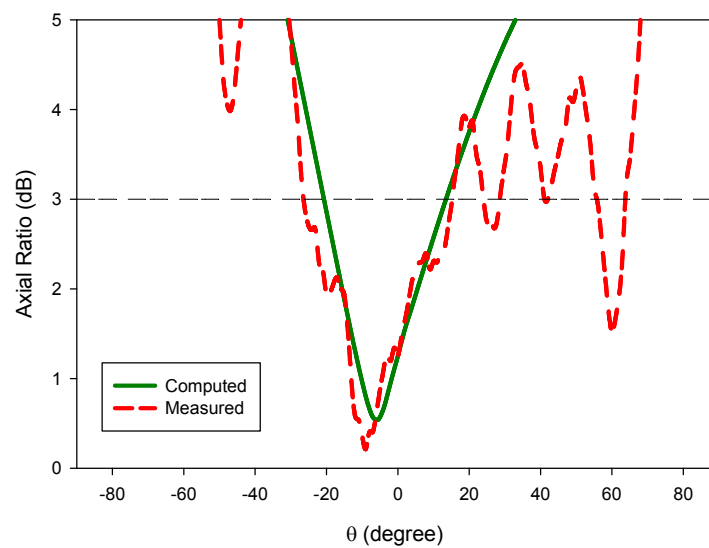
Figure 5.22: Axial ratio beam-width of the cylindrical DRA at $\phi = 90°$

Additionally, the gain of the cylindrical DRA has been measured at bore-sight. The results are shown in Figure 5.23, where it can be observed that the antenna offers a satisfactory gain of more than 4dBi across the frequency range in which a CP wave is radiated. Comparisons between the calculated and measured radiation patterns across the AR frequencies are shown in Figure 5.24 with reasonable agreement, where it can be noticed that the patterns are stable throughout the whole frequency range of the achieved circular polarization. With reference to Figure 5.24 (b), it is evident that this is a right-hand CP DRA, in which the RHCP field is stronger than the LHCP field by more than 18 dB and 22 dB in the bore-sight direction in the $\phi = 0°$ and $\phi = 90°$ plane, respectively.
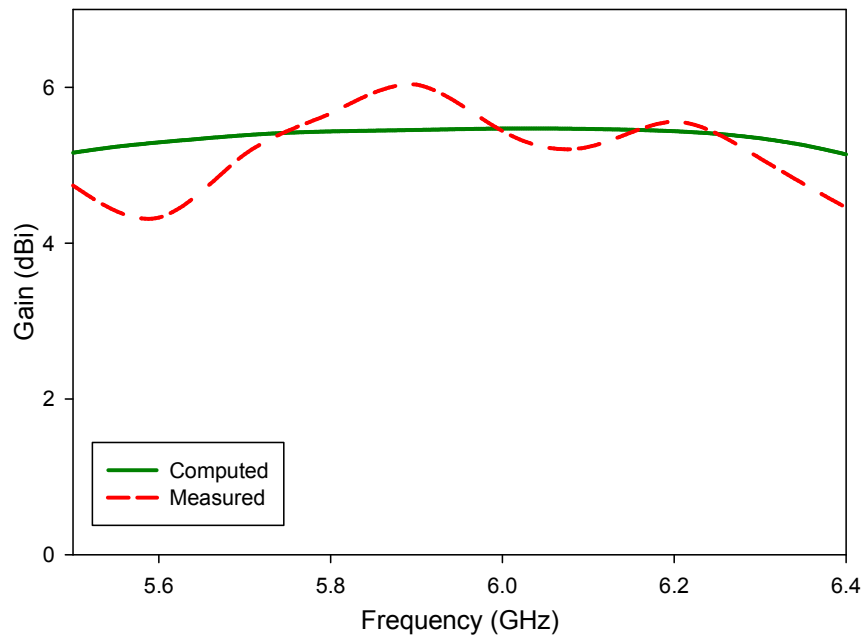
Figure 5.23: Gain of a cylindrical DRA fed by an open half-loop.
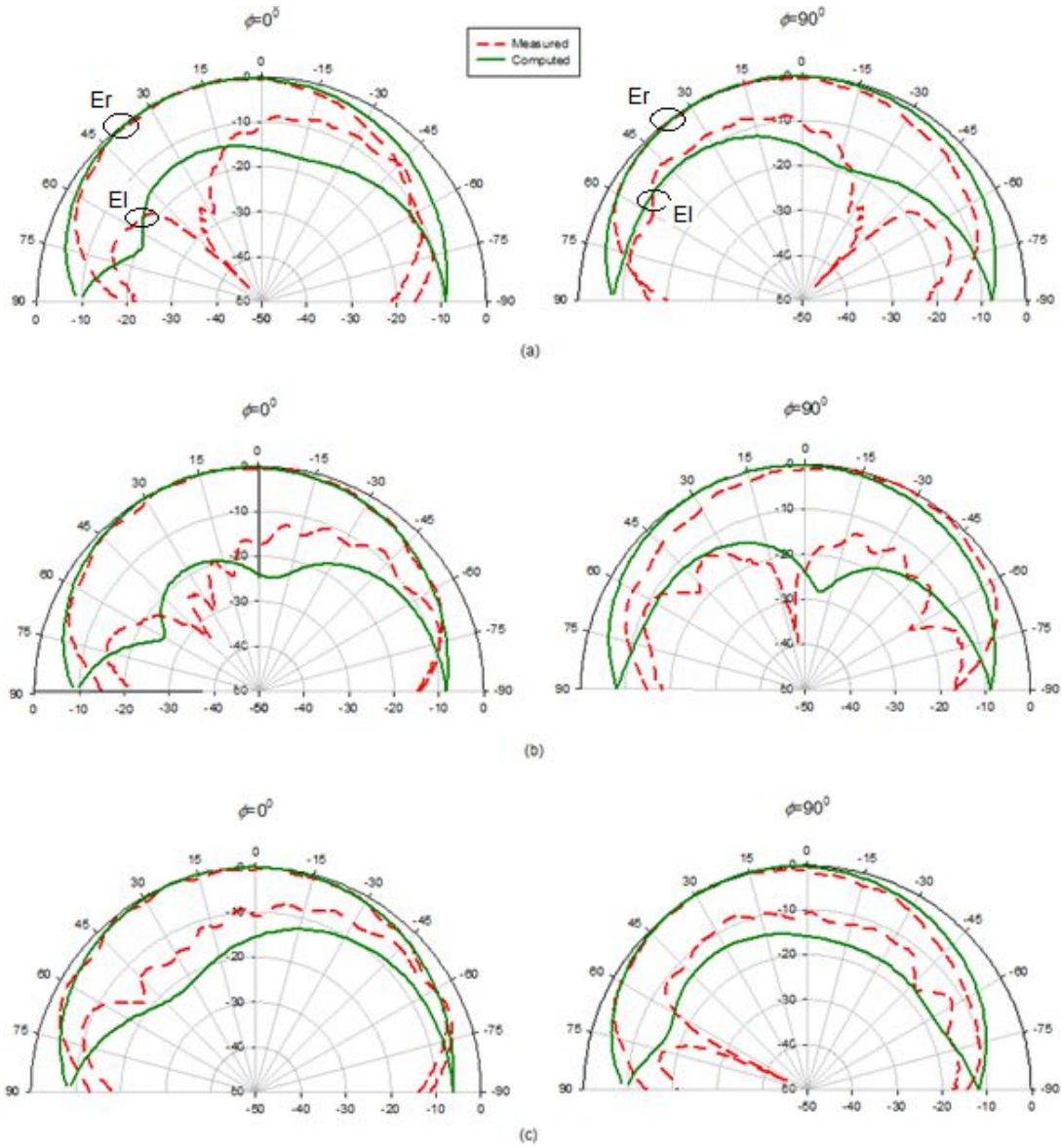
Figure 5.24: Radiation pattern of the cylindrical DRA at

(a) starting, (b) minimum, and (c) ending of AR frequencies

The performances of the rectangular and cylindrical DRAs fed using the excitation schemes proposed in this research are summarized in Tables 5.6 and 5.7. For comparison purposes, the results from published literature are included in the reference column. From the tables, it is evident that the DRAs excited using the new feeding methods have produced considerably wider CP bandwidths compared to those reported in the literature for identical singly-fed DRAs. The discrepancy in the S_{11} bandwidth achieved using square spiral and open half-loop excitation can be attributed to the relative strength of power coupled between the feed and the DRA, which is highly dependent on the location and type of feed [12]. Also, it should be noted that the DWM method is an approximate technique. The resonance frequency computed using a more rigorous method such as MoM usually lies within 10% [7] from those predicted by the simple DWM method, owing to several factors such as coupling efficiency and load of feed.

	-10dB S11 Bandwidth (%)	3dB AR Bandwidth (%)	Resonance Frequency (GHz)	Excited Mode & Frequency predicted using DWM method
Reference [6]	**14**	**2.7**	**3.55**	
Square spiral	8.5	6.6	4.1	**$TE^{y}_{1\delta1}$ (3.80 GHz)**
Rectangular open half-loop	18.7	6.5	3.5	

Table 5.6: Performance for various rectangular DRA configurations

	-10dB S11 Bandwidth	3dB AR Bandwidth	Resonance Frequency (GHz)	Excited Mode & Frequency predicted using DWM method
Reference [10]	**22**	**2.2**	**6.38**	
Square spiral	15.7	3.48	5.89	**$TE_{01\delta}$(5.61 GHz)**
Rectangular open half-loop	22.23	3.63	5.76	

Table 5.7: Performance for various cylindrical DRA configurations

5.4   Circularly Polarized Hemispherical DRA

The versatility of this excitation scheme is demonstrated further by employing the conformal rectangular half-loop metal feed onto a hemispherical DRA. Since this is the first time such geometry is used in this research, it would be appropriate to briefly discuss the characteristics of a hemispherical DRA.

5.4.1   Degree of Freedom and Resonant Modes

In comparison with other regular DRA shapes, such as rectangular and cylindrical, hemispherical offers the least flexibility in choosing the design parameters. The hemispherical DRA has zero degree of freedom since both the resonance frequency and the radiation Q-factor are exclusively dependent on the radius, as well as the DRA permittivity. Furthermore, the fabrication of a hemispherical DRA is relatively difficult and more expensive than other regular DRA geometries. However, interest in hemispherical DRA remains strong since this is the only shape for which an exact analytical solution to describe the various field mode configurations is possible.

A hemispherical DRA is able to support TM and TE modes. The modes in each category are classified as TM_{mnr} and TE_{mnr}. The mode indices denote the variation of the fields in the elevation (m), azimuth (n) and radial directions (r), respectively. The lowest order and most common mode of the hemispherical DRA is TE_{111} mode. The far field radiation pattern emanates from DRA in this mode is similar to those radiated from a short horizontal magnetic dipole. For the TE_{111} mode of a hemispherical DRA, the resonance frequency can be calculated by solving the characteristics equation given in [13]:

$$\frac{J_{1/2}\left(\sqrt{\varepsilon_r}\,k_0 a\right)}{J_{3/2}\left(\sqrt{\varepsilon_r}\,k_0 a\right)} = \frac{H^{(2)}_{1/2}(k_0 a)}{\sqrt{\varepsilon_r}\,H^{(2)}_{1/2}(k_0 a)} \tag{5-1}$$

where k_o is a complex number that denotes the free space wavenumber, $J_{(x)}$ is the first order Bessel function and $H^{(2)}_{(x)}$ is the second order Henkel function. Once the solution of k_o, has been obtained, the resonance frequency, f_0 can be determined using the following expression [14].

$$f_0 = \frac{4.7713\,\mathrm{Re}(k_0 a)}{a} \tag{5-2}$$

where *a* denotes the radius of the hemisphere in cm, and f_0 is expressed in GHz.

5.4.2 Antenna Configuration
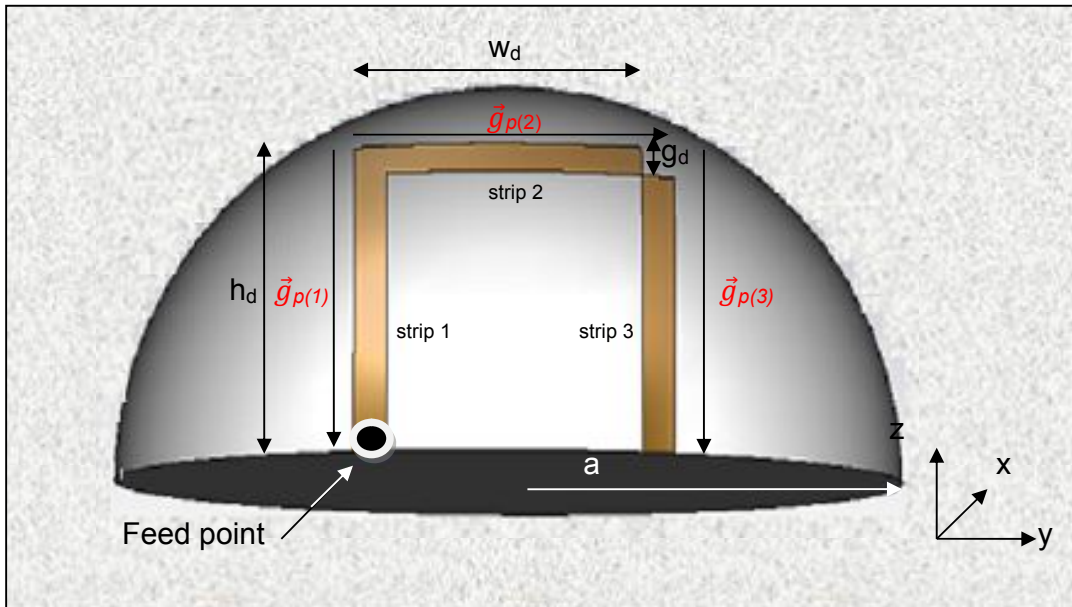
Figure 5.25: Configuration of a hemispherical DRA

excited by a rectangular half-loop antenna

The geometry of a single layer hemispherical DRA that has been excited using a half-loop antenna is presented in Figure 5.25, where the DRA has a radius of *a,* and a dielectric constant of ε_r. The feeding half-loop has a width of w_d, a height of h_d and a gap size of g_d that is placed at a distance of $\vec{g}_p$ from the beginning of a strip. The antenna configuration has been modeled using the method of moments together with the combined RWG and SWG basis functions, where the hemispherical dielectric has been meshed to 2352 tetrahedrons and the metallic strips to 74 triangular patches, giving a total of 5124 unknowns.

The parameters of the hemispherical dielectric are similar to those used in [15], that is, *a* = 12.55 mm and ε_r = 9.5. An iterative design procedure has been applied to determine the optimum dimensions of the feeding metallic strips that are required to attain a travelling-wave current distribution. For the initial simulations to determine the gap position, $\vec{g}_p$, the half-loop dimensions have been fixed to h_d = w_d = 10 mm with a gap width of g_d = 1 mm. Figure 5.26 shows the actual and effective AR bandwidths as functions of $\vec{g}_p$ when the gap was placed within each individual strip. It can be noticed from these results that the highest effective AR bandwidth of 2.22% has been obtained when the gap was placed within strip 3 at $\vec{g}_{p(3)}$ = 0 mm (essentially the same as when the gap was placed within strip 2 at $\vec{g}_{p(2)}$ = 9 mm). This effectively means the optimum $\vec{g}_p$ is located between the last two metallic strips as illustrated in Figure 5.25. The minimum S_{11} obtained using this feeding structure configuration has been computed at a frequency of 5.66 GHz.
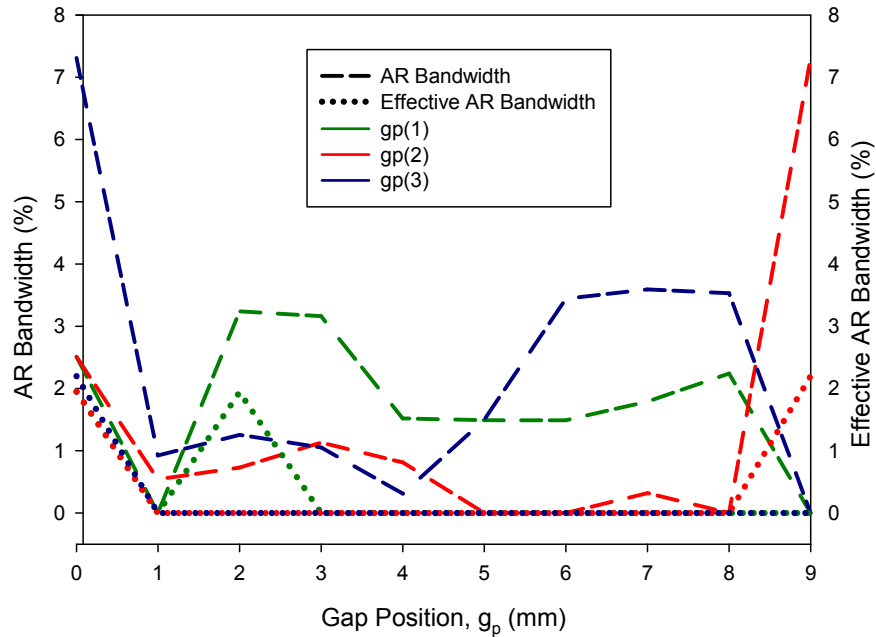
Figure 5.26: AR bandwidth and Effective AR bandwidth as a function of gap

position, for gap placed within strip 1, strip 2 and strip 3

Table 5.8 presents the AR and impedance matching bandwidths as well as

the percentage overlapping bandwidth for various values of h_d, and w_d when g_d =

1 mm and the optimized $\vec{g}_p$ has been employed. The optimization process has

shown that the CP radiation is achieved for various dimensions of the half-loop,

which is a desired feature in the DRA design. With reference to the results of

these simulations, the optimized parameters which yield maximum effective AR

bandwidth (i.e. 2.22%) are given by h_d = w_d = 10 mm. Additionally, the results for

different values of g_d are shown in Table 5.9, after these optimized parameters of

h_d, w_d and $\vec{g}_p$ have been applied.

Height, h_d	Width, w_d	3db AR Bandwidth (%)	-10dB S11 Bandwidth (%)	Overlapping AR & S11 Bandwidth (%)
9	9	0	5.90	0
	10	5.45	6.80	0
	11	6.86	12.02	18
	12	6.94	7.91	15
10	9	0	6.14	0
	10	**7.31**	**8.31**	**30**
	11	6.98	6.02	32
	12	5.47	13.76	17
11	9	3.43	9.50	48
	10	7.52	4.26	18
	11	6.36	5.52	20
	12	5.10	6.78	25
12	9	2.99	5.15	56
	10	6.21	13.91	12
	11	5.34	4.01	0
	12	4.28	7.58	0

Table 5.8: AR and S11 bandwidths for different dimensions of the half-loop feed

Gap size, g_d	3db AR Bandwidth (%)	-10dB S11 Bandwidth (%)	Overlapping AR & S11 Bandwidth (%)
0.5	4.31	8.43	38
1.0	**7.31**	**8.31**	**30**
1.5	3.63	8.23	18
2.0	0	8.11	0
2.5	0	8.12	0
3.0	0	8.12	0

Table 5.9: AR and S11 bandwidths for different gap sizes

Although several simulations have been conducted to determine the optimized parameters of the half-loop, the achieved effective AR bandwidth of 2.22% is relatively smaller than what has been achieved in earlier studies for a singly-fed CP hemispherical DRA discussed in section 1.3.2.2. As can be observed from Table 5.8, the overlapping AR and S_{11} bandwidth can be increased if a wider impedance matching bandwidth is obtained or if the S_{11} bandwidth is

shifted closer AR frequency band. This can be achieved by incorporating an integrated stub to the feeding structure so that input impedance matching can be adjusted as desired [16]. The stub's length l_s, width w_s, and position p_s play an important role towards achieving a perfectly matched system. Figure 5.27 shows the geometry of a hemispherical DRA that has been excited using an open half-loop antenna with a stub matching connected along strip 1.
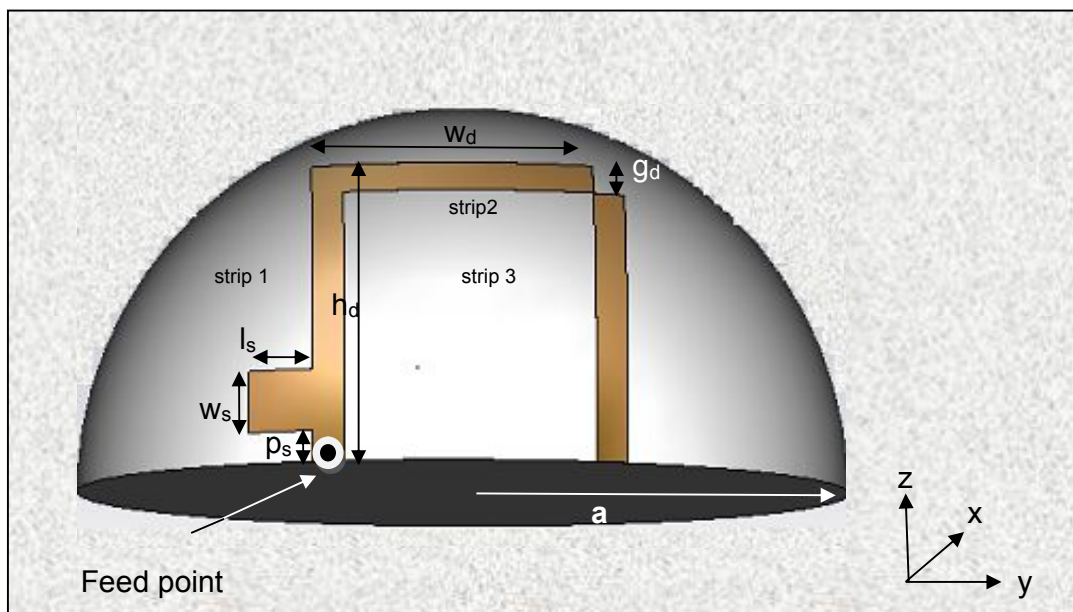
Figure 5.27: Configuration of a hemispherical DRA

excited by a rectangular half-loop antenna with a matching stub.

Table 5.10 shows the results for the optimization of p_s and l_s when $h_d = w_d =$ 10 mm, $\vec{g}_p$ = 0 mm, g_d = 1 mm and w_s is fixed at 1 m. Subsequently, once the optimized parameters of p_s and l_s have been applied, the stub width, w_s, can also be adjusted as shown in Table 5.11. From these tables, the optimized parameters of the stub are p_s = 4 mm, l_s = 2 mm and w_s =2.5 mm. The minimum S_{11} obtained using this configuration has been computed at a frequency of 5.66 GHz.

Stub position, p_s (mm)	Stub length, l_s (mm)	3db AR Bandwidth (%)	-10dB S11 Bandwidth (%)	Overlapping AR & S11 Bandwidth (%)
1	1	6.19	5.77	87
	2	4.52	4.7	93
2	1	5.8	5.96	97
	2	3.56	5.53	100
3	1	5.75	6.69	100
	2	5.85	6.29	100
4	1	6.40	7.48	100
	2	**6.69**	**8.08**	**100**
5	1	6.58	7.66	100
	2	6.31	8.14	100
6	1	1.86	7.49	100
	2	1.77	7.82	100
7	1	1.74	7.29	100
	2	0.91	7.08	100
8	1	2.15	6.61	100
	2	0.24	6.53	100

Table 5.10: AR and S_{11} bandwidths for different dimensions of p_s and l_s

Stub width, w_s (mm)	3db AR Bandwidth (%)	-10dB S11 Bandwidth (%)	Overlapping AR & S11 Bandwidth (%)
0.5	5.27	8.03	98
1	6.69	8.08	100
1.5	6.88	8.43	100
2	7.06	8.74	100
2.5	**7.61**	**9.36**	**100**
3	1.62	9.29	100

Table 5.11: AR and S_{11} bandwidths for different stub widths

Figure 5.28 compares the performances of the DRA when the optimized matching stub is added onto the feed. It is evident that the inclusion of the stub has negligible impact on the AR bandwidth in contrast to the drastic change in the value of return loss. This is expected since the stub produces pure reactance at the attachment point [16]. The addition of this reactance which can be either capacitive or inductive, depending on the electrical length of the stub, alters the

total reactance of the half-loop feed. Hence, the S_{11}, derived from the antenna's input impedances changes significantly. Additionally, it can be observed from the figure that the DRA has excited two modes at ~4 GHz and ~5.6 GHz. Those modes have been identified using an Eigen mode solver in CST microwave studio as TE_{111} and TE_{122}, with predicted resonance frequencies of 3.98 GHz and 5.2 GHz, respectively. The EM fields of a spherical DRA, with radius of a, operating in these modes are shown in Figures 5.27 and 5.28. As can be seen from Figure 5.29 (b) and 5.30 (b), there is a strong magnetic field presence along the DRA surface near the ground plane. Therefore, it is possible to excite both modes by attaching the half-loop to this area, as the maximum current magnitude at the feed point induces strong coupling between the feed and the DRA.
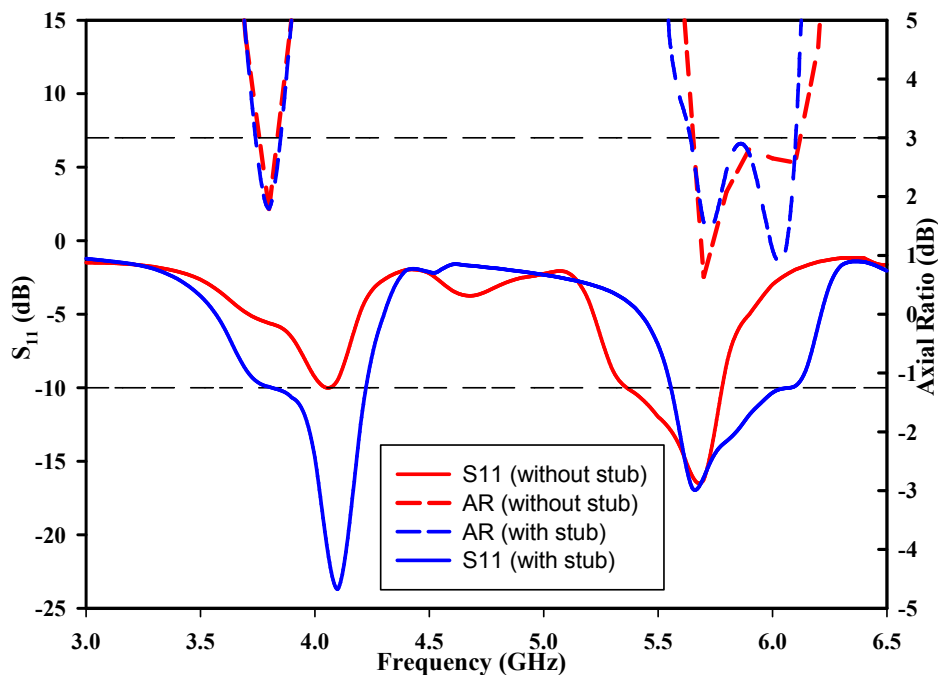
Figure 5.28: Axial ratio and return loss of DRA fed by half loop with or without stub
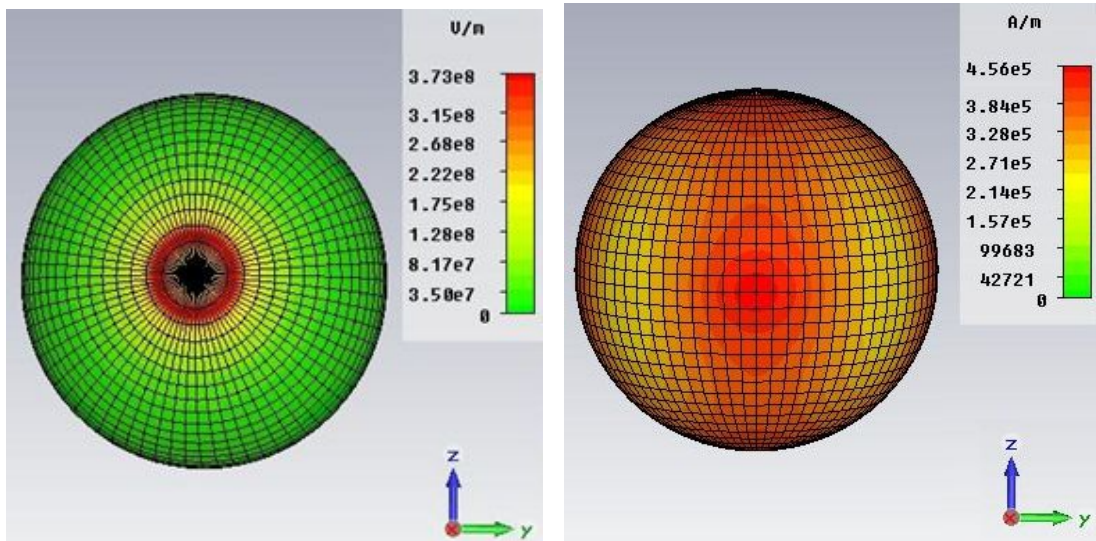
Figure 5.29: EM Fields distribution for TE$_{111}$ mode; (a) E-field and (b) H-field
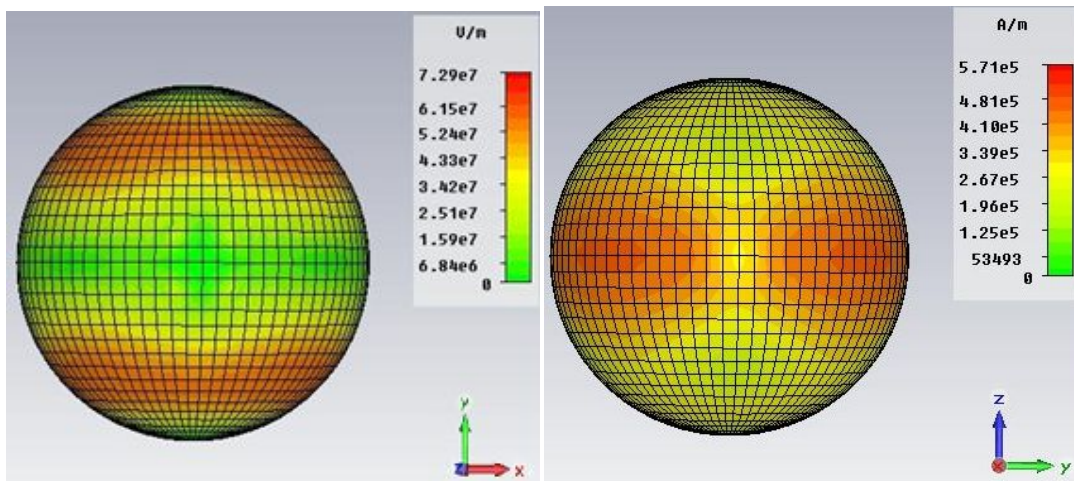
Figure 5.30: EM Fields distribution for TE$_{122}$ mode; (a) E-field and (b) H-field

Further enhancement of the wideband CP radiation can be made by employing a multilayer structure as discussed in section 4.3.1. Therefore, a hemispherical air gap has been introduced inside the existing DRA as shown in Figure 5.31. The parameters of the half-loop metal strips used in section 5.3 are retained. Several simulations have been conducted using different radii of the inner layer air gap, a_2. The AR bandwidth and its corresponding resonance

frequency versus the dimensions of inner layer air gap are presented in Figure 5.32. It should be noted the graph only shows the AR bandwidth achieved when the DRA is operating in the TE_{111} mode. As a_2 increases, the resonance frequency also increases due to the decrease in the effective permittivity as the air gap dominates the structure. Additionally, the results have been compared with Figure 2 (a) in [17], which shows the resonance frequency of an identical multilayer hemispherical DRA calculated using mode-matching method, where close agreement can be observed for the resonance frequency. The performances of the multilayer hemispherical DRA with an optimized radius of a_2 = 7 mm is illustrated in Figure 5.33. In comparison with single layer DRA, it is evident that the addition of inner layer air gap has significantly increased the AR bandwidth from 3.56% to 11.19% as well as the S_{11} bandwidth from 9.36% to 10.43%.
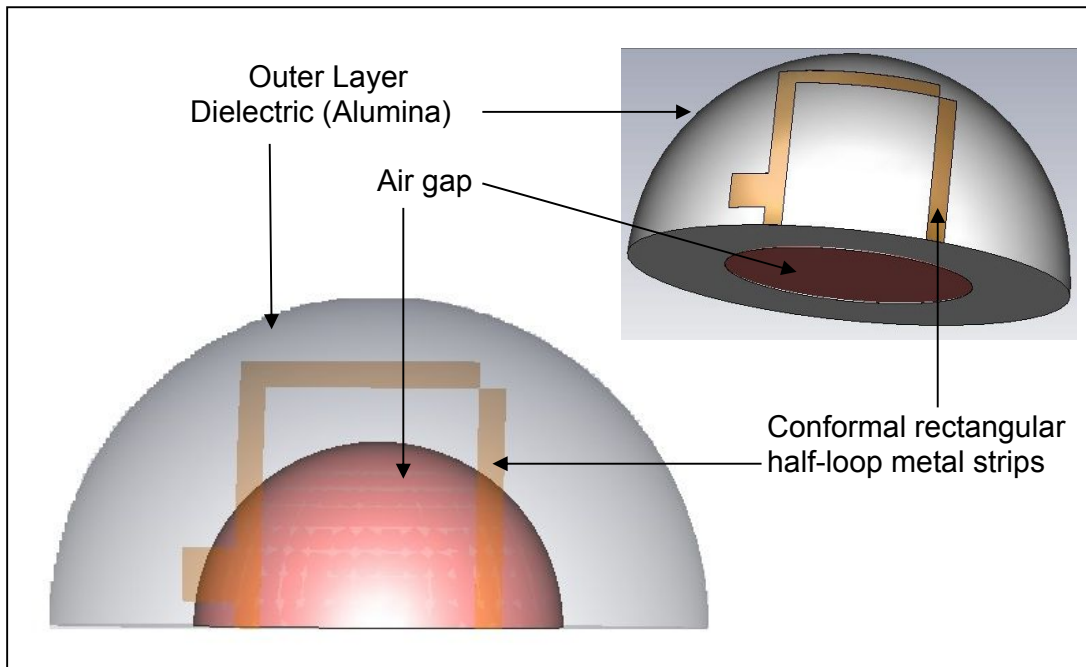
Figure 5.31: Configuration of a multilayer hemispherical DRA

(**Inset**: side-bottom view of the multilayer hemispherical DRA)
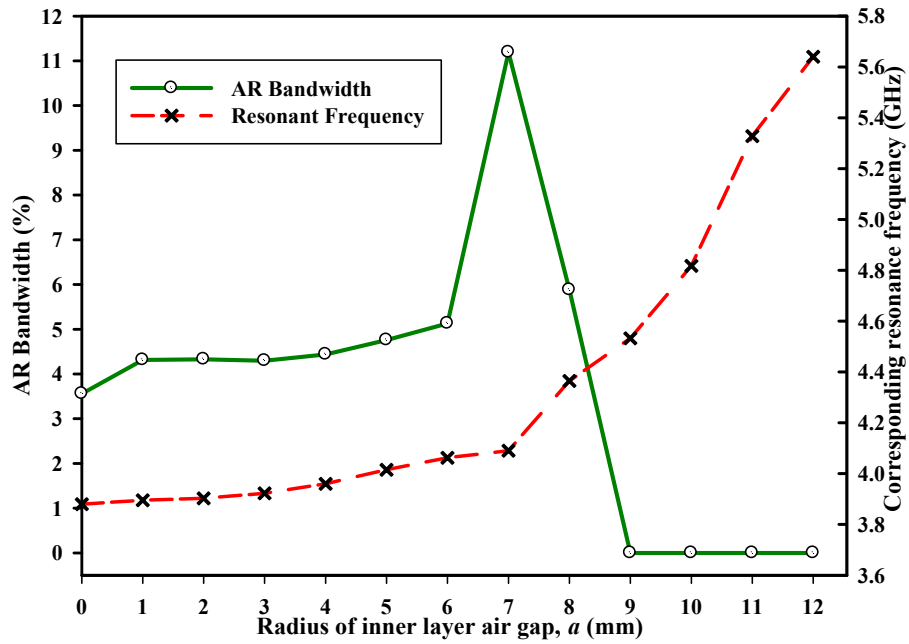
Figure 5.32: Axial ratio bandwidth and corresponding resonance frequency as a function of the radius of inner air gap
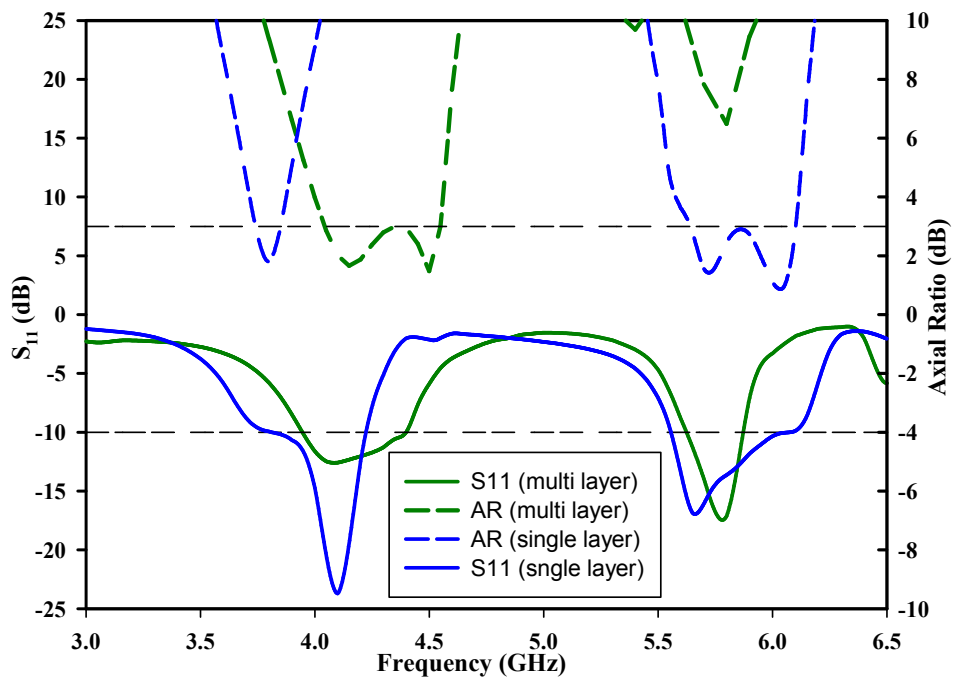
Figure 5.33: Axial ratio and return loss of DRA fed by half loop with or without stub

5.4.3 Results and Discussions

5.4.3.1 Circularly Polarized Single Layer Hemispherical DRA

Due to a cost constraint, only a prototype of a multilayer hemispherical has been built. For the single layer hemispherical, the results from simulation by MoM have been compared with those obtained from the commercial CST microwave studio software. From results obtained using iterative design procedure, the optimized dimensions of the feeding structure are found to be $h_d = w_d$ = 10 mm, g_d = 1 mm, p_s = 5.5 mm, l_s = 2 mm and w_s = 2.5 mm. In the CST simulations, a discrete port of length 0.25 mm has been used as a source feed to the half-loop metal, which has a strip width of 1 mm. Additionally, a hexahedral mesh type of 30 mesh lines per wavelength with an accuracy of -50 dB has been used within a wide frequency range of 4.5 to 6.5 GHz.

The computed return losses are presented in Figure 5.34, where it can be seen that a good agreement has been achieved between the MoM and CST results. The corresponding input impedances are shown in the inset of Figure 5.34. It is found that the impedance matching has been attained over bandwidths of 9.36% and 9.92% in the MoM and CST computations, respectively. The minimum S_{11} frequency points have been computed as 5.66 GHz and 5.55 GHz in the MoM and CST simulations, respectively, which represents a marginal difference of ~2% between the two sets of results. These resonance frequencies agree reasonably well with that of 5.2 GHz for the TE_{122} mode in which the DRA is excited, as predicted by CST Eigen mode sover.
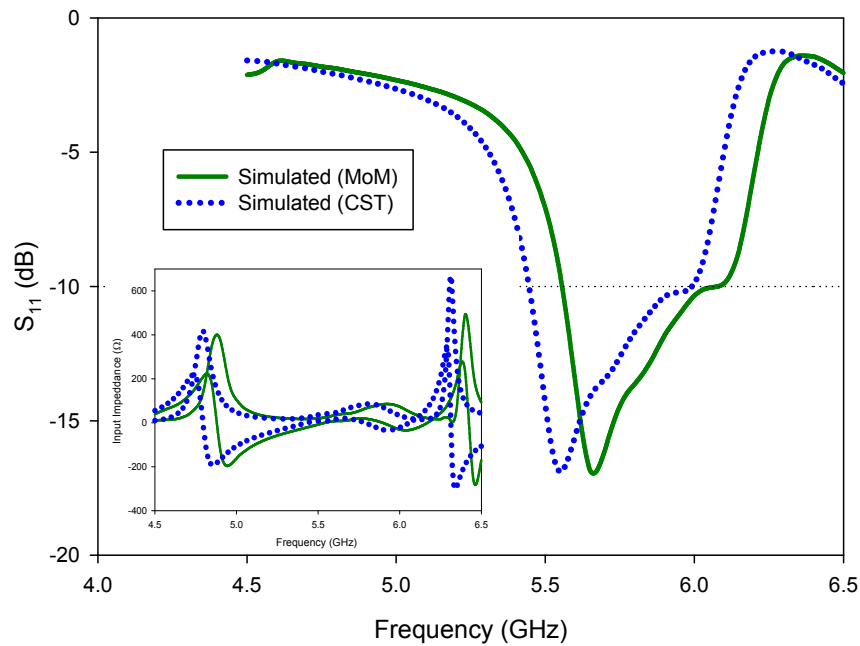
Figure 5.34: Return losses and input impedances of the hemispherical DRA

The variation of the bore-sight axial ratio as a function of frequency is presented in Figure 5.35, where it can be noticed that the 3 dB AR bandwidth has been achieved over bandwidths of 7.61% and 7.42% in the MoM and CST computations, respectively, which is significantly higher than the typical singly-fed CP hemispherical DRA bandwidth of ~4%. With reference to Figure 5.36, it can be noticed that a sufficient impedance matching bandwidth has been obtained throughout the whole frequency band of the achieved circular polarization. Furthermore, analysis of the axial ratio as a function of the elevation angle at the minimum AR frequency shows that the hemispherical DRA offers CP radiation over a beam-widths of 17° and 11° in $\phi = 0^\circ$ and $\phi = 90^\circ$ planes, respectively. Figure 5.37 shows the radiation patterns for MoM and CST computations, where it can be noticed that an excellent agreement has been achieved between the two sets of results. An isolation of more than 20 dB has been achieved between the

co-, and cross-, polarization components in both planes and it is evident from these results that this is a right-hand CP DRA.
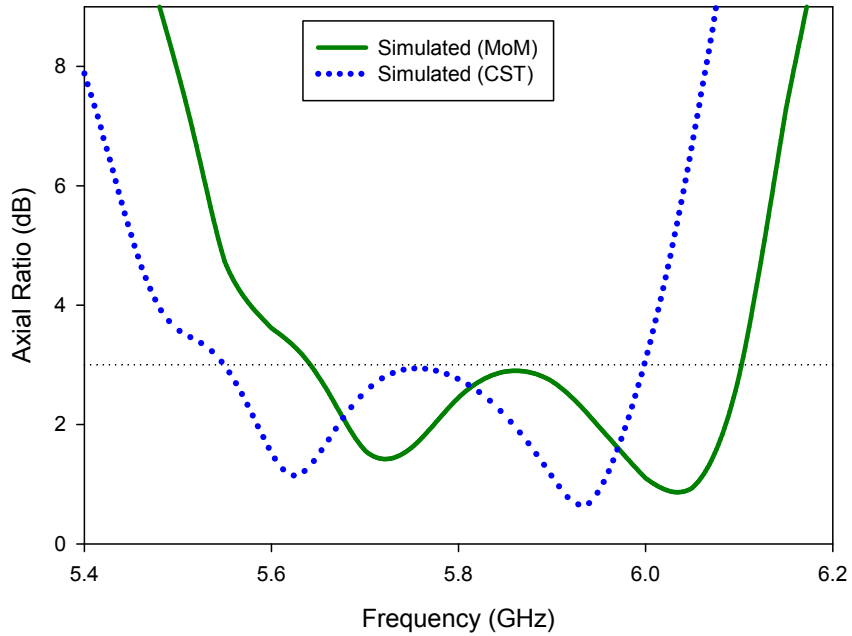
Figure 5.35: Axial ratio of a hemispherical DRA fed by half-loop strip
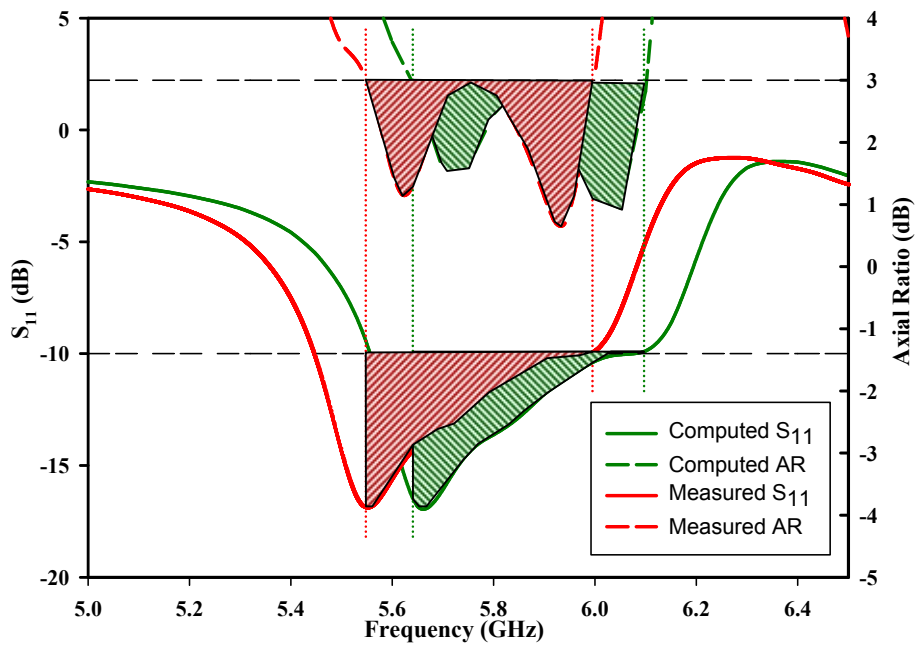
Figure 5.36: Region of overlapping bandwidths for S_{11} and AR
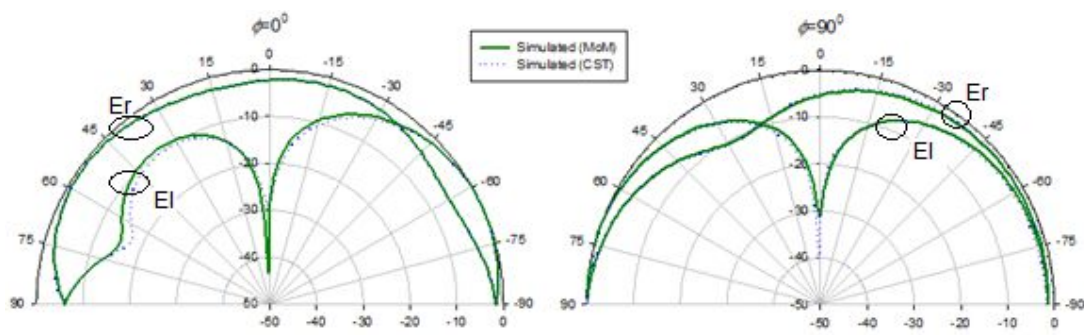
Figure 5.37: Radiation pattern of the DRA at minimum AR frequencies

5.4.3.2   Circularly Polarized Multilayer Hemispherical DRA

Figure 5.38 presents a prototype of the hollow, or multilayer, hemispherical DRA that is excited using a rectangular half-loop. The antenna has been built based on the optimized parameters obtained using the iterative design procedure.
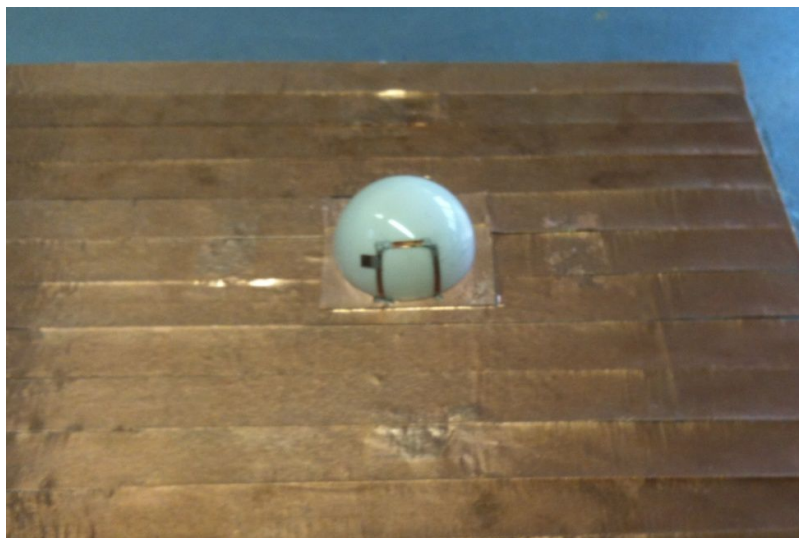
Figure 5.38: A multilayer hemispherical DRA excited by

a rectangular half-loop antenna

The computed and measured input impedance and return losses are shown in Figures 5.39 and 5.40, respectively, where it can be seen that a reasonable agreement has been obtained between theory and experiment. The return losses bandwidth has been computed to be 10.43% which is slightly higher than 10.32% in the measurements. The minimum S_{11} has been computed at 4.09 GHz compared to a measured value of 4.3 GHz. Consequently, the results agree well with the expected resonance frequency of 3.98 GHz for the TE_{111} mode in which the DRA is excited, as predicted by the CST Eigen mode solver. Furthermore, a travelling-wave current distribution has been achieved along the rectangular half-loop at the frequency band of operation as illustrated in Figure 5.41. The half-loop has perimeter of $1.05\lambda_g$ at 4.5 GHz that supports the first-mode of radiation, for which the conditions are ideal for wave radiation.
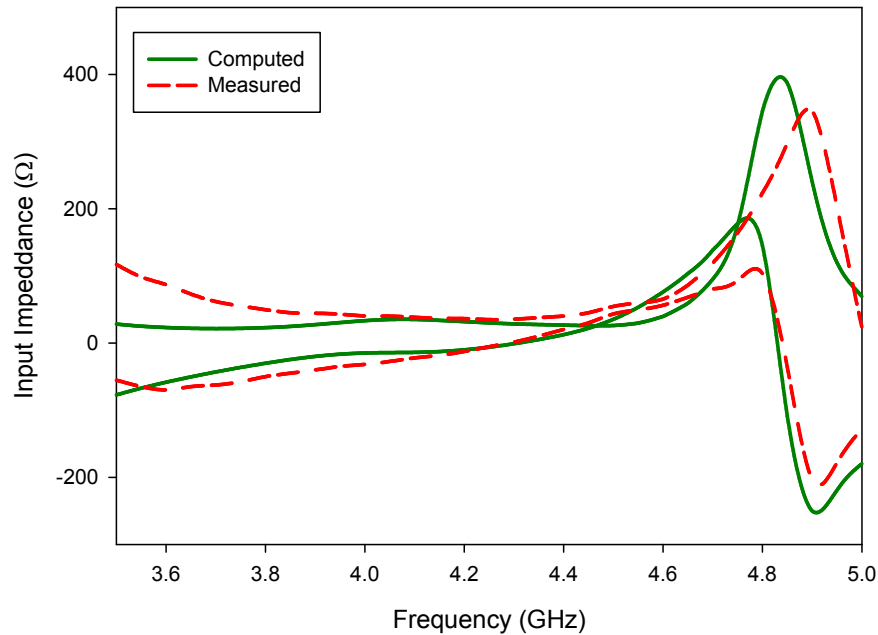
Figure 5.39: Input impedance of the multilayer hemispherical DRA
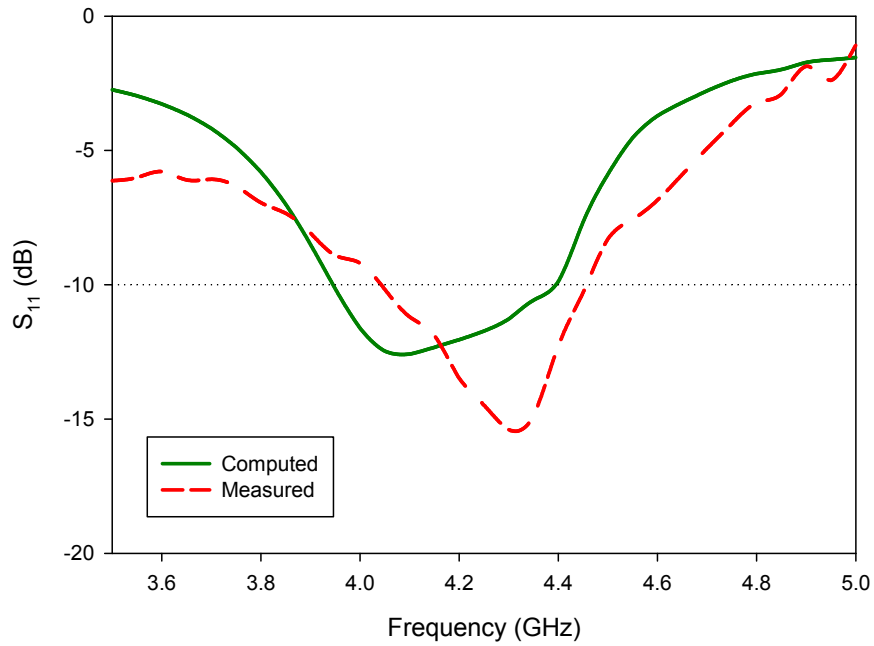
Figure 5.40: Return losses of the multilayer hemispherical DRA
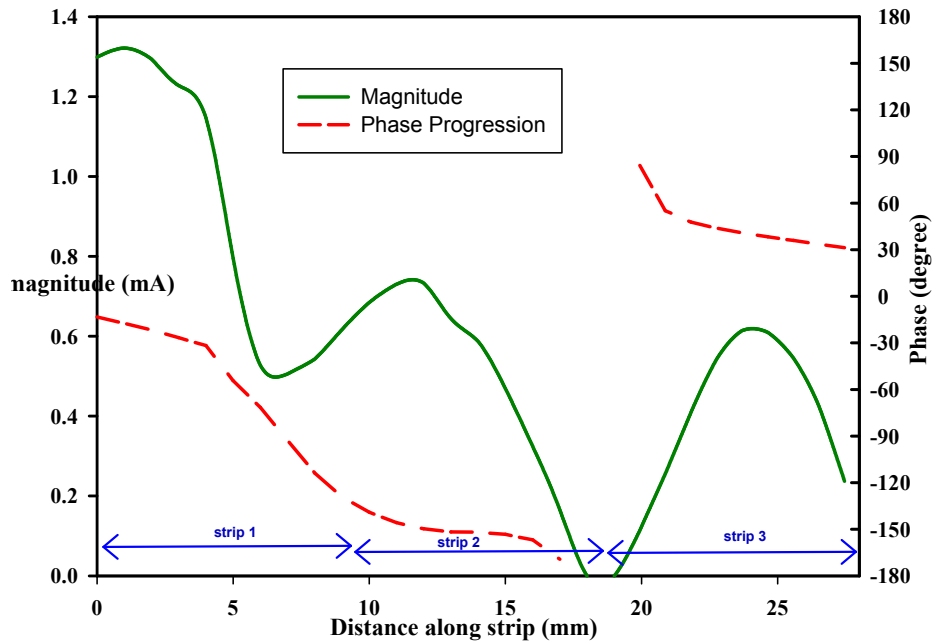
Figure 5.41: Current distribution along the half-loop strip at 4.50 GHz.

Figure 5.42 presents the computed and measured axial ratio at the bore-sight direction, where it can be seen that the minimum computed AR value is 1.55 dB at 4.5 GHz, compared to the corresponding measured value of 1.58 dB at 4.56 GHz. From these results, the achieved 3 dB AR bandwidths are 11.19% and 11.15% in the analysis and measurements, respectively. Furthermore, the overlapping AR and S_{11} bandwidths from computations and measurements are shown in Figure 5.43. Based on the results, the theoretical effective AR bandwidth is found to be 8.5% compared to 8.4% in the experiment. It should be noted that the effective AR bandwidth can be increased to 10.4% and 10.7% in the computations and measurements, respectively, if a threshold of $S_{11}<-7.5dB$ is considered, which corresponds to a voltage standing wave ratio (VSWR) of 2.5. Such an impedance matching criteria has been employed in earlier studies and has been considered to be acceptable [18]-[19].
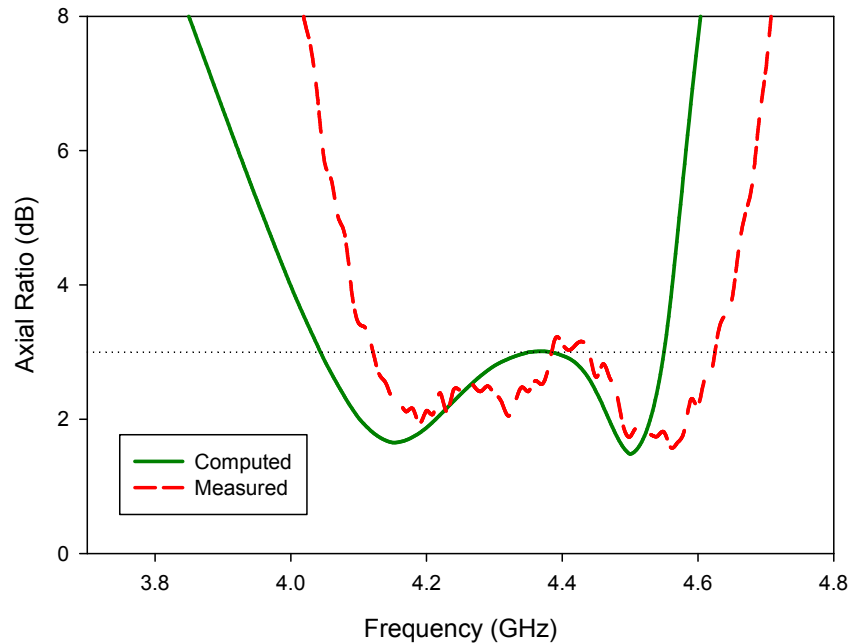
Figure 5.42: Axial ratio of the multilayer hemispherical DRA fed by a rectangular half-loop strips.
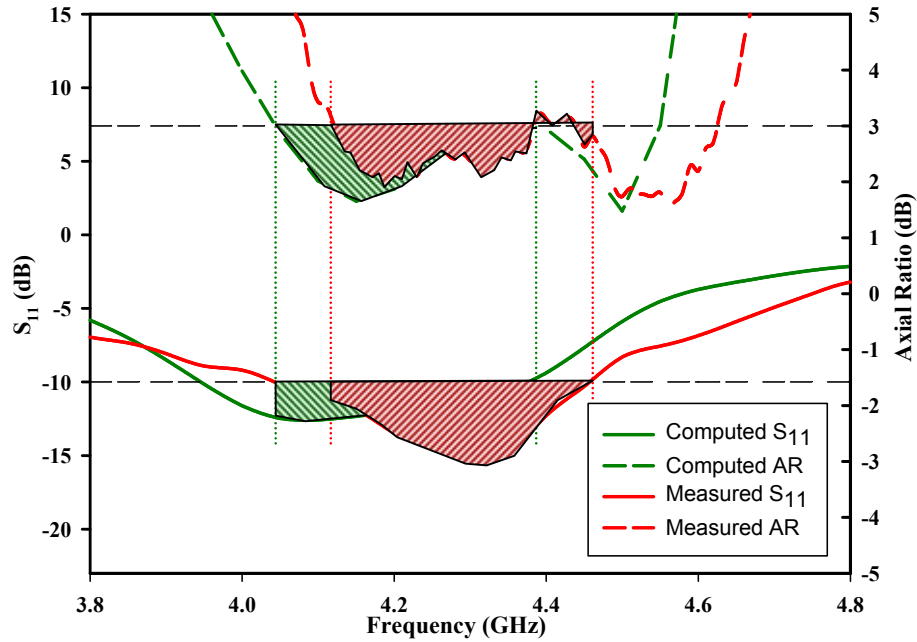
Figure 5.43: Region of overlapping bandwidths for S_{11} and AR

The variation of the axial ratio as a function of elevation angle is shown in Figures 5.44 and 5.45, where it can be notice that the computed AR beam-widths are $26°$ and $81°$ in the $\phi = 0°$ and $\phi = 90°$ plane, respectively. Furthermore, the calculated and measured radiation patterns across the AR bandwidth are shown in Figure 5.46, where a reasonable agreement can be observed between the two sets of results. It is noticeable that the patterns are stable throughout the whole CP frequency range. From Figure 5.46 (b), it is evident that this is a right-hand CP DRA, in which the RHCP field is stronger than the LHCP field by more than 20 dB in the bore-sight direction for both principal planes. Finally, the antenna gain of the multilayer DRA is shown in Figure 5.47, where it can be observed that the DRA offers a useful gain of more than 4dBi across the frequency range of the achieved

circular polarization until 4.40 GHz where the gain decreases steadily to approximately 1.50 dB at the ending AR frequency
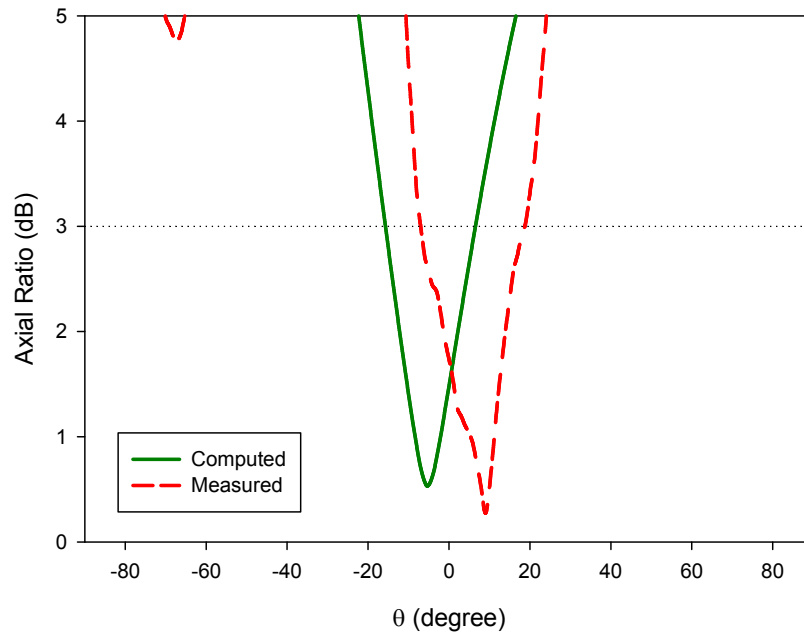
Figure 5.44: Axial ratio beam-width of the DRA at $\phi = 0°$
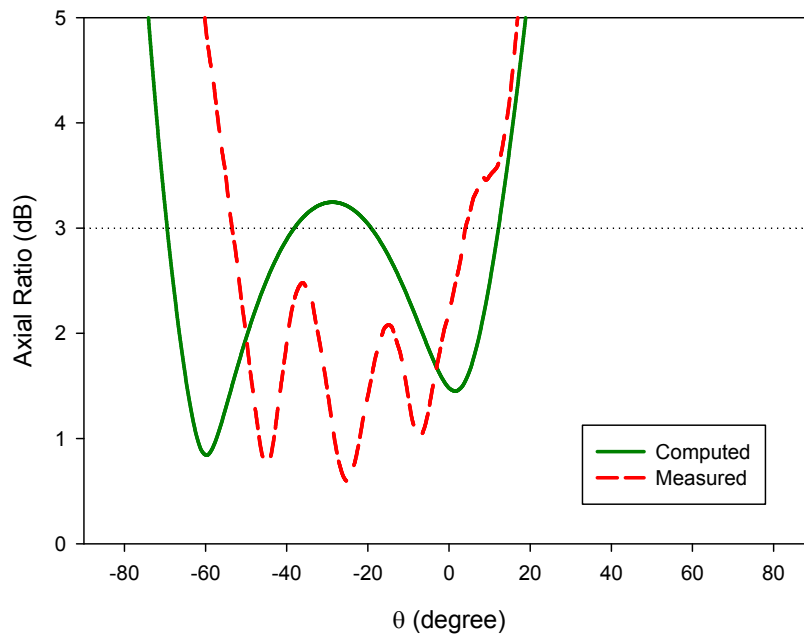
Figure 5.45: Axial ratio beam-width of the DRA at $\phi = 90°$
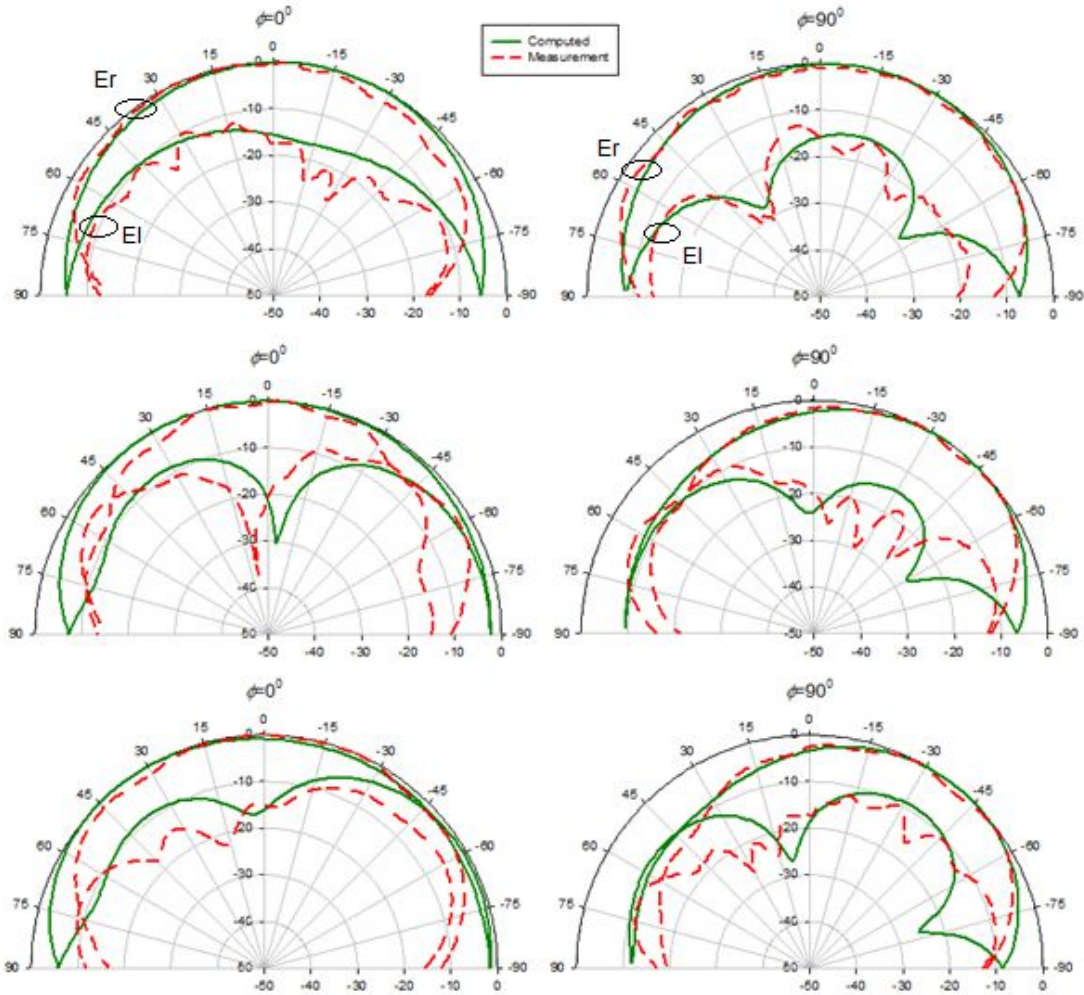
Figure 5.46: Radiation pattern of the hemispherical DRA at

(a) starting, (b) minimum, and (c) ending of AR frequencies
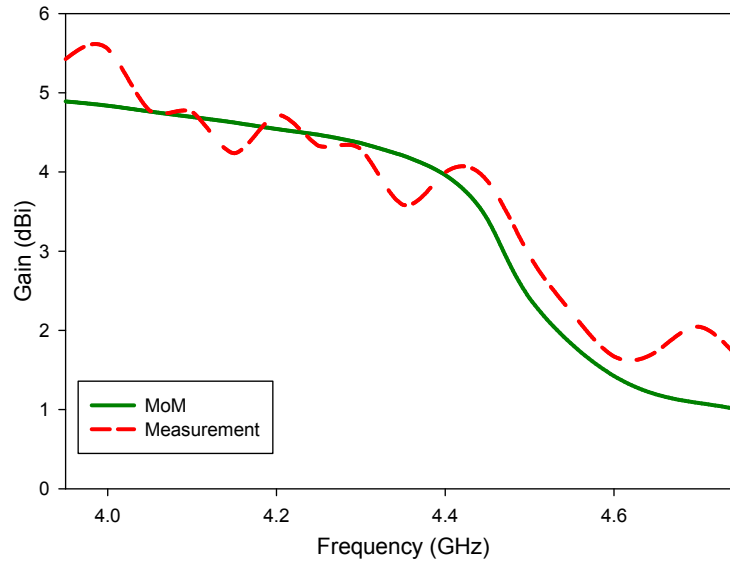
Figure 5.47: Gain of the multilayer hemispherical DRA

5.5   Conclusions

A simpler feeding method that can be used to achieve broadband circularly polarized singly-fed DRAs is presented. The proposed method is general and applicable to DRAs of any geometry as proven by application of the rectangular half-loop onto a rectangular, cylindrical and hemispherical dielectric. The CP bandwidth achieved in each case is considerably higher than those reported in the literature for a singly-fed DRA of the same shape. In all cases, the theoretical and experimental results agree reasonably well with each other. Additionally, the CP radiation is not sensitive to the dimensions of the half-loops, which means it can be obtained without difficulty.

References

[1] C.A. Balanis, "Antenna Theory: Analysis and Design," pp.203-248, Wiley & Sons Inc., New York,1997

[2] R. L. Li, and H. Nakano, "Numerical analysis of arbitrarily shaped probe excited single-arm printed wire antenna", *IEEE Trans. Antennas Propag.,* vol. 46, pp. 1307-1317, Sept 1998.

[3] H. Morishita and K. Hirasawa, "Wideband circularly-polarized loop antenna," in *Proc. IEEE AP-S Int. Symp.*, 1994, pp. 1286–1289.

[4] H. Morishita, K. Hirasawa, and T. Nagao, "Circularly polarized wire antenna with a dual rhombic loop," *Proc. Inst. Elect. Eng. Microw. Antennas Propag.*, pt. H, vol. 145, no. 3, pp. 219–224, Jun. 1998.

[5] R. L. Li, V. Fusco, and H. Nakano, "Circularly polarized open-loop antenna," *IEEE Trans. Antennas Propag.*, vol. 51, no. 9, pp. 2475–2477, Sep. 2003.

[6] B. Li, and K.W. Leung, "Strip-fed rectangular dielectric resonator antenna with/without a parasitic patch", *IEEE Trans. Antennas Propag.,* vol. 53, pp. 2200-2207, July 2005.

[7] R.K. Mongia, "Theoretical and Experimental Investigations on Rectangular Dielectric Resonators*," IEEE Proc.H*, vol.139, pp.98-104, Feb 1992

[8] H. Nakano, K. Nogami, S. Arai, H. Mimak, and J. Yamauchi, "A spiral antenna backed by a conducting plane reflector", *IEEE Trans. Antennas Propag.*, vol. 34, pp. 791-796, June 1986.

[9] J.A. Kaiser, "Two Archimedian Two-Wire Spiral Antenna", *IEEE Trans. Antennas Propag.*, vol. 8, pp. 312-323, May 1960.

[10] M.T. Lee, K.M. Luk, E.K.N. Yung, and K.W. Leung, "Microstrip line fed circularly polarized cylindrical dielectric resonator antenna", *Microwave and Optic. Tech. Lett.* , Vol. 24, pp. 206-207, Feb 2000

[11] L. RongLin, J. Laskar, and M. M. Tentzeris, "Broadband circularly polarized rectangular loop antenna with impedance matching," *IEEE Microwave and Wireless Components Letters*, vol. 16, pp. 52-54, 2006.

[12] A. Petosa, "Dielectric Resonator Antenna Handbook," Chapter 3, pp.49, Artech House, 2007

[13] M. Gastine, L. Courtois and J.J. Dormann, "Electromagnetic Resonances of Free Dielectric Spheres," *IEEE Transc. Microwave Theory and Techniques*, vol.15, pp.694-700, no. 12, Dec 1967

[14] A. Petosa, "Dielectric Resonator Antenna Handbook," Chapter 2, pp.18, Artech House, 2007

[15] K.W. Leung, "Conformal strip excitation of dielectric resonator antenna", *IEEE Trans Antennas Propagat.,* vol. 48, pp. 961-967, Jul. 2000.

[16] C. A. Balanis, "Antenna Theory", 3rd Ed., John Wiley & Sons. Inc, 2005

 [17] K.W. Leung, "Complex Resonance and Radiation of Hemispherical Dielectric-Resonator Antenna with a Concentric Conductor", *IEEE Trans Antennas Propagat.,* vol. 49, no. 3, pp. 24-531, Mar 2001

[18] H.l Choi, S. Jeon, J. Yeom, O. Cho and H. Kim, "Controlling Resonances for a Multi-Wideband Antenna by Inserting Reactive Components," *IEEE Trans Antennas Propagat* , vol.59, no.8, pp.3040-3045, Aug. 2011

[19] Y-W Chi, K-L Wong and S-W Su , "Broadband Printed Dipole Antenna With a Step-Shaped Feed Gap for DTV Signal Reception," *IEEE Trans Antennas Propagat*, vol.55, no.11, pp.3353-3356, Nov. 2007

CHAPTER 6

AR BANDWIDTH ENHANCEMENT

OF CP DRAs USING a PARASITIC

HALF-LOOP

6.1   Introduction

In addition to its simplicity, the rectangular open half-loop excitation scheme facilitates the incorporation of a concentric parasitic half-loop. For a single loop antenna, the addition of a parasitic element can create another minimum AR point. By optimizing the dimensions of the two loops, two minima AR points, which resonate at frequencies that are close to each other, can be generated. As a result, the combination of the two AR bands leads to a significant enhancement in the overall circular polarization bandwidth. Employing this approach results in

improving the AR bandwidth without a noticeable increase in the antenna's complexity and profile since the parasitic element can be conveniently placed inside the driven half-loop antenna.

Enhancing the CP bandwidth of a loop antenna by adding a parasitic element is a well known procedure that has been reported in earlier studies [1-5]. For instance, the addition of a parasitic element inside a circular loop antenna has resulted in the increase of AR bandwidth from 6.5% to 20% [1]. In a later study [2], a pair of parasitic rhombic loops has been placed inside a dual-rhombic loop. The AR bandwidth of this configuration was found to be 46%, which is more than three times wider than those achieved without the parasitic element. Additionally, the combination of two AR bands from a dual rhombic loop antenna with double parasitic loops has contributed to a very significant increase in the AR bandwidth from 3% to 23.7%, as reported in [3]. The effects of adding a pair of parasitic loop inside dual rectangular loop antenna has been investigated in [4], in which the 3dB AR bandwidth has been reported as 46% compared to 18% without the parasitic elements. Furthermore, the incorporation of a parasitic circular loop onto a probe-fed CP circular loop antenna has generated a wide CP bandwidth of 16%, compared to less than 6% for a single loop [5].

In this chapter, CP rectangular and cylindrical DRAs that are excited using driven and parasitic half-loops are studied rigorously. The addition of the parasitic elements has significantly increased the CP bandwidths compared to those from the same DRAs excited using a driven element only.

6.2   CP Rectangular DRA Excited Using Concentric Half-Loops

6.1.1   Antenna Configuration

The geometry of a rectangular DRA fed by an open half-loop antenna in the presence of a concentric parasitic open half-loop is presented in Figure 6.1. The feeding structure consists of driven and parasitic elements. The driven half-loop is connected to the coaxial cable, while the parasitic half-loop is excited through electromagnetic coupling with the driven counterpart. As explained earlier, the driven element has a width of w_d, a height h_d and a gap size of g_d located at a gap position of g_p. The parasitic element is placed inside the driven loop antenna and has respective width and height of w_p and h_p. The parameters of the gap within this parasitic element follow those within the driven element.
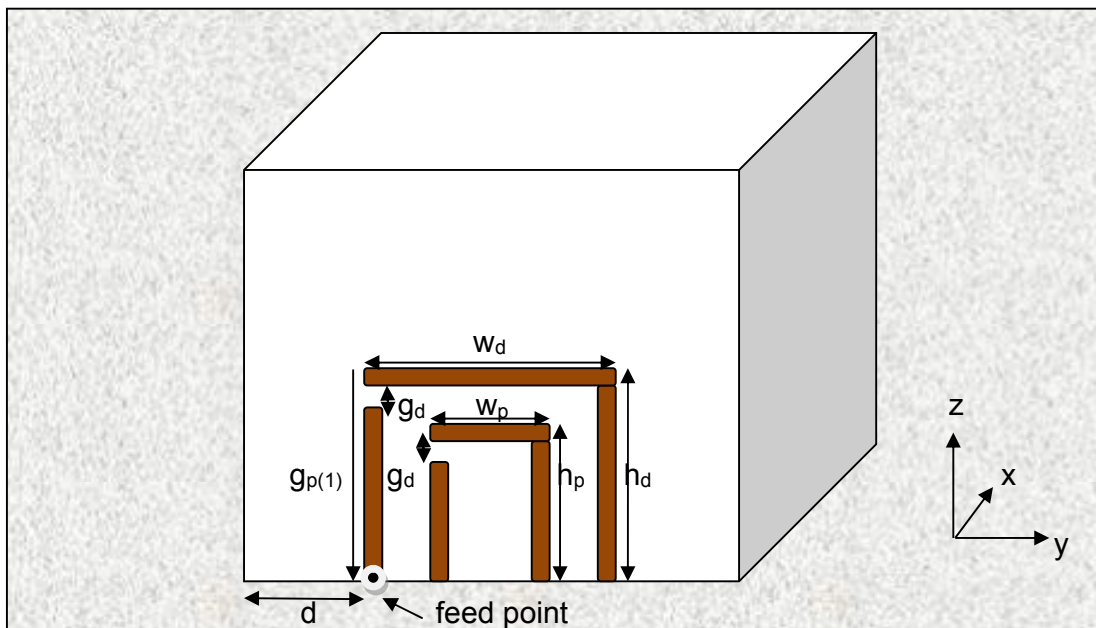
Figure 6.1: Configuration of a rectangular DRA excited by an open half-loop in the presence of a concentric parasitic open half-loop

The configuration has been modeled rigorously using the method of moments together with the combined RWG and SWG basis functions described in Chapter 2, where the rectangular dielectric has been meshed to 2407 tetrahedrons, and the metallic strips to 82 triangular patches, giving a total of 5289 unknowns. The optimized dimensions of the driven half-loop have been used as given in section 5.2.2. An iterative design procedure has been followed to determine the optimum dimensions of the parasitic element that are needed to establish another travelling-wave current distribution in addition to that along the driven half-loop. These travelling-wave currents produce two minima AR points at frequencies that are close to each other, which lead to a broadband CP radiation.

The dimensions of the parasitic half-loop, h_d and w_d, have been optimized when the parameters of the driven element are fixed as $h_d = w_d = 13$ mm, $g_d = 1$ mm and $g_p = 11$ mm. Table 6.1 presents the AR, impedance matching and the percentage of overlapping bandwidths for parasitic half-loop dimensions ranges of $7 \leq h_p \leq 10$ mm and $7 \leq w_p \leq 10$ mm. Throughout these simulations, a gap of size $g_d = 1$ mm has been placed between the first two parasitic metallic strips of the parasitic half-loop as shown in Figure 6.1. The results demonstrate that the CP radiation can be attained easily using strips' dimensions range of 7 to 10 mm, which is a desired feature in the CP DRA design. Based on these results, the highest overlapping bandwidths of 12.71% has been obtained when $h_p = 7$ mm and $w_p = 9$ mm. For this optimized configuration, the resonance frequency occurs at 3.5 GHz, which corresponds to the TE^y_{111} excited mode

Height, h_p (mm)	Width, w_p (mm)	3db AR Bandwidth (%)	-10dB S_{11} Bandwidth (%)	Overlapping AR & S_{11} Bandwidth (%)
7	7	10.27	21.81	100
	8	11.31	22.82	100
	9	**12.71**	**21.32**	**100**
	10	8.02	26.05	100
8	7	9.09	32.47	100
	8	8.26	32.02	100
	9	*12.12*	*30.04*	*100*
	10	8.75	28.88	95
9	7	8.92	21.82	93
	8	8.93	21.6	98
	9	*8.61*	*20.56*	*98*
	10	8.33	19.32	84
10	7	5.85	16.27	66
	8	6.15	14.83	29
	9	*6.81*	*12.08*	*0*
	10	10.84	11.31	0

Table 6.1: AR and S_{11} bandwidths for different dimensions

of the parasitic half-loop

Graphical representations of Table 6.1 are presented in Figures 6.2 and 6.3. These figures show the variation of return loss and AR as functions of frequency, respectively, for different values of h_p when w_p is fixed at 9 mm. As a reference, the results achieved without the presence of the parasitic element is included in both graphs. Based on the figures, it is noticeable that the S_{11} changes significantly for different h_p, in contrast to the relative stability in AR. From these results, it can be seen clearly that the inclusion of the parasitic element has created another AR minimal point at 3.5 GHz in addition to the AR minimal point at 3.24 GHz generated by the driven half-loop. The wider bandwidth can be achieved by merging the two minima AR points, which can be accomplished using half-loop heights that range between 7 and 8 mm. When h_p exceeds 8 mm, the AR minimal

point generated by the parasitic half-loop falls outside the AR≤3dB threshold. Hence, the overall AR bandwidth is significantly reduced.
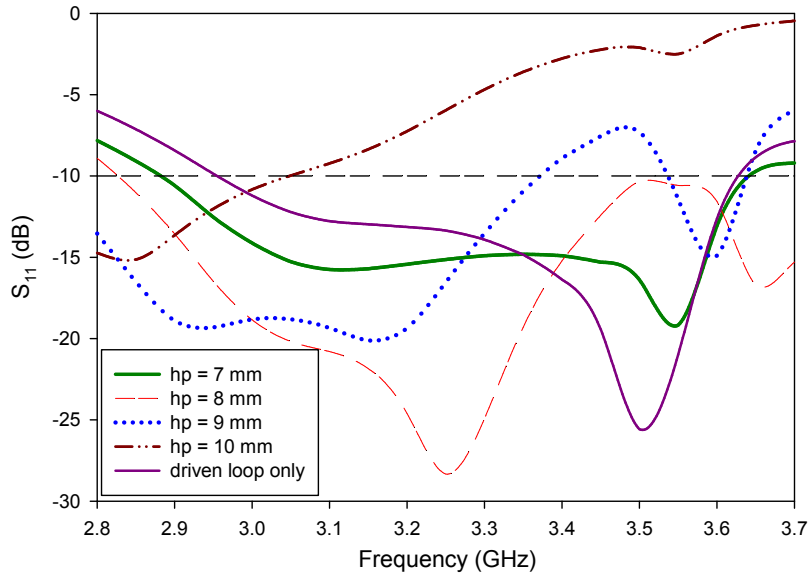
Figure 6.2: Return loss for different heights of parasitic half-loop
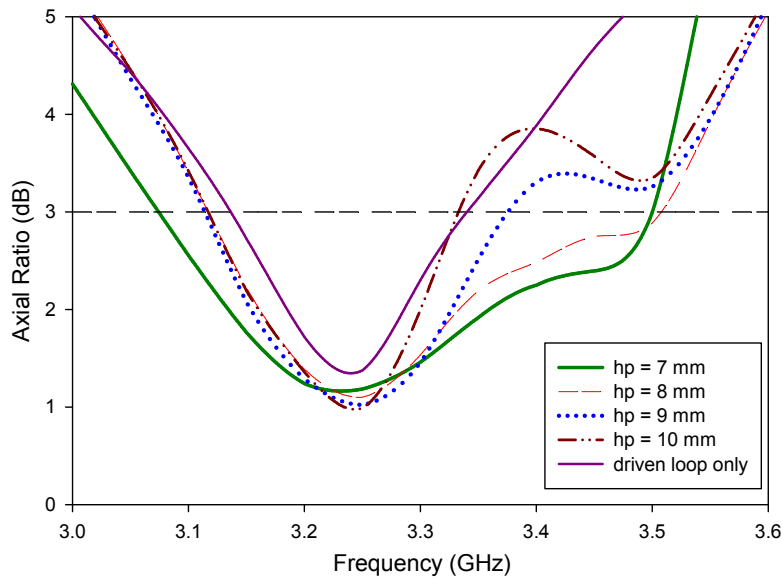
Figure 6.3: Axial ratio for different heights of parasitic half-loop

6.1.2 Results and Discussions

Figure 6.4 illustrates a fabricated rectangular DRA that is excited using open half-loop antenna in conjunction with a concentric parasitic half-loop. This is the same DRA that has been used in Chapters 3 and 5, which has a relative permittivity of ε_r = 9.2, and dimensions of *a* = 26.1 mm, *b* = 25.4 mm and *c* = 14.3 mm [6]. Based on the results of the iterative design procedure, the used optimized dimensions of the parasitic element which are h_p = 7 mm, w_p = 9 mm, and g_d = 1 mm. The parameters of the driven element used in section 5.2.2 are retained, that is, h_d = w_d = 13 mm, g_d = 1 mm, *d* = 6.5 mm and the gap is located at a distance of 11 mm from the feed point. Each half-loop has been connected to the ground plane at two ends using a conductive silver paint. As mentioned earlier, potential air gaps between the DRA and the ground plane, which could cause error in the measurements, have been eliminated by attaching the DRA to a double sided adhesive conducting tape that is placed above the ground-plane as shown in Figure 6.4.
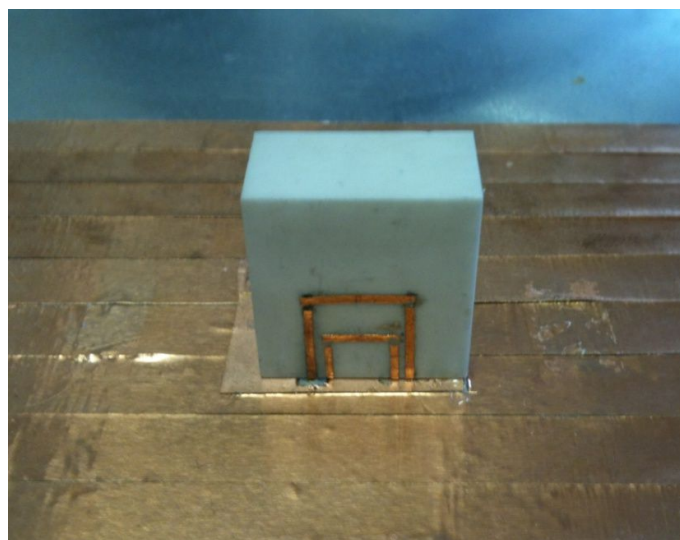
Figure 6.4: A rectangular DRA excited using concentric half-loops

The input impedance has been measured and compared to the MoM computation with close agreement as illustrated in Figure 6.5. Additionally, the simulated and measured return losses agree well with each other as shown in Figure 6.6. Based on these results, S_{11} bandwidths of 21.32% and 19.30% have been achieved in theory and measurements, respectively. The minimum S_{11} has been computed at a frequency of 3.53 GHz compared to 3.47 GHz in the measurements, which represents a marginal difference of 0.6%. These results agree reasonably well with a predicted resonance frequency of 3.8 GHz for the TE^{y}_{111} mode in which the DRA is excited, as calculated using DWM method proposed in [7]. The DRA operating in this broadside TE^{y}_{111} mode has a strong magnetic field near the ground plane, thus it can be excited by the half-loops that have maximum current magnitudes at these points to generate CP radiation within this mode.
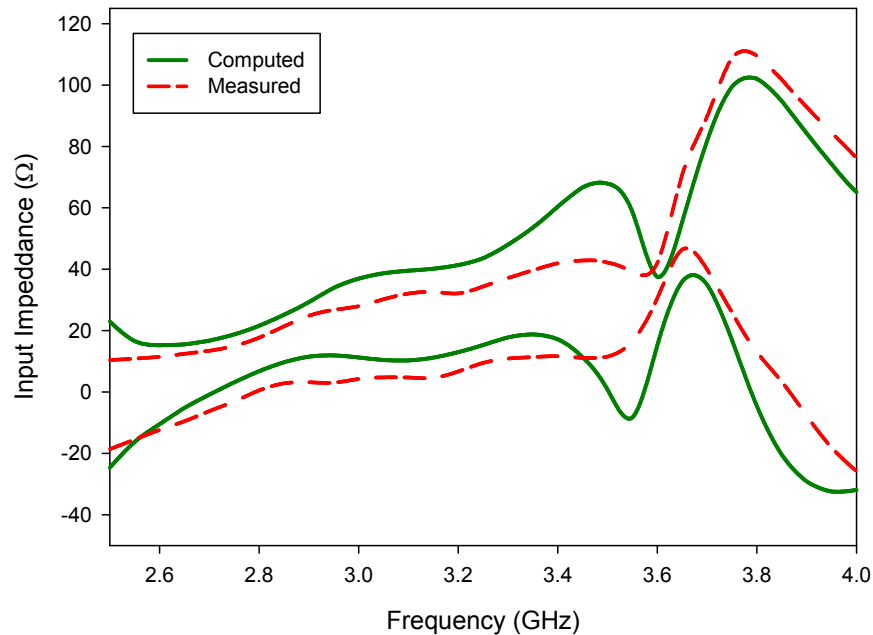
Figure 6.5: Input impedances of a rectangular DRA excited

using concentric half-loop.
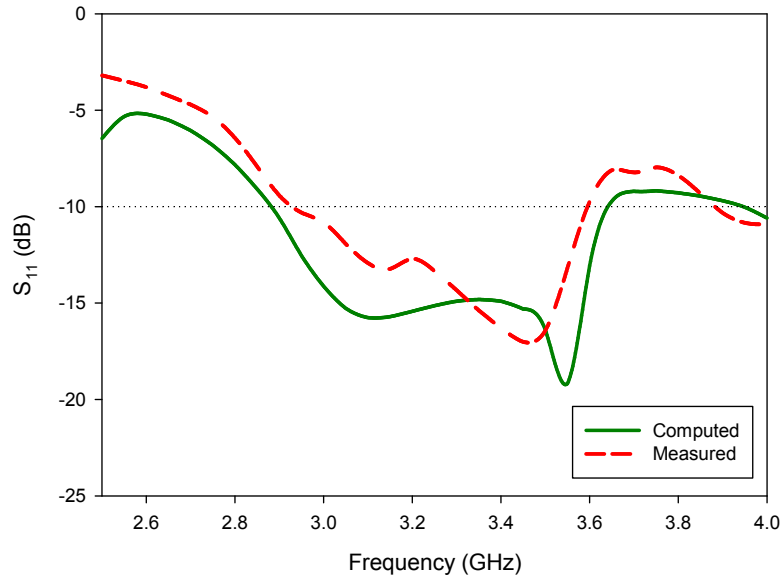
Figure 6.6: Return losses of the rectangular DRA

Additionally, the distribution of current along the two half-loops at the frequency band of operation has been studied, where it is evident from Figure 6.7 that a travelling wave current distribution has been attained with a smoothly decaying magnitude and approximately linear phase progression.
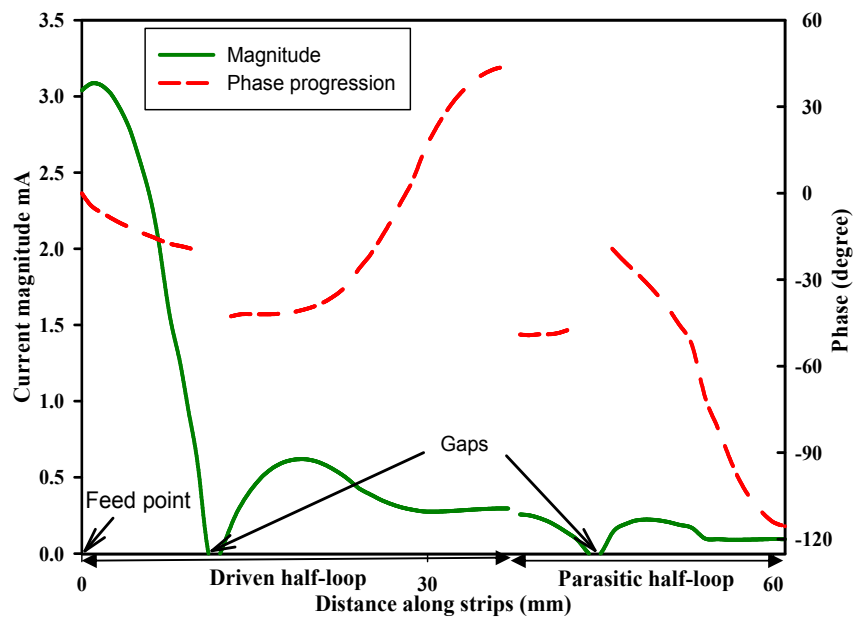
Figure 6.7: Current distribution along the concentric half-loops at 3.24 GHz

Figure 6.8 presents the computed and measured axial ratio at the bore-sight direction, where it can be observed that the minimum computed AR is 1.18 dB at 3.24 GHz, which is close to the corresponding measured value of 0.99 dB at 3.21 GHz. Based on these results, the calculated 3 dB AR bandwidth is 12.71%, which is slightly narrower than the measured bandwidth of 13.74%. This constitutes at least a 95% AR bandwidth increment compared to that obtained from a DRA excited using the driven half-loop only. Furthermore, with reference to Figures 6.9, it can be noticed that a sufficient impedance matching bandwidth has been attained throughout the achieved circular polarization bandwidth. Additionally, the theoretical and experimental variations of the axial ratio, as functions of the elevation angle, are illustrated in Figures 6.10 and 6.11, where it is evident that the DRA produces a CP radiation over computed beam-widths of $110°$ and $95°$ in both $\phi = 0°$ and $\phi = 90°$ principle planes, respectively, at the minimum AR frequency. In terms of measurements, the beam-widths have been achieved over $98°$ in the $\phi = 0°$ plane and $94°$ in the $\phi = 90°$ planes.
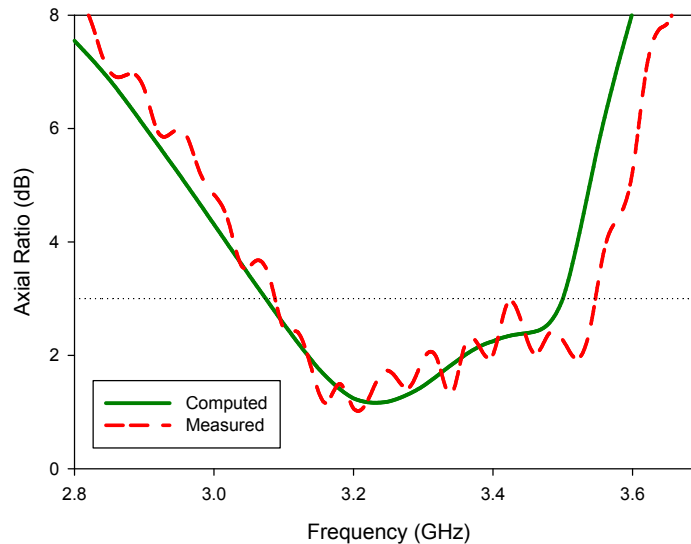
Figure 6.8: Axial ratio of the rectangular DRA excited using concentric half-loops
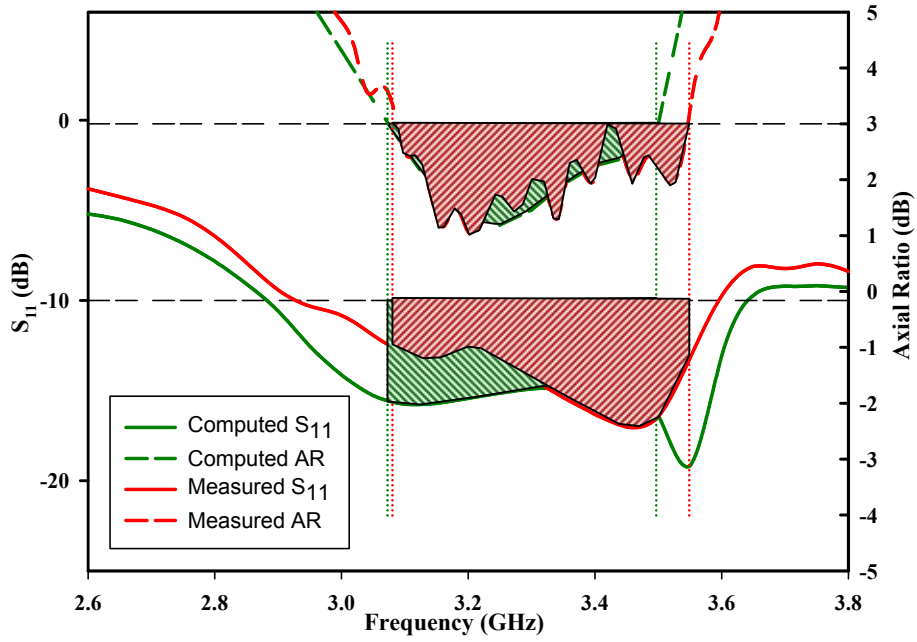
Figure 6.9: Region of overlapping bandwidths for S_{11} and AR
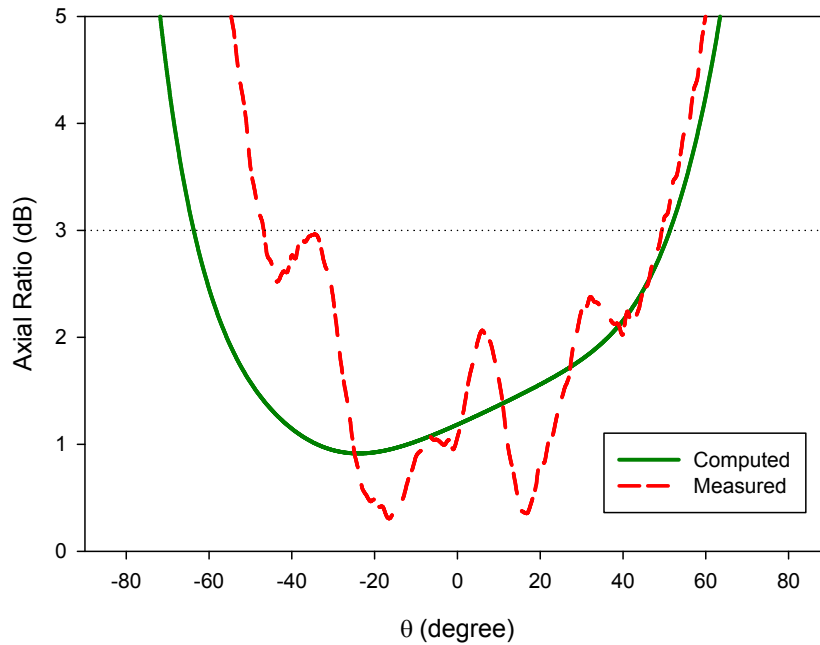
Figure 6.10: Axial ratio beam-width of the rectangular DRA at $\phi = 0°$
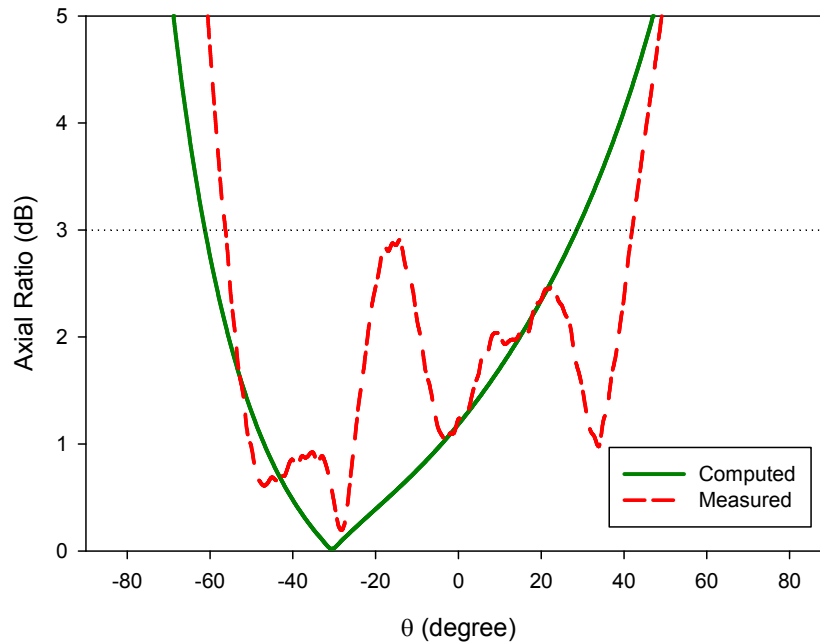
Figure 6.11 Axial ratio beam-width of the rectangular DRA at $\phi = 90°$

The calculated and measured bore-sight gains are shown in Figure 6.12, which demonstrates that a satisfactory gain of over 4dBi has been attained throughout the achieved circular polarization bandwidth.
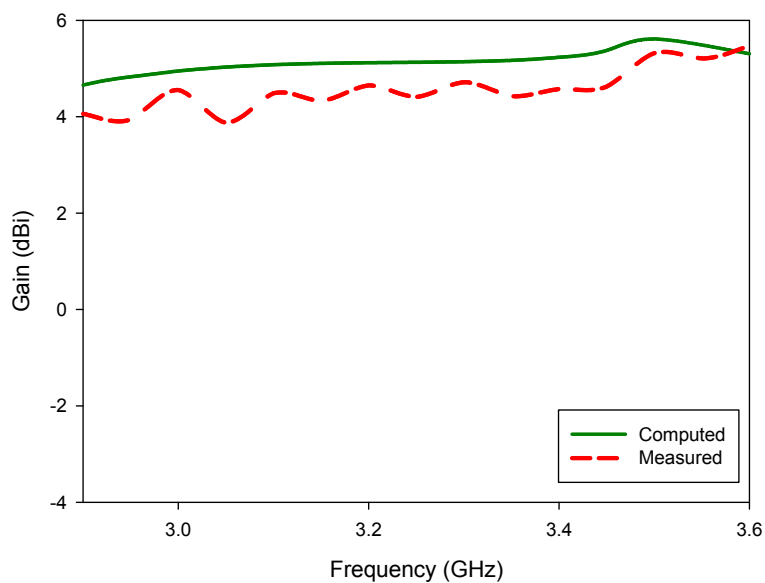
Figure 6.12: Gain of the rectangular DRA excited using concentric half-loops

Furthermore, the computed and measured radiation patterns are shown in Figure 6.13, where it can be observed that the radiation patterns are stable across the CP frequency band. Based on Figure 6.12 (b), an isolation of more than 23 dB has been achieved between the co-and cross-, polarization components. The results clearly show that the DRA radiates right-hand CP wave, as RHCP field is the much stronger component than LHCP field.
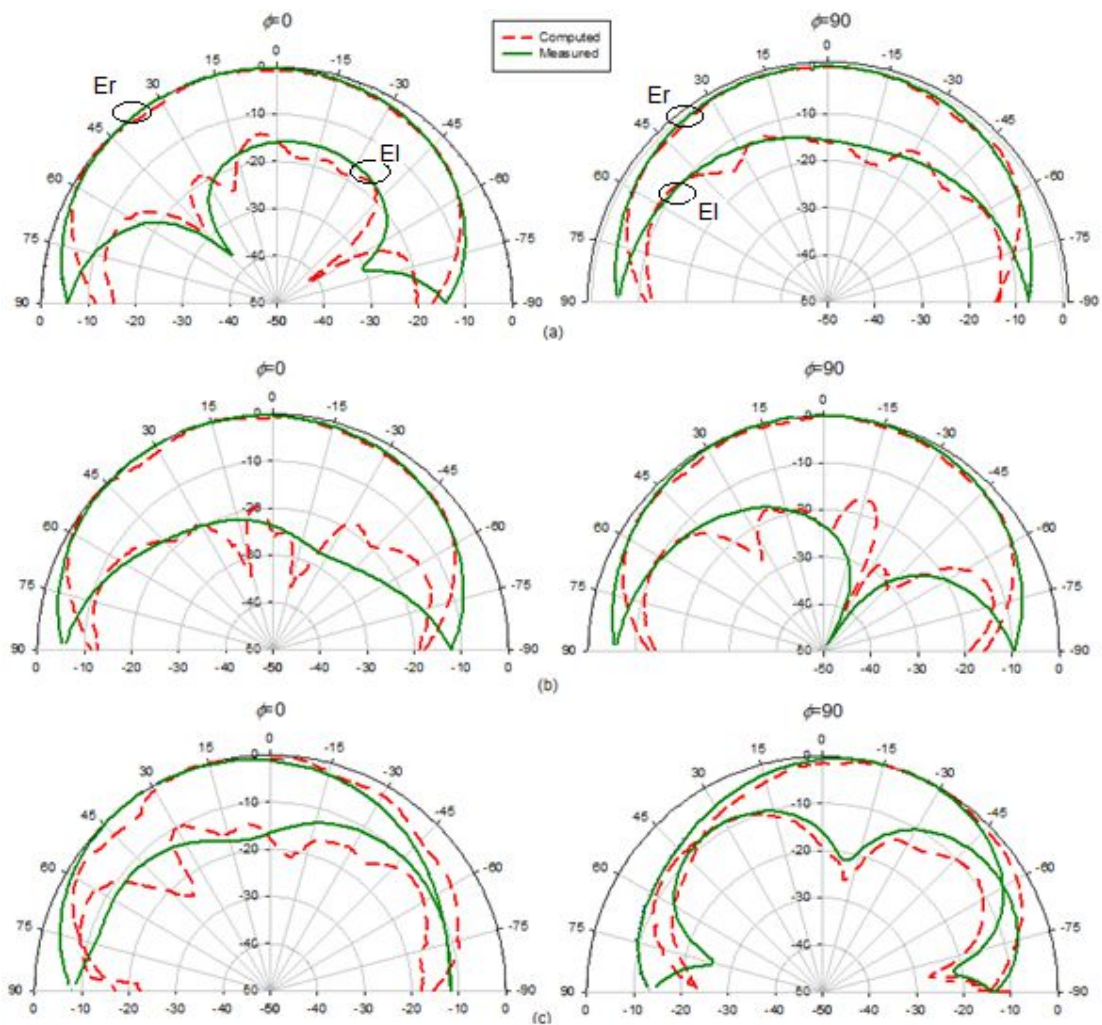
Figure 6.13: Radiation pattern of the rectangular DRA at

(a) starting, (b) minimum, and (c) ending of AR frequencies

6.3   CP Cylindrical DRA Excited using Concentric Half-Loops

6.3.1   Antenna Configuration

Figure 6.14 illustrates the geometry of a multilayer cylindrical DRA that is excited using concentric open half-loops. The multilayer design is used since the inclusion of parasitic loop for single layer design does not significantly enhance the AR bandwidth. The outer layer has a radius of *a*, a height of *h* and a dielectric constant of ε_r while the inner layer has parameters of a_2, h_2 and ε_{r2}. As explained earlier, the driven half-loop has a width of w_d, a height h_d and a gap size of g_d located at a gap position of g_p. The parasitic half-loop that is placed inside the driven element has dimensions of w_p and h_p, and the parameters of the gap within this parasitic element follow those within the driven element.
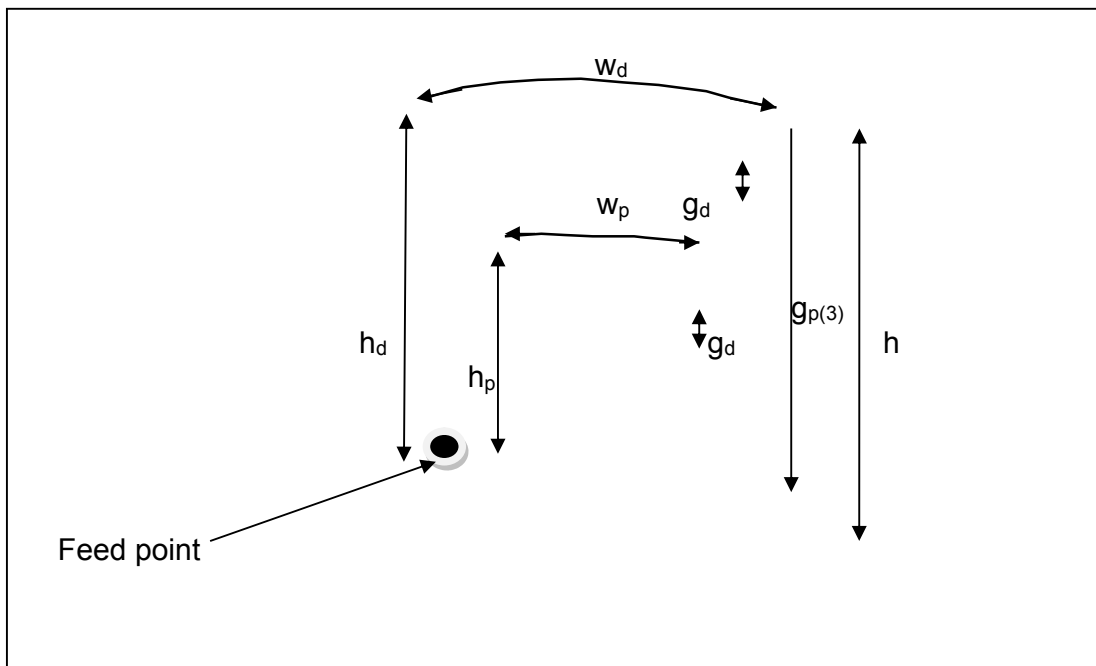
Figure 6.14: Configuration of a multilayer cylindrical DRA excited using concentric half-loops

The antenna configuration has been modeled using the method of moments in conjunction with the combined RWG and SWG basis functions, where the cylindrical dielectric has been meshed to 2432 tetrahedrons and the metallic strips to 87 triangular patches, giving a total of 4989 unknowns. The optimum dimensions of the feeding metallic strips that are required to establish a travelling-wave current distribution along the half-loops, as well as exciting a DRA mode within the same frequency range, have been determined following the same iterative design procedure that has been employed for the RDRA.

In order to assess the performance of the cylindrical DRA, the dimensions have been chosen to be as the same as those reported in [8], that is h = 10.54 mm, a = 7.01 mm and ε_r = 9.2. The dimensions of both half-loops have been optimized after employing the parameters of the inner dielectric layer used previously in section 4.4. Throughout these simulations, a gap of size g_d = 1 mm has been placed between the last two metallic strips of each half-loop as shown in Figure 6.13. The results of this optimization procedure are shown in Table 6.2. Most of the conducted simulations indicate that the DRA radiates CP wave, which is desirable in the CP antenna design. However, impedance matching has been totally lost for some dimensions, which suggests that no mode has been excited at the obtained CP frequency. As a result, the optimized parameters that generate maximum overlapping between the AR and S_{11} bandwidths have been determined as h_d = w_d = 9 mm, h_p = 6 mm and w_p = 5 mm. Using these antenna configurations, an effective AR bandwidth of 4.64% has been obtained and consequently the resonance frequency is found to be 6.81 GHz, which is close to the predicted resonance frequency of 6.55 GHz for the broadside $TE_{01\delta}$ mode as calculated using equation (4-4).

h_d and w_d (mm)	h_p (mm)	w_p (mm)	3db AR Bandwidth (%)	-10dB S11 Bandwidth (%)	Overlapping AR & S11 Bandwidth (%)
9	4	5	0	0	0
		6	0	6.74	0
		7	0	2.32	0
	5	5	9.38	6.94	0
		6	6.13	11.32	0
		7	3.96	6.67	0
	6	**5**	**10.47**	**8.91**	**44.3**
		6	7.21	5.24	12.4
		7	3.08	0	0
9.5	4	5	8.66	4.63	52.3
		6	2.41	6.06	0
		7	3.77	0	0
	5	5	6.82	12.11	22.2
		6	1.97	5.41	0
		7	4.84	7.75	47.9
	6	5	5.08	7.49	0
		6	5.07	5.54	0
		7	3.63	0	0
10	4	5	6.94	5.65	11.7
		6	1.45	6.64	0
		7	4.96	8.32	0
	5	5	1.05	12.72	0
		6	2.23	5.38	14.2
		7	4.94	6.19	0
	6	5	0.3	6.94	0
		6	2.96	4.89	0
		7	4.22	3.98	0
10.54	4	5	0.47	10.13	0
		6	3.13	4.63	0
		7	4.06	7.67	0
	5	5	0.52	12.98	0
		6	4.31	5.19	0
		7	4.14	6.37	0
	6	5	0	9.51	0
		6	5.95	7.95	0
		7	3.75	5.15	0

Table 6.2: AR and S_{11} bandwidths for different

dimensions of the concentric half-loops

As can be seen from Table 6.2, only 44.3% of the AR bandwidth achieved using the optimized dimensions, has been attained within sufficient impedance matching bandwidth. Therefore, an integrated stub has been incorporated with the driven element so that a wider overlapping between the bandwidths can be obtained. The stub has been attached to the first metallic strip at position of p_s. The dimensions of the stub are given by l_s *and* w_s.

Table 6.3 shows the results for the stub optimization when the parameters of h_d = w_d = 9 mm, h_p = 6 mm, w_p = 5 mm, and g_d = 1 mm have been employed. With reference to the table, the widest effective AR bandwidth has been obtained when l_s = p_s = 1. After employing these optimized stub length and position, the results for different value of w_s are presented in Table 6.4, where it can be seen the effective AR bandwidth has increased to 7.35% when w_s = 2 mm. Furthermore, the resonance frequency of this antenna has been found to be 6.7 GHz, which corresponds to the $TE_{01\delta}$ mode. The performances of the DRA when the optimized matching stub is included are shown in Figure 6.15. In comparison to the DRA design without stub, it is evident that the addition of the stub has shifted the matching bandwidth to be closer to the AR bandwidth, thus increasing the effective AR bandwidth.

Stub postion, p_s(mm)	Stub length, l_s (mm)	3db AR Bandwidth (%)	-10dB S11 Bandwidth (%)	Overlapping AR & S11 Bandwidth (%)
1	**1**	**9.01**	**7.23**	**75.1**
	2	10.85	5.77	54.12
	3	5.99	12.86	0
2	1	9.05	23.69	63.3
	2	7.78	8.69	61.8
	3	2.19	12.03	0
3	1	9.28	21.74	34.1
	2	6.5	11.44	0
	3	0	12.14	0
4	1	8.48	15.85	0
	2	6.15	9.06	0
	3	0	10.51	0
5	1	8.41	13.31	0
	2	5.72	6.96	0
	3	0	5.26	0

Table 6.3: AR and S_{11} bandwidths for different dimensions of p_s and l_s

Stub width, ws (mm)	3db AR Bandwidth (%)	-10dB S11 Bandwidth (%)	Overlapping AR & S11 Bandwidth (%)
0.5	8.85	6.37	72.2
1	9.01	7.23	75.1
1.5	9.21	7.46	78.9
2	**9.17**	**7.69**	**80.2**
2.5	8.55	7.96	79.4
3	7.9	8.39	78.2

Table 6.4: AR and S_{11} bandwidths for different stub width
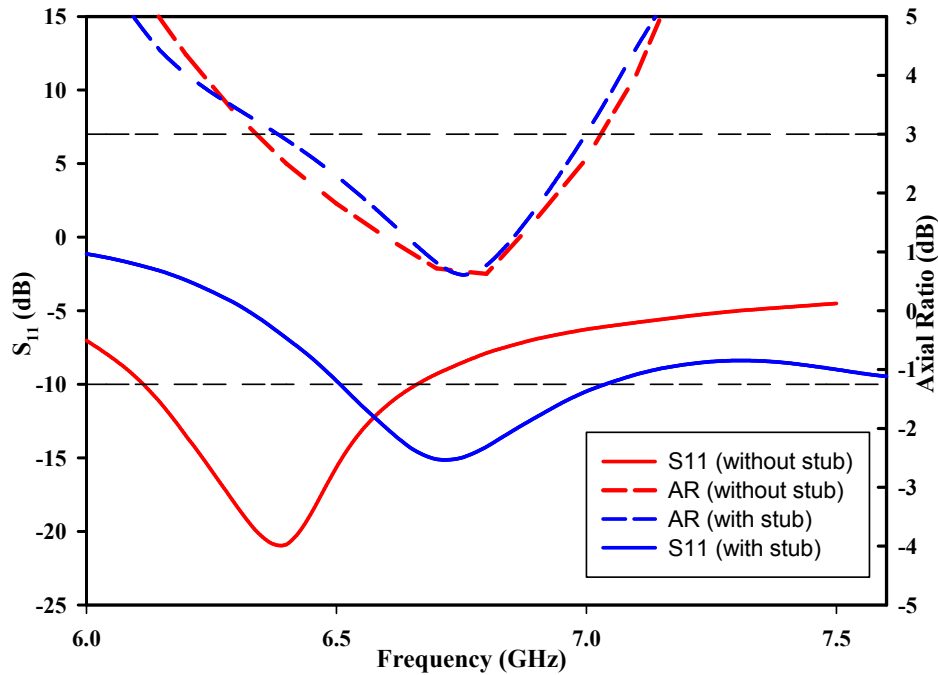
Figure 6.15: Axial ratio and return loss of DRA fed by half loop with or without stub

Figure 6.16 and 6.17 illustrate the CP bandwidth enhancement caused by the presence of the parasitic half-loop. The graphs show the variation of S_{11} and AR as functions of frequency for different dimensions of h_p and w_p when the optimized parameters of stub and the driven half-loop are employed. Additionally, the performance of the DRA without the presence of the parasitic element is also included as a reference. The inclusion of the parasitic element has created another AR minimal point at 6.45 GHz in addition to that generated by the driven half-loop at 6.75 GHz. The combination of these two points a constitutes an ~84% increase in the effective AR bandwidth compared to those achieved at the absence of the inner half-loop.
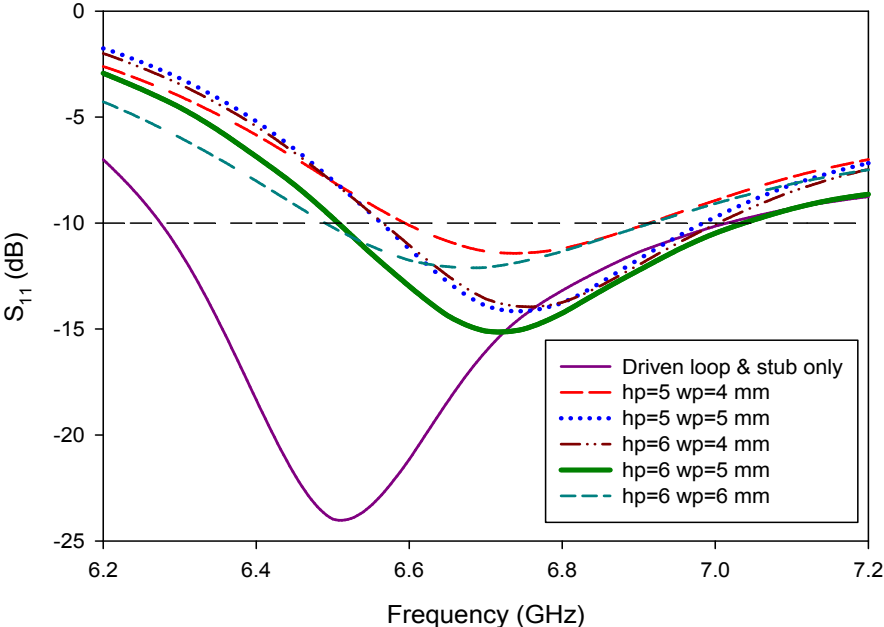
Figure 6.16: Return loss for different dimensions of parasitic half-loop
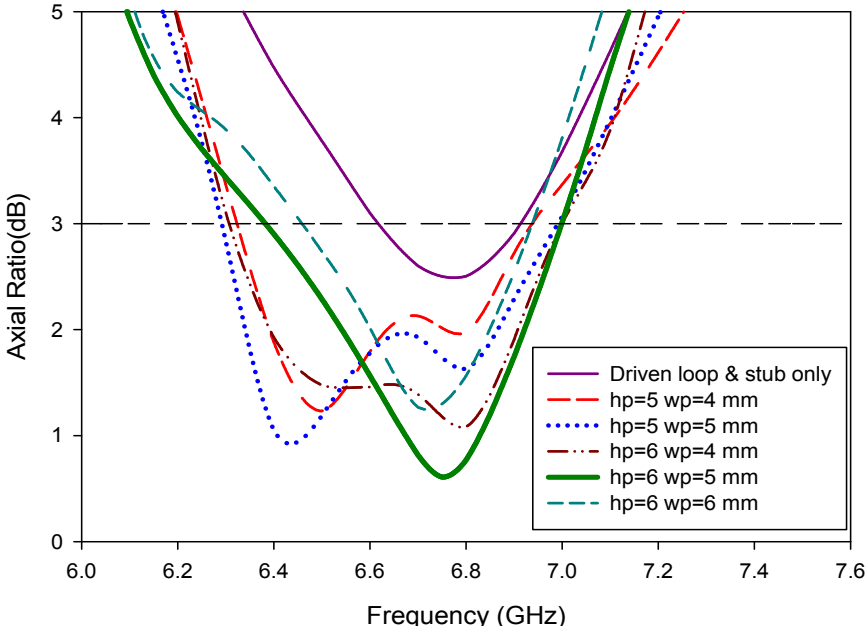
Figure 6.17: Axial ratio for different dimensions of parasitic half-loop

6.3.2   Results and Discussions

A prototype of a multilayer cylindrical DRA that is excited using concentric half-loops is illustrated in Figure 6.18. The inner layer height, radius, and relative permittivity are h_2 = 9.49 mm, a_2 = 6.31 mm and ε_{r2} = 5.67, respectively, while the outer layer has been designed using h = 10.54 mm, a = 7.01 mm and ε_r = 9.2 [8]. The optimized parameters of the feeding half-loops have been determined using the aforementioned iterative design procedure as $h_d = w_d$ = 9 mm, g_d = 1 mm, h_p = 6 mm, w_p = 5 mm, $p_s = l_s$ = 1 mm, and w_s = 2 mm.
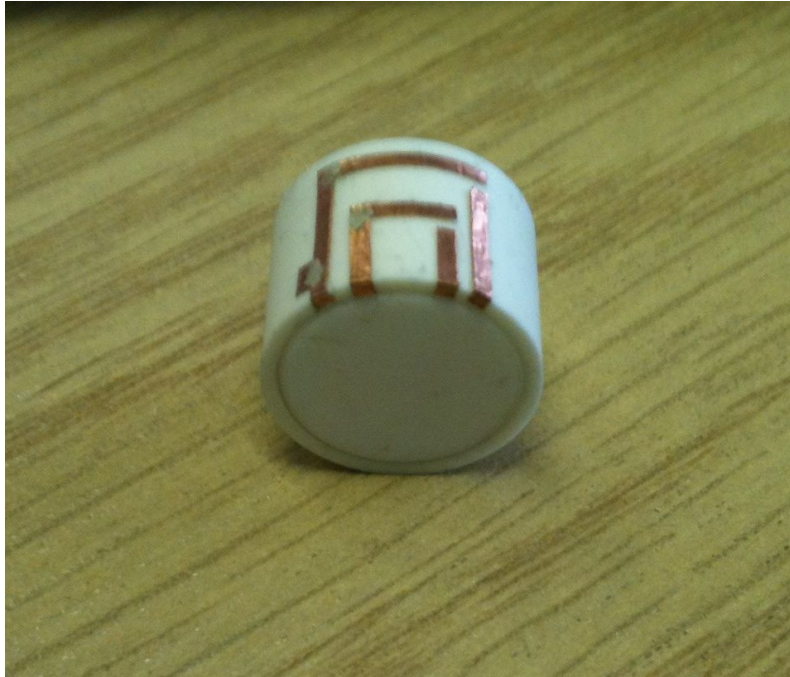
Figure 6.18: A multilayer cylindrical DRA fed by concentric half-loops.

Reasonable agreement has been obtained between the computed and measured input impedances as demonstrated in Figure 6.19. The experimental and theoretical return losses are presented in Figure 6.20, where it can be noticed that an $S_{11} \leq$ -10 dB bandwidth of 7.69% has been achieved in computations compared to 8.23% in measurements. The minimum S_{11} has been computed at

6.74 GHz compared to 6.92 GHz in the measurements, which represents a difference of 2.77% between the two results. This discrepancy can be attributed to measurements error, as the air gaps between the PEC ground plane and the antenna can not be fully eliminated since the cylindrical DRA is very lightweight, which has caused some difficultly in positioning it firmly on the ground plane. As demonstrated earlier in section 4.3.2, the predicted resonance frequency for the multilayer design operating in broadside $TE_{01\delta}$ mode has been calculated as 6.55 GHz, which is reasonably close to those obtained by the theory and experiment. Additionally, a travelling wave current distribution, which generates CP wave, has been attained along the half-loops as illustrated in Figure 6.21.
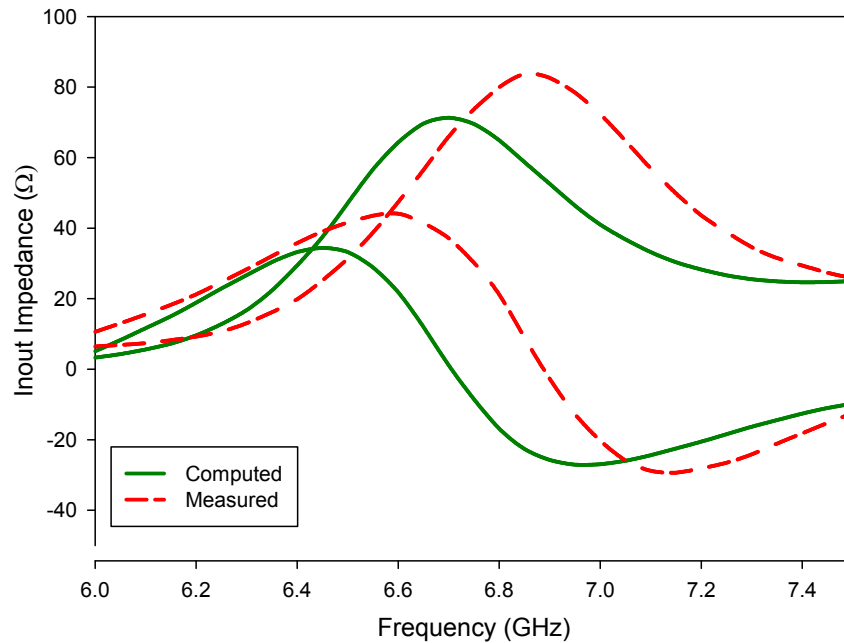
Figure 6.19: Input impedance of the multilayer cylindrical DRA excited using concentric half loop
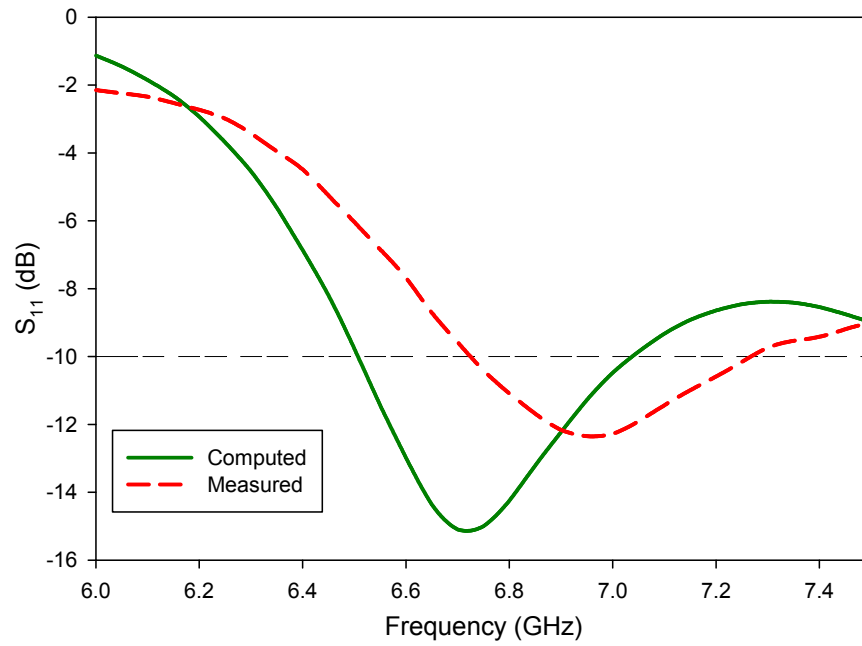
Figure 6.20: Return losses of the multilayer cylindrical DRA
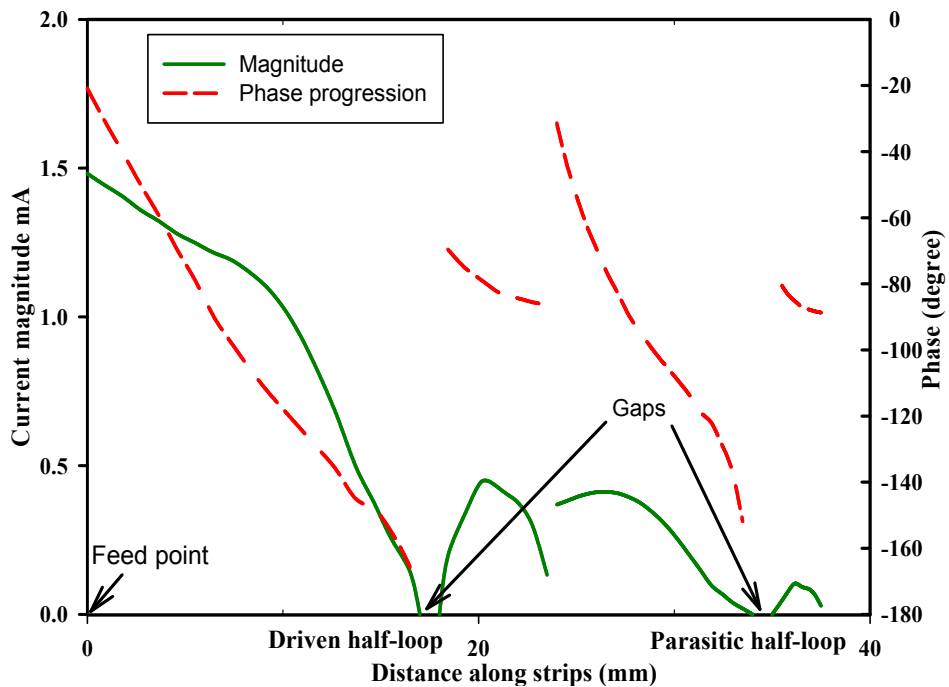
Figure 6.21: Current distribution along the concentric half-loops at 6.75 GHz

The bore-sight axial ratio has been computed and measured as demonstrated in Figure 6.22, where it can be seen that the minimum computed AR is 0.61 dB at 6.75 GHz compared to a corresponding measured value of 1.53 dB at 6.88 GHz. With reference to the figure, the theoretical 3 dB AR bandwidth extends from 6.38 to 7. GHz compared to 6.59 to 7.15 GHz in the measurements. Therefore, CP radiation has been achieved over bandwidths of 9.17% and 8.12% in the analysis and the measurements, respectively, which is more than double of what has been achieved for the CP cylindrical DRA excited by a driven half-loop only as discussed in section 5.3.2. Additionally, it is several folds higher than the AR bandwidth of ~2% reported in [8] for a cylindrical DRA with the same outer layer's dimensions and permittivity. Furthermore, the overlapping AR and S_{11} bandwidths from computations and measurements are shown in Figure 6.23. Based on the results, the theoretical effective AR bandwidth is found to be 7.35% compared to 6.45% in the experiment. It should be noted that if an $S_{11}<-7.5dB$ bandwidth (VSWR = 2.5) is considered, the effective AR bandwidth can be increased to 8.6% and 8.12% in the computations and measurements, respectively,
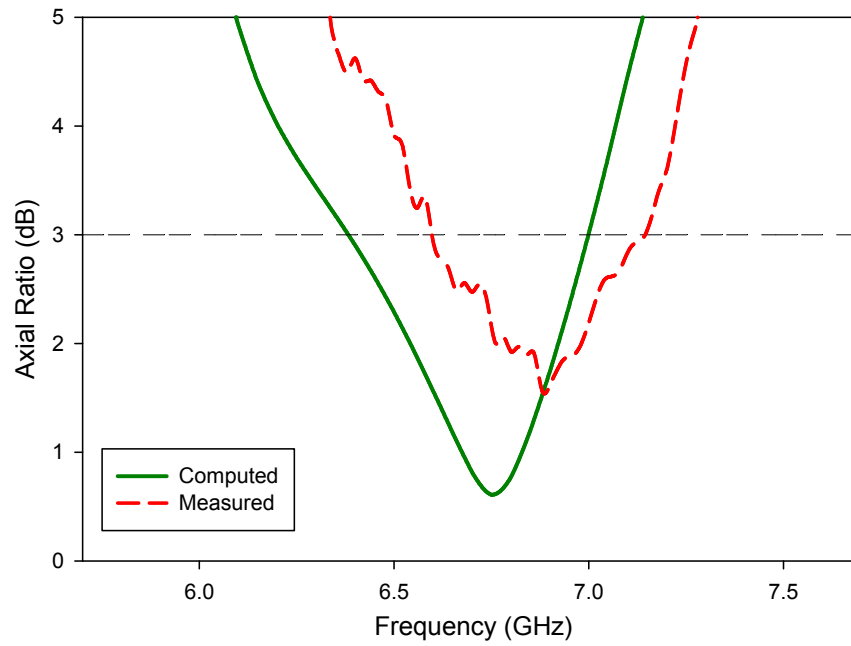
Figure 6.22: Axial ratio of the multilayer cylindrical DRA
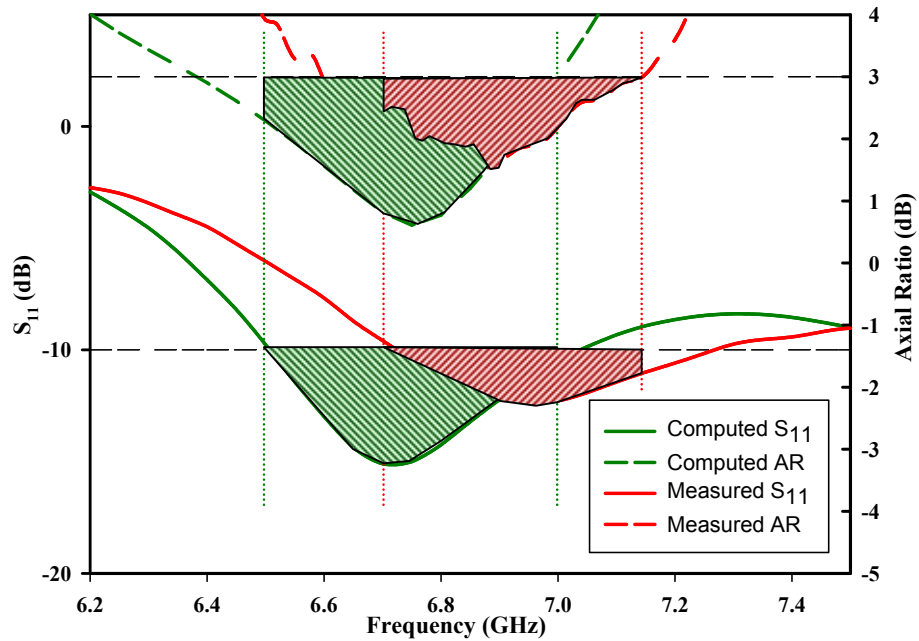
Figure 6.23: Region of overlapping bandwidths for S_{11} and AR

The axial ratio beam-width is demonstrated in Figures 6.24 and 6.25, where it can be noticed that the DRA offers circular polarization over measured beam-widths of over $39°$ in the both planes
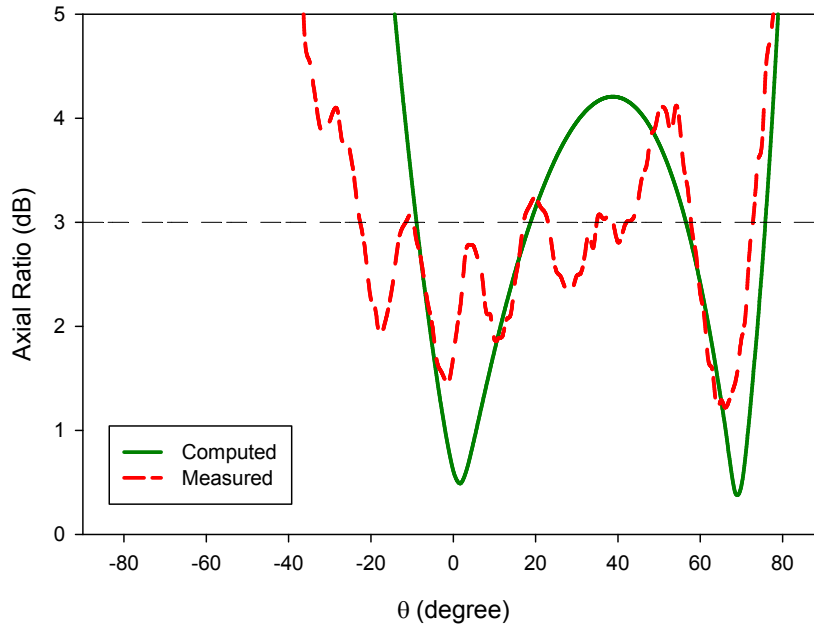
Figure 6.24: Axial ratio beam-width of the multilayer cylindrical DRA at $\phi = 0°$
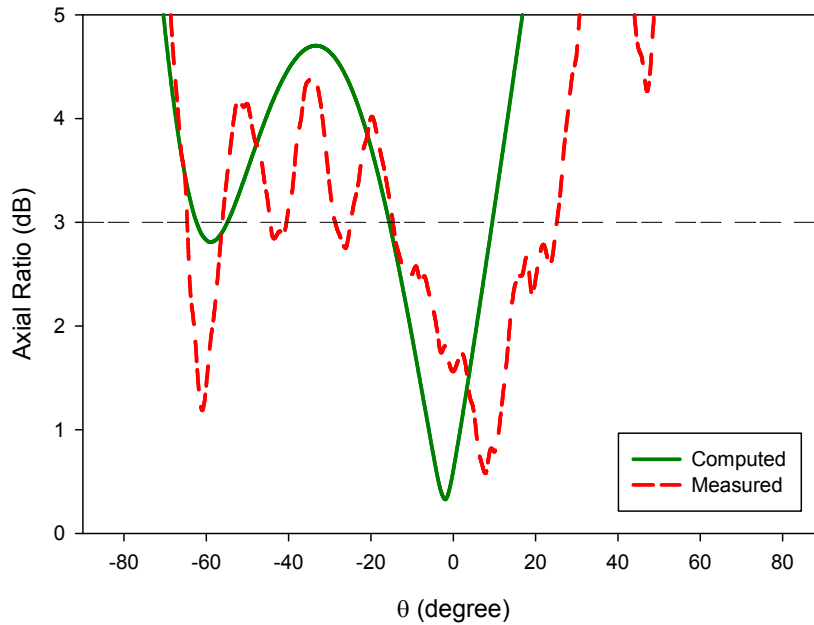
Figure 6.25: Axial ratio beam-width of the multilayer cylindrical DRA at $\phi = 90°$

Furthermore, the stability of the radiation pattern has been studied as shown in Figure 6.26, where it is evident that the patterns are stable across the whole CP bandwidth, and an isolation of more than 21 dB has been achieved between the co-, and cross-, polarization components at the minimum AR frequency point. As the RHCP field component is much stronger than LHCP field, the DRA radiates right-hand CP wave.
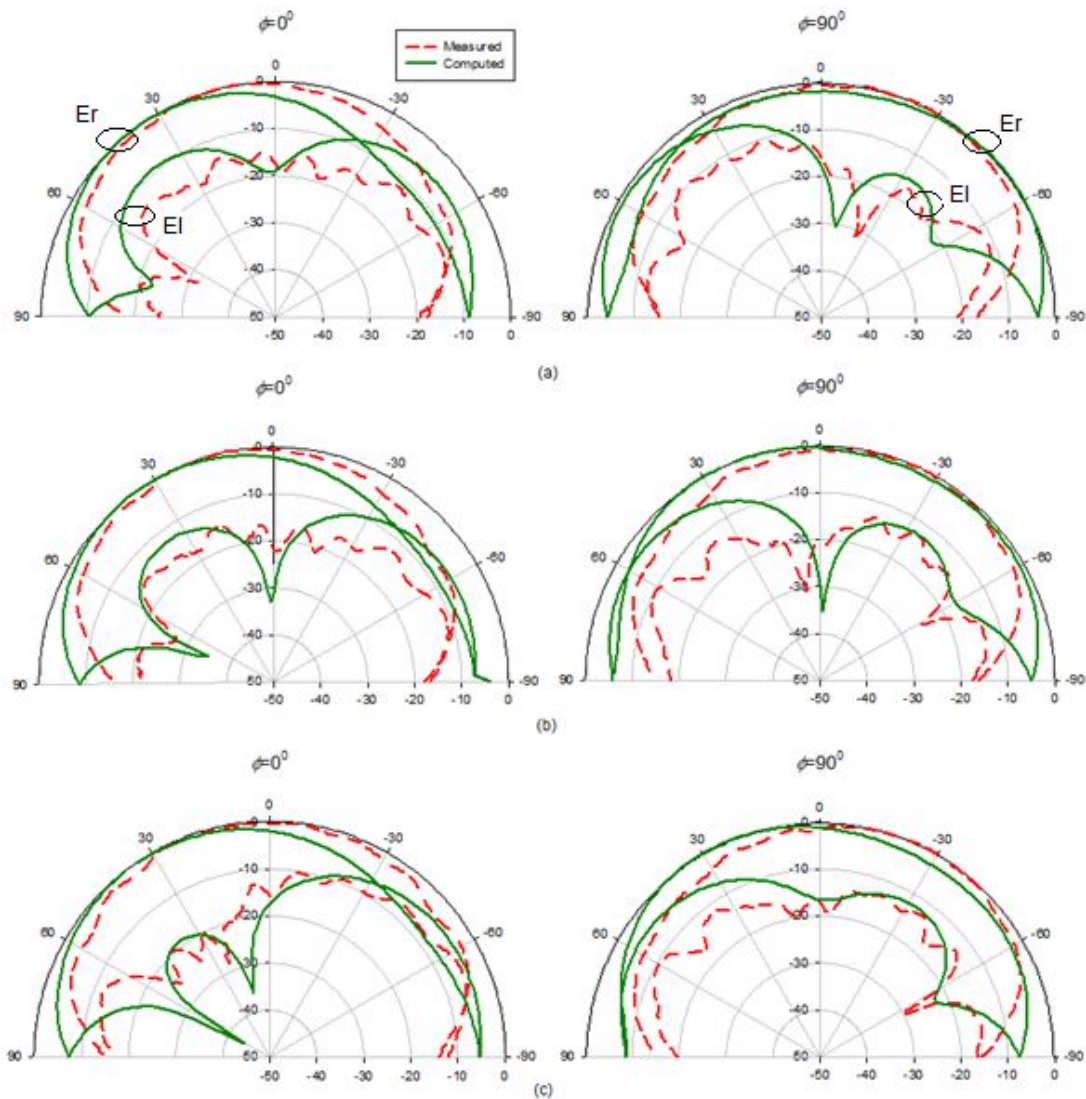
Figure 6.26: Radiation patterns of the multilayer cylindrical DRA at (a) beginning, (b) centre, and (c) end of the CP bandwidth.

Finally, Figure 6.27 presents the calculated and measured bore-sight gain of the antenna configuration, where it can be seen that a reasonable gain of approximately   3 dBi has been achieved throughout the circular polarization bandwidth in the theoretical and experimental results.
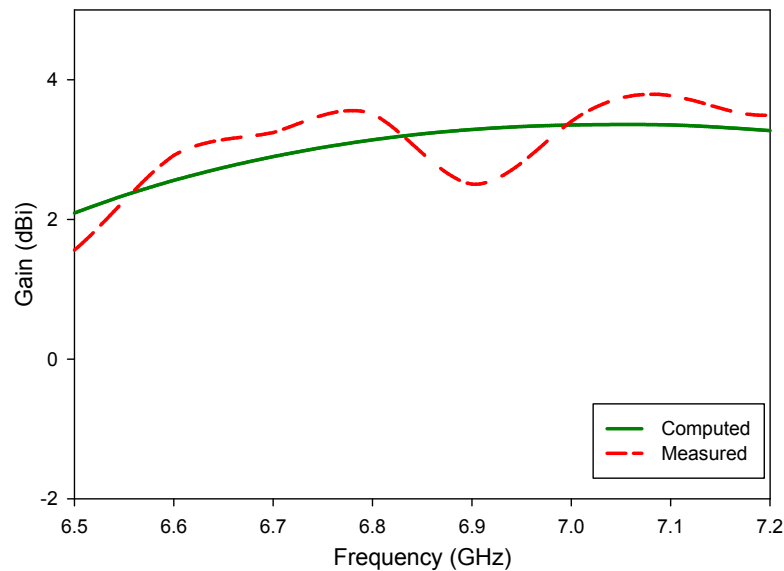
Figure 6.27: Gain of the multilayer cylindrical DRA

excited using concentric half-loop

6.4   Conclusions

The AR bandwidths of rectangular and cylindrical DRA have been increased substantially through the incorporation of an inner parasitic half-loop within the driven half-loop. With appropriate dimensions and placement of the parasitic element, the parasitic half-loop creates another minimum AR point at frequency close to that created by the driven half-loop. Thus, merging the two AR minimal points results in a wider circular polarization bandwidth. In both rectangular and

cylindrical DRA a configuration, the inclusion of concentric parasitic elements has approximately doubled the CP bandwidths compared to those obtained using the driven half-loops only. This is very desirable, since the parasitic half-loop has been included in the structure without increasing the antenna size or complexity. Throughout the research, reasonable agreement has been obtained between computations and measurements with some discrepancies that can be attributed to experimental tolerances, as well as fabrication and measurement errors.

References

[1] L. RongLin, G. DeJean, J. Laskar, and M. M. Tentzeris, "Investigation of circularly polarized loop antennas with a parasitic element for bandwidth enhancement," *IEEE Trans. Antennas Propagat.*, vol. 53, pp. 3930-3939, 2005.

[2] L. RongLin, A. Traille, J. Laskar, and M. M. Tentzeris, "Bandwidth and Gain Improvement of a Circularly Polarized Dual-Rhombic Loop Antenna," *IEEE Antennas and Wireless Propagation Letters*, vol. 5, pp. 84-87, 2006.

[3] Y. Xue-Xia, Z. Jian-Yong, and G. Yan-Yan, "Circularly polarized broadband dual loop antenna fed by coplane stripline," *IEEE International Symposium on Radio-Frequency Integration Technology*, pp. 315-318, 2009.

[4] L. RongLin, J. Laskar, and M. M. Tentzeris, "Broadband circularly polarized rectangular loop antenna with impedance matching," *IEEE Microwave and Wireless Components Letters*, vol. 16, pp. 52-54, 2006.

[5] L. RongLin, J. Laskar, and M. M. Tentzeris, "Wideband probe-fed circularly polarised circular loop antenna," *Electronics Letters*, vol. 41, pp. 997-999, 2005.

[6] B. Li, and K.W. Leung, "Strip-fed rectangular dielectric resonator antenna with/without a parasitic patch", *IEEE Trans. Antennas Propag.,* vol. 53, pp. 2200-2207, July 2005.

[7] R.K. Mongia, "Theoretical and Experimental Investigations on Rectangular Dielectric Resonators*," IEEE Proc.H*, vol.139, pp.98-104, Feb 1992

[8] M.T. Lee, K.M. Luk, E.K.N. Yung, and K.W. Leung, "Microstrip line fed circularly polarized cylindrical dielectric resonator antenna", *Microwave and Optic. Tech. Lett.* , Vol. 24, pp. 206-207, Feb 2000

[9] D.S. Killips, L. Kempel, D. Nyquist and E. Rothwell , "Analysis of layering dielectrics on effective permittivity using wave matrices"*, IEEE Antennas and Propag. Soc. International Symposium,* vol. 3A, pp. 216-, 2005.

CHAPTER 7

CONCLUSIONS AND

FUTURE WORK

7.1   Summary and Conclusions

The thesis focuses on the design of singly-fed DRAs with a wideband circular polarization. Two new single-point excitation schemes have been introduced that can be easily used to excite an arbitrarily shaped DRA. The proposed feeding methods are based on employing conformal conducting metal strips on the DRA surface. The generated broad CP bands have been achieved in conjunction with sufficient impedance matching bandwidths. The studied geometries have been modeled using a self developed MoM code, and the computed results have been validated against those obtained from measurements or CST simulations.

In chapter one, the theory of circular polarization has been discussed together with a concise literature review of dual and singly-fed CP DRAs. Additionally, the basic characteristics of several CEM modelling methods have been described. The second chapter provides details of the employed modelling method, where the steps involved in MoM computations, in conjunction with specialized basis and testing functions, have been described comprehensively.

In the third chapter, a new feeding scheme based on using a conformal square spiral has been employed to excite a rectangular DRA. The feeding spiral parameters have been optimized using an iterative design procedure to establish a travelling wave current distribution. This approach has produced a CP bandwidth of ~7%, which is considerably wider than the typical bandwidth of < 3% reported in earlier studies for singly-fed rectangular DRAs. Additionally, the frequency tuning ability of the wideband CP rectangular DRA has been demonstrated, where shifting the spiral from the centre to the right of the DRA surface has reduced the antenna operating frequency from 4.10 GHz to 2.93 GHz. This shift in the resonant frequency corresponds to a change in the excited mode from TE^y_{111} to TE^x_{111}. However, the achieved CP bandwidth is comparable to those obtained using a centrally located feeding spiral.

In Chapter 4, the versatility of the spiral excitation has been assessed by employing the feed to a cylindrical DRA to generate a wideband circular polarization radiation. Once more, using optimized parameters to achieve a travelling current distribution has generated a CP bandwidth of ~4% compared to ~2% reported in literature for singly-fed CP cylindrical DRAs. Additionally, the CP bandwidth of the cylindrical antenna has been enhanced further by employing a multilayer DRA configuration, where a smaller dielectric cylinder of different

permittivity has been embedded within the cylindrical DRA. This has provided an increase of more than 66% in the AR bandwidth compared with that using a single layer cylindrical DRA.

Despite the advantages of utilizing a square spiral excitation, it has been observed that the achieved CP radiation is very sensitive to the spiral dimensions. Furthermore, the required precise dimensions are particularly difficult to achieve when the spiral needs to be placed on a conformal surface. Therefore, a simpler feeding method that is capable of generating wideband CP radiation, without the aforementioned limitations, has been proposed in chapter 5. The new feed is based on exciting the DRA using a rectangular half-loop that consists of three metallic strips. The flexibility of this feeding method has been demonstrated by employing the half-loop to excite regular shaped DRAs such as rectangular, cylindrical and hemispherical geometries. Again, the achieved CP bandwidths are considerably higher than those reported in the literature for singly-fed DRAs of the same shapes and dimensions.

A further CP bandwidth enhancement has been achieved by incorporating a parasitic half-loop inside the driven element. Employing the optimized dimensions of the two concentric half-loops have produced two AR minima frequency points that are close to each other. Consequently, merging these two AR bands leads to a significant enhancement in the overall circular polarization bandwidth. The inclusion of a concentric parasitic element has approximately doubled the CP bandwidths compared to those obtained using only the driven half-loop for rectangular and cylindrical DRA configurations.

Tables 7.1-7.3 summarize the achieved CP bandwidths and the corresponding resonance frequencies for the studied DRAs configurations. The

results from published literature are included in the reference column for comparison purposes. From the tables, it is evident that the DRAs fed using introduced excitation schemes have produced considerably wider CP bandwidths compared to those reported in the literature for identical singly-fed DRAs. Furthermore, the bandwidth can be significantly enhanced by placing a parasitic element, with appropriate dimensions, inside the driven half-loop or by adding another dielectric layer.

	Reference [1]	Square spiral	Shifted square spiral	Rectangular half-loop	Rectangular half-loop with parasitic
Effective AR Bandwidth (%)	**2.7**	6.6	6.4	6.5	12.71
Resonance Frequency (GHz)	**3.55**	4.1	2.93	3.5	3.53

Table 7.1: Effective AR bandwidth and the corresponding resonance frequency for various rectangular DRA configurations

	Reference [2]	Square spiral	Square spiral, multi layer	Rectangular half-loop	Rectangular half-loop with parasitic, multilayer
Effective AR Bandwidth (%)	**2.2**	3.48	5.63	3.63	7.35
Resonance Frequency (GHz)	**6.38**	5.89	6.25	5.76	6.74

Table 7.2: Effective AR bandwidth and the corresponding resonance frequency for various cylindrical DRA configurations

	Reference [3]	Rectangular half-loop	Rectangular half-loop, multilayer
Effective AR Bandwidth (%)	**4.5**	7.61	8.5
Resonance Frequency (GHz)	**3.98**	5.66	4.09

Table 7.3: Effective AR bandwidth and the corresponding resonance frequency for various hemispherical DRA configurations

7.2   Future Work

This research has demonstrated the ability of the proposed new excitation schemes to obtain wideband circular polarizations in conjunction with sufficient impedance matching bandwidths for each of the considered DRA configurations. For the future work, the following topics are worthy of further investigations;

Due to limited cost and time constraint, each of the excitation schemes have been employed for the excitation of regular shaped DRAs. Thus, it would be interesting to see how the feeding methods fare in comparison with other published excitation schemes when used to excite irregular shaped DRAs such as staircase and trapezoidal geometries. Furthermore, it is possible to investigate the design of CP DRA using a square spiral slot excitation. From extensive review of earlier studies, this DRA configuration has never been done in contrast to the open loop slot excitation schemes. Although this requires additional development of the existing complex MoM code, there is a very good potential of such feeding method to generate a wideband CP.

The proposed excitation methods can also be used to feed DRAs with higher permittivities to investigate the possibility of achieving a CP radiation from a reduced size DRA. It is expected that such DRAs will offer narrower CP bandwidths in conjunction with a lower profile. Additionally, a further measure to reduce the CP DRA profile is to employ an artificial magnetic conducting (AMC) surface in conjunction with the proposed excitation approaches.

Additionally, a better representation of curved geometries can be obtained using higher order RWG and SWG basis functions. The application of a more refined triangle and tetrahedron elements, as opposed to the flat elements used in

the first order basis function, leads to higher accuracy and less memory requirements for the solution of problem in 3-D.

References

[1] B.Li and K.W.Leung, "Strip-Fed Rectangular Dielectric Resonator Antennas With/Without a Parasitic Patch," *IEEE Trans. Antennas Propag*, vol.53, no.7, pp. 2200-2207, July 2005

[2] M.T. Lee, K.M. Luk, E.K.N. Yung, and K.W. Leung, "Microstrip line feed circularly polarized cylindrical dielectric resonator antenna", *Microwave and Optic. Tech. Lett.* , Vol. 24, pp. 206-207, Feb 2000

[3] H.K. Ng and K.W. Leung, "Excitation of CP Aperture Coupled Dielectric Resonator Antenna with a Parasitic Patch", *IEEE Antennas and Propagat Soc. Int. Symposium,* Vol. 4, pp. 202-205, 2001

APPENDIX A

1. Code execution flowchart

Collect inputs describing antenna mesh → Collect inputs from user → Display information based on raw data → Define basis functions and calculate their parameters

Collect inputs from user:
- Frequency range
- Antenna mode
- Permittivity of dielectric

Antenna mode:
- Transmitter
- Receiver

Transmitter: Solution method
- Normal
- Image theory

Receiver: Angle of plane wave incidence
- θ (in π)
- Φ (in π)

- Treatment of surface metal using RWG basis function
  Obtain parameters of
  - single triangle
  - triangle pair
- Treatment of dielectric volume using SWG basis function
  Obtain parameters of
  - single tetrahedron
  - tetrahedron pair
  - single triangle (boundary)
  - triangle pair (boundary)

Calculate integrals
- Surface integrals
  - For self integrals: Analytical formula
  - Gaussian quadrature
- Volume integrals
  - For self integrals: Analytical formula
  - Gaussian quadrature

Calculate potentials and fill impedance matrices
- Z_{mn}^{MM}
- Z_{mn}^{DD}
- Z_{mn}^{DM}
- Z_{mn}^{MD}

Calculate antenna parameters
- Near-field
  - Input Impedance
  - Current Distribution
- Far-field
  - E_θ and E_Φ
  - E_R and E_L
  - Axial Ratio
  - Gain

2. Code segments of core modules

2.1 Calculation of Surface Integrals

```
-------------------------------
CALCULATION OF INTEGRALS
DO p=1,n_total_M_tri
  DO q=1,n_total_M_tri
    d1=c_x(p)-c_x(q)            !c_x(p)=centroid of triangle p in x-axis
    d2=c_y(p)-c_y(q)
    d3=c_z(p)-c_z(q)
    dist=sqrt(d1**2+d2**2+d3**2)  !Distance between source&observation points
    IF(dist.LT.0.001) THEN      !If distance less than 0.0001
    i_counter=1
    CALL ANALYTICAL             !Calculation using analytical formula
    CALL SUR_SING_QUAD
    ELSE                        !Else distance bigger than 0.0001
    i_counter=4
    CALL SUR_NUM_QUAD           !Calculation using Gaussian quadrature
    ENDIF
  ENDDO
ENDDO
```

i) Calculation using analytical formula

Variables required for calculation of self integrals using analytical formula are shown in eq. (2-100) to (2-111) in chapter 2. For ease of understanding, the code is shown for each equation separately.

$$\hat{l}_i = \frac{\vec{\rho}_i^{+} - \vec{\rho}_i^{-}}{\left| \vec{\rho}_i^{+} - \vec{\rho}_i^{-} \right|} \qquad\qquad (2\text{-}100)$$

```
-------------------------------
side_x1=x1-x2                              !x1=rho_x(1), x2=rho_x(2)
side_y1=y1-y2
side_z1=z1-z2
mag=sqrt(side_x1**2+side_y1**2+side_z1**2)  !magnitude of l(1)
unit_l1=(/ side_x1/mag,side_y1/mag,side_z1/mag /)   !unit l(1)

side_x2=x2-x3                              !x2=rho_x(2), x3=rho_x(3)
side_y2=y2-y3
side_z2=z2-z3
mag=sqrt(side_x2**2+side_y2**2+side_z2**2)  !magnitude of l(2)
unit_l2=(/ side_x2/mag,side_y2/mag,side_z2/mag /)   !unit l(2)

side_x3=x3-x1                              !x3=rho_x(3), x1=rho_x(1)
side_y3=y3-y1
side_z3=z3-z1
mag=sqrt(side_x3**2+side_y3**2+side_z3**2)  !magnitude of l(3)
unit_l3=(/ side_x3/mag,side_y3/mag,side_z3/mag /)   !unit l(3)
```

$$\boxed{l_i^{\,\pm} = \left(\vec{\rho}_i^{\,\pm} - \vec{\rho}\right)\bullet \hat{l}} \qquad\qquad (2\text{-}101)$$

```
------------------------------------
l1_p=(/ rho1_p(1)-rho(1),rho1_p(2)-rho(2),rho1_p(3)-rho(3) /) !rho1_p(1)=rho(1) positive
l1_n=(/ rho1_n(1)-rho(1),rho1_n(2)-rho(2),rho1_n(3)-rho(3) /) !rho1_n(1)=rho(1) negative
l2_p=(/ rho2_p(1)-rho(1),rho2_p(2)-rho(2),rho2_p(3)-rho(3) /)
l2_n=(/ rho2_n(1)-rho(1),rho2_n(2)-rho(2),rho2_n(3)-rho(3) /)
l3_p=(/ rho3_p(1)-rho(1),rho3_p(2)-rho(2),rho3_p(3)-rho(3) /)
l3_n=(/ rho3_n(1)-rho(1),rho3_n(2)-rho(2),rho3_n(3)-rho(3) /)

el1_p=dot_product(l1_p,unit_l1) !el1_p=l(1) positive
el1_n=dot_product(l1_n,unit_l1) !el1_n=l(1) negative
el2_p=dot_product(l2_p,unit_l2)
el2_n=dot_product(l2_n,unit_l2)
el3_p=dot_product(l3_p,unit_l3)
el3_n=dot_product(l3_n,unit_l3)
```

$$\boxed{P_i^{\,0} = \left|\left(\vec{\rho}_i^{\,\pm} - \vec{\rho}\right)\bullet \hat{u}_i\right|} \qquad \text{where } \hat{u}_i = \hat{l}_i \times \hat{n}_i \qquad\qquad (2\text{-}102)$$

```
------------------------------------
side1=(/ side_x1,side_y1,side_z1 /)
side2=(/ side_x2,side_y2,side_z2 /)

CALL CROSS_PRO(side1,side2,vec_n)        !normal vector=cross product of side 1&2
mag=sqrt(vec_n(1)**2+vec_n(2)**2+vec_n(3)**2)        !magnitude of normal vector
unit_n=(/ vec_n(1)/mag,vec_n(2)/mag,vec_n(3)/mag /)!unit normal vector

CALL CROSS_PRO(unit_l1,unit_n,unit_u1) !unit u=cross product unit l&unit n
CALL CROSS_PRO(unit_l2,unit_n,unit_u2)
CALL CROSS_PRO(unit_l3,unit_n,unit_u3)
```
```
Po1=abs(dot_product(l1_p,unit_u1))
Po2=abs(dot_product(l2_p,unit_u2))
Po3=abs(dot_product(l3_p,unit_u3))
```

$$\boxed{P_i^{\,\pm} = \left|\vec{\rho}_i^{\,\pm} - \vec{\rho}\right| = \sqrt{\left(P_i^{\,0}\right)^2 + \left(l_i^{\,\pm}\right)^2}} \qquad\qquad (2\text{-}103)$$

```
------------------------------------
Po1_p=sqrt(Po1**2+el1_p**2)
Po1_n=sqrt(Po1**2+el1_n**2)
Po2_p=sqrt(Po2**2+el2_p**2)
Po2_n=sqrt(Po2**2+el2_n**2)
Po3_p=sqrt(Po3**2+el3_p**2)
Po3_n=sqrt(Po3**2+el3_n**2)
```

$$\hat{P}_i^0 = \frac{\left(\vec{\rho}_i^{\pm} - \vec{\rho}\right) - l_i^{\pm}\hat{l}}{P_i^0}$$

(2-104)

```
-----------------------------------
u1x=(l1_p(1)-el1_p*unit_l1(1))/Po1
u1y=(l1_p(2)-el1_p*unit_l1(2))/Po1
u1z=(l1_p(3)-el1_p*unit_l1(3))/Po1
u2x=(l2_p(1)-el2_p*unit_l2(1))/Po2
u2y=(l2_p(2)-el2_p*unit_l2(2))/Po2
u2z=(l2_p(3)-el2_p*unit_l2(3))/Po2
u3x=(l3_p(1)-el3_p*unit_l3(1))/Po3
u3y=(l3_p(2)-el3_p*unit_l3(2))/Po3
u3z=(l3_p(3)-el3_p*unit_l3(3))/Po3

unit_Po1=(/ u1x,u1y,u1z /)
unit_Po2=(/ u2x,u2y,u2z /)
unit_Po3=(/ u3x,u3y,u3z /)
```

$$R_i^0 = \sqrt{\left(P_i^0\right)^2 + d^2}$$

(2-105)

```
-------------------------------
R1_o=sqrt(Po1**2+d**2)
R2_o=sqrt(Po2**2+d**2)
R3_o=sqrt(Po3**2+d**2)
```

$$R_i^{\pm} = \sqrt{\left(P_i^{\pm}\right)^2 + d^2}$$

(2-106)

```
-------------------------------
R1_p=sqrt(Po1_p**2+d**2)
R1_n=sqrt(Po1_n**2+d**2)
R2_p=sqrt(Po2_p**2+d**2)
R2_n=sqrt(Po2_n**2+d**2)
R3_p=sqrt(Po3_p**2+d**2)
R3_n=sqrt(Po3_n**2+d**2)
```

$$d = \hat{n}_i \bullet \left(\vec{r} - \vec{r}_i^{\pm}\right)$$

(2-107)

```
-------------------------------
r_r1=(/ r(1)-r1(1),r(2)-r1(2),r(3)-r1(3) /)
d=dot_product(unit_n,r_r1)
```

The calculations of eq. (2-108) and (2-109) are not required since the eq. have already been determined in terms of $\vec{\rho}_i^{\,+}$, $\vec{\rho}_i^{\,-}$ and $\vec{\rho}$. Finally, using the variables derived previously, the self-integrals can be calculated by eq. (2-110) and (2-111)

$$\int_S \frac{dS'}{R} = \sum_i \hat{P}_i^0 \bullet \hat{u}_i \left[P_i^0 \ln \frac{R_i^+ + l_i^+}{R_i^- - l_i^-} - |d| \left(\tan^{-1} \frac{P_i^0 l_i^+}{\left(R_i^0\right)^2 + |d| R_i^+} - \tan^{-1} \frac{P_i^0 l_i^-}{\left(R_i^0\right)^2 + |d| R_i^-} \right) \right] \quad (2\text{-}110)$$

```
-----------------------------------
 IF(i_counter.EQ.1.OR.i_counter.EQ.33.OR.i_counter.EQ.11) THEN
 Sum1=dot_product(unit_Po1,unit_u1)*
7      (Po1*log((R1_p+el1_p)/(R1_n+el1_n))
7      -abs(d)*(atan((Po1*el1_p)/(R1_o**2+abs(d)*R1_p))
7                -atan((Po1*el1_n)/(R1_o**2+abs(d)*R1_n))))
 Sum2=dot_product(unit_Po2,unit_u2)*
7      (Po2*log((R2_p+el2_p)/(R2_n+el2_n))
7      -abs(d)*(atan((Po2*el2_p)/(R2_o**2+abs(d)*R2_p))
7                -atan((Po2*el2_n)/(R2_o**2+abs(d)*R2_n))))
 Sum3=dot_product(unit_Po3,unit_u3)*
7      (Po3*log((R3_p+el3_p)/(R3_n+el3_n))
7      -abs(d)*(atan((Po3*el3_p)/(R3_o**2+abs(d)*R3_p))
7                -atan((Po3*el3_n)/(R3_o**2+abs(d)*R3_n))))
 Sum_l(q)=(Sum1+Sum2+Sum3)
```

$$\int_S \frac{\vec{\rho}' - \vec{\rho}}{R} dS' = \frac{1}{2} \sum_i \hat{u}_i \left[\left(R_i^0\right)^2 \ln \frac{R_i^+ + l_i^+}{R_i^- + l_i^-} + l_i^+ R_i^+ - l_i^- R_i^- \right] \quad (2\text{-}111)$$

```
-----------------------------------
 Sum1v=unit_u1*(R1_o*R1_o*log((R1_p+el1_p)/(R1_n+el1_n))
7               +el1_p*R1_p-el1_n*R1_n)
 Sum2v=unit_u2*(R2_o*R2_o*log((R2_p+el2_p)/(R2_n+el2_n))
7               +el2_p*R2_p-el2_n*R2_n)
 Sum3v=unit_u3*(R3_o*R3_o*log((R3_p+el3_p)/(R3_n+el3_n))
7               +el3_p*R3_p-el3_n*R3_n)
 Sum_v(:,q)=0.5*(Sum1v+Sum2v+Sum3v)
```

ii) Calculation using Gaussian quadrature

The Gaussian quadrature formula for surface integrals is shown in Table 2.1. As calculation of surface integrals does not significantly affect the computational time compared to volume integrals, maximum number of source points (i.e. $n_p=7$), has been used to maintain computational accuracy. The following code shows the calculation of surface integrals, based on the formula given in the table.

```
x1=rx(1,q)      !rx(1,q)=the x-axis coordinate of nodes 1 in source triangle
y1=ry(1,q)
z1=rz(1,q)
x2=rx(2,q)      !rx(2,q)=the x-axis coordinate of nodes 2 in source triangle
y2=ry(2,q)
z2=rz(2,q)
x3=rx(3,q)      !rx(3,q)=the x-axis coordinate of nodes 3 in source triangle
y3=ry(3,q)
z3=rz(3,q)


----------------------------------
a=0.
b=1./3.
c=1./2.
d=1.

Rx1=a*(x1-x3)+a*(x2-x3)+x3-Xcp    !Xcp=centroid of observation triangle in x-axis
Ry1=a*(y1-y3)+a*(y2-y3)+y3-Ycp    !Ycp=centroid of observation triangle in y-axis
Rz1=a*(z1-z3)+a*(z2-z3)+z3-Zcp    !Zcp=centroid of observation triangle in z-axis
R_1=sqrt(Rx1*Rx1+Ry1*Ry1+Rz1*Rz1)!magnitude of R1

Rx2=c*(x1-x3)+a*(x2-x3)+x3-Xcp
Ry2=c*(y1-y3)+a*(y2-y3)+y3-Ycp
Rz2=c*(z1-z3)+a*(z2-z3)+z3-Zcp
R_2=sqrt(Rx2*Rx2+Ry2*Ry2+Rz2*Rz2)

Rx3=d*(x1-x3)+a*(x2-x3)+x3-Xcp
Ry3=d*(y1-y3)+a*(y2-y3)+y3-Ycp
Rz3=d*(z1-z3)+a*(z2-z3)+z3-Zcp
R_3=sqrt(Rx3*Rx3+Ry3*Ry3+Rz3*Rz3)

Rx4=c*(x1-x3)+c*(x2-x3)+x3-Xcp
Ry4=c*(y1-y3)+c*(y2-y3)+y3-Ycp
Rz4=c*(z1-z3)+c*(z2-z3)+z3-Zcp
R_4=sqrt(Rx4*Rx4+Ry4*Ry4+Rz4*Rz4)

Rx5=a*(x1-x3)+d*(x2-x3)+x3-Xcp
Ry5=a*(y1-y3)+d*(y2-y3)+y3-Ycp
Rz5=a*(z1-z3)+d*(z2-z3)+z3-Zcp
R_5=sqrt(Rx5*Rx5+Ry5*Ry5+Rz5*Rz5)

Rx6=a*(x1-x3)+c*(x2-x3)+x3-Xcp
Ry6=a*(y1-y3)+c*(y2-y3)+y3-Ycp
Rz6=a*(z1-z3)+c*(z2-z3)+z3-Zcp
R_6=sqrt(Rx6*Rx6+Ry6*Ry6+Rz6*Rz6)
```

```
Rx7=b*(x1-x3)+b*(x2-x3)+x3-Xcp
Ry7=b*(y1-y3)+b*(y2-y3)+y3-Ycp
Rz7=b*(z1-z3)+b*(z2-z3)+z3-Zcp
R_7=sqrt(Rx7*Rx7+Ry7*Ry7+Rz7*Rz7)

G1 =cexp(-j*k*R_1)/R_1      !G=ejkR/R
G2 =cexp(-j*k*R_2)/R_2
G3 =cexp(-j*k*R_3)/R_3
G4 =cexp(-j*k*R_4)/R_4
G5 =cexp(-j*k*R_5)/R_5
G6 =cexp(-j*k*R_6)/R_6
G7 =cexp(-j*k*R_7)/R_7

e=1./40.
f=1./15.
h=9./40.

ANS1(p,q)=G1*e+G2*f+G3*e+G4*f+G5*e+G6*f+G7*h          !Integral I(p,q)
ANS2(p,q)=G1*e*a+G2*f*c+G3*e*d+G4*f*c+G5*e*a+G6*f*a+G7*b*h  !Integral I_zeta(p,q)
ANS3(p,q)=G1*e*a+G2*f*a+G3*e*a+G4*f*c+G5*e*d+G6*f*c+G7*b*h  !Integral I_eta(p,q)
```

2.2 Calculation of Volume Integrals

```
CALCULATION OF INTEGRALS
DO p=1,n_D_in_tet
  DO q=1,n_D_in_tet
  d1=c_x_v(p)-c_x_v(q)        !c_x_v(p)=Centroid of tetrahedron p in x-axis
  d2=c_y_v(p)-c_y_v(q)
  d3=c_z_v(p)-c_z_v(q)
  dist=sqrt(d1**2+d2**2+d3**2)   !Distance between source&observation points
  IF(dist.LT.0.001) THEN          !If distance less than 0.001
  DO i_counter=41,44
  CALL ANALYTICAL                 !Calculation using analytical formula
  ENDDO
  CALL VOL_SING_QUAD
  ELSE
  i_counter=25
  CALL VOL_NUM_QUAD               !Calculation using Gaussian quadrature
  END IF
  ENDDO
ENDDO
```

i) Calculation using analytical formula

Variables required for calculation of self integrals (for volume integration) using analytical formula are shown in eq. (2-100) to (2-109) and (2-112) to (2113). The codes to calculate variables in eq. (2-100) to (2-109) have been shown previously.

$$\int_V \frac{dV'}{R} = \sum_j d_j \sum_i \hat{P}_i^0 \bullet \hat{u}_i$$

$$\times \left[|d_j| \left(\tan^{-1} \frac{P_{ij}^0 l_{ij}^+}{\left(R_{ij}^0\right)^2 + |d_j| R_{ij}^+} - \tan^{-1} \frac{P_{ij}^0 l_{ij}^-}{\left(R_{ij}^0\right)^2 + |d_j| R_{ij}^-} \right) - P_{ij}^0 \ln \frac{R_{ij}^+ + l_{ij}^+}{R_{ij}^- + l_{ij}^-} \right] \qquad (2\text{-}112)$$

```
 Sum1=dot_product(unit_Po1,unit_u1)*
7      (abs(d)*(atan((Po1*el1_p)/(R1_o**2+abs(d)*R1_p))
7               -atan((Po1*el1_n)/(R1_o**2+abs(d)*R1_n)))
7      -(Po1*log((R1_p+el1_p)/(R1_n+el1_n))))
 Sum2=dot_product(unit_Po2,unit_u2)*
7      (abs(d)*(atan((Po2*el2_p)/(R2_o**2+abs(d)*R2_p))
7               -atan((Po2*el2_n)/(R2_o**2+abs(d)*R2_n)))
7      -(Po2*log((R2_p+el2_p)/(R2_n+el2_n))))
 Sum3=dot_product(unit_Po3,unit_u3)*
7      (abs(d)*(atan((Po3*el3_p)/(R3_o**2+abs(d)*R3_p))
7               -atan((Po3*el3_n)/(R3_o**2+abs(d)*R3_n)))
7      -(Po3*log((R3_p+el3_p)/(R3_n+el3_n))))
 Sum_11=(Sum1+Sum2+Sum3)
```

$$\int_S \frac{\vec{r}' - \vec{r}}{R} dV' = \frac{1}{3} \sum_j \hat{n}_j \left\{ \sum_i \hat{P}_{ij}^0 \bullet \hat{u}_{ij} \left[\frac{P_{ij}^0 \left[\left(R_{ij}^0\right)^2 + 2d_j^2 \right]}{2} \ln \frac{R_{ij}^+ + l_{ij}^+}{R_{ij}^- + l_{ij}^-} \right. \right.$$

$$(2\text{-}113)$$

$$\left. \left. + \frac{P_{ij}^0}{2} \left(l_{ij}^+ R_{ij}^+ - l_{ij}^- R_{ij}^- \right) - |d_j|^3 \left(\tan^{-1} \frac{P_{ij}^0 l_{ij}^+}{\left(R_{ij}^0\right)^2 + |d_J| R_{ij}^+} - \tan^{-1} \frac{P_{ij}^0 l_{ij}^-}{\left(R_{ij}^0\right)^2 + |d_j| R_{ij}^-} \right) \right] \right\}$$

```
 Sum1v=dot_product(unit_Po1,unit_u1)*(((Po1*(R1_o**2+2*d*d)/2))*
7      log((R1_p+el1_p)/(R1_n+el1_n))+Po1/2*(el1_p*R1_p-el1_n*R1_n)
7      -(abs(d))**3*(atan((Po1*el1_p)/(R1_o**2+abs(d)*R1_p))
7                    -atan((Po1*el1_n)/(R1_o**2+abs(d)*R1_n))))
 Sum2v=dot_product(unit_Po2,unit_u2)*(((Po2*(R2_o**2+2*d*d)/2))*
7      log((R2_p+el2_p)/(R2_n+el2_n))+Po2/2*(el1_p*R2_p-el2_n*R2_n)
7      -(abs(d))**3*(atan((Po2*el2_p)/(R2_o**2+abs(d)*R2_p))
7                    -atan((Po2*el2_n)/(R2_o**2+abs(d)*R2_n))))
 Sum3v=dot_product(unit_Po3,unit_u3)*(((Po3*(R3_o**2+2*d*d)/2))*
7      log((R3_p+el3_p)/(R3_n+el3_n))+Po3/2*(el3_p*R3_p-el3_n*R3_n)
7      -(abs(d))**3*(atan((Po3*el3_p)/(R3_o**2+abs(d)*R3_p))
7                    -atan((Po3*el3_n)/(R3_o**2+abs(d)*R3_n))))
 Sum_v1=(Sum1v+Sum2v+Sum3v)
```

ii) Calculation using Gaussian quadrature

The Gaussian quadrature formula for volume integrals is shown in Table 2.2. In order to ensure efficient calculation of the integrals, the formula is applied based on the separation distance between the source point, $\vec{r}'$, and the observation point, $\vec{r}$, i.e. $R = |\vec{r} - \vec{r}'|$. In order to maintain the required accuracy, more number of points, n_p, is needed for smaller R. In this case, the number of points, n_p used in the calculation is 11. For the integrals calculation involving points separated by larger R, it is more efficient to use a smaller n_p since the solution yields results just as accurate as that obtained using a higher n_p. The n_p used for such cases are 1 and 5.

```
x1=rx_v(1,q)  !rx_v(1,q)=the x-axis coordinate of nodes 1 in source tetrahedron
y1=ry_v(1,q)
z1=rz_v(1,q)
x2=rx_v(2,q)  !rx_v(1,q)=the x-axis coordinate of nodes 2 in source tetrahedron
y2=ry_v(2,q)
z2=rz_v(2,q)
x3=rx_v(3,q)  !rx_v(1,q)=the x-axis coordinate of nodes 3 in source tetrahedron
y3=ry_v(3,q)
z3=rz_v(3,q)
x4=rx_v(4,q)  !rx_v(1,q)=the x-axis coordinate of nodes 4 in source tetrahedron
y4=ry_v(4,q)
z4=rz_v(4,q)
```

➤ If R > 0.2 λ, then n_p=1 is used

```
-----------------------------------
IF(dist.GT.0.2*wv_lgth) THEN
a=1./4.
r=1./6.

Rx1=a*(x1-x4)+a*(x2-x4)+a*(x3-x4)+x4-Xcp
Ry1=a*(y1-y4)+a*(y2-y4)+a*(y3-y4)+y4-Ycp
Rz1=a*(z1-z4)+a*(z2-z4)+a*(z3-z4)+z4-Zcp
R_1=sqrt(Rx1*Rx1+Ry1*Ry1+Rz1*Rz1)

G1 =(cexp(-j*k*R_1))/R_1

ANS1(p,q)=G1*r
ANS2(p,q)=G1*r*a
ANS3(p,q)=G1*r*a
ANS4(p,q)=G1*r*a
```

➢ If 0.1 λ <*R* < 0.2 λ, then *n_p*=5 is used

```
ELSE IF(dist.GT.0.1*wv_lgth.AND.dist.LE.0.2*wv_lgth) THEN
a=1./4.
b=1./6.
c=1./2.

Rx1=a*(x1-x4)+a*(x2-x4)+a*(x3-x4)+x4-Xcp
Ry1=a*(y1-y4)+a*(y2-y4)+a*(y3-y4)+y4-Ycp
Rz1=a*(z1-z4)+a*(z2-z4)+a*(z3-z4)+z4-Zcp
R_1=sqrt(Rx1*Rx1+Ry1*Ry1+Rz1*Rz1)

Rx2=c*(x1-x4)+b*(x2-x4)+b*(x3-x4)+x4-Xcp
Ry2=c*(y1-y4)+b*(y2-y4)+b*(y3-y4)+y4-Ycp
Rz2=c*(z1-z4)+b*(z2-z4)+b*(z3-z4)+z4-Zcp
R_2=sqrt(Rx2*Rx2+Ry2*Ry2+Rz2*Rz2)

Rx3=b*(x1-x4)+c*(x2-x4)+b*(x3-x4)+x4-Xcp
Ry3=b*(y1-y4)+c*(y2-y4)+b*(y3-y4)+y4-Ycp
Rz3=b*(z1-z4)+c*(z2-z4)+b*(z3-z4)+z4-Zcp
R_3=sqrt(Rx3*Rx3+Ry3*Ry3+Rz3*Rz3)

Rx4=b*(x1-x4)+b*(x2-x4)+c*(x3-x4)+x4-Xcp
Ry4=b*(y1-y4)+b*(y2-y4)+c*(y3-y4)+y4-Ycp
Rz4=b*(z1-z4)+b*(z2-z4)+c*(z3-z4)+z4-Zcp
R_4=sqrt(Rx4*Rx4+Ry4*Ry4+Rz4*Rz4)

Rx5=b*(x1-x4)+b*(x2-x4)+b*(x3-x4)+x4-Xcp
Ry5=b*(y1-y4)+b*(y2-y4)+b*(y3-y4)+y4-Ycp
Rz5=b*(z1-z4)+b*(z2-z4)+b*(z3-z4)+z4-Zcp

G1 =(cexp(-j*k*R_1))/R_1
G2 =(cexp(-j*k*R_2))/R_2
G3 =(cexp(-j*k*R_3))/R_3
G4 =(cexp(-j*k*R_4))/R_4
G5 =(cexp(-j*k*R_5))/R_5

r=-4./30.
f=9./120.

ANS1(p,q)=G1*r+G2*f+G3*f+G4*f+G5*f
ANS2(p,q)=G1*r*a+G2*f*c+G3*f*b+G4*f*b+G5*f*b
ANS3(p,q)=G1*r*a+G2*f*b+G3*f*c+G4*f*b+G5*f*b
ANS4(p,q)=G1*r*a+G2*f*b+G3*f*b+G4*f*c+G5*f*b
```

➢ If *R* < 0.1 λ, then *n_p*=11 is used

```
ELSE
a=1./4.
b=1./14.
c=11./14.
d=0.3994035761667992
e=0.1005964238332008
```

```
Rx1=a*(x1-x4)+a*(x2-x4)+a*(x3-x4)+x4-Xcp
Ry1=a*(y1-y4)+a*(y2-y4)+a*(y3-y4)+y4-Ycp
Rz1=a*(z1-z4)+a*(z2-z4)+a*(z3-z4)+z4-Zcp
R_1=sqrt(Rx1*Rx1+Ry1*Ry1+Rz1*Rz1)

Rx2=c*(x1-x4)+b*(x2-x4)+b*(x3-x4)+x4-Xcp
Ry2=c*(y1-y4)+b*(y2-y4)+b*(y3-y4)+y4-Ycp
Rz2=c*(z1-z4)+b*(z2-z4)+b*(z3-z4)+z4-Zcp
R_2=sqrt(Rx2*Rx2+Ry2*Ry2+Rz2*Rz2)

Rx3=b*(x1-x4)+c*(x2-x4)+b*(x3-x4)+x4-Xcp
Ry3=b*(y1-y4)+c*(y2-y4)+b*(y3-y4)+y4-Ycp
Rz3=b*(z1-z4)+c*(z2-z4)+b*(z3-z4)+z4-Zcp
R_3=sqrt(Rx3*Rx3+Ry3*Ry3+Rz3*Rz3)

Rx4=b*(x1-x4)+b*(x2-x4)+c*(x3-x4)+x4-Xcp
Ry4=b*(y1-y4)+b*(y2-y4)+c*(y3-y4)+y4-Ycp
Rz4=b*(z1-z4)+b*(z2-z4)+c*(z3-z4)+z4-Zcp
R_4=sqrt(Rx4*Rx4+Ry4*Ry4+Rz4*Rz4)

Rx5=b*(x1-x4)+b*(x2-x4)+b*(x3-x4)+x4-Xcp
Ry5=b*(y1-y4)+b*(y2-y4)+b*(y3-y4)+y4-Ycp
Rz5=b*(z1-z4)+b*(z2-z4)+b*(z3-z4)+z4-Zcp
R_5=sqrt(Rx5*Rx5+Ry5*Ry5+Rz5*Rz5)

Rx6=d*(x1-x4)+d*(x2-x4)+e*(x3-x4)+x4-Xcp
Ry6=d*(y1-y4)+d*(y2-y4)+e*(y3-y4)+y4-Ycp
Rz6=d*(z1-z4)+d*(z2-z4)+e*(z3-z4)+z4-Zcp
R_6=sqrt(Rx6*Rx6+Ry6*Ry6+Rz6*Rz6)

Rx7=d*(x1-x4)+e*(x2-x4)+d*(x3-x4)+x4-Xcp
Ry7=d*(y1-y4)+e*(y2-y4)+d*(y3-y4)+y4-Ycp
Rz7=d*(z1-z4)+e*(z2-z4)+d*(z3-z4)+z4-Zcp
R_7=sqrt(Rx7*Rx7+Ry7*Ry7+Rz7*Rz7)

Rx8=d*(x1-x4)+e*(x2-x4)+e*(x3-x4)+x4-Xcp
Ry8=d*(y1-y4)+e*(y2-y4)+e*(y3-y4)+y4-Ycp
Rz8=d*(z1-z4)+e*(z2-z4)+e*(z3-z4)+z4-Zcp
R_8=sqrt(Rx8*Rx8+Ry8*Ry8+Rz8*Rz8)

Rx9=e*(x1-x4)+d*(x2-x4)+d*(x3-x4)+x4-Xcp
Ry9=e*(y1-y4)+d*(y2-y4)+d*(y3-y4)+y4-Ycp
Rz9=e*(z1-z4)+d*(z2-z4)+d*(z3-z4)+z4-Zcp
R_9=sqrt(Rx9*Rx9+Ry9*Ry9+Rz9*Rz9)

Rx10=e*(x1-x4)+d*(x2-x4)+e*(x3-x4)+x4-Xcp
Ry10=e*(y1-y4)+d*(y2-y4)+e*(y3-y4)+y4-Ycp
Rz10=e*(z1-z4)+d*(z2-z4)+e*(z3-z4)+z4-Zcp
R_10=sqrt(Rx10*Rx10+Ry10*Ry10+Rz10*Rz10)

Rx11=e*(x1-x4)+e*(x2-x4)+d*(x3-x4)+x4-Xcp
Ry11=e*(y1-y4)+e*(y2-y4)+d*(y3-y4)+y4-Ycp
Rz11=e*(z1-z4)+e*(z2-z4)+d*(z3-z4)+z4-Zcp
```

```
G1 =(cexp(-j*k*R_1))/R_1
G2 =(cexp(-j*k*R_2))/R_2
G3 =(cexp(-j*k*R_3))/R_3
G4 =(cexp(-j*k*R_4))/R_4
G5 =(cexp(-j*k*R_5))/R_5
G6 =(cexp(-j*k*R_6))/R_6
G7 =(cexp(-j*k*R_7))/R_7
G8 =(cexp(-j*k*R_8))/R_8
G9 =(cexp(-j*k*R_9))/R_9
G10=(cexp(-j*k*R_10))/R_10
G11=(cexp(-j*k*R_11))/R_11

r=-74./5625.
f=343./45000.
h=56./2250.

ANS1(p,q)=G1*r+G2*f+G3*f+G4*f+G5*f+G6*h+G7*h
+         +G8*h+G9*h+G10*h+G11*h
ANS2(p,q)=G1*r*.25+G2*f*c+G3*f*b+G4*f*b+G5*f*b+G6*h*d+G7*h*d
+         +G8*h*d+G9*h*e+G10*h*e+G11*h*e
ANS3(p,q)=G1*r*.25+G2*f*b+G3*f*c+G4*f*b+G5*f*b+G6*h*d+G7*h*e
+         +G8*h*e+G9*h*d+G10*h*d+G11*h*e
ANS4(p,q)=G1*r*.25+G2*f*b+G3*f*b+G4*f*c+G5*f*b+G6*h*e+G7*h*d
+         +G8*h*e+G9*h*d+G10*h*e+G11*h*d
```

3. Instructions on running the programs

<div align="center">

Mesh antenna structure using GiD

⬇

Run a FORTRAN program called 'RWG SWG.for' to obtain

the antenna's input impedance and current distribution

⬇

Run a FORTRAN program called 'Far Field.for' to obtain

the far-field antenna parameters

</div>

i) Mesh antenna structure using GiD

- o Mesh dielectric volume into small tetrahedrons and surface metal into small triangles.
- o Collect information about the mesh. Record the data describing
    - ➢ nodes and coordinates as 'I – <DRA shape> <Number of tetrahedrons> Nodes.dat'

Node number   Coordinate in x   Coordinate in y   Coordinate in z

```
I - Hemispherical 2520 Nodes - Notepad
File  Edit  Format  View  Help
1       -1.25      -7.65379e-017 -1.53076e-016
2       -1.24214 -0.139956     -1.52113e-016
3       -1.24199  0.141326     -1.52094e-016
4       -1.24164 -4.46274e-011  0.14433
5       -1.06426 -0.0597677     5.62816e-018
6       -1.04878  0.179981      5.89493e-018
7       -1.21895  0.226216      0.159625
8       -1.21866 -0.278151     -1.49238e-016
9       -1.21804  0.28084      -1.49162e-016
10      -1.21667 -1.77913e-010  0.28673
```

➢ metal triangles and nodes as 'I – <DRA shape> <Number of tetrahedrons> Metal.dat'

Triangle Number   Node Numbers
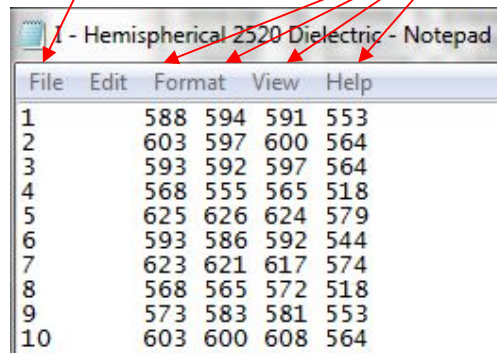
➢ boundary triangles and nodes as 'I – <DRA shape> <Number of tetrahedrons> Boundary.dat'

Triangle Number   Node Numbers

➤ tetrahedrons and nodes as 'I – <DRA shape> <Number of tetrahedrons>

   Dielectric.dat'

Tetrahedron Number   Node Numbers

ii) Run a Fortran program called 'RWG SWG.for'

o Ensure the mesh input files are located in the same folder as this Fortran
   program.

o Run the program. Enter inputs as requested by the program such as the
   operating frequency range, permittivity of dielectric and antenna mode of
   operation.

o The important outputs from this program are the antenna's

   ➤ Input impedance, saved as 'O – Zin.dat'

   Real part of Z_{in} Imaginary part of Z_{in}

➢ Current Distribution, saved as 'O – Current.dat'

Real part of current   Imaginary part of current

Current
associated
with each
basis function

ii) Run a Fortran program called 'Far field.for'

o Ensure the output files from the previous program, i.e. 'O – Zin.dat' and 'O – Current.dat' are located in the same folder as this Fortran program.

o Run the program. Enter inputs as requested by the program such as the operating frequency, permittivity of dielectric and far-field plane orientation.

o The outputs from this program are the far-field parameters of

➢ E_θ and E_Φ, saved as 'O – Eth(polar).dat' and 'O – Eph(polar).dat'

➢ E_R and E_L, saved as 'O – ER(polar).dat' and 'O – EL(polar).dat'

➢ Axial Ratio, saved as 'O – AR.dat'

➢ Gain, saved as 'O – Gain.dat'